Copper Diffusion in Silicate Melts and Melt Inclusion Study on Volatiles in The Lunar Interior

by

Peng Ni

A dissertation submitted in partial fulfillment
of the requirements for the degree of
Doctor of Philosophy
(Earth and Environmental Sciences)
in the University of Michigan
2017

Doctoral Committee:
Professor Youxue Zhang, Chair
Professor Rebecca A. Lange
Professor Jie (Jackie) Li
Associate Professor Adam C. Simon
Associate Professor Angela Violi

Peng Ni

pengni@umich.edu

ORCID ID: 0000-0002-1178-6892

To

my wife, Shuang and our families

ACKNOWLEDGEMENTS

I would like to express the deepest appreciation to my dissertation advisor, Youxue Zhang, who always conveyed an enthusiasm for science, a thorough knowledge on various fields, and a spirit of hard working. Without his support and patience, I won't be able to successfully finish my dissertation. I would also like to thank my other committee members, Adam Simon, Jie Li, Becky Lange and Angela Violi, for their valuable suggestions and insightful comments that greatly improved my dissertation.

I would also like to thank all my lab-mates who discussed with me to solve the experimental problems I've faced. I would like to especially thank Zhengjiu Xu for her systematic training on a variety of experimental techniques. I thank Dr. Gordon Moore for help with electron microprobe analyses and discussion on scientific problems, Dr. Yunbin Guan, Dr. Joel Gagnon, J. C. Barrette, Dr. Matt Newville and Dr. Tony Lanzirotti for their help with various analytical instruments. My thanks go to all the faculty members, friends and fellow graduate students in the department who helped make it enjoyable to study and work here.

I would like to thank my parents and grandparents for their love and support through all the years. Thanks to all the friends I met through this journey, who added spices into my life. Last but most importantly, thanks to my wife Shuang, for her love and accompany, they mean everything to me and are essential for the accomplishment of this work.

TABLE OF CONTENTS

LIST OF TABLES

Table Page

LIST OF FIGURES

LIST OF APPENDICES

ABSTRACT

This thesis focuses on the application of diffusion kinetics to both terrestrial and lunar geochemistry. In Chapters II and III, diffusivities of Cu in silicate melts were experimentally determined and used to discuss the role of Cu diffusion in formation of Cu ore deposits and also Cu isotope fractionation in tektites. In Chapters IV and V, lunar olivine-hosted melt inclusions are studied to understand their volatile loss during homogenization in lab, to estimate cooling rate for lunar Apollo sample 74220, and to estimate volatile abundance in the lunar mantle.

Magmatic sulfide deposits and porphyry-type Cu deposits are two major types of Cu deposits that supply the world's Cu. In particular, porphyry-type Cu deposits provide ~57% of the world's total discovered Cu. Recent studies suggest a potential role of diffusive transport of metals (e.g. Cu, Au, PGE, Mo) in the formation of magmatic sulfide deposits and porphyry-type deposits. Diffusivities of Cu in silicate melts, however, are poorly determined. In Chapters II and III of this thesis, Cu diffusion in basaltic melt and rhyolitic melts are studied by diffusion couple and chalcocite "dissolution" methods. Our results indicate high diffusivities of Cu and a general equation for Cu diffusion in silicate melts is obtained. The high diffusivity of Cu indicate that partition of Cu between the silicate phase and the sulfide or fluid phase can be assumed to be in equilibrium during the formation of magmatic sulfide deposits or porphyry-type deposits. In addition, our Cu diffusion data helps explain why Cu isotopes are more fractionated than Zn isotopes in tektites.

Volatile abundances in the lunar mantle have profound implications for the origin

of the Moon, which was thought to be bone-dry till about a decade ago, when trace amounts of H_2O were detected in various types of lunar samples. In particular, high H_2O concentrations comparable to mid-ocean ridge basalts were reported in lunar melt inclusions. There are still uncertainties, however, for lunar melt inclusion studies in at least two aspects. One is whether the low H_2O/Ce ratios measured in homogenized crystalline inclusions are affected by the homogenization process. The other is that current estimation of volatile abundances in lunar mantle relies heavily on 74220, which is argued to be a local anomaly by some authors. In order to reach a conclusive answer on volatile abundances in lunar mantle, the above two questions have to be answered. To improve our understanding about these questions, in Chapter IV of this thesis, a series of experiments are carried out to understand possible volatile loss from lunar melt inclusions during homogenization. Our results indicate significant H_2O loss from inclusions during homogenization in minutes, whereas loss of F, Cl or S is unlikely a concern under our experimental conditions. The most applicable way to preserve H_2O during homogenization is to use large inclusions. In Chapter V of this thesis, volatile, trace and major element data for melt inclusions from 10020, 12040, 15016, 15647 and 74235 are reported. Our new data indicate large variation in H_2O/Ce ratios from ~77 to ~1 across different lunar samples, which is at least partially due to H_2O loss on lunar surface during cooling. In addition, evidences were found in F/Nd and S/Dy ratios that might suggest lunar mantle heterogeneity in terms of its volatile abundances.

CHAPTER 1

Introduction

Kinetics is a powerful tool in understanding various geological processes. One of the most important applications is isotope geochronology, which uses radiogenic isotope systems to determine the age of rocks. Kinetic studies are also often conducted to understand thermal histories, formation and retention of compositional zonation in minerals, bubble growth and volcanic eruptions, fractionation of elements during kinetically controlled processes and diffusion-controlled isotope fractionation. With rapid development in advanced analytical methods such as secondary ion mass spectrometry (SIMS), laser ablation -inductively coupled plasma –mass spectrometry (LA-ICP-MS) and micro absorption near-edge structure (μXANES), micrometer-scale trace element profiles, volatile element profiles and even valance state profiles are becoming more and more readily available, which brings more opportunities in kinetic studies. This thesis focuses on kinetic studies to understand various terrestrial and lunar geological processes. In chapters II and III, Cu diffusivities in silicate melts are studied to understand the role of kinetic control on formation of Cu-bearing ore deposits and on Cu isotope fractionation in tektites. In chapters IV and V, experiments are done to understand diffusive loss of volatiles (H_2O, F, Cl and S) from lunar melt inclusions during homogenization, and the results are applied in interpreting new and old melt inclusion data to understand volatile abundances in the lunar mantle and their implications on Moon formation.

1.1 Copper diffusion in silicate melts

As an important base metal tightly bound with infrastructure construction, enrichment of Cu from 30 ppm in the bulk silicate earth (McDonough and Sun 1995) to a typically minable

grade of 1000s of ppm is mainly due to its strong compatibility in sulfides, and its ability to form soluble complexes (e.g. CuCl, $NaCuCl_2$) in magmatic fluid phases. Magmatic sulfide deposits and porphyry-type Cu deposits are two major types of deposits that produce Cu. In particular, porphyry-type deposits account for ~57% of total discovered Cu in the world (Singer 1995).

Magmatic sulfide deposits typical form in a mafic or ultramafic magma. Possible sulfur saturation during cooling lead to the formation and separation of sulfide drops from the silicate magma. Since the sulfide drops are denser than the silicate magma, they sink through the magma chamber, at the same time scavenging chalcophile elements (e.g. Cu, Au, Pt) from the surrounding melt. During this process, the enrichment of metals into the sulfide phase is a balance between their diffusivities in the silicate magma, and the sinking and growth of the sulfide drops (e.g. Mungall 2002; Zhang 2015). In that case, metal elements with high diffusivities might be more efficiently enriched into the sulfide drops than those with low diffusivities, resulting in a fractionation of metal ratios in the final deposit. A similar scenario occurs during porphyry-type deposit formation, where a saturated fluid phase scavenges and transports metals (e.g.Cu, Au, Mo) from the silicate magma to the shallower crust, forming economically valuable deposits. Recent studies by Huber et al. (2012) suggest that, if the fluid phase upwells rapidly in fluid channels, diffusivities of these metal elements in the silicate melt might control the efficiency in their enrichment and transport by the fluid phase.

Besides the possible role in affecting Cu deposit formation, Cu diffusivity also has important applications in discussing isotope fractionation in tektites. Moynier et al. (2010) measured Cu isotopes in tektites, and found that Cu isotopes are more fractionated compared to Zn isotopes in the same set of tektite samples (Moynier et al. 2009). This is in contrary to the expectation that fractionation is due to volatile loss because Zn has a lower half-condensation temperature ($T_{1/2}$=726K, Lodders 2003) and should be more easily lost compared to Cu ($T_{1/2}$=1037 K, Lodders 2003). The authors invoked a "diffusion-limited" mechanism, which suggests that the more fractionated Cu isotopes in tektites are due to the higher diffusivity of Cu^+

compared to Zn^{2+} in silicate melt, and the higher diffusivity of Cu^{+} leads to more rapid loss of Cu during the short period of high-temperature heating experienced by tektites.

Despite the potential role of kinetically control in various geological processes as discussed above, Cu diffusivities in silicate melts are poorly determined. According to our knowledge, prior to this dissertation work only one experimental study determined Cu diffusivities in a $Na_2Si_2O_5$ melt by voltammetry method (von der Gönna and Rüssel 2000). Such a melt composition, however, is significantly different from natural melts and cannot be directly applied in discussing natural processes. To improve our understanding on Cu diffusion in silicate melts, first half of this dissertation is dedicated to experimentally constraining Cu diffusivities in natural silicate melts, and applying measured data to natural processes such as magmatic sulfide and porphyry-type Cu deposit formation, and fractionation of Cu isotopes in tektites.

1.2 Melt inclusion study on volatiles in the lunar interior

The most widely accepted model for Moon formation is the giant impact theory, in which the Moon formed after a giant impact between a Mars-sized planetary body and the proto-earth. Prior to 2006, the Moon was thought to be bone-dry because of the un-detectable amount of water and absence of hydrous minerals (Taylor et al. 2006). Since about a decade ago, however, evidences for a relatively "wet" Moon emerged as trace amounts of H_2O were detected in lunar volcanic glass beads (Saal et al. 2008, 2013; Chen et al. 2015; Hauri et al. 2015), nominally anhydrous minerals (Hui et al. 2013), and lunar olivine-hosted melt inclusions (Hauri et al. 2011; Chen et al. 2015; Hauri et al. 2015). Among these types of samples, olivine-hosted melt inclusions are small pieces of magma trapped in olivine crystal structure. As protected by the hosted olivine crystal, melt inclusions have better chances to preserve pre-eruptive amount of volatiles during eruption (e.g. Anderson 1974; Sobolev 1996; Danyushevsky et al. 2002). Indeed, highest concentrations of H_2O directly detected in lunar samples are from olivine-hosted melt inclusions (up to ~1400 ppm, Hauri et al. 2011). More recently, the lunar melt inclusion study by

Chen et al. (2015) estimated volatile abundances (H_2O, F, S) in lunar mantle based on H_2O/Ce, F/Nd and S/Dy ratios, and concluded that lunar mantle contains similar or slightly lower amount of H_2O, F and S compared to terrestrial upper mantle.

Despite the powerful role of lunar melt inclusions in estimating volatiles in the lunar interior, uncertainties occur, however, in at least two aspects for lunar melt inclusions studies. One uncertainty is that, most inclusions identified in mare basalts are highly crystallized and require homogenization experiments to form a glassy phase for precise major and trace element analyses. Hence, whether H_2O and other elements could be lost from inclusions during such a process becomes a critical issue to be resolved. Although similar experiments have been conducted previously (e.g. Hauri 2002; Portnyagin et al. 2008; Chen et al. 2011; Gaetani et al. 2012), they might not be suitable for lunar melt inclusions because of the significantly lower oxygen fugacity on Moon that might affect diffusive H exchange between inclusions and the exterior. One concern in the study by Chen et al. (2015) was that, whether the low H_2O/Ce ratios in crystalline melt inclusions were due to H_2O loss during heating in lab. Another uncertainty is that, results obtained in Chen et al. (2015) relies heavily on the lunar soil sample 74220, which is interpreted as a local anomaly by some authors (Albarede et al. 2013, 2015). Therefore, a more thorough understanding of volatiles in the Moon requires studies on a wider collection of lunar basalt samples. Second half of this dissertation is a melt inclusion study aiming at improving our understanding on the above two issues.

1.3 Structure of the dissertation

Chapter II and Chapter III are dedicated to experimentally study Cu diffusion in silicate melts. In Chapter II, Cu diffusion in an anhydrous basaltic melt was determined by the diffusion couple method in the temperature range of 1298 to 1581 ºC and pressure range between 0.5 and 1.5 GPa. In Chapter III, Cu diffusion in anhydrous and hydrous rhyolitic melts containing up to 5.95 wt% H_2O were studied by chalcocite (Cu_2S) "dissolution" experiments at temperatures of

750 to 1391 ºC. A more general equation for Cu diffusivity in natural silicate melts was also obtained by incorporating Cu diffusion data in basaltic melt from Chapter II. The results were used to discuss the role of Cu diffusion in various geological processes such magmatic sulfide or porphyry-type Cu deposits formation, and Cu isotope fractionation in tektites.

In Chapter IV, a series of homogenization experiments were done on lunar melt inclusions from 74220 to systematically study the possible loss of H_2O and other volatiles during homogenization of lunar melt inclusions. The depletion trend for H_2O concentrations in inclusions after homogenization was fit by a diffusive equilibrium model to be compared with previous experiments in the literature using terrestrial inclusions. Based on our results, the variation in H_2O/Ce across different lunar samples is confirmed, which needs to be explained by either H_2O loss during magma eruption and cooling on lunar surface, or lunar mantle heterogeneity.

In Chapter V, newly obtained lunar melt inclusion data from 5 lunar samples (10020, 12040, 15016, 15647 and 74235) are reported. Volatile versus refractory element ratios (H_2O/Ce, F/Nd, Cl/K and S/Dy) were used to assess volatile abundances in lunar mantle. By comparing such ratios across different samples from this study and in the literature, possible heterogeneities of volatile abundances in the Moon were also assessed.

1.4 References

Albarede, F., Ballhaus, C., Blichert-Toft, J., Lee, C.-T., Marty, B., Moynier, F., and Yin, Q.-Z. (2013) Asteroidal impacts and the origin of terrestrial and lunar volatiles. Icarus, 222, 44–52.

Albarede, F., Albalat, E., and Lee, C.-T.A. (2015) An intrinsic volatility scale relevant to the Earth and Moon and the status of water in the Moon. Meteoritics & Planetary Science, 50, 568–577.

Anderson, A.T. (1974) Chlorine, Sulfur, and Water in Magmas and Oceans. Geological Society of America Bulletin, 85, 1485–1492.

Chen, Y., Provost, A., Schiano, P., and Cluzel, N. (2011) The rate of water loss from olivine-hosted melt inclusions. Contributions to Mineralogy and Petrology, 162, 625–636.

Chen, Y., Zhang, Y., Liu, Y., Guan, Y., Eiler, J., and Stolper, E.M. (2015) Water, fluorine, and sulfur concentrations in the lunar mantle. Earth and Planetary Science Letters, 427, 37–46.

Danyushevsky, L.V., McNeill, A.W., and Sobolev, A.V. (2002) Experimental and petrological studies of melt inclusions in phenocrysts from mantle-derived magmas: an overview of techniques, advantages and complications. Chemical Geology, 183, 5–24.

Gaetani, G.A., O'Leary, J.A., Shimizu, N., Bucholz, C.E., and Newville, M. (2012) Rapid reequilibration of H2O and oxygen fugacity in olivine-hosted melt inclusions. Geology, 40, 915–918.

Hauri, E. (2002) SIMS analysis of volatiles in silicate glasses, 2: isotopes and abundances in Hawaiian melt inclusions. Chemical Geology, 183, 115–141.

Hauri, E.H., Weinreich, T., Saal, A.E., Rutherford, M.C., and Orman, J.A.V. (2011) High Pre-Eruptive Water Contents Preserved in Lunar Melt Inclusions. Science, 333, 213–215.

Hauri, E.H., Saal, A.E., Rutherford, M.J., and Van Orman, J.A. (2015) Water in the Moon's interior: Truth and consequences. Earth and Planetary Science Letters, 409, 252–264.

Huber, C., Bachmann, O., Vigneresse, J.-L., Dufek, J., and Parmigiani, A. (2012) A physical model for metal extraction and transport in shallow magmatic systems. Geochemistry, Geophysics, Geosystems, 13, Q08003.

Hui, H., Peslier, A.H., Zhang, Y., and Neal, C.R. (2013) Water in lunar anorthosites and evidence for a wet early Moon. Nature Geoscience, 6, 177–180.

Lodders, K. (2003) Solar System Abundances and Condensation Temperatures of the Elements. The Astrophysical Journal, 591, 1220.

McDonough, W.F., and Sun, S. -s. (1995) The composition of the Earth. Chemical Geology, 120, 223–253.

Moynier, F., Beck, P., Jourdan, F., Yin, Q.-Z., Reimold, U., and Koeberl, C. (2009) Isotopic fractionation of zinc in tektites. Earth and Planetary Science Letters, 277, 482–489.

Moynier, F., Koeberl, C., Beck, P., Jourdan, F., and Telouk, P. (2010) Isotopic fractionation of Cu in tektites. Geochimica et Cosmochimica Acta, 74, 799–807.

Mungall, J.E. (2002) Kinetic Controls on the Partitioning of Trace Elements Between Silicate and Sulfide Liquids. Journal of Petrology, 43, 749–768.

Portnyagin, M., Almeev, R., Matveev, S., and Holtz, F. (2008) Experimental evidence for rapid water exchange between melt inclusions in olivine and host magma. Earth and Planetary Science Letters, 272, 541–552.

Saal, A.E., Hauri, E.H., Cascio, M.L., Van Orman, J.A., Rutherford, M.C., and Cooper, R.F. (2008) Volatile content of lunar volcanic glasses and the presence of water in the Moon's interior. Nature, 454, 192–195.

Saal, A.E., Hauri, E.H., Orman, J.A.V., and Rutherford, M.J. (2013) Hydrogen Isotopes in Lunar Volcanic Glasses and Melt Inclusions Reveal a Carbonaceous Chondrite Heritage. Science, 340, 1317–1320.

Singer, D.A. (1995) World class base and precious metal deposits; a quantitative analysis. Economic Geology, 90, 88–104.

Sobolev, A.V. (1996) Melt inclusions in minerals as a source of principle petrological information. Petrology, 4, 209–220.

Taylor, S.R., Pieters, C.M., and MacPherson, G.J. (2006) Earth-Moon System, Planetary Science, and Lessons Learned. Reviews in Mineralogy and Geochemistry, 60, 657–704.

von der Gönna, G., and Rüssel, C. (2000) Diffusivity of various polyvalent elements in a Na2O·2SiO2 glass melt. Journal of Non-Crystalline Solids, 261, 204–210.

Zhang, Y. (2015) Toward a quantitative model for the formation of gravitational magmatic sulfide deposits. Chemical Geology, 391, 56–73.

CHAPTER II

Copper diffusion in a basaltic melt

2.1 Abstract

Recent studies suggest a potential role of diffusive transport of metals (e.g. Cu, Au, PGE) in the formation of magmatic sulfide deposits and porphyry-type ore deposits. However, diffusivities of these metals are poorly determined in natural silicate melts. In this chapter, diffusivities of copper in an anhydrous basaltic melt (<10 ppm H_2O) were measured at temperatures from 1298 to 1581 ºC, and pressures of 0.5 GPa, 1 GPa and 1.5 GPa. Copper diffusivities in anhydrous basaltic melt at 1 GPa can be described as:

$$D_{Cu}^{basalt} = \exp\left[-(14.12 \pm 0.50) - \frac{11813 \pm 838}{T}\right]$$

where D_{Cu}^{basalt} is the diffusivity in m^2/s, T is the temperature in K, and errors are given at 1σ level. A fitting of all experimental data considering the pressure effect is:

$$D_{Cu}^{basalt} = \exp\left[-(13.59 \pm 0.81) - \frac{(12153 \pm 1229) + (620 \pm 241)P}{T}\right]$$

where P is the pressure in GPa, which corresponds to a pre-exponential factor D_0 = (1.25 $\times\div$ 2.2)×10^{-6} m^2/s, an activation energy E_a = 101±10 kJ/mol at P = 0, and an activation volume V_a= (5.2±2.0)×10^{-6} m^3/mol.

The diffusivity of Cu in basaltic melt is high compared to most other cations, similar to that of Na. The high Cu diffusivity is consistent with the occurrence of Cu mostly as Cu^+ in silicate melts at or below NNO. Compared to the volatile species, Cu diffusivity is generally smaller than water diffusivity, but about 1 order of magnitude higher than S and

Cl diffusivities. Hence, Cu partitioning between a growing sulfide liquid drop and the surrounding silicate melt is roughly in equilibrium, whereas that between a growing fluid bubble and the surrounding melt can be out of equilibrium if the fluid is nearly pure H_2O fluid. Our results are the first Cu diffusion data in natural silicate melts, and can be applied to discuss natural processes such as Cu transport and kinetic partitioning behavior in ore formation, as well as Cu isotope fractionation caused by evaporation during tektite formation.

2.2 Introduction

As an important base metal widely used in construction and industry, enrichment of Cu from a crustal average of 27 ppm (Rudnick and Gao 2014) to a typical minable concentration of a few thousand ppm has attracted much attention from economic geologists. Magmatic sulfide deposits and porphyry Cu deposits are two main types of deposits that produce Cu. In particular, porphyry-type deposits account for ~57% of world's total discovered Cu (Singer 1995).

As described by Naldrett (1989), magmatic sulfide ore deposits are typically related to a mafic or ultramafic magma. Cooling of the magma leads to the saturation of S, and results in the nucleation and growth of sulfide liquid drops. Since sulfide drops have higher density than the silicate melt, they will sink through the magma chamber, at the same time growing and scavenging ore elements (e.g. Cu, Ni, Au, and Pt-group elements) from the surrounding magma. Given enough time, these sulfide drops will settle to the bottom of the magma chamber and form sulfide ore deposits (Zhang 2015). The mechanism for porphyry-type ore deposits to enrich Cu is similar, but instead of a sulfide liquid phase settling down in the magma chamber for magmatic sulfide deposits, a fluid phase is saturated inside the magma, and rises through the magma chamber, scavenging and transporting ore metals (e.g. Cu, Au, Mo) to the top of the magma chamber. In both types of ore deposits, enrichment of the metals into the sulfide phase or fluid phase is controlled by at least two factors: (i) partitioning of the metal elements into the sulfide or fluid phase, which may depend on the presence of other elements, such as Cl in the fluid phase,

and (ii) diffusion of the metal elements through the silicate melt to the sulfide or fluid phase. For magmatic sulfide deposits, Mungall (2002a) modeled the kinetic control of metal partitioning assuming a sulfide drop is static inside the magma, and found that the enrichment factors of metals can differ by as large as a factor of 5 depending on the diffusivity of each metal. Zhang (2015) developed a quantitative model for magmatic sulfide deposits considering both sulfide sinking and growth in silicate magma. Metal behavior was also modeled in Zhang (2015) parametrically, concluding that as long as the metal diffusivity is larger than or similar to S diffusivity that controls sulfide drop growth, partition of the metal into the sulfide liquid phase is close to equilibrium. Both Mungall (2002a) and Zhang (2015) used the empirical model by Mungall (2002b) to estimate metal diffusivities. The model of Mungall (2002b) indicates that Cu diffusion is much faster than sulfur diffusion. Therefore, both authors concluded that partition of Cu into the sulfide phase is close to equilibrium. On the other hand, Huber et al. (2012) developed a model for metal enrichment and transport by a fluid phase in a porphyry system, and suggested that the efficiency of Cu enrichment is dependent on the relative diffusivity of Cu to that of Cl. Huber et al. (2012) used Cu diffusion data from von der Gonna and Russel (2000), with copper diffusivity being 1 order of magnitude smaller than Cl diffusivity. Therefore, copper partition into the fluid phase would not reach equilibrium if the fluid bubbles ascend rapidly according to Huber et al. (2012).

In addition to metal enrichment processes discussed above, some other processes in ore formation might also be kinetically controlled. For example, in magmatic sulfide deposits, after sulfide liquid accumulation at the bottom of the magma chamber to form a sulfide liquid pool, the interaction between the sulfide liquid pool and the magma might be diffusion-controlled (Mungall 2002a). At the same time, metal extraction from other minerals into the sulfide melts is controlled by diffusion of the metal in the mineral phase (e.g., extraction of Ni from olivine; Zhang 2015). For porphyry-type ore deposits, re-dissolution of the sulfides and transport of their metal elements

from the more mafic magma to the silicic magma by a magmatic volatile phase is also partially controlled by diffusivities of the metal elements in the melts (Nadeau et al. 2010, 2013).

Besides roles in Cu ore formation, Cu diffusivity is also an important parameter in discussing Cu isotope fractionation. Moynier et al. (2010) measured Cu isotopes in tektites, and found that Cu isotopes are more fractionated than Zn isotopes in the same set of tektite samples. This is contrary to the notion that fractionation is due to volatile loss because Zn has lower half-condensation temperature and is hence more easily lost than Cu. The authors explained their results by a higher diffusivity of Cu than Zn in silicate melts, implying that the isotope fractionation was diffusion-limited.

Copper diffusion data in silicate melts are limited. Although there is a single study of Cu diffusivity in a $Na_2Si_2O_5$ melt by von der Gonna and Russel (2000), there are currently no Cu diffusion data in natural silicate melts. Cu diffusivity in the $Na_2Si_2O_5$ melt is unlikely applicable to Cu diffusion during Cu ore formation from a natural silicate melt. Even though there is an empirical model by Mungall (2002b) to estimate diffusivity, as Behrens and Hahn (2009) and Zhang et al. (2010) pointed out, Mungall (2002b)'s diffusivity model may be orders of magnitude off in predicting diffusivities. Hence, experimental data are necessary for more quantitative prediction of the diffusion effects.

In this study, diffusion couple experiments are carried out to obtain Cu diffusivities in a basaltic melt, and the results are used to discuss Cu enrichment in ore formation, and to speculate on kinetic controls of Cu isotope fractionation.

2.3 Experimental and analytical methods

2.3.1 Starting glasses

Two glasses with the same major element composition but different Cu concentrations were synthesized for the diffusion couple experiments. A major element composition of Etna basalt was chosen since it has been well studied in terms of melt properties: both melt viscosity

and S diffusivity have been measured for this melt composition (Giordano and Dingwell 2003; Freda et al. 2005).

In order to synthesize the starting glasses, a total weight of ~6.5 g of oxides (SiO_2, TiO_2, Al_2O_3, Fe_2O_3, MgO) and carbonates ($CaCO_3$, Na_2CO_3, K_2CO_3) were weighed based on the target composition of Etna basalt (Freda et al. 2005) and well mixed under alcohol in an agate mortar. Then the mixture of the oxides and carbonates was divided into two halves, one of which was doped with Cu_2O to contain ~1200 ppm Cu. Afterwards, approximately 0.6 g of the Cu-free mixture and Cu-containing mixture were put into separate graphite crucibles and fused at 1300 ºC for 3 hours together inside a Deltech furnace under a constant N_2 flow. After fusing, the two crucibles were taken out of the furnace and cooled in air to form two glass beads with a diameter of ~8 mm.

The glasses synthesized were examined under optical microscope to ensure that they are bubble free, crystal free and homogeneous in color. A center section was cut from each glass bead and analyzed by electron microprobe to check its homogeneity before it was used for diffusion couple experiments. Average compositions of the synthesized glasses are shown in Table 2.1. In general, microprobe data show that the composition of the synthesized glass matches the target composition fairly well (difference <1 wt% for each major component). FeO concentration was found to decrease slightly (~8% relative) towards the surface of the glass beads. Cu concentration was also found to be slightly inhomogeneous, with lower concentration near the surface of the glass beads (~1000 ppm) than at the center of the glass beads (~1300 ppm) (Fig. 2.1). To avoid possible effects of inhomogeneity in glass composition to our experiments, only center parts of the synthetic glasses were used for diffusion couple experiments.

H_2O and CO_2 concentrations in the synthetic Etna basaltic glasses are below ~10 ppm and ~100 ppm, respectively, based on FTIR measurements using a Perkin-Elmer Spectrum GX FTIR spectrometer at the University of Michigan.

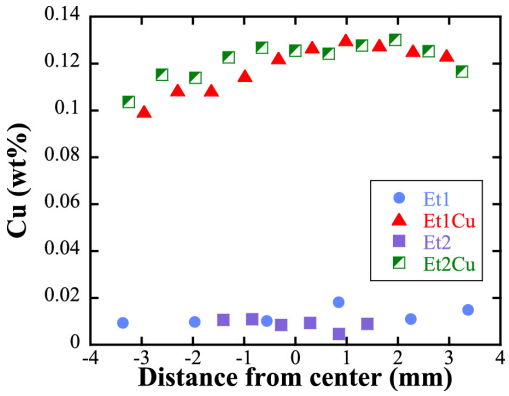

Figure 2.1. Copper concentration profiles measured across the center sections of four synthesized glass beads. Distances shown in the figure are relative to the approximate center of the glass beads.

2.3.2 Experimental procedure

All diffusion couple experiments were conducted in a piston-cylinder apparatus at the University of Michigan. An illustration of the experimental design for our diffusion couple experiments can be found in Fig. 2.2, and the experimental procedures are as follows. First, two glass cylinders with a diameter of 2.0 mm and height of 1.5 mm were prepared, one from Cu-free and the other from Cu-containing synthetic glass beads. The choice of 1.5 mm height of each glass cylinder used in our experiments is a compromise between two factors. One factor is that shorter cylinders lead to shorter experimental charge and hence smaller temperature variation across the whole charge. The other is that the cylinder must be tall enough so that Cu diffusion would not reach the boundary of the glass during the experiment. The glass cylinders were doubly polished using progressively finer silicon carbide sandpapers and a finish on 0.1-µm alumina powder. Afterwards, the two glass cylinders were ultrasonically cleaned in acetone and then in alcohol. After drying in vacuum for about 1 hour, the two glass cylinders were placed together and fit snugly into a 4.0-mm outer-diameter graphite capsule. The Cu-free glass was placed on top since it is expected to have a slightly lower density. The graphite capsule was fit into an MgO pressure medium, then placed inside a graphite furnace, and then into a $BaCO_3$ outer pressure medium. Geometry of the sample assemblage was designed so that the interface is at the center of the graphite furnace to minimize temperature gradient across the capsule (Fig. 2.2). A type-S

thermocouple (Pt90Rh10-Pt) was used to measure the temperature during an experiment. The length of each part of the sample assemblage was measured after an experiment to examine whether the interface was at the center of the graphite furnace during the experiment. The distance of the thermocouple tip to the diffusion interface was typically 2.5 to 3 mm. Temperature correction was made using the calibration of Hui et al. (2008). Temperature at the interface of the diffusion couple was used as the experimental temperature. The temperature at the two ends of the diffusion couple is estimated to be 10 to 20 ºC below the interface temperature using the calibration of Hui et al. (2008).

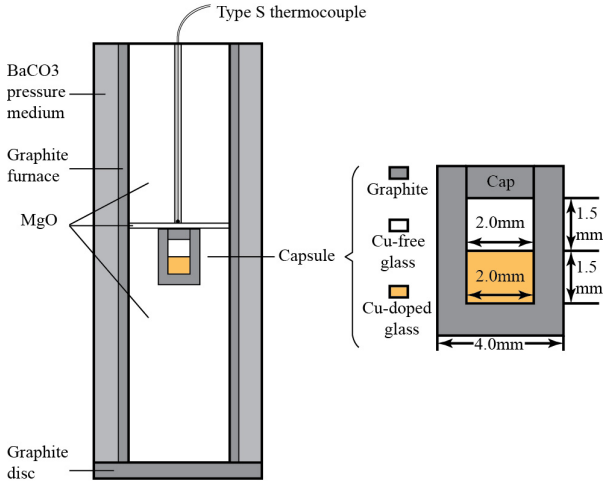

Figure 2.2. Illustration of the experimental design for our diffusion couple experiments (modified from Wang et al. 2009). Interface between the two glass halves are aligned to be at the center of the graphite heater to minimize temperature gradient. The scale in the figure is not exact.

Experiments were conducted at pressures of 0.5 to 1.5 GPa at a 0.5 GPa increment. A 5% pressure correction is applied based on calibration by Ni and Zhang (2008) on the same piston cylinder apparatus. During an experimental run, the pressure was first increased slowly and smoothly to 15% higher than the target pressure (10% in the case of 1.5 GPa experiment) using a pressure controller. Then the whole sample assemblage was relaxed at this pressure and 200 ºC for at least 2.5 hours to close gaps inside the assemblage. Both pressure and temperature were maintained automatically in this step. After relaxation, the temperature was brought up to the designated temperature in ~60 s by a programed heating procedure. No temperature overshoot

occurred during heating-up, and temperature fluctuation was within ±1 ºC during the experiments. Due to high Cu diffusivity, only a short duration was needed in the diffusion couple experiments (2 to 7 minutes at 1298 ºC to 1581 ºC) to generate a long enough profile. After a designated duration, the assemblage was quenched with a cooling rate of about 100 ºC/s (based on direct measurement) by turning off the power. During quench, the pressure was maintained by a manually controlled ENERPAC electric pump (except for Cudiffcp 4.4 and Cudiffcp 7.2, for which the pressure was maintained by the pressure controller). The whole sample assemblage was then preserved inside an epoxy resin disc and polished to expose the center section for electron microprobe analysis.

Since the experimental duration was only 2 to 7 minutes, the effect of heating up (taking ~1 min) needs to be considered. Quenching is rapid and hence the effect is small, but the small effect is also accounted for in the following correction applied to obtain the effective duration for all experiments. Based on the solution to the diffusion problem for time-dependent D (e.g., Zhang, 2008, Eq. 3-54b), the following equation was used to calculate the effective duration at the experimental temperature T_0:

$$t_c = \frac{\int_0^t \exp(-E/RT)\,dt}{\exp(-E/RT_0)} \tag{2.1}$$

where t_c is the effective duration, E is the activation energy for Cu diffusion, R is the gas constant, T is recorded experiment temperature (including temperature recorded during heating up and that during cooling down) corrected to the interface position, and T_0 is the plateau interface temperature. At the beginning an estimated E was used for the effective duration correction. After enough experiments were done, E was obtained by fitting the Arrhenius equation and t_c was corrected again until t_c and E do not change anymore. Copper diffusion has a small activation energy, leading to a relatively large duration correction of ~35 s.

2.3.3 Analytical methods

Major element composition and Cu concentration profiles were measured in WDS mode using the Cameca SX-100 electron microprobe at the University of Michigan. Major oxide concentrations (SiO_2, TiO_2, Al_2O_3, FeO_t, MgO, CaO, Na_2O and K_2O) of the synthetic glasses were measured with an acceleration voltage of 15 kV, a beam current of 10 nA in focused mode, and a counting time of 30 to 40 seconds on the peak and 15 to 20 seconds on each side of the backgrounds. The following standards were used for the microprobe analysis: albite (ALBA) for Na, forsterite (FOBO) for Mg and Si, sillimanite (SILL) for Al, potassium feldspar (GKFS) for K, wollastonite (WOLL) for Ca, geikielite (GEIK) for Ti, and ferrosilite (FESI) for Fe. Copper concentrations were measured in separate sessions using a point beam with an acceleration voltage of 15 kV and a beam current of 40 nA. The standard for Cu concentration measurement is chalcopyrite (CPY). Three spectrometers were employed to count Cu at the same time. The counting time is 240 s on the Cu Ka peak and 120 s on either side of the background to achieve a detection limit of ~80 ppm for Cu. The analytical error given by the microprobe based on counting statistics is ~80 ppm (1σ). NIST SRM 610 was used as a secondary standard for Cu in our analysis. The average concentration of Cu in SRM 610 was reported by Pearce et al. (1997) to be 422±42 ppm. Our microprobe analysis yielded a Cu concentration of 464 ppm to 516 ppm on SRM 610. The shift of absolute concentrations results in a shift of the entire Cu diffusion profile. However, since the amount of the shift was similar for both the low and high Cu concentration ends, the diffusivity obtained from the profile is not affected. To evaluate whether the shift in absolute Cu concentration has significant effect on Cu diffusivity, the sample Cudiffcp 3.1 was analyzed twice on two different days. The entire Cu concentration profile measured on two days shifted by 194 ppm from each other. After subtracting a constant concentration of 194 ppm from the profile in day 2, the profiles measured on different days closely match each other (Fig. 2.3).

The diffusivities fitted from the two analyses of different days are <2% different from each other, which is much smaller than the fitting error (1σ fitting error is about 10%) and hence negligible.

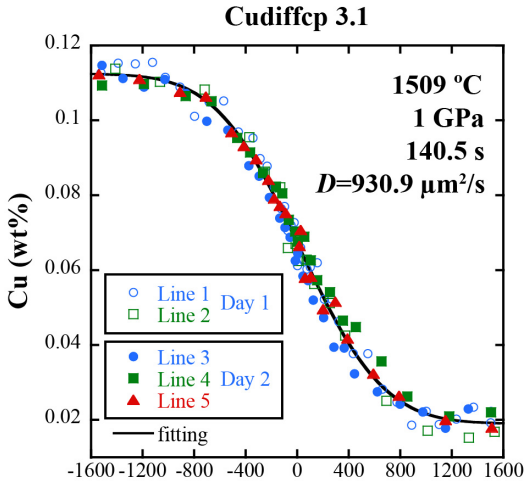

Figure 2.3. Cu diffusion profile of experiment Cudiffcp 3.1. Probe results obtained on two different days are in open symbols and closed symbols respectively. Traverses 3 to 5 were moved down by 194 ppm to account for the background shift relative to traverses 1 and 2. The diffusivity given in the figure is based on fit of all 5 traverses after the correction for the background shift.

2.4 Results

2.4.1 Copper diffusion profiles and fitting

Ten successful diffusion couple experiments have been conducted. In addition to the 10 experiments reported here in Table 2.2, two more experiments were carried out but are classified as unsuccessful. One experiment at 0.5 GPa and 1300 ºC shows abnormal concentration profile, which might be due to initial Cu concentration inhomogeneity. The other experiment at 1.5 GPa and 1300 ºC crystallized because the pressure was too high for the given temperature. Both experiments are excluded from the data.

Fig. 2.4 shows optical microscope images of two successful experiments. For each diffusion couple, at least three Cu concentration traverses ~250 µm apart from each other were measured to examine the reproducibility and possible convection. In five out of the ten experiments (Cudiffcp 1.2, Cudiffcp 3.1, Cudiffcp 4.2, Cudiffcp 4.3 and Cudiffcp 4.4), the interface survived the quench process and the sample glasses were crack-free after the experiment.

Table 2.1. Chemical compositions of the synthesized basaltic glasses.

	Et1		Et1Cu		Et2		Et2Cu	
wt%	ave.	s.d. (1σ)	ave.	s.d. (1σ)	ave.	s.d. (1σ)	ave.	s.d. (1σ)
SiO_2	47.26	0.39	46.18	0.72	46.92	0.51	47.27	0.46
TiO_2	1.62	0.06	1.63	0.04	1.67	0.05	1.66	0.05
Al_2O_3	17.52	0.27	18.17	0.64	17.72	0.85	17.21	0.40
FeO_t	10.47	0.21	10.67	0.14	10.58	0.20	10.73	0.25
MgO	5.83	0.07	5.84	0.10	5.89	0.13	5.88	0.08
CaO	10.69	0.06	10.69	0.06	10.51	0.08	10.58	0.05
Na_2O	4.45	0.12	4.45	0.08	4.40	0.11	4.43	0.08
K_2O	2.03	0.04	1.90	0.04	2.06	0.04	2.10	0.04
Cu	122	35	1174	121	82	22	1193	93
Total	99.88		99.65		99.76		99.98	

Reported data are electron microprobe measurements of far-field compositions on the samples after experiments, except for Cu, whose concentrations are measured on original glasses before experiments. At least 20 points were analyzed and averaged for each glass composition. Details about the microprobe analysis can be found in Analytical Methods.

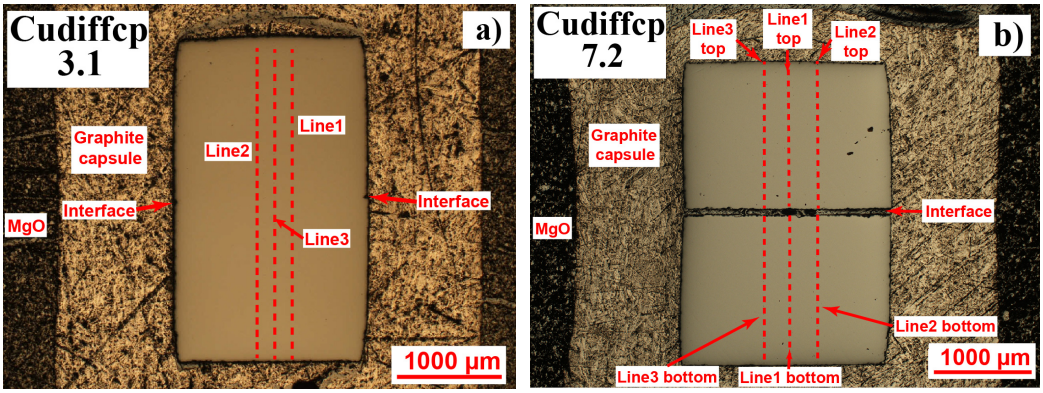

Figure 2.4. Optical microscope images of experimental charges. (a) Cudiffcp 3.1; (b) Cudiffcp 7.2. The Cu-free glass is on the top while the Cu-bearing glass is at the bottom. In (a), two pieces of glasses were welded together after the experiment; position of the interface is indicated by the two dents on both sides of the glasses. In (b), there is a large crack right at the interface after the experiment. Red dashed lines show the position of microprobe traverses.

In these cases, the physical interface position was indicated by the two dents on both sides of the glasses, as shown in Fig. 2.4a.

For the other five experiments (Cudiffcp 1.1, Cudiffcp 2.1, Cudiffcp 5.1, Cudiffcp 6.1 and Cudiffcp 7.2), a crack occurred almost exactly along the interface (Fig. 2.4b). In order to prevent loss of glass during polish, epoxy was added multiple times to protect the cracks. After microprobe analyses, Cu concentration profiles on both sides of the crack were compared: if

necessary, a distance correction is made so that the profile across the crack is smooth. As a result, a 7.5 μm and 12.5 μm correction to the concentration profiles was applied for experiments Cudiffcp 2.1 and Cudiffcp 6.1, while no correction was applied to experiments Cudiffcp 1.1, Cudiffcp 5.1 and Cudiffcp 7.2.

Cu concentration profiles in all experiments besides Cudiffcp 3.1 are shown in Fig. 2.5. The concentration profiles were fit by the solution to a one-dimensional diffusion couple with constant diffusivity (Crank 1975):

$$C = \frac{C_0 + C_1}{2} + \frac{C_0 - C_1}{2} \operatorname{erf} \frac{x - x_0}{\sqrt{4Dt}} \tag{2.2}$$

where C_0 is the initial Cu concentration at the Cu-free half of the diffusion couple (defined as $x–x_0 > 0$); C_1 is the initial Cu concentration at the Cu-bearing half (defined as $x–x_0 < 0$); D is Cu diffusivity and x_0 is the position of the interface. Since Cu diffusivity is high, there is concern that Cu diffusion might have reached the ends of the diffusion couple. This would cause error in fitting using Eq. 2.2, which assumes an infinite diffusion medium. Visual examination of the data and fitting of the profiles indicate that for the longer-duration or higher-temperature experiments (Cudiffcp 1.1, Cudiffcp 5.1 and Cudiffcp 7.2) diffusion seems to have reached the two ends. Numerical fitting using the solution for finite diffusion medium was carried out for these three experiments (curves shown in Fig. 2.5), and the resulting diffusivities were only 3-5% higher than that assuming infinite diffusion medium.

2.4.2 Temperature and pressure dependence of Cu diffusivity

Experimental run conditions and results for all successful experiments are summarized in Table 2.2. An Arrhenius plot of all Cu diffusivities obtained in this study is shown in Fig. 2.6. Diffusion data of the five experiments at 1 GPa and 1314-1575 ºC in anhydrous basaltic melt can be expressed by the following Arrhenius relation:

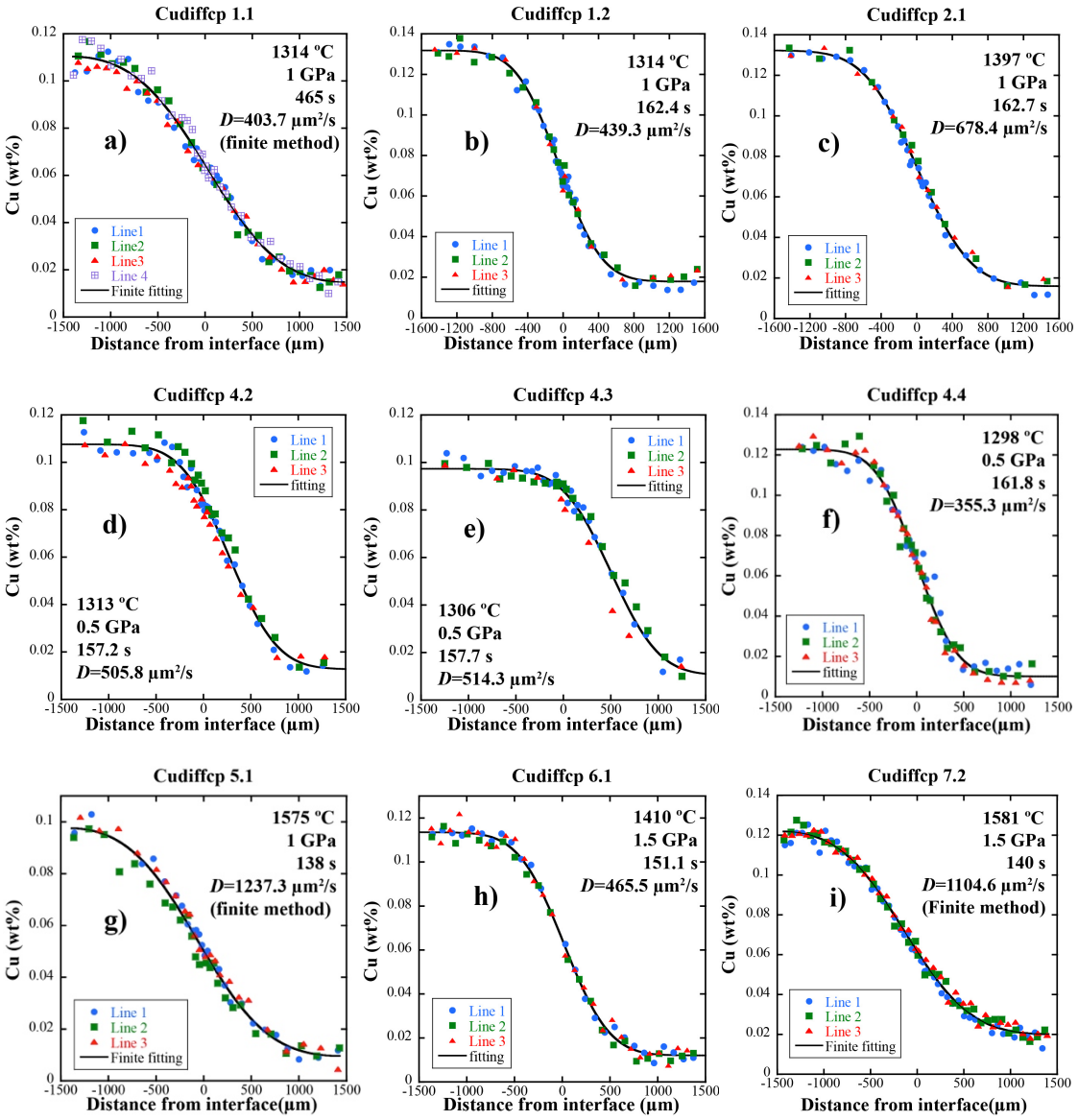

Figure. 2.5. Cu concentration profiles for all diffusion couple experiments in this study. Different symbols in each plot represent different traverses analyzed on the sample perpendicular to the interface.

$$D_{\mathrm{Cu}}^{\mathrm{basalt}} = \exp\left[-(14.12 \pm 0.50) - \frac{11813 \pm 838}{T}\right], \quad r^2=0.985 \tag{2.3}$$

where $D_{\mathrm{Cu}}^{\mathrm{basalt}}$ is in m^2/s, T is temperature in K, and errors are at 1σ level. The above equation reproduces the five experimental ln$D$ values to within 0.09 ln$D$ units. The activation energy corresponding to Eq. 2.3 is 98.2 ± 7.0 kJ/mol. This small activation energy (~100 kJ/mol) means

that the temperature dependence of Cu diffusivity is relatively small compared to other elements, and is consistent with Cu diffusing as Cu^{+}.

Table 2.2. Summary of experimental conditions and results.

Exp#	*P* (GPa)	*T* (ºC)	Duration (s)		*D* (10^{-12} m^2/s)	Error (1σ)
			t_1 (s)	t_2(s)		
Cudiffcp 1.1	1	1314	429.3	464.6	403.7*	37.1
Cudiffcp 1.2	1	1314	124.2	162.4	439.4	26.8
Cudiffcp 2.1	1	1397	126.4	162.7	678.3	43.7
Cudiffcp 3.1	1	1509	105.1	140.5	930.9	6.3
Cudiffcp 4.2	0.5	1313	122.1	157.2	505.8	55.9
Cudiffcp 4.3	0.5	1306	119.9	157.7	514.3	71.7
Cudiffcp 4.4	0.5	1298	131.2	161.8	355.3	31.9
Cudiffcp 5.1	1	1575	95.6	137.7	1237.3*	157.5
Cudiffcp 6.1	1.5	1410	125.7	151.1	465.5	28.9
Cudiffcp 7.2	1.5	1581	107.9	140.4	1104.6*	68.8

P is corrected pressure; *T* is corrected temperature; t_1 is the recorded duration at the target temperature ±1 ºC; t_2 is the corrected duration using the method described in Experimental Procedure.
*Diffusivities of these three experiments were fitted using the solution for a finite diffusion medium as explained in the text.

To evaluate the pressure effect on Cu diffusivity, two experiments were done at 1.5 GPa and three experiments were done at 0.5 GPa (see Fig. 2.6). Two of the three 0.5 GPa experiments gave diffusivities that are ~20% higher than the 1 GPa diffusivities, while diffusivity from the other 0.5 GPa experiment fell 12% below the 1 GPa trend. Two 1.5 GPa experiments gave diffusivities 12% and 29% below the 1 GPa diffusivities respectively. Although the 0.5 GPa experiments have relatively larger errors (these are still small errors for diffusion studies), a fit of all measured Cu diffusivities at 1298 ºC to 1581 ºC and 0.5 to 1.5 GPa gives:

$$D_{\mathrm{Cu}}^{\mathrm{basalt}} = \exp\left[-(13.59\pm0.81)-\frac{(12153\pm1229)+(620\pm241)P}{T}\right],\ r^2=0.938 \qquad (2.4)$$

where $D_{\mathrm{Cu}}^{\mathrm{basalt}}$ is diffusivity in m^2/s, *T* is temperature in K, *P* is pressure in GPa, and errors are at 1σ level. Eq. 2.4 corresponds to a pre-exponential factor $D_0=(1.25\overset{\times}{\div}2.2)\times10^{-6}$ m^2/s, an activation energy E_a=101±10 kJ/mol and an activation volume $V_a=(5.2\pm2.0)\times10^{-6}$ m^3/mol for Cu diffusion in

anhydrous basaltic melt. The above equation is able to reproduce all our experimental ln*D* values to within 0.23 ln*D* units.

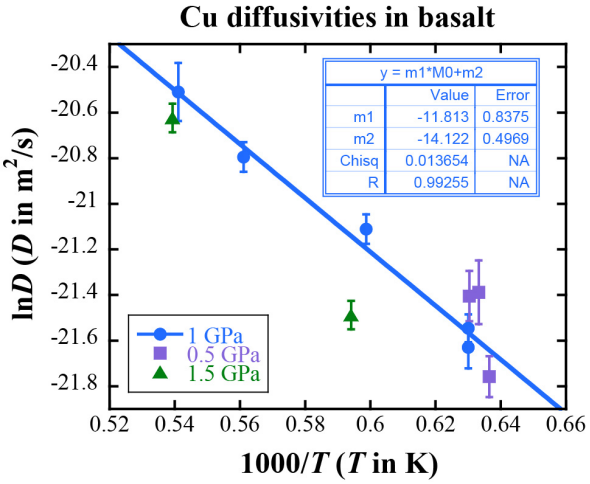

Figure 2.6. Arrhenius plot of all Cu diffusion data obtained in this study. The linear fit is for 1 GPa experiments only. Error bars shown on diffusivities are at 1σ level.

2.4.3 Possible complications and other sources of error

Since basaltic melts have low viscosities at our experimental condition (about 10^0 to $10^{1.3}$ Pa·s at temperatures from 1581 ºC to 1298 ºC using the viscosity model for Etna basalt by Giordano and Dingwell 2003), there is concern about whether convection has occurred during the experiments. Effort was made to examine whether convection is an issue in our experiments. First, at least three traverses 200 µm to 300 µm apart from each other were measured on every sample. If convection occurred, the three traverses would likely diverge, and diffusivities obtained from these traverses may be significantly different from each other. The results show that, diffusivities fitted to individual traverses in one sample are typically within ~20% from the overall diffusivity, indicating no obvious convection. Second, two experiments (Cudiffcp 1.1 and Cudiffcp 1.2) were conducted at the same temperature and pressure but with different duration (465 s vs 163 s, almost a factor of 3 difference). As can be found in Table 2.2, relative diffusivity difference between the two experiments is only about 8%, within our experimental error. Both the consistency between diffusivities from Cudiffcp 1.1 and Cudiffcp 1.2 and the agreement between

different traverses in the same experiment suggest that the occurrence of convection is unlikely in our experiments.

Temperature uncertainty may cause error in the data. As discussed in Methods, temperature at the two ends of the diffusion couple can be 10 to 20 ºC lower than the interface temperature. Hence, the error caused by temperature uncertainty is estimated using this maximum temperature uncertainty of 20 ºC. Based on the activation energy of 98.2 kJ/mol for Cu diffusivity at 1 GPa, the uncertainty of 20 ºC can result in errors in D_{Cu} of 10% at 1300 ºC and 7% at 1600 ºC. The uncertainty in Cu diffusivity due to pressure uncertainty is negligible because Cu diffusivity changes less than 20% when pressure changes by 0.5 GPa.

Another possible source of error is the effective run duration contributed by heating and cooling. As a compromise to the high Cu diffusivity, most of our experiments were designed to be only ~2 min long. Under this circumstance, the heating and quenching processes contribute about 20% to 30% to the effective run duration, meaning Cu diffusivity is changed by 20% to 30% with the duration correction. However, the method we used to correct the duration (Eq. 2.1) is accurate if the activation energy of Cu diffusion is constant.

As mentioned earlier, cracks occurred along the interface of five samples during quench (Cudiffcp 1.1, Cudiffcp 2.1, Cudiffcp 5.1, Cudiffcp 6.1 and Cudiffcp 7.2) and the cracks are almost perfectly horizontal, and hence the distance across the crack cannot be determined by comparing different traverses. For these five experiments, corrections were done by comparing the trend of Cu concentration profiles on both sides of the crack. As a result, a 7.5 μm and 12.5 μm correction to the concentration profiles was applied for experiments Cudiffcp 2.1 and Cudiffcp 6.1, while no correction was applied to experiment Cudiffcp 1.1, Cudiffcp 5.1 and Cudiffcp 7.2. This resulted in a 3% increase in diffusivity obtained from Cudiffcp 2.1 and a 2% increase in diffusivity obtained from Cudiffcp 6.1.

The synthetic starting glasses are not perfectly homogeneous in Cu concentration. In the 8-mm-diameter Cu-bearing synthetic glass, Cu concentration can be ~1300 ppm at the center and

~1000 ppm near the boundary (Fig. 2.1). However, considering that the glass cylinder used for experiments is only about 1.5-mm tall, the Cu concentration difference across the glass cylinder is ≤100 ppm, which is only slightly above our analytical error of ~80 ppm. Therefore the Cu concentration gradient in the starting glasses is unlikely to cause significant error.

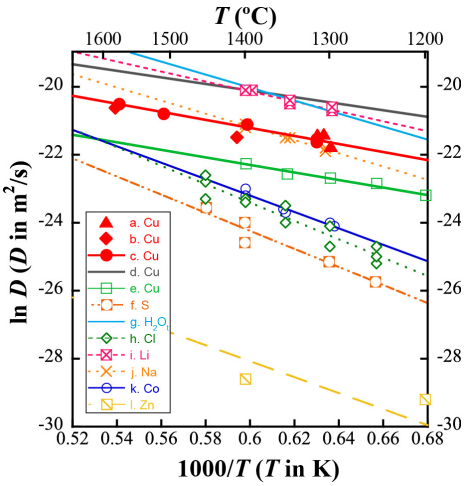

Figure. 2.7. Comparison of Cu diffusivities obtained in this study to literature diffusivity data for other elements in anhydrous basaltic melts unless otherwise indicated. a. Cu diffusivities at 0.5 GPa from this study; b. Cu diffusivities at 1.5 GPa from this study; c. Cu diffusivities at 1 GPa from this study; d. Calculated Cu diffusivities in dry basaltic melt by Mungall's model (Mungall 2002b); e. Cu diffusivities in $Na_2Si_2O_5$ melt at 1000-1400°C and1 bar (von der Gonna and Russel 2000); f. S diffusivities at 1225-1450 ºC and 0.5-1 GPa (Freda et al. 2005); g. H_2O_t diffusivities at 1 wt% water, 400-1500 ºC, and ≤ 1 GPa (Zhang and Ni 2010); h. Cl tracer diffusivities at 1250-1450 ºC and 0.5-1 GPa (Alletti et al. 2007); i. Li tracer diffusivities at 1300-1400 ºC and 1 bar (Lowry et al. 1981); j. Na tracer diffusivities at 1300-1400 ºC and 1 bar (Lowry et al. 1982); k. Co tracer diffusivities at 1300-1400 ºC and 1 bar (Lowry et al. 1982); l. Zn diffusivities in anhydrous rhyolite melt at 898-1400 ºC and 0.01–1 GPa (Baker and Watson 1988).

2.5 Discussion

2.5.1 Comparison with existing Cu diffusivity data

For multivalent ions, valence state of the ion plays an important role in its diffusivity in silicate melts and minerals. Ions in the lower valence state typically have higher diffusivities because of the weaker bonding between these ions and surrounding melt structure (Zhang 2010). Examples of multivalent ions in silicate melts include Fe^{2+} and Fe^{3+}, Sn^{2+} and Sn^{4+}, etc. Copper is also a multivalent element in the natural system, and is commonly found as 0, +1 or +2 in natural occurrence. In the study of Cu solubility in a mafic melt, Ripley and Brophy (1995) plotted log

(Cu solubility) versus log $f(O_2)$, and found that Cu dissolves into the melt predominantly in +1 valence state at or below NNO. The high Cu diffusivity and low activation energy for Cu diffusion observed in our study are consistent with Cu being univalent. Therefore in this study, we regard our measured Cu diffusivity as Cu^+ diffusivity.

As mentioned in the Introduction, we know of only one study reporting Cu^+ diffusivities in $Na_2Si_2O_5$ melt (von der Gonna and Russel 2000) using a voltammetry method. They reported Cu^+ diffusivity to be 5.01×10^{-11} m^2/s at 1100 ºC with activation energy of 92.1 kJ/mol. Their diffusivities of Cu in $Na_2Si_2O_5$ glass melt are plotted in Fig. 2.7 (green open squares) to compare with those measured in this study (red solid circles, diamonds and triangles). Cu^+ diffusivities in $Na_2Si_2O_5$ glass melt are smaller than those in basaltic melt by a factor of about 3 with similar activation energy.

Mungall (2002b) developed a model to calculate ion diffusivities in silicate melt. Calculated Cu^+ diffusivities in basaltic melt using his model are plotted in Fig. 2.7 as a grey solid line, and are about 3 to 5 times the diffusivities determined by our experiments. The model by Mungall (2002b) shows larger errors in reproducing the diffusivities in the $Na_2Si_2O_5$ melt. At 1100ºC, calculated Cu^+ diffusivities using his model are two orders of magnitude larger than the experimental data by von der Gonna and Russel (2000).

2.5.2 Comparison of Cu diffusivity with that of other elements in anhydrous basaltic melts

Diffusivity data for selected elements in basaltic melts are also plotted in Fig. 2.7. From the figure, Cu diffusivity is almost identical to Na diffusivity at ~1400 ºC, lower than Li diffusivity by a factor of about 3 and significantly higher than diffusivities of all other cations shown in Fig. 2.7. At 1300 ºC, Cu diffusivity is ~10 times Ca and Co diffusivity, 18 times Mg diffusivity, and ~30 times S and Fe diffusivity. Since Cu diffusion has smaller activation energy than all other elements shown in Fig. 2.7, when temperature increases, Cu diffusivity increases slower than other elements. At 1500 ºC Cu diffusivity is only 5 to 10 times higher than that of Mg,

Fe, Co, S and Ca. However when temperature decreases, Cu diffusivity decreases slower than all other elements shown in Fig. 2.7, and becomes larger than Na diffusivity. At 1100 ºC, Cu diffusivity will be ~200 times Fe diffusivity, 67 times Mg diffusivity, 35 times Co diffusivity, ~25 times Ca diffusivity and 2.5 times Na diffusivity.

To examine the role of valence and size of cations, the radius of Cu^+ is compared to other monovalent cations. For self-consistency, the ionic radii of Li^+, Cu^+ and Na^+ in octahedral sites (0.076, 0.077, and 0.102 nm, respectively, Shannon 1976) are compared. If diffusivities of univalent cations in a given melt are mainly determined by the ionic radii (Mungall 2002b), Cu^+ diffusivity would be similar to Li^+ diffusivity. The fact that Cu^+ diffusivity is a factor of 3 smaller than Li^+ diffusivity but similar to Na^+ diffusivity indicates that other ionic characters (e.g., electronegativity, the presence of d electrons, different co-ordination number, etc.) also play a role in determining the diffusion rate.

2.5.3 Applications

The role of Cu diffusion in magmatic sulfide deposit formation has been discussed in the Introduction. The major conclusions by Mungall (2002a) and Zhang (2015) were consistent in that, if the diffusivity of a metal is much larger than sulfur diffusivity in basaltic melt, the partitioning of the metal into the sulfide phase can be regarded as in equilibrium. Both Mungall (2002a) and Zhang (2015) used the diffusivity model by Mungall (2002b) to estimate metal diffusivities in their study, and found Cu^+ to be one of the most mobile elements in basaltic melt. Our results suggest that Mungall's model overestimated Cu diffusivity in basaltic melt by a factor of 2 to 4. However, our measured Cu diffusivity is still ~30 times higher than sulfur diffusivity in basaltic melt. Therefore Cu partition into the sulfide melt can be regarded as equilibrium partitioning in most cases.

High Cu diffusivity in basaltic melt might also play a role in metal transport by a magmatic vapor phase (MVP). Nadeau et al. (2013) carried out a melt-inclusion study on samples

from Merapi volcano, Indonesia, and found that Cu was more enriched in shallower felsic melts (~45 ppm) than in deeper mafic melts (~25 ppm), which is opposite to the trend normally observed in arc magmas. The unusual behavior of Cu could not be explained by crystal fractionation or combined assimilation and fractionation. Nadeau et al. (2010) suggested a mechanism in which Cu was transported from the mafic magma to the felsic magma by an MVP enriched in Cu. Since water diffusivity in basalt is high (Fig. 2.7), the growth of an MVP inside the magma is rapid. In this process, because the diffusivity of Cu is lower than that of H_2O but higher than that of other metal elements (except for Li and Na), Cu would not reach equilibrium concentration in the MVP but would be more efficiently enriched in the aqueous volatile phase than the other metal elements. One complication is that, the partition coefficient of Cu between the volatile phase and the silicate melt phase strongly depends on chlorine and sulfur contents in the volatile phase (e.g., Candela and Holland 1984;Williams et al. 1995; Simon et al. 2006 and Zajacz et al. 2008). Hence, enrichment of Cu in the MVP would be controlled by diffusion of sulfur or chlorine from the silicate melt to the MVP. As can be seen in Fig. 2.7, $D_{Cu} > D_{Cl} > D_S$ assuming water content in silicate melt does not change the sequence. Therefore, in pure H_2O fluid phase, Cu concentration in the fluid phase would be even lower than that indicated by the low partition coefficient, but if the fluid bubble is enriched in chlorine or sulfide, Cu partitioning between the fluid and melt phases would be roughly in equilibrium, while Cl and S concentrations in the fluid bubble would be lower than that indicated by equilibrium partitioning. Nadeau et al. (2013) did not specify the composition of the MVP in his study, but a study by Zajacz and Halter (2009) found evidence for sulfur-rich vapor in melt and vapor inclusions hosted by plagioclase. In that case, Cu partitioning during the metal transportation by an MVP is likely equilibrium partitioning again.

High Cu diffusivity may also be responsible for rapid Cu loss from tektites, resulting in large kinetic Cu isotope fractionation. Moynier et al. (2010) measured Cu isotope ratios in tektites, and found almost all the tektites are greatly enriched in heavy Cu isotope ($+1.99‰ < \delta^{65}Cu <$

+6.98‰), where $\delta^{65}Cu = (((^{65}Cu/^{63}Cu)_{sample}/(^{65}Cu/^{63}Cu)_{standard}-1)\times1000‰$. Because tektites might have been heated to a temperature as high as >2800 ºC (Walter 1967) for a short period of time, and the half-condensation temperature for Cu is 1037 K (Lodders 2003), Moynier et al. (2010) proposed that Cu isotopes were fractionated by evaporation loss, with lighter isotopes escaping more rapidly into the volatile phase. However, by comparing with their previous study of Zn isotope fractionation in tektites (Moynier et al. 2009), the authors found Zn isotopes to be less fractionated than Cu isotopes in the same set of samples ($\delta^{66/64}Zn$ up to 2.49‰ compared to $\delta^{65/63}Cu$ up to 6.98‰). If Cu and Zn loss is due to open system volatization (such as Raleigh fractionation in which a tektite droplet is uniform compositionally and isotopically), because Zn has a much lower half-condensation temperature ($T_c \sim 726$ K, Lodders 2003) than Cu, Zn loss would be more severe than Cu loss and Zn isotopes would be more fractionated than Cu isotopes, opposite to the observations. Moynier et al. (2010) explained the more fractionated Cu isotopes than Zn isotopes by the higher diffusivity of Cu^+ than Zn^{2+} in silicate melts, and argued that the isotopic fractionation in tektites was controlled by the competition between the evaporation flux and the diffusion flux. They employed the diffusivity model by Mungall (2002b) and found Cu^+ diffusivity to be about 2 orders of magnitude higher than Zn^{2+} diffusivity, and used this result to explain why Cu isotopes are more fractionated than Zn isotopes. Using literature Zn^{2+} diffusion data in rhyolitic melt (Baker and Watson, 1988) and our Cu^+ diffusion data, and assuming melt composition does not affect Cu^+ diffusivity significantly (our preliminary data reported in Ni et al., 2015 show that Cu^+ diffusivity in anhydrous rhyolitic melt is only ~50% smaller than Cu^+ diffusivity in basalt), Cu^+ diffusivity is about 3 orders of magnitude higher than Zn^{2+} diffusivity (Fig. 2.7). Hence, Cu and Zn diffusion data are consistent with the explanation by Moynier et al. (2010).

2.6 Implications

Our Cu diffusion data in basaltic melt show that, Cu diffusivity in anhydrous basaltic melt is as high as that of sodium at ~1400 ºC, and has a small activation energy (~100 kJ/mol). The measured Cu diffusivities are ~3 times smaller than the values predicted by a previous diffusivity model in the same melt, and ~3 times larger than reported Cu diffusivities in the $Na_2Si_2O_5$ melt. In basaltic melt, Cu diffusivity is ~30 times higher than sulfur diffusivity, indicating that during the formation of magmatic sulfide deposit, when immiscible sulfide liquid drops separate from the host magma and settle to the bottom of the magma chamber, the partitioning of Cu into the sulfide liquid phase can be regarded as equilibrium partitioning. In the process of porphyry-type deposit formation, where metal transport from the more mafic magma to the more felsic magma by a magmatic volatile phase is possible, high diffusivity of Cu also ensures the efficiency of Cu diffusion into and away from the volatile phase. Because of the high diffusivity of Cu in basaltic melt, kinetic limitation of Cu partitioning during ore formation is less likely a concern. This also means Cu may be diffusively fractionated from other ore elements with smaller diffusivity. In addition, the high diffusivity of Cu combined with phases that can incorporate high Cu concentrations imply that there is no kinetic barrier for Cu to be enriched, and hence it is easier for Cu than for other metals to form ore deposits.

The results of our study can also be used to discuss the kinetic role in evaporation loss and isotope fractionation of volatile elements in impact glasses. The more fractionated Cu isotopes than Zn isotopes as observed in tektites can be explained by the higher diffusivity of Cu^+ than Zn^{2+} in silicate melts, despite the lower condensation temperature for Zn than Cu. Similar processes may also happen to lunar volcanic and impact glasses on the surface of Moon.

2.7 Acknowledgements

We thank two anonymous reviewers for their constructive comments, and James Jolles for informal comments. P. Ni thanks Zhengjiu Xu for training and help with piston-cylinder

experiments, Gordon Moore, Yang Chen and Yi Yu for help with microprobe analysis and Chenghuan Guo for discussion about synthesizing glasses. This work was partially supported by NSF grants EAR-1019440 and EAR-1524473. The electron microprobe used in this study was acquired using NSF grant EAR-9911352.

2.8 References

Alletti, M., Baker, D.R., and Freda, C. (2007) Halogen diffusion in a basaltic melt. Geochimica et Cosmochimica Acta, 71, 3570-3580.

Baker, D.R., and Watson, E.B. (1988). Diffusion of major and trace elements in compositionally complex Cl-and F-bearing silicate melts. Journal of Non-Crystalline Solids, 102, 62-70.

Behrens, H., and Hahn, M. (2009) Trace element diffusion and viscous flow in potassium-rich trachytic and phonolitic melts. Chemical Geology, 259, 63-77.

Candela, P.A., and Holland, H.D. (1984) The partitioning of copper and molybdenum between silicate melts and aqueous fluids. Geochimica et Cosmochimica Acta, 48, 373-380.

Crank, J. (1975) The Mathematics of Diffusion. Oxford, UK: Clarendon Press.

Freda, C., Baker, D.R., and Scarlato, P. (2005) Sulfur diffusion in basaltic melts. Geochimica et cosmochimica acta, 69, 5061-5069.

Giordano, D., and Dingwell, D. (2003) Viscosity of hydrous Etna basalt: implications for Plinian-style basaltic eruptions. Bulletin of Volcanology, 65, 8-14.

Huber, C., Bachmann, O., Vigneresse, J.L., Dufek, J., and Parmigiani, A. (2012) A physical model for metal extraction and transport in shallow magmatic systems. Geochemistry, Geophysics, Geosystems, 13.

Hui, H., Zhang, Y., Xu, Z., and Behrens, H. (2008) Pressure dependence of the speciation of dissolved water in rhyolitic melts. Geochimica et Cosmochimica Acta, 72, 3229-3240.

Lodders, K. (2003) Solar system abundances and condensation temperatures of the elements. The Astrophysical Journal, 591, 1220.

Lowry, R.K., Reed, S.J.B., Nolan, J., Henderson, P., and Long, J.V.P. (1981) Lithium tracer-diffusion in an alkali-basaltic melt—an ion-microprobe determination. Earth and Planetary Science Letters, 53, 36-40.

Lowry, R.K., Henderson, P., and Nolan, J. (1982) Tracer diffusion of some alkali, alkaline-earth and transition element ions in a basaltic and an andesitic melt, and the implications concerning melt structure. Contributions to Mineralogy and Petrology, 80, 254-261.

Moynier, F., Beck, P., Jourdan, F., Yin, Q.Z., Reimold, U., and Koeberl, C. (2009) Isotopic fractionation of zinc in tektites. Earth and Planetary Science Letters, 277, 482-489.

Moynier, F., Koeberl, C., Beck, P., Jourdan, F., and Telouk, P. (2010) Isotopic fractionation of Cu in tektites. Geochimica et Cosmochimica Acta, 74, 799-807.

Mungall, J.E. (2002a) Kinetic controls on the partitioning of trace elements between silicate and sulfide liquids. Journal of Petrology, 43, 749-768.

Mungall, J.E. (2002b) Empirical models relating viscosity and tracer diffusion in magmatic silicate melts. Geochimica et Cosmochimica Acta, 66, 125-143.

Nadeau, O., Williams-Jones, A.E., and Stix, J. (2010) Sulphide magma as a source of metals in arc-related magmatic hydrothermal ore fluids. Nature Geoscience, 3, 501-505.

Nadeau, O., Stix, J., and Williams-Jones, A.E. (2013) The behavior of Cu, Zn and Pb during magmatic–hydrothermal activity at Merapi volcano, Indonesia. Chemical Geology, 342, 167-179.

Naldrett, A.J. (1989) Magmatic sulfide deposits. Oxford University Press.

Ni, H., and Zhang, Y. (2008) H_2O diffusion models in rhyolitic melt with new high pressure data. Chemical Geology, 250, 68-78.

Ni, P., Zhang Y., Simon A. & Gagnon J. (2015) Cu and Fe diffusion in rhyolitic melts during chalcocite "dissolution". Goldschmidt Abstracts, 2015 2269.

Pearce, N.J., Perkins, W.T., Westgate, J.A., Gorton, M.P., Jackson, S.E., Neal, C.R., and Chenery, S.P. (1997) A compilation of new and published major and trace element data for NIST SRM 610 and NIST SRM 612 glass reference materials. Geostandards newsletter, 21, 115-144.

Ripley, E.M., and Brophy, J.G. (1995) Solubility of copper in a sulfur-free mafic melt. Geochimica et cosmochimica acta, 59, 5027-5030.

Rudnick, R.L., and Gao, S. (2014) Composition of the continental crust, Treatise on Geochemistry (2nd edition), pp. 1-51.

Shannon, R.T. (1976) Revised effective ionic radii and systematic studies of interatomic distances in halides and chalcogenides. Acta Crystallographica Section A: Crystal Physics, Diffraction, Theoretical and General Crystallography, 32, 751-767.

Simon, A.C., Pettke, T., Candela, P.A., Piccoli, P.M., and Heinrich, C.A. (2006) Copper partitioning in a melt–vapor–brine–magnetite–pyrrhotite assemblage. Geochimica et Cosmochimica Acta, 70, 5583-5600.

Singer, D.A. (1995) World class base and precious metal deposits; a quantitative analysis. Economic Geology, 90, 88-104.

von der Gonna, G., and Russel, C. (2000) Diffusivity of various polyvalent elements in a $Na_2O \cdot 2SiO_2$ glass melt. Journal of non-crystalline solids, 261, 204-210.

Walter, L.S. (1967) Tektite compositional trends and experimental vapor fractionation of silicates. Geochimica et Cosmochimica Acta, 31, 2043-2063.

Wang, H., Xu, Z., Behrens, H., and Zhang, Y. (2009) Water diffusion in Mount Changbai peralkaline rhyolitic melt. Contributions to Mineralogy and Petrology, 158, 471-484.

Williams, T.J., Candela, P.A., and Piccoli, P.M. (1995) The partitioning of copper between silicate melts and two-phase aqueous fluids: an experimental investigation at 1 kbar, 800 C and 0.5 kbar, 850 C. Contributions to Mineralogy and Petrology, 121, 388-399.

Zajacz, Z., Halter, W.E., Pettke, T., and Guillong, M. (2008) Determination of fluid/melt partition coefficients by LA-ICPMS analysis of co-existing fluid and silicate melt inclusions: controls on element partitioning. Geochimica et Cosmochimica Acta, 72, 2169-2197.

Zajacz, Z., and Halter, W. (2009) Copper transport by high temperature, sulfur-rich magmatic vapor: Evidence from silicate melt and vapor inclusions in a basaltic andesite from the Villarrica volcano (Chile). Earth and Planetary Science Letters, 282, 115-121.

Zhang, Y. (2008) Geochemical Kinetics. Princeton University Press.

Zhang, Y. (2010) Diffusion in minerals and melts: theoretical background. Reviews in Mineralogy and Geochemistry, 72, 5-59.

Zhang, Y. (2015). Toward a quantitative model for the formation of gravitational magmatic sulfide deposits. Chemical Geology, 391, 56-73.

Zhang, Y., and Ni, H. (2010) Diffusion of H, C, and O components in silicate melts. Reviews in Mineralogy and Geochemistry, 72, 171-225.

Zhang, Y., Ni, H., and Chen, Y. (2010) Diffusion data in silicate melts. Reviews in Mineralogy and Geochemistry, 72, 311-408.

CHAPTER III

Cu and Fe diffusion in rhyolitic melts during chalcocite "dissolution": Implications for porphyry ore deposits and tektites

3.1 Abstract

Copper diffusion plays an important role in natural processes, such as metal transport during the formation of magmatic-hydrothermal porphyry-type ore deposits and Cu isotope fractionation during tektite formation. Copper diffusion data in natural silicate melts, however, are limited. In this chapter, chalcocite (Cu_2S) "dissolution" experiments were carried out using chalcocite-rhyolite diffusion "couples" to study Cu (and S) diffusion in rhyolitic melts. Instead of chalcocite dissolution as initially expected, our experiments show that Cu is transferred from the chalcocite crystal to the rhyolitic melt, and Fe is transferred from the rhyolitic melt to chalcocite, whereas the S concentration profile in the rhyolitic melt is essentially flat. From the Cu and Fe exchange profiles in the rhyolitic melts, Cu diffusivities and Fe diffusivities are obtained and reported.

Copper diffusivity in rhyolitic melts containing 0.10 to 5.95 wt% H_2O at temperatures of 750 to 1391ºC and pressures of 0.5 to 1.0 GPa can be described as:

$$D_{Cu}^{Rhy} = \exp\left[-(14.75 \pm 0.35) - (0.23 \pm 0.10)w - \frac{(11647 \pm 491) - (698 \pm 117)w}{T}\right],$$

which allows the estimation of an activation energy for diffusion in dry rhyolitic melts to be 96.8±4.1 kJ/mol. In the above equation, diffusivity (D) is in m^2/s, T is the temperature in K, w is the H_2O concentration in the rhyolitic melts in wt% and all errors reported are at 1σ level. Combining Cu diffusion data from this study and previous data in basaltic melt gives a general equation for Cu diffusivity in natural silicate melts:

$$D_{Cu} = \exp\left[-(17.3 \pm 0.9) + (3.8 \pm 1.5)(\text{Si+Al-H}) - \frac{(4403 \pm 1094) + (9700 \pm 1921)(\text{Si+Al-H})}{T}\right],$$

where Si+Al-H is the cation mole fraction of Si plus Al minus H in the silicate melt on a wet basis.

Iron diffusivities obtained in this study in anhydrous to 6 wt% H_2O rhyolite are combined with previous data to get a general equation for Fe diffusion in rhyolitic melts:

$$D_{Fe}^{Rhy} = \exp\left[-(16.1 \pm 1.7) - \frac{(19859 \pm 2541) - (1218 \pm 135)w}{T}\right].$$

Our data demonstrate that Cu diffusion is faster than H_2O or Cl in rhyolitic melts containing 6 wt% water, which indicates that the scavenging and transport of Cu by a magmatic volatile phase during formation of porphyry-type ore deposits is not limited by diffusion of Cu. Based on our experimental data, Cu diffusivity is almost 4 orders of magnitude higher than Zn in anhydrous rhyolitic melts, which supports the explanation of more diffusive loss of Cu leading to more fractionated Cu isotopes than Zn isotopes in tektites.

3.2 Introduction

Porphyry-type ore deposits are important sources for metals, such as Cu, Au, Mo and Ag, comprising~57%, 10%, 99% and 13%, respectively, of the world's total discovered quantities of these metals (Singer 1995). In order to form a porphyry-Cu deposit, the Cu concentration must be enriched from a crustal average concentration of ~30 ppm (Rudnick and Gao 2014) to a typical mineable grade of ~0.2 to 2 wt% in the porphyry environment (Simon and Ripley 2011). This 2 to 3 orders of magnitude enrichment is accomplished by, among other things, the efficient scavenging of Cu by a magmatic volatile phase (MVP) exsolved from silicate melts in Earth's upper continental crust (e.g. Candela 1997; Wilkinson 2013). The exsolution of an MVP from silicate melts can occur by decompression, which reduces the solubility of volatiles in the melt (i.e., first boiling; Audetat and Simon 2012), or crystal fractionation that occurs during cooling of

magma in shallow level magma chambers (i.e., second boiling, Candela 1997; Audetat and Simon 2012). Since the exsolved MVP bubbles are less dense than the surrounding silicate magma, at a volume fraction >10% the bubbles can form an interconnected network and rise through the magma chamber (Candela 1991; Parmigiani et al. 2016), simultaneously scavenging ore metals, such as Cu, Au, Mo and Ag from the surrounding melt, and possibly also via resorption of metal sulfides (Audetat and Simon 2012). Huber et al. (2012) quantitatively modeled the partitioning and transport of metals by an MVP that ascends through a magma chamber, and determined that the efficiency of metal extraction (i.e., the total quantity of a metal removed from the magma chamber and transported into the overlying porphyry environment) is dependent on a balance between diffusion of the metal in the silicate melt, and the advection of the MVP through the magma chamber. They showed that elements with high diffusivities will more likely reach equilibrium with the MVP and be efficiently transported, whereas elements with low diffusivities might not equilibrate with a rapidly ascending MVP and, therefore, become less efficiently scavenged and transported. Such an effect can lead to diffusive fractionation of metals, and hence variability of metal ratios in magmatic-hydrothermal ore deposits.

Moynier et al. (2009, 2010) studied Cu and Zn isotope systematics in tektites, and found that Cu isotopes are more fractionated than Zn isotopes in the same batch of tektites. The fractionation of Cu and Zn isotopes in tektites can be explained by the evaporative loss of Cu and Zn from the tektites during their formation, when a short period of high temperature was experienced (as high as >2800 ºC, Walter 1967). However, if condensation temperature alone controlled isotope fractionation, the greater degree of fractionation of Cu isotopes relative to Zn isotopes is inconsistent with the lower half condensation temperature of Zn ($T_{1/2}$ ~ 726 K, Lodders 2003) than Cu ($T_{1/2}$ ~ 1037 K, Lodders 2003). The authors invoked a "diffusion-limited" mechanism, and suggested that the more fractionated Cu isotope signature is due to the higher diffusivity of Cu^{+} than Zn^{2+} in silicate melt. The higher diffusivity of Cu would lead to more rapid

loss of Cu from the tektite during heating, and would result in more fractionated Cu isotopes than Zn isotopes in tektites.

Despite the potential role of Cu diffusion in magmatic-hydrothermal porphyry-type ore formation and tektite and other isotope fractionation processes, Cu diffusion data are limited. To our knowledge, only two experimental studies on Cu diffusion have been conducted. Von der Gonna and Russel (2000) studied Cu diffusion in a $Na_2O{\cdot}2SiO_2$ melt using a voltammetry method. Ni and Zhang (2016) investigated Cu diffusion in anhydrous basaltic melt by the diffusion couple method. Because porphyry-type deposits typically originate from water-saturated intermediate to felsic magmas (Simon and Ripley 2011), and tektites are often "rhyolitic" in terms of their silica content (e.g., Cassidy et al. 1969), Cu diffusion data from these two studies cannot be directly applied to elucidate the evolution of porphyry-type ore deposits or isotope fractionation in tektites. In this study, we report Cu diffusion data in rhyolitic melts containing 0.1 to 5.9 wt% H_2O from chalcocite "dissolution" experiments, and discuss the implications of the data in the context of natural processes of porphyry-type Cu deposit formation and Cu isotope fractionation in tektites.

3.3 Experimental and analytical methods

3.3.1 Starting materials

In this study, chalcocite "dissolution" experiments were carried out to determine Cu diffusivities over the temperature range of 750 ºC to 1391 ºC in silicate melts with rhyolitic compositions and with H_2O concentrations ranging from "anhydrous" (0.10 ~ 0.24 wt%) to 5.9 wt%. "Dissolution" is referred to in quotation marks because, even though the experiments were initially designed as chalcocite dissolution to study the diffusion of both Cu and S, the actual chemical reaction observed in our experiments is close to "metal exchange" as discussed below.

A cluster of chalcocite (Cu_2S) crystals purchased from a gem dealer was used as the starting material. As examined using scanning electron microscope (SEM) and election microprobe (EMP), the chalcocite crystals are mostly pure Cu_2S (20.36 wt% S, 81.10 wt% Cu and 0.00 wt% Fe), but occasionally have inclusions of bornite (Cu_5FeS_4) and Cu metal (compositions plotted in Fig. 3.1). When preparing samples for the experiments, care was taken to avoid any impurities in the chalcocite crystal. Six rhyolitic glasses with H_2O concentrations from 0.1 wt% to 5.9 wt% were used for this series of experiments. The major element compositions and H_2O concentrations of the starting glasses are summarized in Table 3.1. Among these rhyolitic glasses, NCO is a natural glass from the Newberry Crater, Oregon; bb7b-25 is a natural obsidian glass from the Mono Crater, California; CIT is a natural obsidian glass from Coso Range, California, which was previously used for infrared (IR) spectral calibration by Newman et al. (1986); and GMR+2, GMR+4 and GMR+6 are glasses synthesized by hydration of obsidians from Glass Mountain, California, which were previously used in studies for viscosity and water speciation of rhyolites (Hui and Zhang 2007; Hui et al. 2008). The SiO_2 concentration in the rhyolites, on a dry weight basis, ranges from 73.4 to 76.7 wt% (the concentrations reported in Table 3.1 include H_2O). Glass cylinders rather than powders were used for the experiments. These starting glass cylinders already contain dissolved H_2O, and no liquid H_2O was added into the capsule during the experiment.

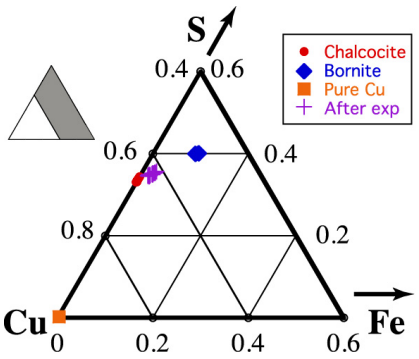

Figure 3.1. Composition of chalcocite, bornite, and pure copper in the natural chalcocite cluster and the "chalcocite" after experiment in Chal-Rhy-2-2 in the Cu-Fe-S ternary system (atomic percent). Composition of the "chalcocite" after experiment (purple crosses) in Chal-Rhy-2-2 roughly falls in between chalcocite and bornite.

Table 3.1. Chemical composition of the rhyolitic glasses used for this study.

	SiO_2	TiO_2	Al_2O_3	FeO_t	MgO	CaO	Na_2O	K_2O	H_2O^*	Total
NCO	73.45	0.23	14.04	2.00	0.14	0.75	5.35	4.30	0.10	100.36
CIT	76.51	0.05	12.48	1.02	0.02	0.41	4.32	4.92	0.24	99.97
bb7b-25	75.26	0.06	12.26	1.05	0.02	0.52	3.96	4.85	1.80	99.78
GMR+2	72.07	0.26	13.41	1.65	0.27	1.22	4.12	4.44	1.99	99.43
GMR+4	70.53	0.26	13.16	1.71	0.27	1.20	4.03	4.35	3.89	99.40
GMR+6	69.22	0.25	12.94	1.66	0.27	1.17	3.90	4.20	5.95	99.56

Note: Major element compositions were measured by electron microprobe on starting glasses. Details for the EMP analyses can be found in "analytical methods". About 15 points were analyzed on each glass sample and the average composition is reported. All compositions are in wt%.
*Concentration of H_2O was measured by FTIR, each value is the average of ~10 analysis on the same sample.

3.3.2 Piston cylinder experiments

In preparation for piston cylinder experiments, a chalcocite crystal and rhyolitic glass were first cut and prepared into long cylinders with a diameter of ~2 mm. A wafer was then cut from each of the cylinders, with a thickness of ~1 mm for the chalcocite wafer and 1 to 2 mm for the rhyolitic glass wafer depending on the estimated profile length for each experiment. The wafers were doubly polished with progressively finer sandpapers, finishing with 0.3-μm alumina powders. After examination under optical microscope, chalcocite and rhyolitic glass wafers with the least amount of impurities were chosen for experiments. After cleaning and drying, the wafers were placed into a graphite capsule, with the rhyolite glass on top and the denser chalcocite at the bottom. The graphite capsule was fit tightly into a drilled hole of an MgO rod, then into a graphite furnace, and finally into a barium carbonate pressure medium. Effort was made to place the interface right at the center of the graphite furnace to minimize temperature gradients across the sample.

All piston cylinder experiments were carried out at the University of Michigan. The pressure was measured by a Heise digital pressure gauge. A 5% correction is applied to the nominal pressure based on the calibration by Ni and Zhang (2008) on the same piston cylinder apparatus. The experimental charge was pressurized to 15% above the target pressure, and then allowed to relax overnight at 200 ºC to close gaps inside the assembly. After relaxation, the

sample was heated up to the target temperature in ~50 s using a programed temperature controller. Pressure was maintained manually using an Enerpac electric pump. The pressure fluctuation was within 1% during the experiment, ~10% during heating up and ~20% during quench. Temperature was measured by a Type-S thermocouple (Pt90Rh10-Pt) and controlled by a Eurotherm controller. Temperature correction based on the distance from the thermocouple tip to the interface was applied using the calibration of Hui et al. (2008). The thermocouple tip is typically 2 to 2.5 mm away from the interface. The temperature variation across the sample is usually ≤13 ºC. No temperature overshoot was observed during the experiment, and the temperature fluctuation recorded by the temperature controller was ±1 ºC during the experiment. After a designated duration, the assembly was quenched to room temperature at a rate of ~100 ºC/s by turning off the power. The whole sample assembly was recovered from the piston cylinder apparatus and preserved in epoxy. Because of the strong secondary fluorescence effect for Cu analysis by EMP as realized in the preliminary analyses (see analytical methods), the chalcocite crystal was removed from the sample charge before probe analysis. Removal of the chalcocite crystal was done by first doubly polishing the sample to a thin wafer (<1 mm thick), and then cutting through the graphite capsule and physically pushing the chalcocite out of the sample disc with tweezers. The hole in the sample disc after chalcocite removal was filled with epoxy to better preserve the sample glass. The rhyolitic melt does not wet the chalcocite crystal, and there is typically a gap between chalcocite and glass produced by expansion of the assembly during depressurization, thus reducing the difficulty in the removal process. The chalcocite crystal is usually a whole undamaged piece after removal, which is then preserved in a separate epoxy disc.

3.3.3 Analytical methods

3.3.3.1 EMP analyses of major elements

Major element compositions and Cu concentrations were analyzed in separate sessions using the CAMECA SX-100 electron microprobe at the University of Michigan. Major oxides were analyzed using a 5 nA focused beam with an accelerating voltage of 15 kV. Standards used for the analyses are: albite (ALBA) for Na, natural rhyolitic glass (VGRH) for Si, potassium feldspar (GKFS) for K, wollastonite (WOLL) for Ca, synthetic ferrosilite (FESI) for Fe, synthetic geikielite (GEIK) for Ti, forsterite (FOBO) for Mg and sillimanite (SILL) for Al. Counting time for each element was 20 to 40 seconds on the peak, and 10 to 20 seconds on each side of the background. A special routine was employed for counting Na (extrapolating to photon counts at zero time) to correct for Na loss during analysis.

3.3.3.2 Secondary fluorescence effect in EMP analysis for Cu

Although the strong secondary fluorescence effect on Cu analysis using EMP was avoided by removing chalcocite crystal from the capsule after experiment, a brief description of the effect is included below as a reference for future studies. Our test analyses before we decided to remove chalcocite from the experimental charge show that secondary fluorescence effect is a significant concern in EMP analysis for trace amount of Cu (i.e. hundreds of ppm) when a Cu-rich phase is within hundreds of micrometers of the analytical spot. In our test analyses, a chalcocite wafer and a rhyolitic glass wafer (CIT) were polished and placed into a graphite capsule, then preserved in epoxy and polished to the center section for EMP analysis. Traverses were measured in the glass perpendicular to the contact between the chalcocite crystal and the glass, and the results are plotted in Fig. 3.2a (Line 1 through Line 3). The results show that the secondary fluorescence effect for Cu is especially large in EMP analysis compared to other elements such as Zr (Harrison and Watson 1983; Zhang and Xu 2016), Cr (Zhao et al. 2015), and Sn (Yang et al. 2016), for example. Copper concentration in this natural glass is low and roughly

uniform (2.7±1.1 ppm, based on analyses of Chal-Rhy-4-2). The secondary fluorescence profile, however, yields over 6000 ppm Cu near the contact with the chalcocite, 1000 ppm Cu at 100-µm distance away from the chalcocite, and extends more than 200 µm into the glass (Fig. 3.2a).

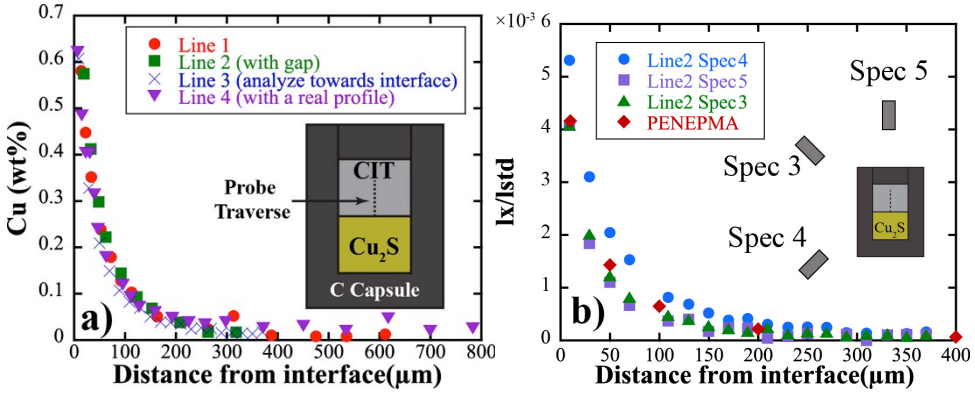

Figure 3.2. a) Apparent Cu concentration profiles due to secondary fluorescence, measured in natural CIT glass next to a piece of chalcocite. Line 1 was measured from the contact to the far field; Line 2 was measured when there is a tiny gap filled with epoxy between the chalcocite and the glass; Line 3 was measured from the far field towards the contact; Line 4 was measured in experimental charge Chal-Rhy-2-2, with a real Cu diffusion profile in the rhyolitic glass but overwhelmed by the secondary fluorescence effect. b). Comparison of Monte Carlo simulated Cu secondary fluorescence profile to electron microprobe measurements. The vertical axis is the raw Cu Kα peak counts ratio on sample over Cu metal standard, without ZAF correction. An Ix/Istd = 0.005 roughly corresponds to a Cu concentration of 0.6 wt%. In the simulation, the effect of the orientation of the spectrometer is also examined: spectrometer 4 is oriented toward the chalcocite side of the chalcocite-rhyolite couple, leading to higher Cu secondary fluorescence signals than spectrometers 3 and 5.

Secondary fluorescence effect for Cu analysis was also estimated by Monte Carlo simulations using the software package PENEPMA (Llovet and Salvat 2006). The geometry used in the simulation was set up following the sample orientation, where a chalcocite crystal (Cu_2S) and a rhyolitic glass (CIT) were placed on a plane right next to each other. The electron beam was applied perpendicular to the glass surface with an initial energy of 15 keV. Movement of the electrons and all secondary particles and X-rays was tracked until their energies were below 7 keV. A pseudo-spectrometer covering the entire sample surface was used to record X-ray spectra from 7 kV to 15 kV. About 5 million electrons were simulated at each spot to achieve a statistical precision of ~1% on the Cu Kα peaks. Then the X-ray spectra obtained from Monte Carlo simulations were convolved assuming a spectral resolution of 40 eV, after which the peak heights

of Cu Kα were measured. The same simulation was run on a target of Cu metal as the standard, and peak count ratios on sample over standard are plotted in Fig. 3.2b, and compared to EMP measurements by three wavelength-dispersive X-ray spectrometers. Two key conclusions can be drawn from the comparison. Firstly, the Monte Carlo simulation matches the measurements well. Secondly, the secondary fluorescence effect on each WDS detector is different based on its relative orientation to the sample (Fig. 3.2b). According to the measurements, the WDS detector records higher counts of secondary fluorescence signal of Cu Kα if the chalcocite side of the couple is facing the detector (Spectrometer 4). This phenomenon is similar to the findings of a previous study on secondary fluorescence effect of Nb Kα in an Nb-Pd_2HfAl couple (Fournelle et al. 2005). One possible explanation is that chalcocite has a smaller mass attenuation coefficient for Cu Kα than rhyolitic glass, so that more Cu Kα X-rays survived the pathway through the chalcocite crystal and reached the detector.

The Cu diffusion profiles in our samples are typically hundreds of micrometers long, with an interface concentration of less than 1000 ppm. The strong secondary fluorescence effect completely overwhelms the actual Cu diffusion profile (Fig. 3.2a, Line 4). Hence, we decided to remove chalcocite from our sample charge after experiment for precise EMP analysis of Cu.

3.3.3.3 EMP analyses of Cu

With chalcocite removed, Cu concentrations were measured on glass in dedicated EMP sessions for Cu alone with three spectrometers counting Cu Kα peak for 240 s at the same time, and then 120 s counting on background on each side of the peak. A focused beam was used for the anhydrous rhyolite glasses (NCO and CIT), while a 10 μm scanning beam was used for the hydrous glasses (bb7b-25, GMR+2, GMR+4 and GMR+6) to minimize the beam damage during the analysis. The beam current was 40 nA when the interface Cu concentrations were high (e.g. higher than 500 ppm), achieving a detection limit of ~80 ppm. Otherwise a beam current of 100

nA was used to achieve a detection limit of ~50 ppm for Cu. Previously analyzed major element compositions of the glasses (Table 3.1) were input into the software for ZAF correction. NIST SRM 610 was used as a secondary standard to verify the EMP analysis of Cu. The reported Cu concentration in NIST 610 is 421.7 ppm (Pearce et al. 1997), and our analyses yielded 420 to 540 ppm Cu during different sessions for this standard, indicating that EMP analyses of Cu may have systematic errors up to 120 ppm. EMP data of Cu concentrations are relatively low in precision compared to laser-ablation ICP-MS (see below), but have higher spatial resolution (<10μm), which helps to capture the short quench profile near the interface. In addition, the multiple electron microprobe traverses verifies the horizontal homogeneity and help to rule out the concern of convection in our experiments.

3.3.3.4 Laser-ablation ICP-MS analyses of Cu

Copper concentration profiles were also analyzed using laser ablation inductively coupled plasma mass spectrometry (LA-ICP-MS) at the University of Windsor. All LA-ICP-MS data reported in this study were obtained by using a PhotonMachines Analyte Excite 193 nm, short-pulse-width (sub 4 ns), Ar-F excimer laser ablation system coupled with an Agilent 7900, fast-scanning quadrupole ICP-MS. The operating conditions are summarized in Table 3.2.

Copper concentration profiles were obtained by analyzing multiple spots along a traverse perpendicular to the interface. For each spot analysis, a 25-μm-diameter laser beam was used to ablate the sample surface at a frequency of 25 Hz for a duration of 30 s. The first few seconds of each transient laser signal were excluded during data processing to eliminate possible signal contribution from surface contamination (Pettke et al. 2012). NIST 610 synthetic glass standard was analyzed at least every hour for use as an external calibration standard and to assess instrumental drift. The isotope ^{44}Ca was used as the internal calibration standard to compensate for differences in ablation behavior between calibration standards and unknowns, and to obtain

Cu concentrations. A detection limit of ~ 0.04 ppm for Cu was achieved for our analysis using the operating conditions presented in Table 3.2.

Table 3.2. Instrumental parameters and operating conditions of LA-ICP-MS

Laser-ablation system	
Laser system	PhotonMachines 193 nm short pulse width Analyte Excite excimer laser ablation system
Energy	6.33 J/cm^2
Spot size	25 µm
Pulse rate	25 Hz
Carrier gas flow	1.2 L/mim (He)
ICP-MS system	
Instrument model	Agilent 7900
RF power	1250 W
Auxiliary gas flow rate	0 L/min (no make up or dilute gas used)
Nebulizer gas flow rate	0.8 L/min (Ar)
Interface cones	Agilent Ni Sampler cone #G3280-67040
Dwell time	10 ms on ^{43}Ca, ^{44}Ca, ^{57}Fe, ^{63}Cu and ^{65}Cu
Background	30 s

3.3.3.5 FTIR analyses

Concentrations of H_2O in the starting glasses and in glasses after diffusion experiments were measured using a Perkin-Elmer GX Fourier Transform Infrared Spectrometer (FTIR) at the University of Michigan. Sample glasses were typically doubly polished to ~500 µm thickness for analysis. An NIR source and a CaF_2 beamsplitter were used. Molecular water and OH concentrations were determined by measuring the absorption peaks at 5230 and 4515 cm^{-1} respectively. The baselines were fit with a flexi curve as shown in Zhang et al. (1997). Total H_2O concentrations were obtained by summing the concentrations of both species calculated by using calibrated molar absorptivities from Newman et al. (1986).

To assess possible H_2O loss during the experiments, the H_2O concentration was measured in hydrous glass after the highest-temperature experiments at each H_2O concentration (Chal-Rhy-1-2, Chal-Rhy-3-1, Chal-Rhy-7-1 and Chal-Rhy-14-1). For all four experiments, the amount of H_2O loss was negligible (<0.1 wt%) near the interface and at the

center part of the glass where Cu diffusion profiles were measured. Therefore, measured H_2O concentrations in the starting glasses (Table 3.1) were adopted as the H_2O concentrations in the melt for all the experiments.

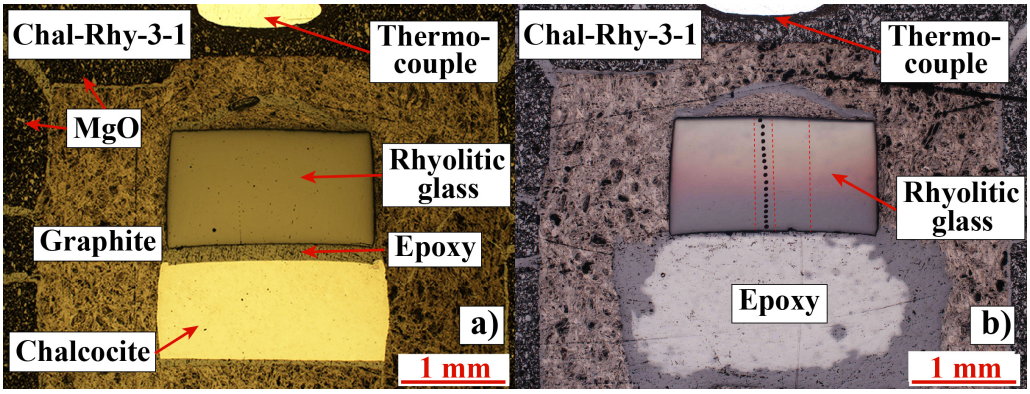

Figure 3.3 a) Microscope image of a sample charge after piston cylinder experiment. The chalcocite and the rhyolitic glass were naturally separated during quench probably because rhyolitic melts do not wet chalcocite. b) Microscope image of the same sample charge after double polishing, the removal of the chalcocite wafer, and analyses. Dark spots on the glass are laser ablation traverse spots and the red dashed lines show probe traverses for Cu concentration analysis.

3.4 Results

One example of the sample charge after an experiment is shown in Fig. 3.3a. The rhyolitic glasses show different optical features after the experiments. In general, synthetic hydrous glasses after low temperature experiments (Chal-Rhy-8-1, Chal-Rhy-11-1, Chal-Rhy-13-1) are opaque and slightly crystallized. Synthetic hydrous glasses after high temperature experiments (Chal-Rhy-3-1, Chal-Rhy-3-2, Chal-Rhy-7-1, Chal-Rhy-12-1, Chal-Rhy-14-1) show reddish color near the interface (e.g. Fig 4a, 4b). The reddish color in these glasses is caused by Cu-bearing nanoparticles in the glasses, as verified by high-magnification SEM images. These particles are too small in size (~75 nm in diameter) for their exact chemical composition to be quantified by SEM or EMP. Consistent diffusivities (within 20% difference) extracted from the time-series experiments (Chal-Rhy-3-1 and Chal-Rhy-3-2) that both contain Cu-bearing nanoparticles (Fig. 3.4a, 4b) suggest that these particles likely formed during quench. Because the analytical spot size is large, which averaged the nanoparticles in each spot, the nanoparticles do

not affect the determination of diffusivities in our experiments. For all other experiments, the resulting glasses are transparent and colorless. An image of the sample charge after removing the chalcocite crystal is shown in Fig. 3.3b. Experimental conditions and results of all successful experiments are summarized in Table 3.3.

Table 3.3. Summary of experimental conditions and results.

Exp#	P (GPa)	T (ºC)	Starting glass	Duration (s)		D_{Cu} ($\times10^{-12}$m^2/s)		D_{Fe} ($\times10^{-12}$m^2/s)
				t_1 (s)	t_2(s)	EMP	ICP-MS	
Chal-Rhy-1-2	0.5	1101	bb7b-25	428.9	464.8	113.0±8.1	**126.1±5.8**	0.185±0.011
Chal-Rhy-2-2*	0.5	1096	GMR+2	n.a.	n.a.	n.a.	**n.a.**	n.a.
Chal-Rhy-3-1**	0.5	1001	GMR+2	1804.4	1830.8	n.a.	**95.5±3.6**	0.166±0.005
Chal-Rhy-3-2	0.5	1003	GMR+2	118.9	146.7	n.a.	**80.7±1.5**	n.a.
Chal-Rhy-4-2	0.5	1099	CIT	909.9	932.9	56±13	**92.8±3.9**	–
Chal-Rhy-4-3	0.5	1088	NCO	906.8	936.1	69±14	**80.2±5.5**	–
Chal-Rhy-5-1	0.5	1006	NCO	902.8	930.2	50±14	**38.6±2.0**	–
Chal-Rhy-7-1	0.5	941	GMR+6	244.7	286.7	277±45	**215.6±6.1**	2.39±0.21
Chal-Rhy-8-1	0.5	750	GMR+6	231.9	279.4	36.2±6.6	**68.1±0.9**	–
Chal-Rhy-9-1	1	1303	NCO	120.8	148.7	223±14	**241.4±4.3**	0.273±0.028
Chal-Rhy-10-1	1	1391	NCO	118.9	153.4	483±20	**372.5±6.6**	1.75±0.11
Chal-Rhy-11-1	0.5	854	GMR+6	246.4	284.3	157±15	**126.6±1.4**	–
Chal-Rhy-12-1	0.5	954	GMR+4	239.3	270.2	97.4±6.6	**110.1±3.4**	0.548±0.025
Chal-Rhy-13-1	0.5	856	GMR+4	247.4	279.4	76±13	**61.9±2.1**	0.195±0.033
Chal-Rhy-14-1	0.5	1049	GMR+4	120.1	152.7	195.7±7.5	**187.5±6.0**	1.482±0.073

Note: P is corrected pressure; *T* is corrected interface temperature; t_1 is recorded duration at target temperature ±1 ºC; t_2 is effective duration calculated using Eq. (3.2). All reported errors are at 1σ level.
*Experiment Chal-Rhy-2-2 was specially designed to study the composition change of chalcocite crystal during experiment. Therefore no diffusivities were determined for the experiment.
**Copper diffusivity in Chal-Rhy-3-1 was fit assuming diffusion in finite medium using the same initial Cu concentration as Chal-Rhy-3-2.

3.4.1 Absence of S diffusion profile

The original purpose of our experimental design was to obtain both Cu and S diffusivities in rhyolitic melts, as the dissolution of chalcocite (Cu_2S) would release Cu and S into the melt at an atomic ratio of 2:1. In addition, S diffusivity is lower than Cu diffusivity by a factor of 30 or more at the experimental temperatures, at least in basaltic melt (Ni and Zhang 2016). Hence, S concentration in the rhyolitic melt near the interface would be high and the difference between interface S and far-field S concentrations would be easily measurable if chalcocite simply

dissolved into the rhyolitic melt. Despite success in obtaining Cu diffusion profiles, however, we were unable to detect any S diffusion profile in the rhyolitic glass after the experiments. That is, S concentration variation in the rhyolitic glass is consistently below the detection limit of 20 ppm. After careful examination of the experimental charge and by repeating the experiments, we recognized that the lack of S diffusion profile was not due to experimental errors, sample preparation, or the analysis. Instead, S stayed in the chalcocite phase at our experimental conditions. However, because:(i) S concentration in chalcocite is high, (ii) the chalcocite wafers used in the experiments are relatively large in size, and (iii) S diffusion distance in chalcocite can be significant, S concentration change in "chalcocite" after the experiments is small and is difficult to detect. In order to better understand the chemical reaction happening during the experiment, one experiment (Chal-Rhy-2-2) was specially conducted at 1096°C, in which we put a 15-µm-thick wafer of chalcocite sandwiched between two 1.5-mm-thick rhyolitic glass wafers (Fig. 3.5). The purpose of this experimental design was to use a small volume of chalcocite relative to rhyolitic glass, with which we might be able to detect a change in chalcocite composition. The composition of the chalcocite before the experiment was verified by EMP to be essentially pure chalcocite ($Cu_{1.96}Fe_{0.00}S$). After the experiment, the composition of run-product "chalcocite" has a composition of $Cu_{7.16}Fe_{0.27}S_4$, which roughly falls between the compositions of chalcocite (Cu_2S) and bornite (Cu_5FeS_4), as shown in Fig. 3.1. This result indicates that during the experiment, chalcocite lost Cu to and gained Fe from the surrounding rhyolitic melt, while S essentially remained in the sulfide phase. In addition to the change of chalcocite composition in Chal-Rhy-2-2, Cu and Fe diffusion profiles in the glass also agree with the loss of Cu to the melt and gain of Fe from the melt. Results of experiment Chal-Rhy-2-2 explain why a S diffusion profile was not observed in the rhyolitic melt, and also show that our experiments are better characterized as Cu-Fe exchange experiments between chalcocite and rhyolitic melt, rather than chalcocite "dissolution" experiments.

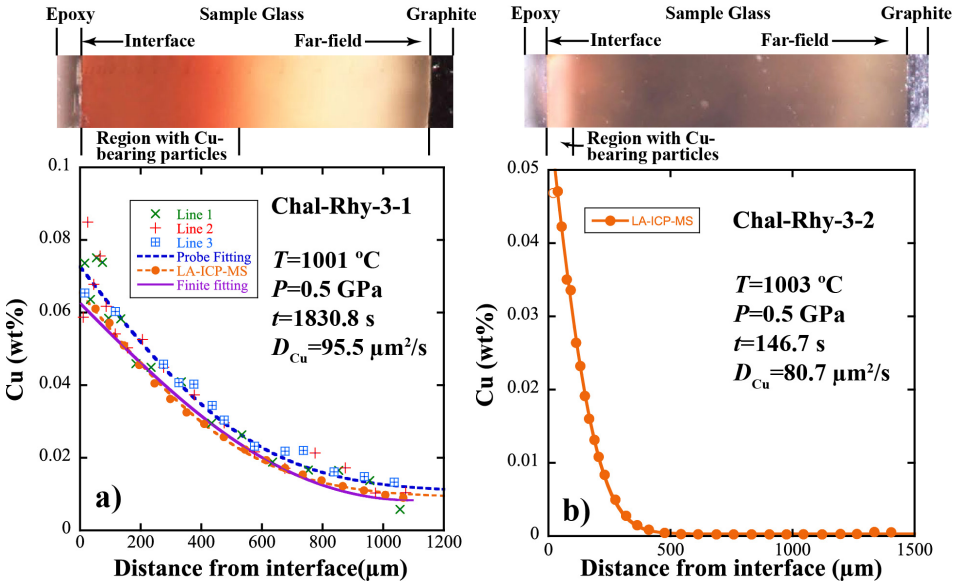

Figure 3.4. Two experiments (forming a time series; one experiment in (a) and the other in (b)) to examine possible convection and the effect of Cu nanoparticles on Cu diffusivity extraction. The two experiments differ in duration by a factor of 12. Both products contain red Cu-bearing nanoparticles after the experiment. The Cu concentration profiles are plotted together with an image section of the sample glass to show correlations between the Cu concentration profile in the glass and existence of the Cu-bearing nanoparticles. The longer-duration experiment (Chal-Rhy-3-1) has a longer Cu diffusion profile, leading to the existence of Cu-bearing particles in a much wider region from the interface. Similar diffusivities (<20% different) obtained from these two experiments indicate that these particles had negligible effect on the diffusivities. a) Three EMP traverses and a traverse of LA-ICP-MS spots were analyzed for Chal-Rhy-3-1. The diffusivity provided in the figure is based on fitting result using the finite method. b) Sample Chal-Rhy-3-2 was measured by LA-ICP-MS only. The first point from the interface in open circle is likely affected by the short quench profile and is excluded from fitting.

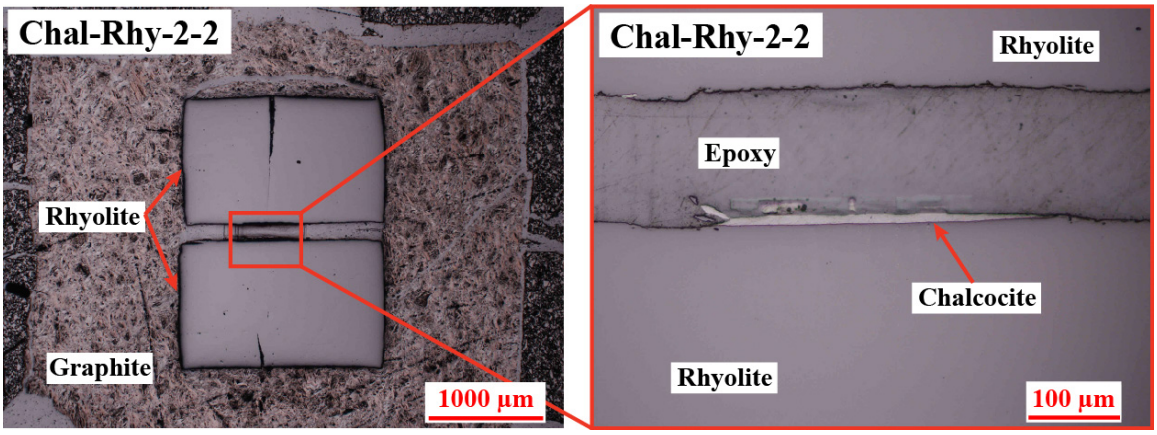

Figure 3.5. Special experiment (Chal-Rhy-2-2) designed to examine the behavior of chalcocite during its "dissolution". "Dissolution" is in quotation marks because the reaction is better described as "metal exchange" instead of "dissolution". One thin wafer of chalcocite was sandwiched between two rhyolitic glasses in the experiment. The two rhyolitic glasses separated during quench, and the gap was filled with epoxy for protection during polish. The chalcocite was found containing 2.4 atom% Fe, 35.0 atom% S and 62.6 atom% Cu after the experiment, indicating an exchange of Cu and Fe with the rhyolitic melts.

3.4.2 Copper diffusion profiles and fitting

Typically three EMP traverses and one LA-ICP-MS traverse were analyzed perpendicular to the interface to obtain the Cu concentration profiles in the separated glass wafer of each sample. All EMP and LA-ICP-MS Cu diffusion profiles besides those in Fig. 3.4 are plotted in Fig. 3.6. The Cu concentrations measured using EMP are often somewhat higher than determined using LA-ICP-MS (e.g., Chal-Ryh-1-2 in Fig. 3.6a), which is likely due to the imperfect choice of the WDS background for EMP analyses. Near (within 45 μm) the interface, the Cu concentration decreases toward the interface in the high-spatial-resolution EMP profile in Fig. 3.6a. This is because during quench, Cu preferentially partitions into the chalcocite phase as temperature decreases, leading to a Cu concentration decrease in the rhyolitic glasses near the interface. Similar effects have been observed previously, typically within ~20 μm distance from the mineral-melt interface (Zhang et al. 1989; Chen and Zhang 2008; Yu et al. 2016; Zhang and Xu 2016). LA-ICP-MS has lower spatial resolution, and only the first point close to the interface might be affected by this decrease. The presence of this quench-affected profile indicates that a negligible amount of melt is lost during separation of the chalcocite crystal (Zhang et al. 1989; Chen and Zhang 2008; Yu et al. 2016). When fitting the profiles to obtain Cu diffusivities, the portion of the profiles affected by quench was excluded. Assuming interface motion is negligible because chalcocite is not dissolving (total Cu mass gained by the melt is less than that contained in 1 μm chalcocite, meaning negligible interface motion anyway), the Cu concentration profiles were fitted by the analytical solution to the one-dimensional diffusion in semi-infinite medium with constant interface concentration (Crank 1975) to obtain Cu diffusivities:

$$C = C_\infty + \left(C_0 - C_\infty\right)\mathrm{erfc}\frac{x}{2\sqrt{Dt}}, \tag{3.1}$$

where C_0 is the Cu concentration at the interface; C_∞ is the initial Cu concentration of the rhyolitic glass; x is the distance in the melt to the interface; D is Cu diffusivity and t is the experimental duration. Three parameters, C_0, C_∞ and D for each experiment, were obtained from

curve fitting of the Cu concentration profile.

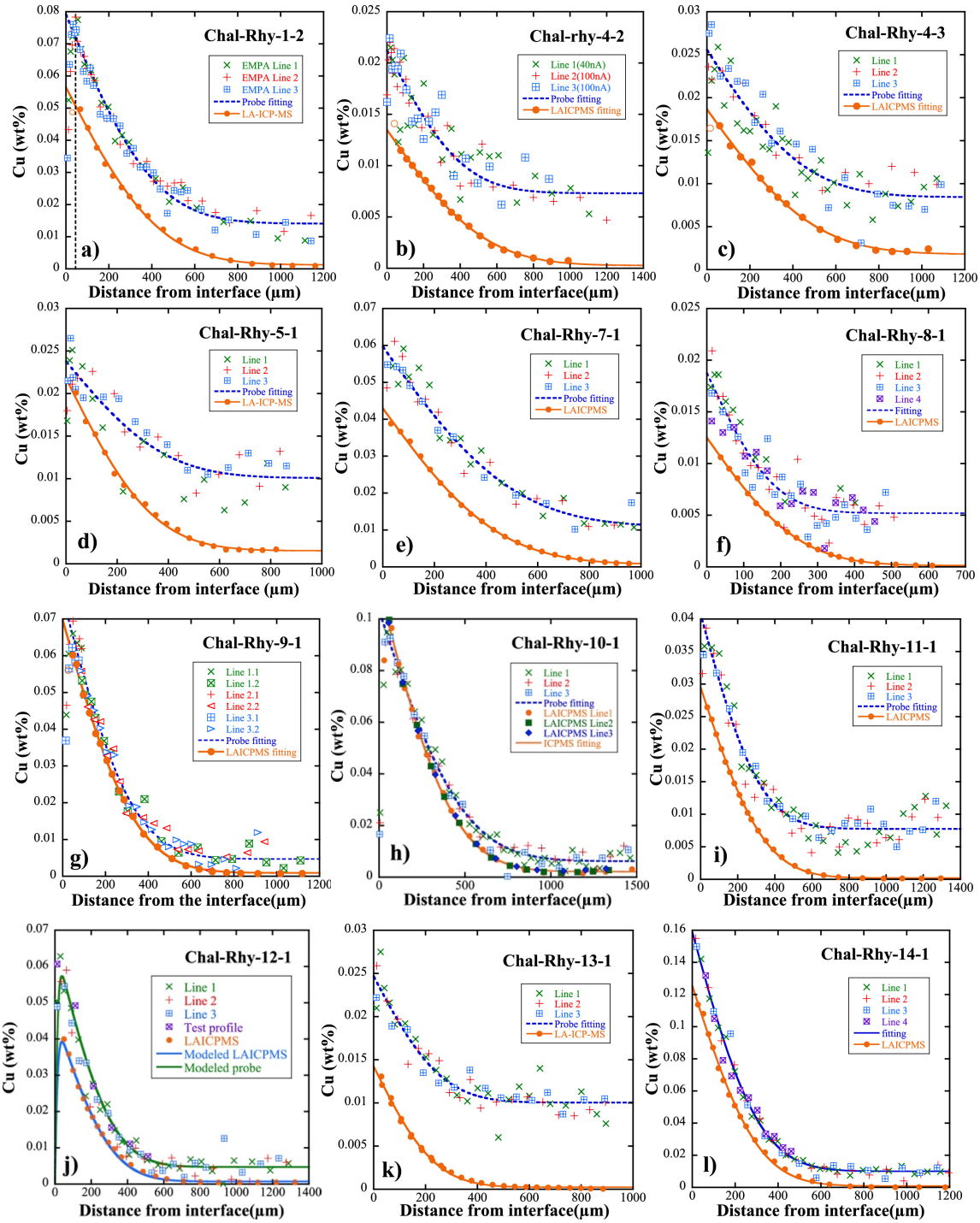

Figure 3.6. Copper diffusion profiles measured in this study (except for Chal-Rhy-3-1 and Chal-Rhy-3-2, which are in Fig. 4). Solid symbols are LA-ICP-MS data (often one traverse only; except for Chal-Rhy-10-1). Open circles indicate LA-ICP-MS data that are affected by the quench effect and excluded from fitting. All other symbols are for EMP traverses (3 or more). In j, the profiles are modeled considering the temperature effect on the interface Cu concentration. Details about the modeling can be found in "sources of error".

For experiment Chal-Rhy-3-1, which had the longest duration, it appears that diffusion reached the far-field boundary (Fig. 3.4a). Therefore, the Cu diffusion profile of Chal-Rhy-3-1 was fit with a different method, assuming a finite diffusion medium and an initial Cu concentration of 3.4 ppm (based on experiment Chal-Rhy-3-2, which used the same starting glass as Chal-Rhy-3-1).

Fitting results of all the experiments for both EMP and LA-ICP-MS results are summarized in Table 3.3. Although both EMP and LA-ICP-MS data were acquired for Cu diffusion profiles, Cu diffusivities fit from the LA-ICP-MS data were adopted for further discussion, while the high spatial resolution EMP data helped capture the short quench profile near the interface, and the multiple EMP traverses in each experiment helped to alleviate the concern of convection.

3.4.3 Iron diffusion profiles and fitting

Iron was observed to partition into the chalcocite during our experiments. Fe concentration profiles were measured by EMP to determine Fe diffusivities in the rhyolitic glasses (Fig. 3.7). Typically four traverses were analyzed by EMP perpendicular to the interface, and the results are consistent with each other. Compared to the Cu diffusion profile in the same sample, the Fe diffusion profile is much shorter (e.g. Fig. 3.6a and Fig. 3.7a), which is consistent with the expectation that divalent Fe^{2+} diffuses at a much lower rate than monovalent Cu^{+} (Ni and Zhang 2016). Among the 15 experiments, resolvable Fe diffusion profiles were obtained in 8 experiments, as reported in Table 3.3. The remaining experiments either have an Fe diffusion profile that is too short (Chal-Rhy-4-2, Chal-Rhy-4-3 and Chal-Rhy-5-1) to be precisely analyzed, or exhibit anomalous behavior of Fe (experiment Chal-Rhy-8-1 has a flat Fe concentration profile in the rhyolitic glass; for Chal-Rhy-10-1, Fe concentration increases towards the interface). The anomalous behavior of Fe in experiments might be caused by the presence of bornite (Cu_5FeS_4) inclusions in the starting chalcocite. A small amount of bornite can greatly affect Fe activity in

the chalcocite, but Cu activity would be affected to a much smaller degree. The Fe concentration profiles are fitted using Eq. (3.1), where the interface concentration (C_0) is lower than the far field concentration (C_∞) for Fe diffusion. All the fitted Fe diffusivities are reported in Table 3.3.

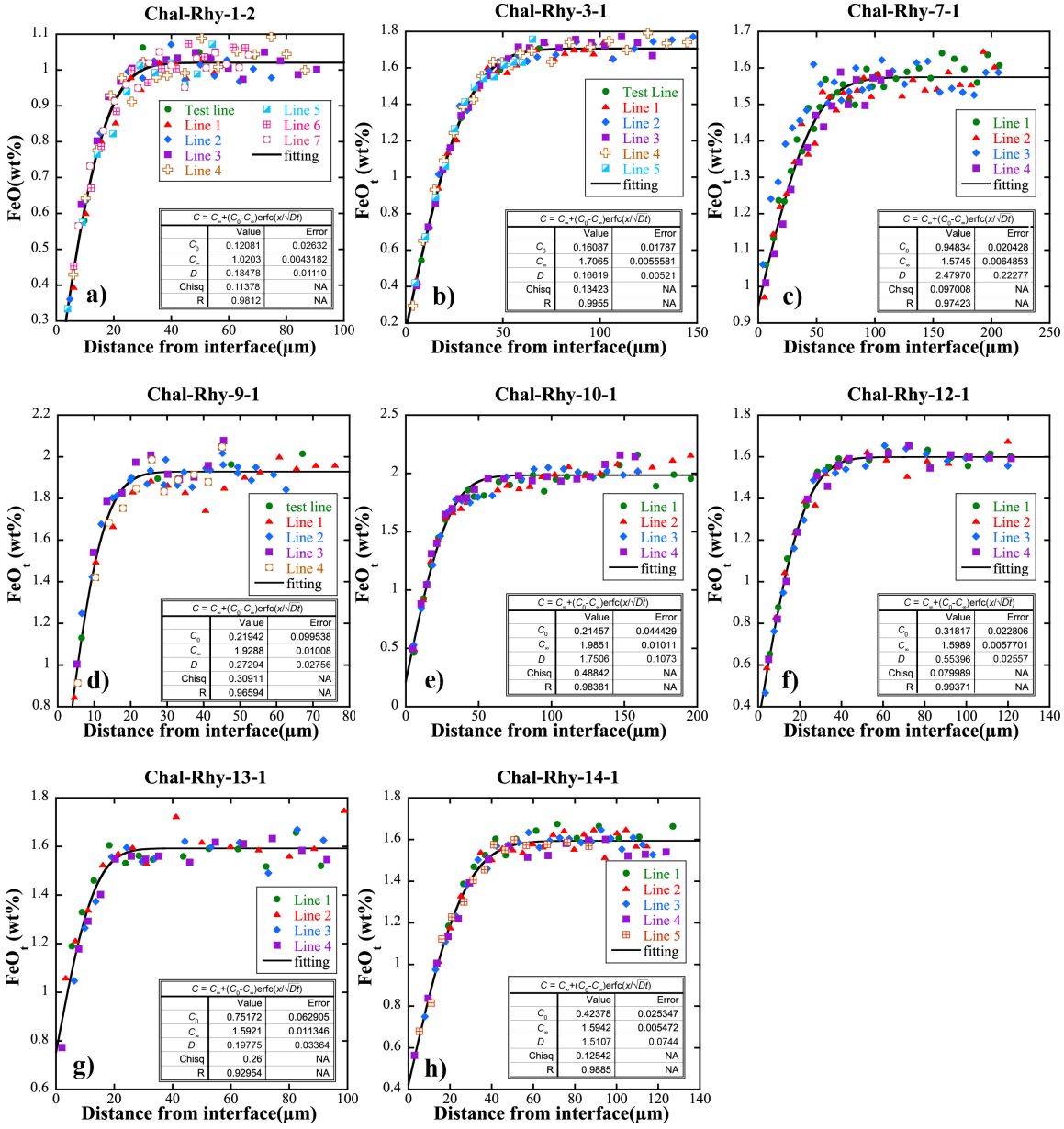

Figure 3.7. Iron diffusion profiles obtained in this study that are used to extract Fe diffusivities in Table 3.3. At least four electron microprobe traverses were analyzed perpendicular to the interface for each sample. Fitting results for the experiments using Eq. (3.1) are also provided in the figures.

3.5 Discussion

3.5.1 Possible convection

Because rhyolitic melts typically have high viscosities (~10^3 to 10^7 Pa·s at our experimental conditions according to the viscosity model by Hui and Zhang 2007), convection is unlikely a problem in our experiments. Nonetheless, two experiments (Chal-Rhy-3-1 and Chal-Rhy-3-2) were conducted with different durations of ~2 min and ~30 min to check for possible convection. The two experiments gave similar Cu diffusivities that are within 20% difference, implying no convection in our experiments (Fig. 3.4a, b). In addition, multiple traverses were measured in each experiment to verify that convection did not affect the diffusion profiles. Typically three EMP traverses ~200 μm away from each other were analyzed in each sample. Convection would lead to inconsistent profiles along different traverses, which is not the case for our experiments (Fig. 3.6). For LA-ICP-MS analysis, typically only one traverse was analyzed for each sample, but three LA-ICP-MS traverses ~300 μm away from each other were analyzed for the experiment at the highest temperature (Chal-Rhy-10-1). As can be seen in Fig. 3.6h, the concentration profiles observed along three traverses match almost perfectly with each other, indicating that convection was unlikely.

3.5.2 Sources of error

Uncertainty in temperature measurements is often an important source of error in diffusion studies. Because the activation energy of Cu diffusion is small, the error caused by temperature measurement uncertainties is within 10% for Cu diffusivities. Uncertainty in pressure measurement is also a negligible source of error, because based on our results, no obvious dependence of Cu diffusivity on pressure can be resolved from the 0.5 GPa and 1 GPa experiments.

Another source of error in our experiments is from diffusion during heating and quenching, especially because our shortest experimental duration is only ~2 min. Correction of

the effective experimental duration was done using the solution to diffusion problems with a time-dependent diffusivity (Zhang 2008):

$$t_c = \frac{\int_0^t \exp(-E/RT)\,dt}{\exp(-E/RT_0)}, \tag{3.2}$$

where t_e is the effective experimental duration in seconds, T_0 is the target temperature in K, T is the recorded temperature corrected to the interface, and E is the activation energy of Cu diffusion. The above equation is theoretically rigorous for diffusion couple experiments, and the effect of heating (~50 s) and cooling (~10 s) is accounted for as equivalent duration at the target temperature. In this study, however, not only the diffusivity (D), but also the interface Cu concentration (C_0) in Eq. (3.1) is temperature dependent. Hence, an error might occur while using this correction method for our study. Because $\ln C_0$ for experiments in 4 wt% and 6 wt% H_2O rhyolitic melts is approximately linearly dependent on $1/T$, the diffusion equation is numerically solved given the recorded temperature history with C_0 and D as a function of temperature. One example of the simulated profile is shown in Fig. 3.6j, where both the EMP profile and the LA-ICP-MS profile were modeled. As can be seen in the figure, the simulated profile fits the measured concentration profile well. In particular, the quench-affected part of the EMP profile is also well reproduced. After excluding the first ~40 μm of the modeled profiles, fitting the simulated "data" using Eq. (3.1) and effective duration from Eq. (3.2) recovers the input diffusivity within 5%. Therefore, effective experimental durations calculated using Eq. (3.2) are valid, and are shown in Table 3.3.

3.5.3 Dependence of Cu diffusivity on temperature, pressure and melt composition

All Cu diffusivities determined in this study are summarized on an Arrhenius plot in Fig. 3.8a, together with Cu diffusivities from previous studies as a comparison. Copper diffusivities obtained using Newberry Crater Obsidian (NCO) at 0.5 GPa and 1 GPa fall onto a single linear

trend, indicating that the pressure dependence of Cu diffusion is insignificant. In order to examine the effect of major element composition on Cu diffusion, we compare Cu diffusion in anhydrous silicate melts with different compositions. As can be seen in Fig. 3.8a, Cu diffusivities measured in two anhydrous rhyolitic glasses NCO (73.5 wt% SiO_2) and CIT (76.5 wt% SiO_2) by this study are in agreement within error. Copper diffusivity in anhydrous rhyolitic melts is about 0.5 natural logarithm units lower than in anhydrous basaltic melt (Ni and Zhang 2016) and about 0.5 natural logarithm units higher than in an anhydrous $Na_2Si_2O_5$ melt, in which Cu diffusivity was determined using a voltammetry method (von der Gonna and Russel 2000). Hence, Cu diffusivity in silicate melts is only weakly dependent on major element composition. The lower Cu^+ diffusivity in anhydrous $Na_2Si_2O_5$ melt with NBO/T = 1 than that in both anhydrous rhyolitic melt with NBO/T ≈ 0 and anhydrous Etna basalt with NBO/T ≈ 3/4 is somewhat unusual and may imply that Cu diffusivity determined using voltammetry is less reliable. Copper diffusivities calculated using the model by Mungall (2002) with a melt composition equivalent to NCO are also plotted in Fig. 3.8a for comparison. The calculated Cu diffusivities are a factor of 3 to 6 higher than our experimental data.

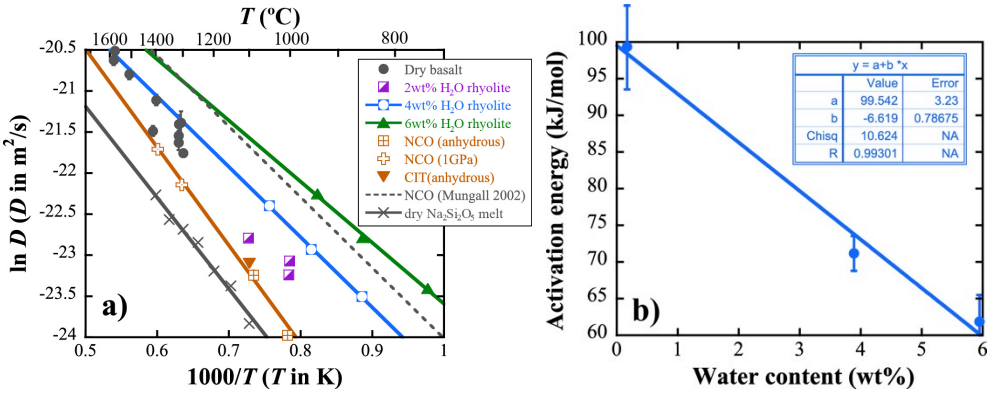

Figure 3.8. a) Arrhenius plot of all Cu diffusivities obtained in this study, together with those in anhydrous basalt (Ni and Zhang 2016, at 0.5, 1 and 1.5 GPa), dry sodium silicate melt (von der Gonna and Russel 2000, at 1bar) and calculated using the model of Mungall 2002 in NCO. Experimental pressure is 0.5 GPa unless otherwise specified. Error bars reported for diffusivities in natural silicate melts are all in 1σ (often smaller than the symbol). Diffusivities in anhydrous rhyolite, 4wt% H_2O rhyolite and 6wt% H_2O rhyolite are fitted with linear functions respectively. In general, Cu diffusivities show negligible dependence on pressure and weak dependence on major element composition, but relatively strong dependence on H_2O concentration. b) Plot of activation energy versus concentration of H_2O in rhyolitic melts. Error bars are in 1σ. Increasing H_2O concentration in rhyolitic melts decreases the activation energy roughly linearly.

The concentration of H_2O in rhyolite has a stronger effect than major element compositions on Cu diffusivity. At 1000°C, every 2 wt% H_2O in the rhyolitic melt approximately doubles Cu diffusivity. Among monovalent elements, the effect of H_2O on Cu diffusion is greater than on Na (Zhang et al. 2010), but smaller than on Cs (Watson 1981). Fitting Cu diffusivities in anhydrous rhyolitic melts and rhyolitic melts containing 4 wt% and 6 wt% H_2O (Fig. 3.8a) give results as follows:

$$D_{Cu}^{anh} = \exp\left[-(14.52 \pm 0.49) - \frac{11950 \pm 699}{T}\right], r^2=0.9898 \quad (3.3a)$$

$$D_{Cu}^{4wt\%H_2O} = \exp\left[-(15.93 \pm 0.23) - \frac{8560 \pm 286}{T}\right], r^2=0.9989 \quad (3.3b)$$

$$D_{Cu}^{6wt\%H_2O} = \exp\left[-(16.15 \pm 0.39) - \frac{7439 \pm 438}{T}\right], r^2=0.9965, \quad (3.3c)$$

where diffusivities are in m^2/s, T is temperature in K, and errors are given in 1σ.

Fitting results show that, increasing H_2O content in rhyolitic melts not only increases Cu diffusivity, but also decreases the activation energy. Activation energy of Cu diffusion in anhydrous rhyolitic melts is 99.4±5.8 kJ/mol, decreasing to 71.2±2.4 kJ/mol in 4 wt% H_2O rhyolitic melts and to 61.8±3.6 kJ/mol in 6 wt% H_2O rhyolitic melts. The decrease of activation energy is approximately linear with increasing H_2O concentration in the rhyolitic glass (Fig. 3.8b). Even in anhydrous rhyolitic melt, activation energy of Cu diffusion is small (~100 kJ/mol), consistent with our expectation that Cu is diffusing as Cu^+ in the silicate melt.

If we consider H_2O concentration in the rhyolitic melt as an independent parameter, and fit all Cu diffusivities by minimizing $\Sigma[(\ln D_{i,meas}-\ln D_{i,calc})/\sigma_i]^2$, where $\ln D_{i,meas}$, $\ln D_{i,calc}$ and σ_i are the logarithm of measured diffusivity, that of calculated diffusivity and 1σ error for $\ln D_{i,meas}$, respectively, we obtain the following expression of Cu diffusivity in rhyolitic melts containing 0.1 to 6 wt% water:

$$D_{Cu}^{Rhy} = \exp\left[-(14.75\pm0.35)-(0.23\pm0.10)w-\frac{(11647\pm491)-(698\pm117)w}{T}\right],$$

$$r^2=0.9849 \qquad (3.4)$$

where w is H_2O concentration in the rhyolitic melt in wt% and T is temperature in K. Eq. (3.4) reproduces all of our Cu diffusivity data to within 0.19 natural logarithm units.

Because we now have Cu diffusion data in rhyolitic melts and basaltic melts (Ni and Zhang 2016), effort was made to model all Cu diffusion data in natural silicate melts. In order to incorporate melt composition as a factor in Cu diffusivity, mole percent of Si+Al on wet basis was first tried to fit the data. Previously, Yu et al. (2015) used the single compositional parameter of Si+Al to successfully model SiO_2 diffusivity in rhyolitic and anhydrous basaltic melts. Zhang and Xu (2016) were also able to use Si+Al to model Zr diffusivity in rhyolitic melts. Fitting our Cu diffusion data with Si+Al, however, does not reproduce the diffusivities in basaltic melts well. After some trials, we found that a single parameter of Si+Al-H can be used to account for melt composition in fitting Cu diffusivities in anhydrous basaltic melts and rhyolitic melts at 750°C to 1575 °C and 0.5 to 1.5 GPa:

$$D_{Cu} = \exp\left\{a+b(\text{Si+Al-H})-\frac{c+d(\text{Si+Al-H})}{T}\right\}, \ r^2=0.9869 \qquad (3.5)$$

with a=-17.3±0.9, b=3.8±1.5, c=4403±1094 and d=9700±1921. In Eq. (3.5) D_{Cu} is in m^2/s and T is temperature in K, and errors are given in 1σ. Eq. (3.5) reproduces Cu diffusivities in rhyolitic and basaltic melts (Ni and Zhang 2016) to within 0.35 natural logarithm units, with a 1σ standard deviation of 0.11 natural logarithm units. The success of using Si+Al-H instead of Si+Al in fitting Cu diffusivities indicates that the effect of H_2O in the melt on Cu diffusion is more than the simple dilution of network-forming cations as previously found for Zr diffusion (Zhang and Xu 2016) and Si diffusion (Yu et al. 2015). The difference in the compositional dependence of Cu diffusivity versus Si and Zr diffusivity may be attributed to the difference between the low-field strength ion Cu and high field strength ions Zr and Si.

As discussed earlier, the pressure effect on Cu diffusion is small. Incorporating pressure in the fitting yields a fitting error that is larger than the absolute value of the fitted parameter. In addition, applying Eq. (3.5) on Cu diffusivities in $Na_2Si_2O_5$ melt (von der Gonna and Russel 2000) yields errors of up to 1.7 ln$D$ units, meaning either our Cu diffusivity model does not apply to a melt composition of $Na_2Si_2O_5$, or Cu diffusivities obtained by the voltammetry method is less reliable, as discussed earlier.

3.5.4 Dependence of Fe diffusivities on temperature and H_2O concentration in rhyolitic melt

Iron diffusivities obtained in this study are summarized on an Arrhenius plot in Fig. 3.9. As can be seen in the figure, our Fe diffusivity data in anhydrous rhyolitic melt at 1 GPa approximate those reported in Baker and Watson (1988). Concentration of H_2O in the starting glass has a strong effect on Fe diffusivity. At 1050°C, every 1 wt% H_2O increases Fe diffusivity by a factor of ~3. Because not all the experiments yielded reliable Fe diffusivities, only in 4 wt% H_2O rhyolitic glasses produced enough data points to fit the Arrhenius equation:

$$D_{\mathrm{Fe}}^{4\mathrm{wt\%H_2O}} = \exp\left[-(14.45\pm0.66)-\frac{16845\pm809}{T}\right],\ r^2=0.9977 \qquad (3.6)$$

where diffusivity is in m^2/s and T is temperature in K. The activation energy corresponding to Eq. (3.6) is 140.0±6.7 kJ. The above equation reproduces our experimental data to within 0.06 ln$D$ units.

Combining our Fe diffusion data in anhydrous and hydrous rhyolite melts with data in Baker and Watson (1988), a general equation for Fe diffusivity in rhyolitic melts as a function of temperature and H_2O concentration is obtained as follows:

$$D_{Fe}^{Rhy} = \exp\left[-(16.1\pm1.7)-\frac{(19859\pm2541)-(1218\pm135)w}{T}\right],\ r^2=0.8359 \qquad (3.7)$$

where diffusivity is in m^2/s and w is H_2O concentration in wt%. For the fitting of Eq. (3.7), because Fe diffusivities from Baker and Watson (1988) have larger errors (~0.25 natural

logarithm units on average) than our data (~0.08 natural logarithm units), Cu diffusivities from this chapter are weighted 9 times as important as the data from Baker and Watson (1988) to reflect the 3 times difference in error. The equation above corresponds to an activation energy of 165±21 kJ/mol for Fe diffusion in dry rhyolitic melts. Eq. (3.7) reproduces most data of this study and the study of Baker and Watson (1988) to less than 0.7 natural logarithm units, except for three data points in anhydrous rhyolitic melts, which are off by 0.9, 0.9 and 1.5 natural logarithm units respectively (Fig. 3.9).

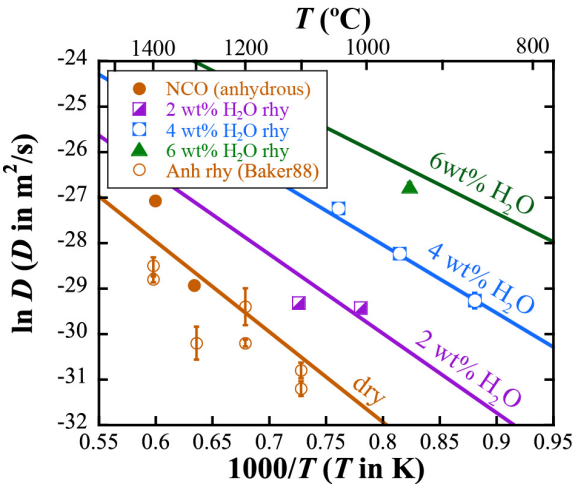

Figure 3.9. Iron diffusivities obtained in this study and from Baker and Watson 1988. All error bars shown are in 1σ. For some of the data points, error bars are smaller than the symbol size. Lines are calculated from the best-weighted fit of all data (Eq. 3.7).

For the diffusion of Fe, there is always concern as to whether Fe is diffusing as Fe^{2+} or Fe^{3+} in the experiments. As discussed in Zhang et al. (2010), Fe diffusion can be expressed as a linear combination of its Fe^{2+} and Fe^{3+} components:

$$D_{Fe} = X_{Fe^{2+}} D_{Fe^{2+}} + X_{Fe^{3+}} D_{Fe^{3+}} \quad (3.8)$$

where $X_{Fe}2+=Fe^{2+}/(Fe^{2+}+Fe^{3+})$ and $X_{Fe}3+=Fe^{3+}/(Fe^{2+}+Fe^{3+})$, respectively. Ferric iron has higher valence and is expected to diffuse at a much lower rate than Fe^{2+} in the melt. Therefore, the diffusion of Fe is usually due to the contribution of Fe^{2+}, as long as its relative abundance is high. Because our experimental durations are short, the oxidation state of Fe in the glass is likely

controlled by the initial ferric/ferrous iron ratio. Rapid diffusion of H_2 or CO, however, can occur along the chalcocite-rhyolite interface and reduce Fe^{3+} in the rhyolitic glasses, thus increasing $X_{Fe}2+$ values. One way to evaluate whether Fe^{2+} or Fe^{3+} is dominant in our experiments is to compare Fe diffusivities to Mg^{2+} diffusivities for a similar melt composition. This is because Fe^{2+} and Mg^{2+} are identical in valence and similar in size and hence are expected to have similar diffusivities. On the other hand, Fe^{3+} is trivalent and is expected to have significantly lower diffusivity than Mg^{2+}. As can be seen in Fig. 3.10, Fe diffusivities in anhydrous rhyolitic melts determined in this study are slightly higher than Mg^{2+} diffusivities in an anhydrous haplogranitic melt (Fig. 3.10), indicating that Fe diffusivities obtained in this study are mostly Fe^{2+} diffusivities.

3.5.5 Comparison to diffusivities of other elements in rhyolitic melts

Diffusivities of Cu and Fe are plotted in Fig. 3.10 to compare with other elements in rhyolitic melts. According to Cu solubility and partitioning studies in basaltic, andesitic, and rhyolitic melts (e.g., Ripley and Brophy 1995; Holzheid and Lodders 2001; Zajacz et al. 2012; Zajacz et al. 2013; Liu et al. 2015), Cu dissolves into the silicate melt mostly as Cu^+ when oxygen fugacity is below FMQ+4.4 (or NNO+3.6). Because oxygen fugacity in natural magmas is usually within NNO±2 (Carmichael and Ghiorso 1990), and assuming that the valence state of Cu does not change significantly with silicate melt composition, Cu should exist in most natural magmas as Cu^+. Although the oxygen fugacity was not controlled during our experiments, the use of graphite capsules provides a relatively reducing environment (below NNO based on measured CO_2 concentrations in the melt; Holloway 1992), and it is expected that Cu is diffusing as Cu^+ in our experiments. This conclusion is in accordance with the high diffusivity and low activation energy of Cu based on our diffusion data. Comparison of Cu diffusivity to diffusivities of alkali elements in anhydrous rhyolitic melt shows that, $D_{Li} \approx D_{Na} > D_{Cu} > D_K$, with D_{Cu} approximately 1

order of magnitude smaller than D_{Li} and D_{Na}, and about 1 natural logarithm unit higher than D_K (Fig. 3.10). According to Shannon (1976), in octahedral sites, Cu^+ has an ionic radius of 0.77Å, similar to Li^+ (0.76 Å), smaller than Na^+ (1.02 Å), and significantly smaller than K^+ (1.38 Å). These cations are compared at a fixed coordination number for self-consistency, although they are not necessarily 6-coordinated in the silicate melt. The fact that Cu diffusivity is larger than K diffusivity, but 1 order of magnitude smaller than that of Li and Na for anhydrous rhyolitic melt means that monovalent cation diffusivity cannot be predicted based on ionic radius. On the other hand, the activation energies for Cu, Li, Na and K in anhydrous rhyolitic melts are similar. Their diffusivity trends are sub-parallel to each other, as can be seen in Fig. 3.10.

As shown in Fig. 3.10, Fe diffusivity in dry rhyolitic melt NCO is slightly higher than that of Mg in a synthetic granitoid (HPG8) melt (Mungall et al. 1999), similar to that of Zn in the same melt (Mungall et al. 1999), and much smaller than those of monovalent cations. The HPG8 melt, which contains 79.6 wt% SiO_2, is more silicic than NCO melt (73.5 wt% SiO_2), and hence the lower Mg diffusivity in HPG8 relative to Fe diffusivity in NCO is probably largely due to the bulk compositional differences. Diffusivity of Fe is about three orders of magnitude smaller than Cu diffusivity, and about four orders of magnitude smaller than Li or Na diffusivity. The activation energy of Fe diffusion is also significantly higher than Cu or alkali elements. This can be seen in Fig. 3.10 from the steeper slope for Fe and Zn diffusivities than for the alkalis. In addition, the effect of H_2O content on Fe diffusion is greater than on Cu diffusion. Iron diffusivity in rhyolitic melt with 6 wt% H_2O is almost 4 orders of magnitude higher than that in anhydrous rhyolitic melts (Fig. 3.9), whereas the difference between Cu diffusivities in 6 wt% H_2O rhyolitic melt and anhydrous rhyolitic melts is only about 1 order of magnitude (Fig. 3.10). The difference is consistent with literature data that demonstrate that dissolved H_2O typically has a much stronger effect on the diffusivity of divalent cations than on monovalent cations in silicate melts, or more generally, H_2O has a larger effect on elements with smaller diffusivities (Zhang et al. 2010).

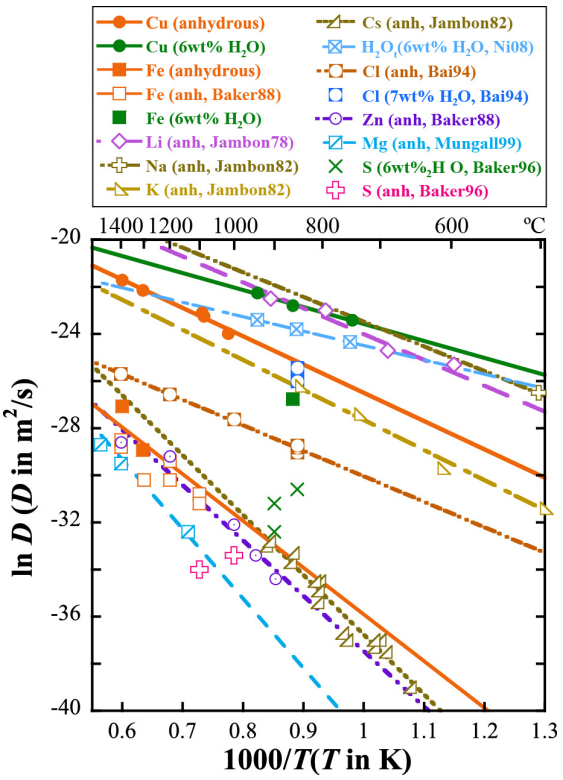

Figure 3.10. Comparison of Cu diffusivities and Fe diffusivities to diffusivities of other elements in rhyolitic melts. Fitting of Fe diffusivities in anhydrous rhyolitic melt is adopted from Fig. 9. Data sources: Cu and Fe (anhydrous and 6 wt% H_2O rhyolitic melt, this study); Fe (anhydrous rhyolitic melt, diffusion couple method, P=1000 MPa, T= 1100 to 1400 ºC, Baker and Watson 1988); Li (anhydrous rhyolitic melt, tracer diffusivity, P=0.1 MPa, T=297 to 909 ºC, Jambon and Semet 1978); Na (anhydrous rhyolitic melt, P=0.1 MPa, extrapolated from T=138 to 502 ºC, Jambon 1982); K (anhydrous rhyolitic melt, P=0.1 MPa, T=372 to 845 ºC, Jambon 1982); Cs (anhydrous rhyolitic melt, P=100 MPa, T=602 to 915 ºC, Jambon 1982); H_2O_t (6wt% H_2O rhyolitic melt, Ni and Zhang 2008); Cl (anhydrous rhyolitic melt, P=0.1 to 100 MPa, T=850 to 1400 ºC, Bai and Koster van Groos 1994); Cl (6.9 wt% H_2O rhyolitic melt, P=100 and 200 MPa, T=850 ºC, Bai and Koster van Groos 1994); Zn (diffusion couple method, P=10 and 1000 MPa, T=898 to 1400 ºC, Baker and Watson 1988); Mg (synthetic granitoid melt HPG8, P=0.1 MPa, T=1137 to 1600 ºC, Mungall et al. 1999); S (anhydrite dissolution, anhydrous and 6.1 to 6.3 wt% H_2O rhyolitic melt, P=100 to 200 MPa, T=850 to 1100 ºC, MNO oxygen buffer, Baker and Rutherford 1996).

The new Cu^+ and Fe^{2+} diffusivities reported here allow us, to update the relative diffusivity sequence of Zhang et al. (2010) in dry rhyolitic melts as follows:

$$Li \approx Na > Cu^+ > K > Ar \approx CO_2 \approx Cl \approx Rb \approx Sb \approx F > Ba \approx Cs \approx Sr > Ca > Fe^{2+} \approx S \approx Mg > Be \approx B \approx Ta \approx Nb \approx Y \approx REE > Zr \approx U \approx Hf \approx Ti \approx Ge \approx Th \approx Si \approx P \quad (3.9)$$

In rhyolitic melts with 6 wt% H_2O, the sequence of diffusivities is:

$$Cu^+ > H_2O > CO_2 > Cl > Fe^{2+} > S \quad (3.10)$$

At 1123 K, Cu diffusivity is ~50 times Cl diffusivity in anhydrous rhyolitic melts and ~30 times Cl diffusivity in rhyolitic melts with 6 wt% water. Also plotted in Fig. 3.10 are S diffusion data in 6 wt% H_2O rhyolitic melts from Baker and Rutherford (1996). Although the S diffusivities vary by almost two orders of magnitude over the temperature range 850 to 900 ºC, the data indicate that S diffusivity is much lower than Cl and Fe^{2+} diffusivity. Copper diffusivity is 4 to 5 orders of magnitude higher than S diffusivity in anhydrous rhyolitic melts and 6 wt% H_2O rhyolitic melt. One complication is that S diffusivities from Baker and Rutherford (1996) were obtained from anhydrite ($CaSO_4$) dissolution at an oxygen fugacity buffered by MNO, which is approximately FMQ+4.5 (O'Neill and Pownceby 1993). This indicates that S was diffusing in the form of S^{6+} or sulfate (SO_4^{2-}) in their experiments, instead of sulfide (S^{2-}) under the more reducing conditions typical of arc-related magmatic systems. Based on a study by Behrens and Stelling (2011), however, diffusivities of sulfide and sulfate are similar, at least in a soda lime (SiO_2-CaO-Na_2O) silicate melt. If diffusivities of sulfide and sulfate in natural silicate melt are also similar, our comparison of Cu and S diffusivities would not be affected by the diffusion species of S in silicate melts.

3.6 Implications

Prior to this study, the complete absence of experimental Cu diffusion data for rhyolitic melts required any assessment of Cu mobility in magmatic systems to use Cu diffusivities in an anhydrous $Na_2Si_2O_5$ melt (von der Gonna and Russel 2000) or theoretical values based on the model of Mungall (2002). Here, we use our new Cu diffusion data for rhyolite melts to assess the transfer and partitioning behavior of Cu in an MVP-saturated magma. Our new Cu diffusion data suggest that, in a fluid-saturated magma (melt + crystals + MVP) wherein Cu behaves incompatibly in the fractionating crystal assemblage, the concentration of Cu in the MVP exsolved from a hydrous rhyolitic melt would always be close to equilibrium partitioning, because Cu diffusivity in the melt is higher than that of water and other elements (Fig. 3.10) (e.g.,

Zhang 2015). Experimental studies show that the Cu content of the MVP increases with increasing Cl content of the MVP (Audetat and Simon 2012; Zajacz et al. 2012) wherein Cu is complexed with Cl (i.e., CuCl; Candela and Holland 1984) or in the form of alkali-copper-chloride complex (e.g., Na(/K)$CuCl_2$; Zajacz et al. 2011). Thus, the diffusion of Cl from the melt to the MVP plays a key role not only in the Cl concentration in the MVP, but also in the partitioning of Cu between the melt and the MVP. That is, once an MVP bubble forms, the ability of the bubble to scavenge Cu depends on the Cl concentration in the MVP and hence the diffusion of Cl from the melt to the MVP. The rapid diffusion of Cu would ensure that Cu partitioning between the MVP and the melt is always approximately in equilibrium, whether the MVP is made of individual bubbles or forms percolation clusters buoyantly rising through the melt. Once Cl concentration in the MVP is modeled, the Cu concentration in the MVP can be estimated from batch equilibrium partitioning. This conclusion is different from the modeling results of Huber et al. (2012), mainly because a much lower Cu diffusivity (almost two orders of magnitude lower than our experimental data) from von der Gonna and Russel (2000) was used in their study.

Our Cu diffusion data can also be applied to elucidate the Cu and Zn isotope signatures of tektites, such as in the studies of Moynier et al. (2009, 2010). These studies reported significant depletion of both Cu (from typical upper crustal concentration of 28 ppm to ~2 ppm) and Zn (from typical upper crustal concentration of 67 ppm to ~20 ppm) in tektites, where the typical upper crustal concentrations are from Rudnick and Gao (2014). In accordance with the depleted abundances of Zn and Cu, both metals exhibit enrichment of their heavy isotopes (+1.22‰ < $\delta^{66/64}$Zn < +2.49‰; +1.98‰ < $\delta^{65/63}$Cu < +6.99‰). To explain the more fractionated Cu isotope signature relative to Zn, Moynier et al. (2010) used the diffusion model of Mungall (2002) to estimate Cu^+ diffusivity to be 2 orders of magnitude greater than Zn^{2+} diffusivity at 1150 ºC. Based on experimental data from this study and from Baker and Watson (1988), however, the difference is almost 4 orders of magnitude at 1150 ºC (Fig. 3.10). In general, our Cu diffusion

data support the explanation by Moynier et al. (2010) that the more fractionated Cu isotope signature in tektites is likely due to the higher Cu diffusivity than Zn. It would be desirable to measure Cu and Zn concentration profiles in individual tektites to assess Cu and Zn loss, and to model the isotopic fractionation.

3.7 Acknowledgments

We thank J. C. Barrette for the assistance in LA-ICP-MS analysis, and Fabio Arzilli and James Mungall for their constructive and insightful reviews. P. Ni thanks Z. Xu for the training and help with FTIR analysis and piston-cylinder experiments. This work was partially supported by NSF grants EAR-1019440 and EAR-1524473 and NASA grant NNX15AH37G, and NSF grants EAR-1264560 and EAR-1250239 to ACS.

3.8 References

Audetat, A., and Simon, A.C. (2012) Magmatic controls on porphyry Cu genesis. Geology and Genesis of Major Copper Deposits and Districts of the World: a Tribute to Richard Sillitoe. Society of Economic Geologists, Special Publication, 16, 553-572.

Bai T.B. and Koster van Groos, A.F. (1994) Diffusion of chlorine in granitic melts. Geochim Cosmochim Acta, 58, 113-123.

Baker, L.L., and Rutherford, M.J. (1996) Sulfur diffusion in rhyolite melts. Contributions to Mineralogy and Petrology, 123(4), 335-344.

Baker D.R., and Watson E.B. (1988) Diffusion of major and trace elements in compositionally complex Cl- and F-bearing silicate melts. J Non-Cryst Solids, 102, 62-70

Behrens, H., and Stelling, J. (2011) Diffusion and redox reactions of sulfur in silicate melts. Reviews in Mineralogy and Geochemistry, 73(1), 79-111.

Carmichael, I.S., and Ghiorso, M.S. (1990) The effect of oxygen fugacity on the redox state of natural liquids and their crystallizing phases. Reviews in Mineralogy and Geochemistry, 24(1), 191-212.

Candela, P.A., and Holland, H.D. (1984) The partitioning of copper and molybdenum between silicate melts and aqueous fluids. Geochimica et Cosmochimica Acta, 48, 373-380.

Candela, P.A. (1991) Physics of aqueous phase evolution in plutonic environments. American Mineralogist, 76, 1081-1091.

Candela, P.A. (1997) A review of shallow, ore-related granites: textures, volatiles, and ore metals. Journal of petrology, 38(12), 1619-1633.

Cassidy, W.A., Glass, B., and Heezen, B.C. (1969) Physical and chemical properties of Australasian microtektites. Journal of Geophysical Research,74(4), 1008-1025.

Chen, Y., and Zhang, Y. (2008) Olivine dissolution in basaltic melt. Geochimica et Cosmochimica Acta, 72(19), 4756-4777.

Crank, J. (1975) The Mathematics of Diffusion. Oxford, UK: Clarendon Press.

Fournelle, J.H., Kim, S., and Perepezko, J.H. (2005) Monte Carlo simulation of Nb Kα secondary fluorescence in EPMA: comparison of PENELOPE simulations with experimental results. Surface and interface analysis, 37(11), 1012-1016.

Harrison, T. M., and Watson, E.B. (1983) Kinetics of zircon dissolution and zirconium diffusion in granitic melts of variable water content. Contributions to Mineralogy and Petrology, 84(1), 66-72.

Holloway, J. R., Pan, V., and Gudmundsson, G. (1992) High-pressure fluid-absent melting experiments in the presence of graphite: oxygen fugacity, ferric/ferrous ratio and dissolved CO_2. European Journal of Mineralogy, 4(1), 105-114.

Holzheid, A., and Lodders, K. (2001) Solubility of copper in silicate melts as function of oxygen and sulfur fugacities, temperature, and silicate composition. Geochimica et Cosmochimica Acta, 65(12), 1933-1951.

Huber, C., Bachmann, O., Vigneresse, J.L., Dufek, J., and Parmigiani, A. (2012) A physical model for metal extraction and transport in shallow magmatic systems. Geochemistry, Geophysics, Geosystems, 13(8).

Hui, H., and Zhang, Y. (2007) Toward a general viscosity equation for natural anhydrous and hydrous silicate melts. Geochimica et Cosmochimica Acta, 71(2), 403-416.

Hui, H., Zhang, Y., Xu, Z., and Behrens, H. (2008) Pressure dependence of the speciation of dissolved water in rhyolitic melts. Geochimica et Cosmochimica Acta, 72(13), 3229-3240.

Jambon A. (1982) Tracer diffusion in granitic melts: experimental results for Na, Rb, Cs, Ca, Sr, Ba, Ce, Eu to 1300ºC and a model of calculation. J Geophys Res 87:10797-10810.

Jambon A., and Semet MP (1978) Lithium diffusion in silicate glasses of albite, orthoclase, and obsidian compositions: an ion-microprobe determination. Earth Planet Sci Lett 37:445-450

Liu, X., Xiong, X., Audetat, A., and Li, Y. (2015) Partitioning of Cu between mafic minerals, Fe–Ti oxides and intermediate to felsic melts. Geochimica et Cosmochimica Acta, 151, 86-102.

Llovet, X., & Salvat, F. (2006). PENEPMA, A Monte Carlo code for the simulation of X-ray emission spectra using PENELOPE. In Madison, WI: Workshop Manual.

Lodders, K. (2003) Solar system abundances and condensation temperatures of the elements. The Astrophysical Journal, 591(2), 1220.

Moynier, F., Beck, P., Jourdan, F., Yin, Q.Z., Reimold, U., and Koeberl, C. (2009) Isotopic fractionation of zinc in tektites. Earth and Planetary Science Letters, 277, 482-489.

Moynier, F., Koeberl, C., Beck, P., Jourdan, F., and Telouk, P. (2010) Isotopic fractionation of Cu in tektites. Geochimica et Cosmochimica Acta, 74, 799-807.

Mungall, J.E., Dingwell, D.B., and Chaussidon, M. (1999) Chemical diffusivities of 18 trace elements in granitoid melts. Geochimica et Cosmochimica Acta, 63(17), 2599-2610.

Mungall, J.E. (2002) Empirical models relating viscosity and tracer diffusion in magmatic silicate melts. Geochimica et Cosmochimica Acta, 66, 125-143.

Newman, S., Stolper, E.M., and Epstein, S. (1986) Measurement of water in rhyolitic glasses--calibration of an infrared spectroscopic technique. American Mineralogist, 71(11), 1527-41.

Ni, P., and Zhang, Y. (2016) Cu diffusion in a basaltic melt. American Mineralogist, 101(6), 1474-1482.

Ni, H., and Zhang, Y. (2008) H_2O diffusion models in rhyolitic melt with new high pressure data. Chemical Geology, 250, 68-78.

O'Neill, H.S.C., and Pownceby, M.I. (1993) Thermodynamic data from redox reactions at high temperatures. II. The MnO-Mn_3O_4 oxygen buffer, and implications for the thermodynamic properties of MnO and Mn_3O_4.Contributions to Mineralogy and Petrology, 114(3), 315-320.

Parmigiani, A., Faroughi, S., Huber, C., Bachmann, O., and Su, Y. (2016) Bubble accumulation and its role in the evolution of magma reservoirs in the upper crust. Nature, 532(7600), 492-495.

Pearce, N.J., Perkins, W.T., Westgate, J.A., Gorton, M.P., Jackson, S.E., Neal, C.R., and Chenery, S.P. (1997) A compilation of new and published major and trace element data for NIST SRM 610 and NIST SRM 612 glass reference materials. Geostandards newsletter, 21(1), 115-144.

Pettke, T., Oberli, F., Audétat, A., Guillong, M., Simon, A.C., Hanley, J.J., and Klemm, L.M. (2012) Recent developments in element concentration and isotope ratio analysis of individual fluid inclusions by laser ablation single and multiple collector ICP-MS. Ore Geology Reviews, 44, 10-38.

Ripley, E.M., and Brophy, J.G. (1995) Solubility of copper in a sulfur-free mafic melt. Geochimica et cosmochimica acta, 59(23), 5027-5030.

Rudnick, R.L., and Gao, S.X. (2014) Composition of the continental crust. Treatise on geochemistry (Second Edition), 4, 1-51.

Shannon, R.T. (1976) Revised effective ionic radii and systematic studies of interatomic distances in halides and chalcogenides. Acta Crystallographica Section A: Crystal Physics, Diffraction, Theoretical and General Crystallography, 32(5), 751-767.

Simon, A.C., and Ripley, E.M. (2011). The role of magmatic sulfur in the formation of ore deposits. Reviews in Mineralogy and Geochemistry, 73(1), 513-578.

Singer, D.A. (1995) World class base and precious metal deposits; a quantitative analysis. Economic Geology, 90(1), 88-104.

von der Gonna, G., and Russel, C. (2000) Diffusivity of various polyvalent elements in a $Na_2O \cdot 2SiO_2$ glass melt. Journal of non-crystalline solids, 261(1), 204-210.

Walter, L.S. (1967) Tektite compositional trends and experimental vapor fractionation of silicates. Geochimica et Cosmochimica Acta, 31, 2043-2063.

Watson, E.B. (1981) Diffusion in magmas at depth in the Earth: The effects of pressure and dissolved H_2O. Earth and Planetary Science Letters, 52(2), 291-301.

Wilkinson, J.J. (2013) Triggers for the formation of porphyry ore deposits in magmatic arcs. Nature Geoscience, 6(11), 917-925.

Yang, Y., Zhang, Y., Simon, A., & Ni, P. (2016). Cassiterite dissolution and Sn diffusion in silicate melts of variable water content. Chemical Geology, 441, 162-176.

Yu, Y., Zhang, Y., and Yang, Y. (2015) Diffusion of SiO2 in rhyolitic melt. In AGU Fall Meeting Abstracts.

Yu, Y., Zhang, Y., Chen, Y., and Xu, Z. (2016) Kinetics of anorthite dissolution in basaltic melt. Geochimica et Cosmochimica Acta, 179, 257-274.

Zajacz, Z., Seo, J.H., Candela, P.A., Piccoli, P.M., and Tossell, J.A. (2011) The solubility of copper in high-temperature magmatic vapors: a quest for the significance of various chloride and sulfide complexes. Geochimica et Cosmochimica Acta, 75(10), 2811-2827.

Zajacz, Z., Candela, P.A., Piccoli, P.M., Walle, M., and Sanchez-Valle, C. (2012) Gold and copper in volatile saturated mafic to intermediate magmas: Solubilities, partitioning, and implications for ore deposit formation. Geochimica et Cosmochimica Acta, 91, 140-159.

Zajacz, Z., Candela, P.A., Piccoli, P.M., Sanchez-Valle, C., and Walle, M. (2013) Solubility and partitioning behavior of Au, Cu, Ag and reduced S in magmas. Geochimica et Cosmochimica Acta, 112, 288-304.

Zhang, Y., Walker, D., and Lesher, C. E. (1989) Diffusive crystal dissolution. Contributions to Mineralogy and Petrology, 102(4), 492-513.

Zhang, Y., Belcher, R., Ihinger, P.D., Wang, L., Xu, Z., and Newman, S. (1997) New calibration of infrared measurement of dissolved water in rhyolitic glasses. Geochimica et Cosmochimica Acta, 61(15), 3089-3100.

Zhang, Y. (2008) Geochemical kinetics. Princeton University Press.

Zhang, Y. (2015). Toward a quantitative model for the formation of gravitational magmatic sulfide deposits. Chemical Geology, 391, 56-73.

Zhang, Y., Ni, H., and Chen, Y. (2010) Diffusion data in silicate melts. Reviews in Mineralogy and Geochemistry, 72, 311-408.

Zhang, Y., and Xu, Z. (2016) Zircon saturation and Zr diffusion in rhyolitic melts, and zircon growth geospeedometer. American Mineralogist, 101(6), 1252-1267.

Zhao, D., Zhang, Y., and Essene, E.J. (2015) Electron probe microanalysis and microscopy: Principles and applications in characterization of mineral inclusions in chromite from diamond deposit. Ore Geology Reviews, 65, 733-748.

CHAPTER IV

Volatile loss during homogenization of lunar melt inclusions

4.1 Abstract

Volatile abundances in lunar mantle are critical factors to consider for constraining the model of Moon formation. Recently, the earlier understanding of a "dry" Moon has shifted to a fairly "wet" Moon due to the detection of measurable amount of H_2O in lunar volcanic glass beads, mineral grains, and olivine-hosted melt inclusions. The ongoing debate on a "dry" or "wet" Moon requires further studies on lunar melt inclusions to obtain a broader understanding of volatile abundances in lunar mantle. One important uncertainty for lunar melt inclusion studies, however, is whether the homogenization of melt inclusions would cause volatile loss. In this chapter of my thesis, a series of homogenization experiments were conducted on olivine-hosted melt inclusions from the sample 74220 to evaluate the possible loss of volatiles during homogenization of lunar melt inclusions. Our results suggest that significant loss of H_2O could occur even during minutes of homogenization, while F, Cl and S in the inclusions remain unaffected.

We model the trend of H_2O loss in homogenized melt inclusions by a diffusive hydrogen loss model. The model can reconcile the observed experimental data well, with a best-fit H diffusivity in accordance with diffusion data explained by the "slow" mechanism for hydrogen diffusion in olivine. Surprisingly, no significant effect for the low oxygen fugacity on the Moon is observed on the diffusive loss of hydrogen during homogenization of lunar melt inclusions under reducing conditions. Our experimental and modeling results show that diffusive H loss is negligible for melt inclusions of >25μm radius. By using these inclusions, we found that H_2O/Ce

ratios in melt inclusions from different lunar samples vary with degree of crystallization. Such a variation is either due to H_2O loss on the lunar surface, or due to heterogeneity in their lunar mantle source. A similar size-dependence trend of H_2O concentrations was also observed in natural unheated melt inclusions in 74220. By comparing the trend of diffusive H loss in the natural MIs and in our homogenized MIs, the cooling rate for 74220 was estimated to be ~1 ºC/s or slower.

4.2 Introduction

Volatile content in the primitive lunar mantle is a fundamental factor to consider for the origin of the Moon, but remains unsolved. The most widely accepted model for Moon formation is the giant impact hypothesis, in which the Moon formed by the collision between a Martian size planetesimal and the proto-earth (e.g. Canup and Asphaug, 2001). Early studies suggest strong depletion of volatile elements on the Moon, with H_2O concentration typically below detection limit, leading authors to conclude that Moon is dry (e.g. <1 ppb H_2O, Taylor et al., 2006), which was thought to be consistent with the giant impact hypothesis. Recently, however, the view of a dry Moon has been challenged due to the detection of magmatic water in lunar volcanic glass beads (Saal et al., 2008, 2013; Hauri et al., 2015; Chen et al., 2015), olivine-hosted melt inclusions (Hauri et al., 2011, 2015; Chen et al., 2015), and lunar plagioclase from highland anorthosites (Hui et al., 2013). Olivine-hosted melt inclusions (will be referred as "MIs" hereafter) are pockets of magma trapped in olivine that provides protection on the pre-eruptive volatile content of the magma (Anderson, 1974; Sobolev, 1996; Danyushevsky et al., 2002). They are also the lunar samples where the highest H_2O concentrations were detected (up to ~1400 ppm, Hauri et al., 2011). Although the high H_2O/Ce ratios measured in 74220 indicate a mantle source containing at least 110 ppm H_2O (Chen et al., 2015), some authors argue that 74220 is a local anomaly unrepresentative of the entire lunar interior (Albarede et al., 2013, 2015). Therefore, melt inclusion studies on a larger collection of lunar volcanic rocks are necessary before reaching

a conclusion on volatile contents of the lunar interior. A major complication is that most lunar olivine-hosted melt inclusions are at least partially crystallized, making it necessary to re-homogenize the melt inclusions for precise electron microprobe (EMP) or secondary ion mass spectrometry (SIMS) analyses (e.g. Roedder and Weiblen, 1970; Bombardieri et al., 2005; Chen et al., 2015). Homogenization of the melt inclusions, however, involves heating up the olivine to 1267 to 1330 ºC for at least a couple of minutes, which might cause volatile loss from the melt inclusions, especially H_2O. One uncertainty in Chen et al. (2015), for example, is whether the relatively low H_2O/Ce ratios in the homogenized lunar melt inclusions are due to H_2O loss during homogenization.

Loss of H_2O from olivine-hosted melt inclusions has been experimentally examined previously using terrestrial samples (e.g. Hauri, 2002; Massare et al., 2002; Portnyagin et al., 2008; Chen et al., 2011 and Gaetani et al., 2012). Hydration and homogenization experiments in these studies show that, H_2O in olivine-hosted melt inclusions can exchange with the surrounding melt in time scales of ten minutes to days. Controversy occurs, however, in terms of the apparent hydrogen diffusivities in olivine suggested by these experiments. For example, the results of Hauri (2002) and Massare et al. (2002) suggest high hydrogen diffusivities, which is in accordance with H diffusion data from Kohlstedt and Mackwell (1998). On the other hand, experiments by Portnyagin et al., 2008; Chen et al., 2011 and Gaetani et al., 2012, are supportive of the lower H diffusivities reported in Demouchy and Mackwell, (2006). The range of H diffusivities in olivine hinders accurate estimation of possible H_2O loss from lunar melt inclusions during homogenization experiments. In addition, the more reducing conditions on the Moon (~IW-1, Sato, 1976; Weitz et al., 1997) mean a higher proportion of molecular hydrogen among all hydrogen species in the melt (e.g. Zhang and Ni, 2010; Zhang, 2011; Hirschmann et al., 2012) that further complicates the degassing rate of H_2O through olivine. In order to constrain the effect of homogenization experiments on concentrations of H_2O and other volatiles in lunar melt inclusions, we use lunar melt inclusions as the starting material. In this study, olivine-hosted melt

inclusions from 74220 were homogenized under reducing conditions and compared with the un-heated ones from the same batch of samples in terms of their H_2O, F, Cl and S concentrations. The results provide crucial guidance to understand and make best use of the volatile data of homogenized lunar MIs.

4.3 Experimental and analytical methods

The lunar soil sample 74220, discovered at Shorty Crater during Apollo 17, was famous for its high-Ti orange glass beads. High concentrations of H_2O (up to ~1410 ppm) were also first detected in olivine-hosted melt inclusions from this sample (Hauri et al., 2011). Since volatile concentrations (e.g. H_2O, F, Cl and S) in melt inclusions from 74220 are relatively well known (Hauri et al., 2011, 2015; Chen et al., 2015), olivine grains from 74220 are used in this study to experimentally understand the possible loss of volatiles during homogenization. Here we want to emphasize that melt inclusions found in 74220 are naturally glassy or mostly glassy. The purpose of the homogenization experiments are not to produce a glassy and homogenized phase for precise EMP or SIMS analyses, but to study the possible loss of volatiles during the homogenization process. Most of the olivine samples in this study are from 74220, 892, except for 74220 OldOL1 and OldOL2, which are from 74220, 871.

The 74220 soil sample was placed in a pan with ethanol, and olivine grains with melt inclusions were manually picked under an optical microscope. These olivine grains are typically ~100 μm in radius and often have a layer of basaltic glass on the surface (Fig. 4.1a). In order to minimize the reaction between the surface melt with the olivine during homogenization, olivine grains were gently polished before experiment to remove most of the surface glass. Melt inclusions in each olivine grain were homogenized by an individual experiment in a one-atmosphere furnace. Graphite crucibles were used for the homogenization experiments. The graphite crucible for each homogenization experiment was machined from a high-purity graphite rod (with less than 50 ppm impurities) to minimize the possibility of contamination. During

homogenization, a graphite crucible containing one olivine grain was gradually inserted in the hot spot of the furnace and kept at 1330 ºC for about 2 min under a constant flow of 99.9999% N_2. Heating rate of the sample was constrained below 200 ºC/min to prevent olivine from cracking. The gradual heating means that the effective heating duration is longer than 2 min (discussed later). Then, the graphite crucible was taken out of the furnace and quenched in water. The quench process typically took 10 to 15 seconds, except for sample 74220 OldOL1, for which a thick graphite crucible was used. The selection of experimental temperature was based on the experimentally determined liquidus of 74220 orange glasses at one bar (~1323 ºC, Green et al., 1975), whereas the homogenization duration was chosen to be similar with previous studies (e.g. Chen et al., 2015). One example of the olivine-hosted melt inclusions after experiment is shown in Fig. 4.1b. After homogenization, each olivine grain was polished separately to expose the melt inclusions inside and loaded into an indium mount for EMP and SIMS analyses. Besides the homogenized melt inclusions from 74220, four unheated MIs from the same batch of sample were also analyzed for a comparison.

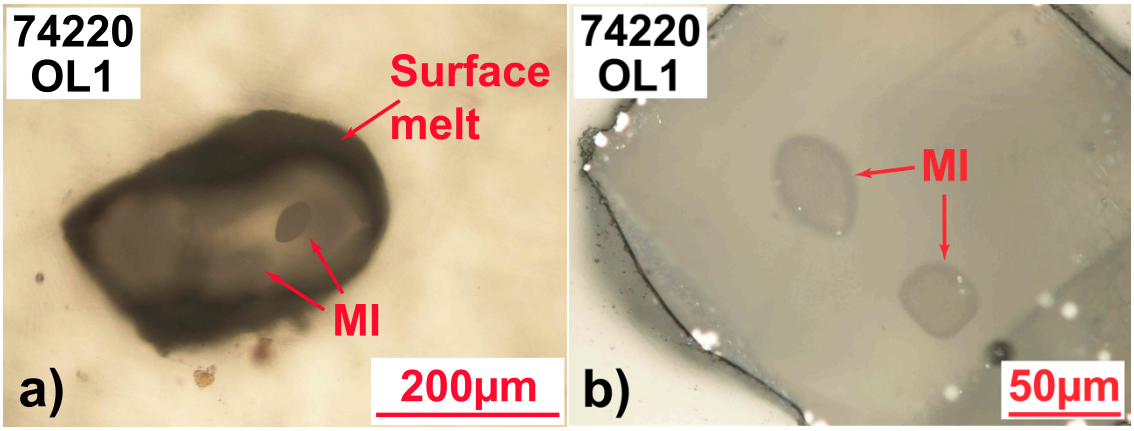

Figure 4.1. Optical microscope images of an olivine with melt inclusions from 74220 a) before homogenization and b) after homogenization. The olivine grain was covered by a layer of basaltic melt when picked from 74220. Melt inclusions inside the olivine were discovered when the surface melt on one side of the olivine was carefully removed, as shown in a).

Major element compositions of olivines and melt inclusions were analyzed by a CAMECA SX-100 electron microprobe at the University of Michigan, with a 15 kV and 10 nA

focused beam. After EMP analyses, carbon coating on the sample surface was gently polished away and the sample was re-coated with gold for SIMS analyses. Volatiles (H reported as H_2O, F, P, S and Cl) and other trace elements (Li, Na, K, Sr, Y, Zr, Nb, Ba, La, Ce, Pr, Nd, Sm, Eu, Gd, Tb, Dy, Ho, Er, Tm, Yb and Lu) were analyzed in two separate sessions using a Cameca IMS 7f-GEO at Caltech following analytical procedures in Chen et al. (2015) as briefly described below.

For the SIMS measurement of volatile abundances, a 10 keV Cs^+ primary ion beam of 3 to 5 nA was used to sputter the samples. Eight secondary ion species, $^{12}C^-$, $^{16}O^1H^-$, $^{18}O^-$, $^{19}F^-$, $^{30}Si^-$, $^{31}P^-$, $^{32}S^-$ and $^{35}Cl^-$ were sequentially collected with an electron multiplier detector. A series of seven MPI-Ding glasses (GOR128-G, GOR132-G, KL2-G, ML3B-G, StHs6/80-G, T1-G, ATHO-G) (Jochum et al., 2006) and a mid-ocean ridge basalt (MORB) glass were used as the calibration standards. Water concentrations in the standard glasses are from Chen et al. (2015), except for the MORB glass, whose H_2O concentration was measured by FTIR at the University of Michigan. For the calibration of F, Cl, S and P, concentrations reported in Jochum et al. (2006) were used. A synthetic basalt glass (Et1) from Ni and Zhang (2016) with 12.8 ± 0.6 ppm H_2O was used to assess the $^{16}O^1H^-/^{18}O^-$ ratio for low H_2O samples under our analytical conditions. With special efforts to lower the hydrogen background during analyses, a $^{16}O^1H^-/^{18}O^-$ of about 1×10^{-3} was achieved on the Et1 glass. When analyzing the melt inclusions, each position was pre-sputtered for 60 to 120 seconds over a 25×25 μm area to remove surface contamination. Melt inclusions could be precisely located with the secondary ion image of $^{27}Al^{16}O^-$ that clearly distinguishes melt inclusions from their host olivine. Cracks were avoided to alleviate the concern of contamination on volatile counts. Data of twenty cycles were counted for the eight secondary ions, and the cycle data were examined for any possibility of beam drilling into olivine during the measurement process.

Twenty-two trace elements (Li, Na, K, Sr, Y, Zr, Nb, Ba, La, Ce, Pr, Nd, Sm, Eu, Gd, Tb, Dy, Ho, Er, Tm, Yb and Lu) were analyzed for the melt inclusions with an 11-14 nA O^- primary ion beam. Trace element analyses on melt inclusions were conducted on or near previous analysis

positions for volatiles, by locating the previous craters with the secondary ion image of $^{27}Al^{+}$. Sensitivity factors were determined with the NIST 610 silicate glass (Pearce et al., 1997). Two additional NIST standards (NIST 612, Pearce et al., 1997 and NIST 614, Gao et al., 2002) and two MPI-DING standards (GOR128-G and KL2-G, Jochum et al., 2006) were used as secondary standards to check the quality of trace element analysis. The results obtained on secondary standards are mostly within error compared with the reference values (Table C2 & Fig. C1), supporting the reliability of our analysis. A combination of the following three criteria were employed to exclude trace element data that indicated the ion beam drilled into olivine during measurement: (a) significant drift of Na counts through cycles; (b) measured Na concentration is more than 20% lower than the EMP data; (c) measured Sr concentration is more than 20% lower than the whole rock data (Wanke et al., 1973).

4.4. Results

4.4.1 Textures of the homogenized and natural unheated melt inclusions

Back-scattered electron images of two homogenized melt inclusions and two unheated melt inclusions analyzed in this study are shown in Fig. 4.2. Melt inclusions in 74220 are usually ellipsoidal in shape. Host olivine grains of the melt inclusions from this study are similar in chemical composition, with forsterite numbers from 78 to 80. Radiuses of the host olivines are typically ~100μm. The homogenized melt inclusions are optically glassy and homogeneous, but may contain a bubble or metallic Fe globules (e.g. Fig. 4.2a). The natural unheated melt inclusions from 74220 (e.g. Fig. 4.2c, 4.2d) often show various degrees of dendritic olivine growth from the inner wall of the inclusion.

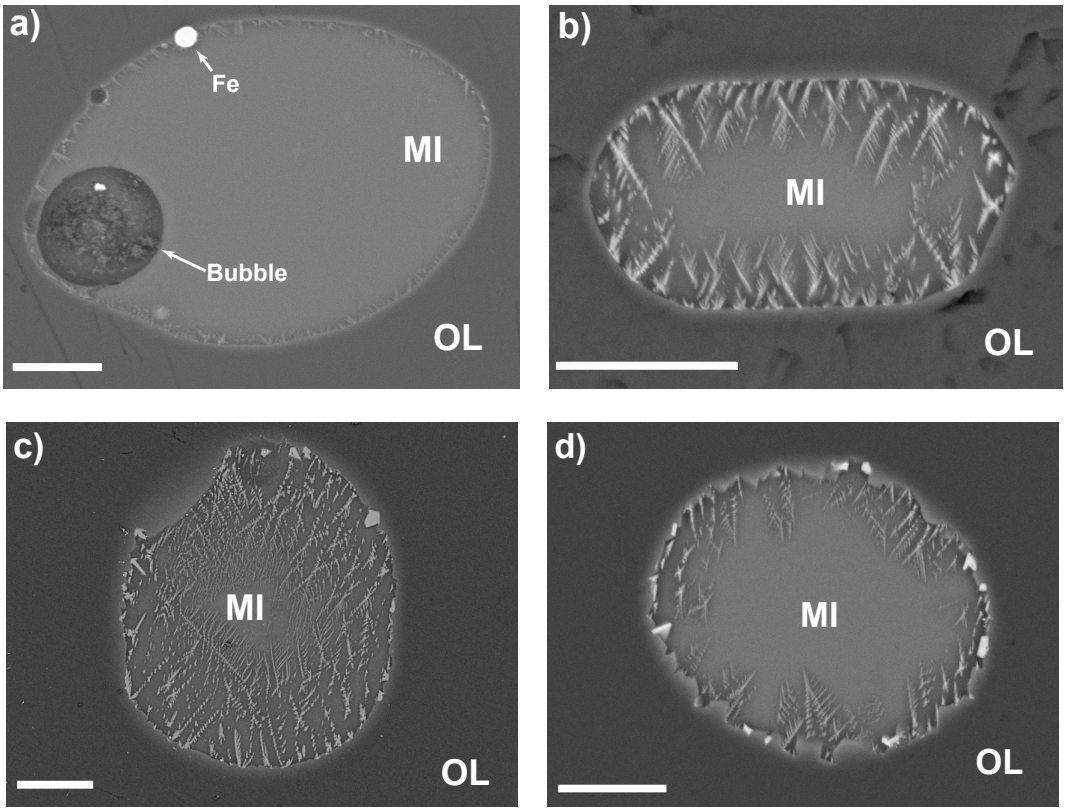

Figure 4.2. Example of BSE images for the melt inclusions in 74220. Scale bars in the images represent 10µm. a) Homogenized melt inclusion 74220 OL1a contains a bubble and a spherical Fe metal after homogenization; b) Melt inclusion 74220 OldOL1 shows more dendritic olivine growth, which might be due to the thick-wall crucible used for its homogenization; c) Natural unheated melt inclusion 74220 OL8 shows extensive dendritic olivine growth almost across the entire inclusion; d). Natural unheated melt inclusion 74220 OldOL2 shows less dendritic olivine growth compared to OL8 in c).

4.4.2 Major elements

Major element compositions of homogenized and unheated melt inclusions from 74220 are reported in Table C1. The major element concentrations of the homogenized melt inclusions are similar to the natural unheated ones in 74220, but differ significantly from the glass bead composition of 74220 (Wanke et al., 1973). The MgO concentrations in the homogenized melt inclusions and natural unheated melt inclusions are 4.0 to 6.5 wt%, lower than the 14 wt% MgO in bulk 74220 (Wanke et al., 1973). On the other hand, concentrations of the incompatible major elements in the melt inclusions are significantly higher than those of the bulk sample. As shown in Fig. 4.3, Al_2O_3 and CaO concentrations in the melt inclusions fall onto a calculated evolution

trend with the orange glass beads. Evolution of the major element compositions for the melt inclusions in 74220 can be attributed to post-entrapment growth of olivine, as suggested by Chen et al. (2015).

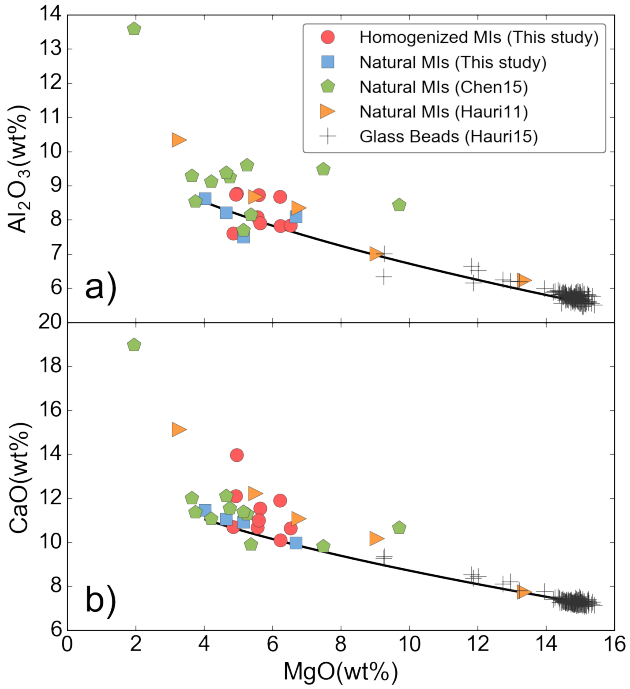

Figure 4.3. Major element compositions of the homogenized and natural melt inclusions in 74220 compared to 74220 orange glass beads. Negative correlations between the incompatible major elements (Al_2O_3 and CaO) and MgO indicate an evolution trend from the orange glass beads, which are more representative of the parental magma composition. Black curve in the figure shows calculated compositional evolution trend controlled by crystallization of olivine.

An assessment of whether the melt inclusions are in equilibrium with the host olivine is the apparent partitioning coefficient (K_D) of Mg^{2+} and Fe^{2+} exchange between olivine and the melt. According to Xirouchakis et al. (2001), equilibrium K_D between olivine and a melt with 12 wt% TiO_2 is ~0.28. The apparent K_D values for the natural unheated melt inclusions are 0.09 to 0.13, consistent with 20% to 30% of post-entrapment crystallization. The apparent K_D values for the homogenized melt inclusions are in the range of 0.10 to 0.17, only slightly higher than those for the unheated ones. The slight increase in the apparent K_D values of the heated inclusions is attributed to the dissolution of post-entrapment crystallized olivine into the melt inclusions during

homogenization. However, lower apparent K_D values than the equilibrium K_D indicate that the homogenization duration was not long enough for the melt inclusions to reach equilibrium with the host olivine. In addition, rapid dendritic growth of olivine on the melt inclusion wall during quench (e.g. Fig. 4.2b) can also partially contribute to the low apparent K_D in the homogenized melt inclusions because only the glassy parts are analyzed. Since the goal of this study is to evaluate volatile loss when homogenizing lunar melt inclusions, the duration was chosen to be representative of typical homogenization experiments for crystalline melt inclusions (e.g. Chen et al., 2015), rather than the time to reach equilibrium between melt inclusions and the host olivine.

4.4.3 Trace element concentrations

Spidergrams for trace elements (plus F) for the 74220 homogenized and natural unheated melt inclusions are shown in Fig. 4.4. The spidergrams show strong depletion in K, P, F and Eu, and enrichment in Nb and Ti. The depletion of volatile elements (F and K) is consistent with the expected volatile-depletion of the Moon. Depletion of P in lunar samples has been explained by lunar core segregation (Newsom, 1986). The average F/Nd ratio for 74220 melt inclusions in this study is 2.1±0.3, consistent with the average ratio in Chen et al. (2015). The enrichment of Nb and Ti in 74220 indicates ilmenite addition at a certain stage during the formation of lunar high-Ti basalts. Depletion of Eu and Sr, on the other hand, is likely related to the removal of plagioclase during the magma ocean stage, resulting in Eu anomaly in the mantle source of 74220.

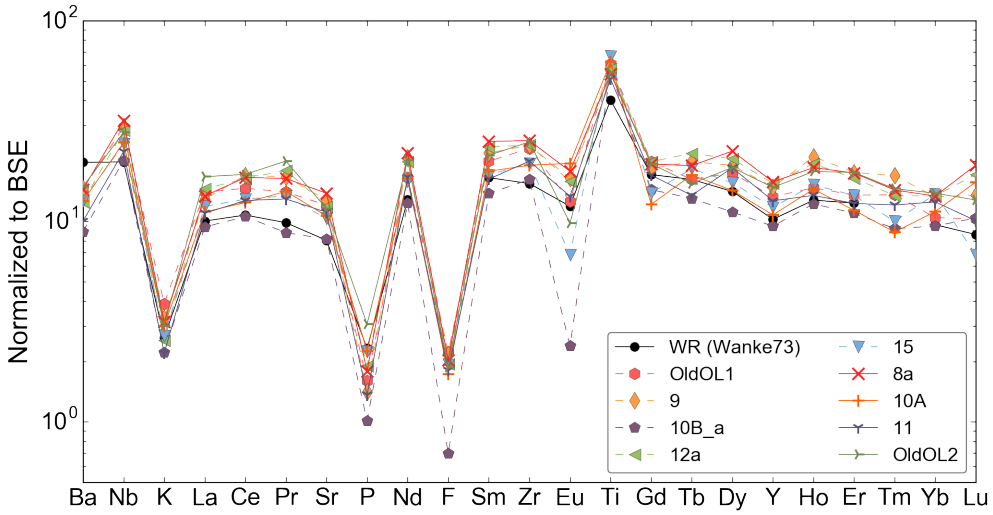

Figure 4.4. Spidergram for 74220 melt inclusions studied in this work. Filled symbols are for homogenized melt inclusions (74220 OldOL1, OL9, OL10Ba, OL12a and OL15), while open symbols are for natural unheated melt inclusions (OL 8a, OL10A, OL11 and OldOL2). Bulk silicate earth (BSE) compositions are from McDonough and Sun, 1995. The whole rock data for 74220 is from (Wanke et al., 1973).

4.4.4 Correlation between volatile concentrations and inclusion radiuses

It is expected that volatile loss (or more generally, diffusive re-equilibrium with the environment) depends on the melt inclusion radius (e.g. Qin et al., 1992; Chen et al., 2013; Lloyd et al., 2013). In Fig. 4.5, H_2O, F, Cl and S concentrations of the homogenized and natural unheated MIs are plotted versus melt inclusion radius. Radiuses of the ellipsoid-shaped melt inclusions are estimated as the geometric mean of the two principle axes exposed after polish. Due to the limited number of MIs with both major element and volatile data available, uncorrected concentrations are used for the plot. A PEC correction of 5% to 30% could affect individual data points slightly, but not the overall trend in Fig. 4.5. In general, H_2O concentrations in homogenized melt inclusions show strong correlation with their radiuses, while no obvious correlation with melt inclusion radius is observed for F, Cl and S. From the largest (22 μm in radius) to the smallest homogenized melt inclusion (6 μm in radius), H_2O concentration decreases from 716 ppm to 97 ppm gradually. This difference indicates that the smallest melt inclusion could have lost more than 80% of its H_2O during homogenization. On the other hand,

concentrations of F, Cl and S in the smallest homogenized melt inclusion are 48.3 ppm, 3.8 ppm and 800 ppm, respectively, not significantly different from those in the largest homogenized one (52.46 ppm F, 3.2 ppm Cl and 716 ppm S). The correlation between H_2O concentrations and radiuses for the homogenized melt inclusions is a strong evidence for the diffusive loss of H during homogenization experiments. While for F, Cl and S, the absence of dependence on size for the concentrations indicates that diffusive loss of these volatiles is unlikely a concern for homogenized melt inclusions when the homogenization time scale is a couple of minutes. One homogenized MI, 74220 OL10Ba contains significantly lower H_2O, F, Cl and S concentrations (Fig. 4.5) than other homogenized MIs. Possible explanations to the relative volatile depletion in this MI are: (a) it contains lower initial concentrations of volatiles before homogenization, which is supported by one natural MI reported in Chen et al. (2015) with similar concentrations of F, Cl and S, as also plotted in Fig. 4.5; (b) this MI suffered volatile loss from micro-cracks in the olivine crystal during homogenization. Hence, data from this MI are not included in quantitative discussion.

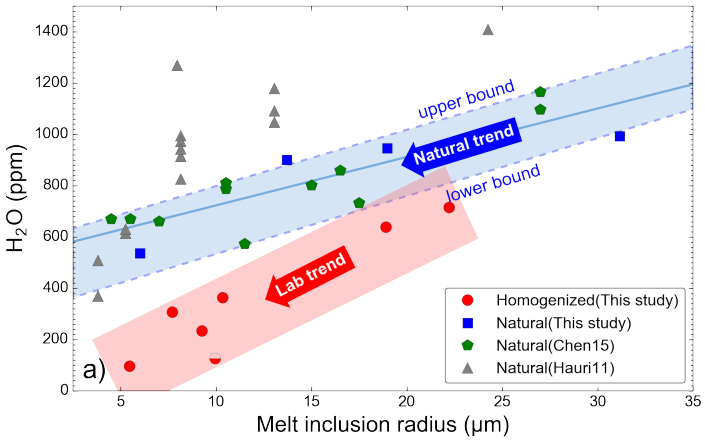

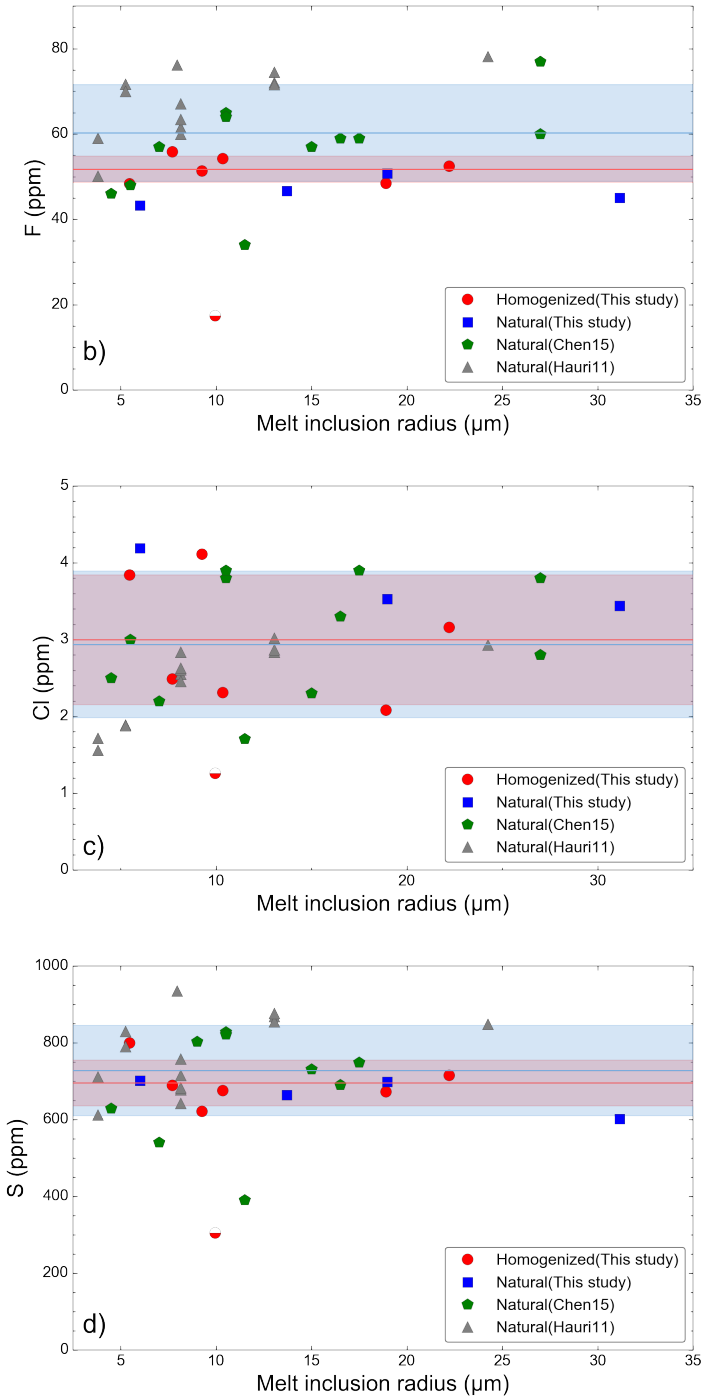

Figure 4.5. Concentrations of a) H_2O, b) F, c) Cl and d) S versus radius of the melt inclusions. In a), Trends of the homogenized and natural unheated melt inclusion data are marked with red and blue, respectively. A linear fit to H_2O concentrations in natural MIs from Chen et al. (2015) and this study is shown as a solid blue line. Upper bound and lower bound of the data are shown in blue dashed lines. In b), c) and d), red and blue horizontal lines are the average concentrations in homogenized and natural MIs, with the color patches representing 1σ error. Data for 74220 OldOL1 is marked as red half-filled circles, as it might have suffered volatile loss from micro-cracks during homogenization.

Interestingly, a similar correlation between H_2O concentration and melt inclusion radius is observed for natural unheated melt inclusions (Fig. 4.5a). Based on natural melt inclusion data from this study, Hauri et al. (2011) and Chen et al. (2015), the smaller melt inclusions (~5μm in radius) contain ~50% less H_2O compared to the larger ones. (The data in Hauri et al. (2011) are systematically higher although they are self-consistent in showing a similar trend. The discrepancy in H_2O concentrations is either due to heterogeneity among subsamples of 74220 or to the difference in calibrations). The most likely explanation for the trend is that, the melt inclusions were affected by diffusive H loss during post-eruptive cooling. Diffusive loss of H from melt inclusions during post-eruptive cooling has been reported for terrestrial samples in the literature. For example, melt inclusion data from Wallace et al. (2003) show that H_2O concentrations in melt inclusions decreas as cooling rate decreases, which can be explained by diffusive H loss from the melt inclusions. More recently, data of olivine-hosted melt inclusions from Volcan de Fuego by Lloyd et al. (2013) show a strong correlation between the degree of H_2O loss and melt inclusion radius. These authors modeled the data by a diffusive re-equilibration model, and concluded that H_2O in the melt inclusions from subaerial eruptions could suffer significant H_2O loss in time periods as short as 10 minutes. Our data on lunar melt inclusions are consistent with these earlier studies.

4.5 Discussion

4.5.1 Modeling H_2O loss from melt inclusions

In order to evaluate the degree of H_2O loss in homogenized MIs, knowledge of the pre-homogenization H_2O content in the MIs is necessary. Unlike previous studies that typically assume the highest H_2O concentration as the initial value, our experiments used natural MIs that show a dependence of H_2O concentration on MI radius (Fig. 4.5a). To incorporate the size correlation of pre-homogenization H_2O concentrations, a linear function was used to fit the trend.

The upper and lower bounds of the data were also fit semi-quantitatively by selecting data points on the higher and lower ends (Fig. 4.5a). For better consistency with the data on homogenized MIs, fitting of the trend in H_2O concentrations was mostly based on data from this study and Chen et al. (2015), which are measured using the same SIMS instrument with similar calibrations, and based on the same subsamples of 74220. After fitting the trend of H_2O concentrations in the natural MIs, the degrees of H_2O depletion in the homogenized MIs were obtained by comparing to the natural trend, and plotted as red circles in Fig. 4.6. The upper and lower bounds of the natural data were also used to estimate the uncertainties caused by scattering of the natural H_2O data, shown as error bars in Fig. 4.6.

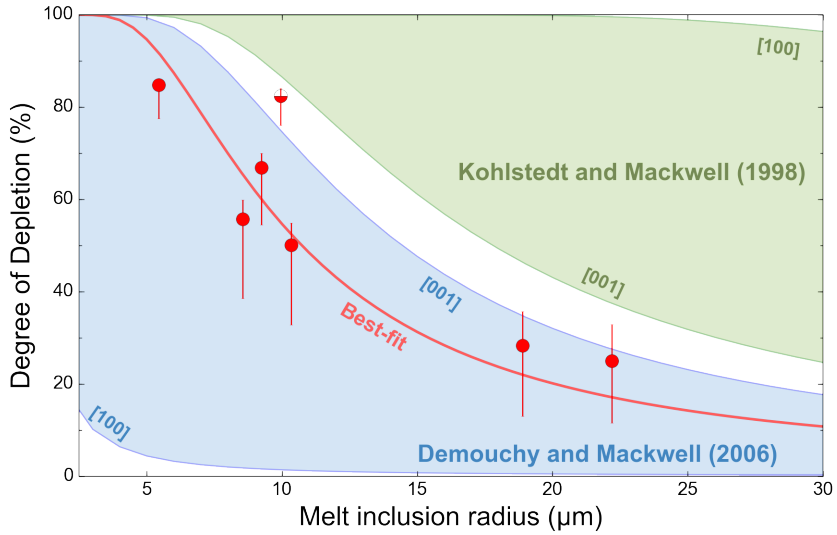

Figure 4.6. Model predictions of diffusive H loss in homogenized MIs from 74220. Concentrations of H_2O in the homogenized MIs are compared with the average trend in the natural MIs for calculating degrees of depletion, which are plotted as red solid circles (OL10Ba is distinguished from others in half-filled circle because of the concern of volatile loss through micro-cracks). Error bars shown in the image are estimated uncertainties based on the upper and lower bounds of H_2O concentrations in the natural MIs (Fig.4.5a). Diffusive H loss from the MIs was modeled assuming an effective duration of 4 min at 1330 ºC and an average olivine radius of 113 μm. Colored regions represent modeling results based on H diffusivities from Kohlstedt and Mackwell (1998), and from Demouchy and Mackwell (2006). The upper and lower bounds of each colored region mark modeling results using diffusivities at the fastest and slowest direction from these two studies. Degrees of depletion modeled with the best-fitted diffusivity of D=9.3×10^{-11}m^2/s are shown as the red curve.

The diffusive re-equilibrium model is similar to those used in Qin et al. (1992), Cottrell et al. (2002) and Chen et al. (2013) on evolution of H_2O concentration in a spherical melt inclusion of radius *a* at the center of a spherical olivine of radius *b*. Following previous studies, concentration of H_2O in the inclusion itself is assumed to be always homogeneous, and any volume change is neglected for either the inclusion or the olivine. The diffusion equation in olivine for the model in spherical coordinate is:

$$\frac{\partial C}{\partial t} = \frac{D}{r^2}\frac{\partial}{\partial r}(r^2\frac{\partial C}{\partial r}), (a \le r \le b), \tag{4.1}$$

with boundary conditions of:

$$\frac{4\pi a^3}{3}\rho_m\frac{\mathrm{d}C_i}{\mathrm{d}t} = 4\pi a^2\rho_c D\frac{\partial C}{\partial r}\Big|_{r=a}, \tag{4.2}$$

$$C(b,t) = C_e, \tag{4.3}$$

and

$$C(a,t) = kC_i(t), \tag{4}$$

where *C* is the concentration of H_2O in olivine and is a function of *r* and *t*, *D* is diffusivity of the H component in olivine, ρ_c and ρ_m mean density of the olivine host and the melt inclusion, C_i means H_2O concentration in the inclusion, C_e means H_2O concentration in olivine that is in equilibrium with the external condition, and *k* is the partition coefficient of H_2O between olivine and melt. Note that the radius *a* of the melt inclusion is fixed, meaning post-entrapment crystallization is ignored. Concentration of H_2O in the olivine is assumed to be initially homogeneous and in equilibrium with the melt inclusion, similar to the approach in Qin et al. (1992) and Chen et al. (2013):

$$C(r,0) = kC_{i,0}, \tag{4.5}$$

Since the experiments were conducted in 99.9999% N_2 flow with extremely low partial pressure of H_2O, C_e=0 is used in the model. In this study, a constant $\rho_c / \rho_m = 1.2$ is used. The

value of k is taken as 0.001 (Koga et al., 2003; Aubaud et al., 2004) in the model. Diffusion of the H component in olivine is complicated in a number of ways. One complexity is that H diffusion in olivine is anisotropic (e.g., Demouchy and Mackwell, 2006; Kohlstedt and Mackwell, 1998). Hence, rigorous treatment would require the use of a diffusion tensor. Even though theories are available to treat anisotropic diffusion (e.g., Zhang, 2008, 2010), because such treatment is complicated, and because we have already ignored the fact that a melt inclusion is often not in the center of an olivine crystal and we did not characterize the orientation of the olivine crystal, we choose to ignore this complexity.

The above equations are solved numerically using a second-order Crank-Nicolson method (Cottrell et al., 2002; Chen et al., 2013) with calculated diffusivities at 1330 ºC for an average olivine radius of 113 μm, and an effective duration of 4 min. Although the samples were kept at 1330 ºC for only 2 min in our homogenization experiments, the heating up was gradual to avoid cracking the olivine during rapid heating. An effective duration was estimated to account for time-dependent diffusivity due to heating and quenching using the following equation (Zhang, 2008, Section 3.2.8):

$$t_e = \frac{\int_0^t \exp(-E/RT)\,dt}{\exp(-E/RT_0)}, \tag{4.6}$$

where t_e is the effective duration, T_0 is the target temperature in K, T is the manually recorded temperature history including heating up and cooling down, and E is the activation energy for H diffusion in olivine (E=200 kJ/mol is adopted, based on Kohlstedt and Mackwell, 1998; Demouchy and Mackwell, 2006; Chen et al., 2013). The estimated t_e is 248 s on average for all the homogenization experiments. For simplicity, a t_e of 4 min is used in our modeling.

There are two sets of H diffusivity in olivine in the literature. Hydrogen diffusivities reported in Kohlstedt and Mackwell (1998) are high:

$$\log D_{H,[100]} = -3.87 - 7566/T\,, \tag{4.7}$$

$$\log D_{\mathrm{H},[010]} = -3.61 - 9675/T\,, \tag{4.8}$$

Those reported by Demouchy and Mackwell (2006) are lower:

$$\log D_{\mathrm{H},[100],[010]} = -4.5 - 10654/T\,, \tag{4.9}$$

$$\log D_{\mathrm{H},[001]} = -1.4 - 13475/T\,. \tag{4.10}$$

Calculated H diffusivity at 1330 ºC using eq. (4.7) and eq. (4.9) are 2.57×10^{-9} m^2/s and 7.15×10^{-12} m^2/s, which differ by more than two orders of magnitude. The different diffusivities were attributed to a fast and a slow diffusion mechanisms operating either sequentially or simultaneously (Kohlstedt and Mackwell, 1998; Demouchy and Mackwell, 2006). More recently, Ferriss et al. (2015) pointed out that the whole-block measurements in Demouchy and Mackwell (2006) did not take into account the path integration effects, although the influence on their extracted diffusivities is small due to the low degrees of H_2O saturation in their experiments. In addition, Ferriss et al. (2015) used a single diffusive mechanism to explain the hydration profiles in Demouchy and Mackwell (2006), but such a mechanism was unable to reconcile data from Kohlstedt and Mackwell (1998). In Fig. 4.6, calculated diffusive H loss is shown using diffusivities reported by Kohlstedt and Mackwell (1998) and Demouchy and Mackwell (2006). For each set of diffusion data (eqs. 4.7-4.8 and eqs. 4.9-4.10), diffusivities along the fastest and slowest directions are used for calculating the upper and lower bounds of the colored patch in the figure. As can be seen in the figure, our experimental results fall slightly below the modeled trend using H diffusivity at [001] direction from Demouchy and Mackwell (2006). Since in an anisotropic system, diffusion along the fastest direction contributes more than along the slower directions, we consider our results to be in rough agreement with the data in Demouchy and Mackwell (2006). On the other hand, adopting H diffusivities of Kohlstedt and Mackwell (1998) would result in much more diffusive H loss than observed in our experiments.

Our data may also be fit to obtain an empirical "isotropic" diffusivity by minimizing χ^2 between the estimated depletion factors and the modeled values (red curve in Fig. 4.6). The best-

fit curve in Fig. 4.6 corresponds to a hypothetical "isotropic" hydrogen diffusivity of 9.3×10^{-11} m^2/s. The fitted hydrogen diffusivity in olivine is plotted with literature data in Fig.4.7 for comparison. Our results are consistent with most other homogenization and re-hydration experiments in the literature (e.g. Portnyagin et al., 2008; Chen et al., 2011; Gaetani et al., 2012), except for one data point reported in Hauri, 2002. In terms of the two diffusion mechanisms for hydrogen diffusion in iron-bearing olivine, our results are more consistent with the "slower" one by Demouchy and Mackwell (2006).

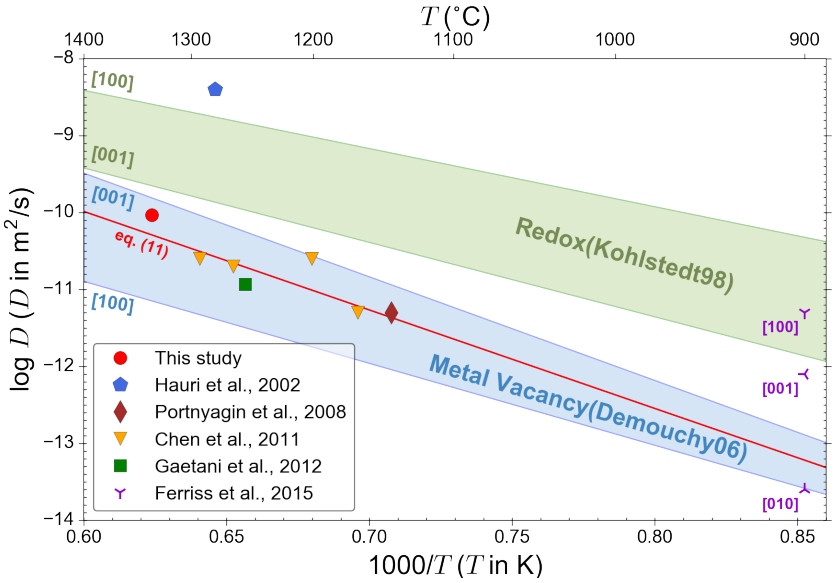

Figure 4.7. Arrhenius plot for comparing best-fit hydrogen diffusivity from the homogenization experiments in this study to literature data. Colored regions represent hydrogen diffusivities from Kohlstedt and Mackwell, 1998, and Demouchy and Mackwell (2006). Diffusivities reported in Ferriss et al. (2015) based on fitting profiles from Demouchy and Mackwell (2006) assuming a single diffusion mechanism are also plotted in the figure. The red straight line illustrates the empirical H diffusion equation based on melt inclusion experiments (eq. 4.11). Sources for other data in this figure are: heating experiments in gas-mixing furnace, Hauri, 2002; stage heating experiments, Chen et al., 2011; rehydration experiments, Portnyagin et al., 2008 and Gaetani et al., 2012. Figure modified from Lloyd et al., 2013.

We initially thought that the low oxygen fugacity on the Moon would play a role in the diffusive H loss from lunar MIs during homogenization. Specifically, a low oxygen fugacity could possibly affect partitioning of H_2 and H_2O between olivine and melt, or affect the diffusion mechanism that controls the process, resulting in a more rapid diffusive H loss from the lunar MIs. Such an effect, however, is not observed in our homogenization experiments, which show

consistent results with experiments on terrestrial melt inclusions. The absence of an observable effect of low oxygen fugacity suggests that diffusive H loss from MIs is insensitive to oxygen fugacity.

4.5.2 Application to volatile data of homogenized lunar melt inclusions

Since our results suggest that significant H_2O loss could occur during minutes of homogenization experiments, related appropriate corrections are necessary for previous and future studies on homogenized lunar MIs. As homogenization conditions might differ for different lunar samples, we extended our model calculation to cover the likely range of lunar MI homogenization experiments. In order to evaluate the effect of homogenization temperature, an empirical equation for H diffusivity in olivine is obtained by combining results from this study, Portnyagin et al. (2008), Chen et al. (2011) and Gaetani et al. (2012):

$$\log D_{\mathrm{H}} = -2.3 - 12808 / T, \tag{4.11}$$

where diffusivity (D_{H}) is in m^2/s and temperature (T) is in K. From the starting point of a lunar MI homogenization experiment at 1300 ºC for an effective duration of 4 min with an olivine radius of 100 µm, we extended the model calculation to cover olivine radiuses from 40 µm to 200 µm, temperatures from 1100 to 1300 ºC, and effective durations from 2 min to 20 min. In addition, diffusive H loss for effective durations of 1 hour to 7 hours is also calculated to reflect possible time scales of slow cooling on lunar surface. The results of the model calculations are shown in Fig. 4.8. As can be seen in Fig. 4.8a, olivine radius has a smaller effect compared to MI radius. Large MIs (e.g. >25 µm in radius) are able to preserve > 80% of their initial H_2O concentrations during homogenization experiments. Radius of olivine, on the other hand, only affects the results slightly as long as olivine radius is about 1.4 times melt inclusion radius. Otherwise, with a fixed olivine radius, increasing MI radius to near olivine radius would result in more diffusive H loss (Fig. 4.8a, 40-µm curve). Homogenization temperature and duration also play a much more

important role than olivine radius on diffusive H loss (Fig. 4.8b, 4.8c). Experiments below 1200 ºC with an effective duration of 4 minutes would result in little H_2O loss, even for MIs as small as 10 μm in radius (<5% loss). At high temperatures ~1300 ºC, small MIs (<10 μm in radius) would lose more than 20% of their initial H_2O in 4 minutes. The effect of homogenization duration is correlated with that of homogenization temperature. With an activation energy of ~200 kJ/mol for H diffusion in olivine, increasing homogenization temperature by 70 ºC is roughly equivalent to doubling the homogenization duration. For homogenization of MIs from a specific lunar basaltic sample, the temperature is usually decided based on the liquidus for its composition, and the duration is controlled by the degree of crystallization in the MIs. Therefore, the most practical way to minimize the concern of H_2O loss in homogenization experiments is to select large MIs from the target sample for study. For example, a melt inclusion with radius of >30 μm would experience less than 20% loss of H_2O under most homogenization conditions in Fig. 4.8. Besides using large MIs for homogenization study, one also needs to be aware of other factors that might cause rapid loss of volatiles (e.g., micro-cracks connecting MI to olivine surface). In terms of other volatile elements, even small lunar MIs with a radius ~5μm can be homogenized to study F, Cl and S concentrations, as our experiments show negligible loss of these volatiles during homogenization.

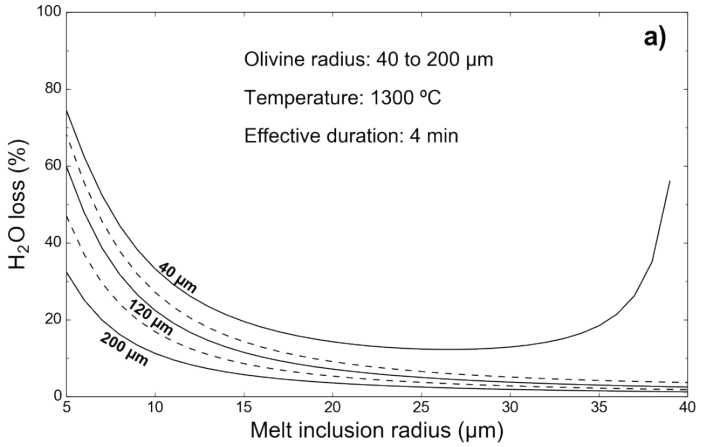

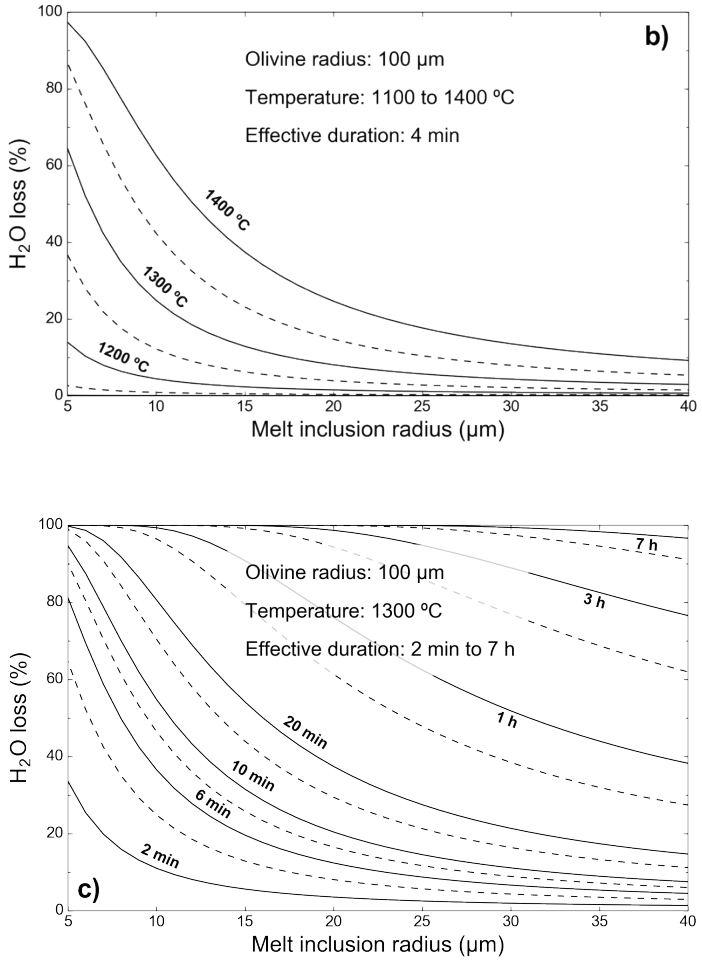

Figure 4.8. Effects of a) olivine radius, b) homogenization temperature and c) effective duration on diffusive H loss from olivine-hosted MIs in homogenization experiments. Values for the input model parameters are specified in each figure. Input value for each dashed curve is the average of its two adjacent solid curves. In a), the "40 μm" curve shows a positive correlation between degree of H_2O loss and MI radius when the ratio of MI radius over olivine radius (a/b) exceeds ~0.7, similar to the results reported in Qin et al., 1992. Effects of homogenization temperature and duration are correlated. Increasing homogenization temperature by 70 ºC is roughly equivalent to doubling the homogenization duration.

As mentioned in the Introduction, one uncertainty in the study by Chen et al. (2015) is whether the relatively low H_2O/Ce ratios in the homogenized MIs are due to diffusive H loss during homogenization. The authors employed the model by Chen et al. (2013) to estimate loss of H_2O from the MI and concluded that this effect was small for the MIs they studied. One possible uncertainty is whether the model by Chen et al. (2013) based on terrestrial MI experiments could be applied to lunar MIs, as the low oxygen fugacity in lunar samples may cause more rapid

diffusive H loss from the homogenized MIs. Our experiments indicate that diffusive H loss during homogenization experiments is not significantly affected by the low oxygen fugacity on Moon, which helps mitigate such a concern. With our new experimental data, the role of diffusive H loss for each of the 8 homogenized MIs in Chen et al. (2015) was re-evaluated. Our model calculations suggest that all the 8 homogenized MIs experienced less than 15% of H_2O loss, which is insignificant compared to the 30 times lower H_2O/Ce ratios in the homogenized MIs than 74220 naturally glassy MIs. In addition, SIMS results show that, H_2O/Ce ratio in one homogenized MI from 10020 is similar to that in a natural unheated MI from the same sample, supporting the results of our model estimation. If we ignore the effect of up to 15% H_2O loss, H_2O/Ce ratios in lunar MIs would vary from ~77 in 74220 to ~8 in 10020 and ~2 in 12008. Since the effect of diffusive H loss during homogenization experiments has been accounted for here, the variation in H_2O/Ce ratios in glassy and crystalline lunar MIs must be due to either H_2O loss from crystalline MIs during post-eruptive cooling on Moon, or heterogeneity in the mantle source of different lunar samples. Based on the modeling results shown in Fig. 4.8c, losing 97% H_2O (decreasing H_2O/Ce by a factor of 30) under vaccum conditions can be achieved in 7 hours for a relatively large melt inclusions with a radius of 40 μm. More systematic investigation of H_2O/Ce ratios in other lunar samples is necessary to resolve the above two possibilities.

4.5.3 Cooling rate for volcanic glass and olivine samples in 74220

Theoretically, the trend of diffusive H loss for MIs in our experiments can be compared with that in the natural samples from 74220 to determine its eruptive/cooling time scale. One significant difference, however, lies between our experiments and the natural conditions. Our experiments were carried out in a high purity nitrogen flow with negligible H_2O partial pressure, while natural MIs cooled down in a hot gaseous phase after fire fountain eruptions (e.g., Heiken et al., 1974; Arndt and von Engelhardt, 1987; Saal et al., 2008). The presence of a gaseous phase surrounding the host olivines during cooling could suppress diffusive H loss from the MIs,

resulting in slower decrease of H_2O concentrations in the MIs compared to our experimental conditions. Modeling the natural lunar melt inclusions as if they cooled in a H-free environment would lead to the highest degree of H_2O loss, or an upper limit of the cooling rate or a lower limit of the cooling time scale.

In order to correlate cooling rate with effective duration (t_e) for our model estimation of diffusive H loss, an asymptotic cooling model below is used (Zhang, 2008, eq. 2-41):

$$T = T_0 / (1 + t / \tau_c), \tag{4.12}$$

where T is temperature in K, T_0 is 1603 K (1330 ºC), t is time in seconds, and τ_c is the cooling time scale in seconds. Cooling rate (q) at any temperature T can then be calculated as:

$$q = -dT / dt = \frac{T^2}{\tau_c T_0}. \tag{4.13}$$

Since the cooling rate is not constant through the cooling history for an asymptotic model, the cooling rate (q) is usually referred to as the cooling rate at t=0, or T=T_0. Hence, cooling rate at t=0 is q_0=T_0/τ_c. From that, the effective duration (t_e) can be obtained by combining eq. (4.12), eq. (4.13) and eq. (4.6) as follows:

$$t_e = \tau_c (RT_0 / E) = \frac{RT_0^2}{q_0 E}, \tag{4.14}$$

where E is the activation energy for H diffusion in olivine (200 kJ/mol; note that eq. (4.11) is in common logarithm). For example, a cooling rate of 1 ºC/s at t=0 corresponds to a cooling time scale of τ_c=1603 s, and the entire cooling process is equivalent to an effective duration of 107 s at 1330 ºC for H diffusion. Since in eq. (4.14), t_e is inversely proportional to q_0, initial cooling rates of 0.1 ºC/s, 10 ºC/s and 100 ºC/s would correspond to effective durations of 1068 s, 10.7 s and 1.07 s, respectively.

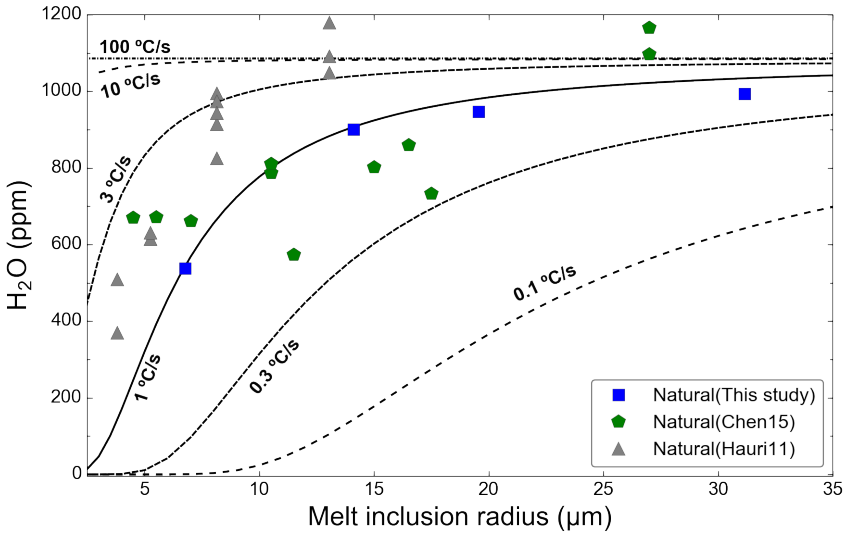

Figure 4.9. Model estimation of H_2O depletion trend in 74220 natural MIs at different cooling rates assuming asymptotic cooling and an exterior environment with 0 ppm H_2O. Data from Hauri et al. (2011) are marked in grey since they are off the trend of data from this study and Chen et al. (2015), either due to the difference in calibration or heterogeneity between subsamples of 74220.

Assuming a pre-eruptive H_2O concentration of 1086 ppm based on the two largest natural MIs measured in Chen et al. (2015) and this study, depletion trends for H_2O in natural MIs in 74220 at different cooling rates are calculated and shown in Fig. 4.9. The H_2O concentrations in the natural MIs show a correlation with MI radius, but the data are relatively scattered, which cannot be perfectly fit by our H diffusion model. Nonetheless, modeled trends in Fig. 4.9 provide rough constraint on the cooling rate for 74220. As can be seen in the figure, if 74220 cooled down at a rate of 10 ºC/s or faster, negligible amount of H_2O would be lost during cooling for MIs as small as 10 μm in diameter, which does not agree with the observed depletion trend observed in 74220 natural MIs. Most of the MI data show degrees of H_2O loss close to the modeled trend for a cooling rate of 1 ºC/s, and fall between 0.3 to 3 °C/s curves (or $1^{\times 3}_{\div 3}$ °C/s). Major uncertainties of our method and their effects on the estimation are summarized below:

1) Our model assumes a H_2O-free environment for the cooling of 74220. Presence of a gaseous phase would suppress H loss from the olivine-hosted MIs, which means a slower cooling rate than modeled here.

2) An initial temperature of 1330 ºC (slightly above the liquidus of 74220, 1323 ºC) was assumed in our model. If the magma erupted at a temperature lower than 1330 ºC, a slower cooling rate would be necessary for the same effective duration at 1330 ºC. For example, cooling from 1250 ºC at a rate of 0.41 ºC/s would lead to similar fraction of H loss from MIs as cooling from 1330 ºC at a rate of 1 ºC/s in terms of their effects on diffusive H loss from the olivine-hosted MIs. On the other hand, an initial temperature higher than the liquidus is unlikely, since we are studying olivine-hosted melt inclusions must have formed below the liquidus of the magma.

3) Estimation of the initial H_2O concentration of 1086 ppm was based on the two largest natural MIs. This assumption is valid when the cooling rate is higher than 1 ºC/s, as diffusive H loss in MIs with a radius of ~30 μm is insignificant. When the cooling rate is lower, however, even large MIs could be affected by diffusive H loss. For example, as shown in Fig. 4.9, at a cooling rate of 0.1 ºC/s, ~50% of H_2O could be lost from 30-μm-radius MIs during cooling. Depending on the actual cooling rate for 74220, the initial H_2O concentration could be higher than the value used in our model, which would also indicate a possible overestimation of the cooling rate by our model.

In summary, all the above uncertainties would lead to smaller cooling rates for 74220. Therefore, we interpret our modeling result to indicate that 74220 cooled down at a rate of $1^{\times 3}_{\div 3}$ ºC/s or lower. Our result is significantly smaller than the cooling rate of 100 ºC/s inferred by Arndt and von Engelhardt (1987) for 74220, but almost consistent with recent heat capacity measurements for orange glass beads (~0.2 ºC/s, Hui et al., 2016). In addition, our result suggests that if the cooling rate for 74220 is on the order of 0.1 ºC/s or lower, original H_2O concentration in the parental magma could be higher than that recorded by the melt inclusions measured so far.

4.6 Conclusions

Our experiments show that H_2O concentrations in lunar melt inclusions in olivine can decrease significantly in minutes during homogenization experiments, while F, Cl and S in the inclusions are well preserved. Hence, when studying volatiles in homogenized lunar melt inclusions, corrections from diffusive loss are necessary for their H_2O concentrations, but usually unnecessary for F, Cl and S concentrations. The loss of H_2O from melt inclusions depends on melt inclusion radius and can be well modeled by diffusive hydrogen loss through olivine, and depends on melt inclusion radius. The lower oxygen fugacity for lunar samples has no observable effect on diffusive hydrogen loss in olivine-hosted lunar melt inclusions. The best-fit H diffusivity based on the H-loss trend in homogenized melt inclusions agrees with most of previous homogenization and hydration experiments, and is consistent with the data by Demouchy and Mackwell (2006). Applying our experimental results to homogenized melt inclusion data in Chen et al. (2015) confirms the variation of H_2O/Ce ratios in lunar melt inclusions from different samples. Such a variation can be explained by diffusive H_2O loss on the lunar surface during various cooling rates, or by heterogeneity in their lunar mantle source. Based on the H_2O degassing trend observed in 74220 natural unheated melt inclusions, the cooling rate for 74220 was estimated to be ~1 ºC/s or lower. This estimation is significantly lower than 100 ºC/s suggested by Arndt and von Engelhardt (1987) based on "free-flight" cooling experiments, but roughly in accordance with recent heat capacity experiments by Hui et al. (2016), which indicate a cooling rate of ~0.2 ºC/s.

4.7 Acknowledgments

We thank NASA CAPTEM for providing the lunar samples, and K. P. Jochum for providing the MPI-DING glass standards. This research is supported by NASA grant NNX15AH37G.

4.8 References

Albarede, F., Albalat, E., Lee, C.-T.A., 2015. An intrinsic volatility scale relevant to the Earth and Moon and the status of water in the Moon. Meteorit. Planet. Sci. 50, 568–577. doi:10.1111/maps.12331

Albarede, F., Ballhaus, C., Blichert-Toft, J., Lee, C.-T., Marty, B., Moynier, F., Yin, Q.-Z., 2013. Asteroidal impacts and the origin of terrestrial and lunar volatiles. Icarus 222, 44–52. doi:10.1016/j.icarus.2012.10.026

Anderson, A.T., 1974. Chlorine, Sulfur, and Water in Magmas and Oceans. Geol. Soc. Am. Bull. 85, 1485–1492. doi:10.1130/0016-7606(1974)85<1485:CSAWIM>2.0.CO;2

Arndt, J., von Engelhardt, W., 1987. Formation of Apollo 17 orange and black glass beads. J. Geophys. Res. Solid Earth 92, E372–E376. doi:10.1029/JB092iB04p0E372

Aubaud, C., Hauri, E.H., Hirschmann, M.M., 2004. Hydrogen partition coefficients between nominally anhydrous minerals and basaltic melts. Geophys. Res. Lett. 31, L20611. doi:10.1029/2004GL021341

Bombardieri, D.J., Norman, M.D., Kamenetsky, V.S., Danyushevsky, L.V., 2005. Major element and primary sulfur concentrations in Apollo 12 mare basalts: The view from melt inclusions. Meteorit. Planet. Sci. 40, 679–693. doi:10.1111/j.1945-5100.2005.tb00973.x

Canup, R.M., Asphaug, E., 2001. Origin of the Moon in a giant impact near the end of the Earth's formation. Nature 412, 708–712. doi:10.1038/35089010

Chen, Y., Provost, A., Schiano, P., Cluzel, N., 2013. Magma ascent rate and initial water concentration inferred from diffusive water loss from olivine-hosted melt inclusions. Contrib. Mineral. Petrol. 165, 525–541. doi:10.1007/s00410-012-0821-x

Chen, Y., Provost, A., Schiano, P., Cluzel, N., 2011. The rate of water loss from olivine-hosted melt inclusions. Contrib. Mineral. Petrol. 162, 625–636. doi:10.1007/s00410-011-0616-5

Chen, Y., Zhang, Y., Liu, Y., Guan, Y., Eiler, J., Stolper, E.M., 2015. Water, fluorine, and sulfur concentrations in the lunar mantle. Earth Planet. Sci. Lett. 427, 37–46. doi:10.1016/j.epsl.2015.06.046

Cottrell, E., Spiegelman, M., Langmuir, C.H., 2002. Consequences of diffusive reequilibration for the interpretation of melt inclusions. Geochem. Geophys. Geosystems 3, 1–26. doi:10.1029/2001GC000205

Danyushevsky, L.V., McNeill, A.W., Sobolev, A.V., 2002. Experimental and petrological studies of melt inclusions in phenocrysts from mantle-derived magmas: an overview of techniques, advantages and complications. Chem. Geol., Melt Inclusions at the Millennium: Toward a Deeper Understanding of Magmatic Processes 183, 5–24. doi:10.1016/S0009-2541(01)00369-2

Demouchy, S., Mackwell, S., 2006. Mechanisms of hydrogen incorporation and diffusion in iron-bearing olivine. Phys. Chem. Miner. 33, 347–355. doi:10.1007/s00269-006-0081-2

Ferriss, E., Plank, T., Walker, D., Nettles, M., 2015. The whole-block approach to measuring hydrogen diffusivity in nominally anhydrous minerals. Am. Mineral. 100, 837–851. doi:10.2138/am-2015-4947

Gaetani, G.A., O'Leary, J.A., Shimizu, N., Bucholz, C.E., Newville, M., 2012. Rapid reequilibration of H2O and oxygen fugacity in olivine-hosted melt inclusions. Geology 40, 915–918. doi:10.1130/G32992.1

Gao, S., Liu, X., Yuan, H., Hattendorf, B., Gunther, D., Chen, L., Hu, S., 2002. Determination of Forty Two Major and Trace Elements in USGS and NIST SRM Glasses by Laser Ablation-Inductively Coupled Plasma-Mass Spectrometry. Geostand. Newsl. 26, 181–196. doi:10.1111/j.1751-908X.2002.tb00886.x

Green, D.H., Ringwood, A.E., Hibberson, W.O., Ware, N.G., 1975. Experimental petrology of Apollo 17 mare basalts. Presented at the Lunar and Planetary Science Conference Proceedings, pp. 871–893.

Hauri, E., 2002. SIMS analysis of volatiles in silicate glasses, 2: isotopes and abundances in Hawaiian melt inclusions. Chem. Geol., Melt Inclusions at the Millennium: Toward a Deeper Understanding of Magmatic Processes 183, 115–141. doi:10.1016/S0009-2541(01)00374-6

Hauri, E.H., Saal, A.E., Rutherford, M.J., Van Orman, J.A., 2015. Water in the Moon's interior: Truth and consequences. Earth Planet. Sci. Lett. 409, 252–264. doi:10.1016/j.epsl.2014.10.053

Hauri, E.H., Weinreich, T., Saal, A.E., Rutherford, M.C., Orman, J.A.V., 2011. High Pre-Eruptive Water Contents Preserved in Lunar Melt Inclusions. Science 333, 213–215. doi:10.1126/science.1204626

Heiken, G.H., McKay, D.S., Brown, R.W., 1974. Lunar deposits of possible pyroclastic origin. Geochim. Cosmochim. Acta 38, 1703–1718. doi:10.1016/0016-7037(74)90187-2

Hirschmann, M.M., Withers, A.C., Ardia, P., Foley, N.T., 2012. Solubility of molecular hydrogen in silicate melts and consequences for volatile evolution of terrestrial planets. Earth Planet. Sci. Lett. 345–348, 38–48. doi:10.1016/j.epsl.2012.06.031

Hui, H., Hess, K.-U., Zhang, Y., Peslier, A.H., Lange, R.A., Dingwell, D.B., Neal, C.R., 2016. Cooling rates of lunar volcanic glass beads. Presented at the American Geophysical Union Fall Meeting, San Francisco, Calif.

Hui, H., Peslier, A.H., Zhang, Y., Neal, C.R., 2013. Water in lunar anorthosites and evidence for a wet early Moon. Nat. Geosci. 6, 177–180. doi:10.1038/ngeo1735

Jochum, K.P., Stoll, B., Herwig, K., Willbold, M., Hofmann, A.W., Amini, M., Aarburg, S., Abouchami, W., Hellebrand, E., Mocek, B., Raczek, I., Stracke, A., Alard, O., Bouman, C., Becker, S., Dücking, M., Brätz, H., Klemd, R., de Bruin, D., Canil, D., Cornell, D., de Hoog, C.-J., Dalpé, C., Danyushevsky, L., Eisenhauer, A., Gao, Y., Snow, J.E., Groschopf, N., Günther, D., Latkoczy, C., Guillong, M., Hauri, E.H., Höfer, H.E., Lahaye, Y., Horz, K., Jacob, D.E., Kasemann, S.A., Kent, A.J.R., Ludwig, T., Zack, T., Mason, P.R.D., Meixner, A., Rosner, M., Misawa, K., Nash, B.P., Pfänder, J., Premo,

W.R., Sun, W.D., Tiepolo, M., Vannucci, R., Vennemann, T., Wayne, D., Woodhead, J.D., 2006. MPI-DING reference glasses for in situ microanalysis: New reference values for element concentrations and isotope ratios. Geochem. Geophys. Geosystems 7, Q02008. doi:10.1029/2005GC001060

Koga, K., Hauri, E., Hirschmann, M., Bell, D., 2003. Hydrogen concentration analyses using SIMS and FTIR: Comparison and calibration for nominally anhydrous minerals. Geochem. Geophys. Geosystems 4, 1019. doi:10.1029/2002GC000378

Kohlstedt, D.L., Mackwell, S.J., 1998. Diffusion of Hydrogen and Intrinsic Point Defects in Olivine. Z. Für Phys. Chem. 207, 147–162. doi:10.1524/zpch.1998.207.Part_1_2.147

Lloyd, A.S., Plank, T., Ruprecht, P., Hauri, E.H., Rose, W., 2013. Volatile loss from melt inclusions in pyroclasts of differing sizes. Contrib. Mineral. Petrol. 165, 129–153. doi:10.1007/s00410-012-0800-2

Massare, D., Métrich, N., Clocchiatti, R., 2002. High-temperature experiments on silicate melt inclusions in olivine at 1 atm: inference on temperatures of homogenization and H2O concentrations. Chem. Geol., Melt Inclusions at the Millennium: Toward a Deeper Understanding of Magmatic Processes 183, 87–98. doi:10.1016/S0009-2541(01)00373-4

McDonough, W.F., Sun, S. -s., 1995. The composition of the Earth. Chem. Geol., Chemical Evolution of the Mantle 120, 223–253. doi:10.1016/0009-2541(94)00140-4

Newsom, H.E., 1986. Constraints on the origin of the Moon from the abundance of molybdenum and other siderophile elements. Presented at the Origin of the Moon, p. 203.

Ni, P., Zhang, Y., 2016. Cu diffusion in a basaltic melt. Am. Mineral. 101, 1474–1482. doi:10.2138/am-2016-5544

Pearce, N.J.G., Perkins, W.T., Westgate, J.A., Gorton, M.P., Jackson, S.E., Neal, C.R., Chenery, S.P., 1997. A Compilation of New and Published Major and Trace Element Data for NIST SRM 610 and NIST SRM 612 Glass Reference Materials. Geostand. Newsl. 21, 115–144. doi:10.1111/j.1751-908X.1997.tb00538.x

Portnyagin, M., Almeev, R., Matveev, S., Holtz, F., 2008. Experimental evidence for rapid water exchange between melt inclusions in olivine and host magma. Earth Planet. Sci. Lett. 272, 541–552. doi:10.1016/j.epsl.2008.05.020

Qin, Z., Lu, F., Anderson, A.T., 1992. Diffuse reequilibration of melt and fluid inclusions. Am. Mineral. 77, 565–576.

Roedder, E., Weiblen, P.W., 1970. Lunar petrology of silicate melt inclusions, Apollo 11 rocks. Geochim. Cosmochim. Acta Suppl. 1, 801.

Saal, A.E., Hauri, E.H., Cascio, M.L., Van Orman, J.A., Rutherford, M.C., Cooper, R.F., 2008. Volatile content of lunar volcanic glasses and the presence of water in the Moon's interior. Nature 454, 192–195. doi:10.1038/nature07047

Saal, A.E., Hauri, E.H., Orman, J.A.V., Rutherford, M.J., 2013. Hydrogen Isotopes in Lunar Volcanic Glasses and Melt Inclusions Reveal a Carbonaceous Chondrite Heritage. Science 340, 1317–1320. doi:10.1126/science.1235142

Sato, M., 1976. Oxygen fugacity and other thermochemical parameters of Apollo 17 high-Ti basalts and their implications on the reduction mechanism. Presented at the Lunar and Planetary Science Conference Proceedings, pp. 1323–1344.

Sobolev, A.V., 1996. Melt inclusions in minerals as a source of principle petrological information. Petrology 4, 209–220.

Taylor, S.R., Pieters, C.M., MacPherson, G.J., 2006. Earth-Moon System, Planetary Science, and Lessons Learned. Rev. Mineral. Geochem. 60, 657–704. doi:10.2138/rmg.2006.60.7

Wallace, P.J., Dufek, J., Anderson, A.T., Zhang, Y., 2003. Cooling rates of Plinian-fall and pyroclastic-flow deposits in the Bishop Tuff: inferences from water speciation in quartz-hosted glass inclusions. Bull. Volcanol. 65, 105–123. doi:10.1007/s00445-002-0247-9

Wanke, H., Baddenhausen, H., Dreibus, G., Jagoutz, E., Kruse, H., Palme, H., Spettel, B., Teschke, F., 1973. Multielement analyses of Apollo 15, 16, and 17 samples and the bulk composition of the moon. Presented at the Lunar and Planetary Science Conference Proceedings, p. 1461.

Weitz, C.M., Rutherford, M.J., Head, J.W., 1997. Oxidation states and ascent history of the Apollo 17 volcanic beads as inferred from metal-glass equilibria. Geochim. Cosmochim. Acta 61, 2765–2775. doi:10.1016/S0016-7037(97)00119-1

Xirouchakis, D., Hirschmann, M.M., Simpson, J.A., 2001. The effect of titanium on the silica content and on mineral-liquid partitioning of mantle-equilibrated melts. Geochim. Cosmochim. Acta 65, 2201–2217. doi:10.1016/S0016-7037(00)00549-4

Zhang, Y., 2011. “Water” in Lunar Basalts: The Role of Molecular Hydrogen (H_2), Especially in the Diffusion of the H Component. Presented at the Lunar and Planetary Science Conference, p. 1957.

Zhang, Y., 2010. Diffusion in Minerals and Melts: Theoretical Background. Rev. Mineral. Geochem. 72, 5–59. doi:10.2138/rmg.2010.72.2

Zhang, Y., 2008. Geochemical Kinetics. Princeton University Press.

Zhang, Y., Ni, H., 2010. Diffusion of H, C, and O Components in Silicate Melts. Rev. Mineral. Geochem. 72, 171–225. doi:10.2138/rmg.2010.72.5

CHAPTER V

A melt inclusion study on volatile concentrations in lunar mantle

5.1 Abstract

Volatiles in Moon were thought to be highly depleted due to its formation by a giant impact. Since the last decade, however, evidences are found in lunar volcanic glass beads, nominally anhydrous minerals and olivine-hosted melt inclusions that support a relatively "wet" Moon. In particular, based on H_2O/Ce, F/Nd and S/Dy ratios, recent melt inclusion work estimated volatile (H_2O, F and S) abundances in Moon to be similar to or slightly lower compared to terrestrial depleted mantle. Uncertainties still occur, however, in that whether the limited numbers of lunar samples studied are representative of the entire lunar mantle. In this chapter, major element, trace element, volatile and transition metal data for 5 mare basalt samples (10020, 12040, 15016, 15647 and 74235) are reported. Our data indicate F, Cl and S abundances of 5 ppm, 0.4 ppm and 65-120 ppm in lunar mantle based on F/Nd, Cl/K and S/Dy ratios in melt inclusions from most samples studied. Inclusions from low-Ti basalt 12040 show high F/Nd ratios (~20), which is almost the same as the bulk silicate earth. S/Dy ratios in MIs from low-Ti basalt and high-Ti basalt also differ by almost a factor of 2. These newly discovered heterogeneities suggest that, unless unique processes occur on Moon that can fractionate F from Nd, and S from Dy significantly on Moon, the lunar mantle might have inherited volatile heterogeneities during its formation. In terms of H_2O abundance in lunar mantle, 74220 is currently still the record keeper of highest H_2O/Ce ratios (as high as 77) measured in lunar melt inclusions. Our new data suggest variations in H_2O/Ce ratios from 9 for 10020 to 3 for 74235 and ~1 for other samples with crystalline melt inclusions. We argue that such a variation is at least partially due to H_2O loss on lunar surface during magma eruption and cooling. Lunar mantle heterogeneity in volatile

abundances inherited during Moon formation could also contribute to the variation in H_2O/Ce ratios, which complicates the estimation of H_2O abundance in the Moon.

5.2 Introduction

As one of the most important contributions by the Apollo missions, geochemical data obtained on the returned samples suggest that the Moon was formed by a giant impact between the proto-earth and a large planetary body. Recent discovery of magmatic water in lunar samples, however, brings uncertainty to the giant impact model, as H_2O was expected to be completely lost during the impact. Among these discoveries, Saal et al. (2008, 2013) reported tens of ppm H_2O in lunar volcanic glass beads, and inferred the pre-degassing H_2O content to be at least 260 ppm in the magma. High concentrations of H_2O (up to 1410 ppm) in olivine-hosted melt inclusions were reported by Hauri et al. (2011). Hui et al. (2013) was able to detect ~6 ppm water in plagioclase grains from lunar anorthosites using Fourier-transform infrared spectroscopy, which provides an estimation of 320 ppm H_2O (updated to ~130 ppm by adopting a more recent partition coefficient, Chen et al., 2015) in lunar magma ocean. Based on H_2O/Ce, F/Nd and S/Dy ratios in melt inclusions from the same sample, Chen et al. (2015) estimated that lunar mantle contains 110 ppm H_2O, 5.3 ppm F and 70 ppm S, similar to or slightly lower than the terrestrial depleted mantle. Despite the emergence of evidences that support a relatively "wet" Moon, controversies occur on whether these evidences are conclusive. For example, Albarede et al. (2013, 2015) argued that 74220 is a local anomaly which should not be used to represent the bulk Moon. Based on the low concentrations of moderately volatile elements, especially Zn, in lunar volcanic rocks, Albarede et al. (2015) estimated that the Moon should contain <1 ppm H_2O. To resolve the controversy, it is necessary to investigate melt inclusions from a larger collection of lunar samples to obtain a broader understanding on volatile concentrations in the lunar interior.

Despite the difficulty of finding olivine-hosted melt inclusions in lunar samples, melt inclusion study on lunar volatiles has its advantages over using glass beads or nominally

anhydrous minerals. First of all, volatiles in the MIs are protected by the host olivine, which provides a better chance to preserve their pre-eruptive concentrations in the parental magma. Volcanic glass beads, on the other hand, typically experienced extensive loss of all volatile elements (e.g. H_2O, F, Cl, S). Interpretation of the pre-eruptive volatile concentrations based on volatile diffusion profiles in the glass beads relies heavily on the cooling history, which is poorly understood, resulting in high levels of uncertainties (Saal et al., 2008). Secondly, estimation of H_2O concentration in the parental magma based on nominally anhydrous minerals such as plagioclase (Hui et al., 2013) or potassium-rich feldspar (Mills et al., 2017) requires the knowledge of the partition coefficient for H_2O between mineral and the basaltic melt, and the degree of crystal fractionation at the time these minerals formed. By paring the concentrations of volatile elements with appropriate trace elements in the MIs that show similar degrees of incompatibility during partial melting and crystal fractionation (e.g. H_2O/Ce, F/Nd, S/Dy, Chen et al., 2015), the above two uncertainties can be greatly alleviated in melt inclusion studies.

In this chapter, we extend previous lunar melt inclusion studies to a broader collection of lunar mare basalt samples (10020, 12040, 15016, 15647 and 74235) to better understand volatile abundances in lunar mantle. Ratios of H_2O/Ce, F/Nd, Cl/K and S/Dy are also compared across different lunar samples to assess possible lunar mantle heterogeneities in volatile abundances.

.

5.3 Sample Preparation and Methods

5.3.1 Lunar samples studied

Three low-Ti basalts (12040, 15016 and 15647) and two high-Ti basalts (10020 and 74235) with identified olivine-hosted melt inclusions investigated in this work are briefly described below. A summary of their bulk compositions is also shown in Table 5.1. More detailed information about these samples can be found from the Lunar Sample Compendium: https://www-curator.jsc.nasa.gov/lunar/lsc/index.cfm.

10020, 49: A fine-grained (~200 μm) low-K, high-Ti ilmenite basalt that cooled down rapidly. It contains olivine phenocrysts with a composition of Fo_{77-59}.

12040, 199: A slowly cooled low-Ti olivine basalt with an average grain size of ~1mm. Average composition of the olivine is reported as Fo_{58}. Evidence of accumulation of olivine was reported, which means the whole rock composition of 12040 might not be representative of its parental liquid.

15016, 47: A highly vesicular (~50% vesicles in volume) olivine-normative basalt returned from Apollo 15. Olivines in this sample are highly variable in composition, with reported forsterite numbers ranging from 70 to 10.

15647, 22: A relatively coarse-grained olivine basalt from Apollo 15 containing anhedral olivines that are <1 mm in diameter.

74235, 22: A vitrophyric high-Ti basalt from Apollo 17 that contains thin blades of ilmenite and phenocrysts of olivine over a matrix of glass and feathery minerals. This sample represents a rapidly quenched volcanic liquid.

Table 5.1. Host rock bulk compositions for the melt inclusions studied in this chapter.

	SiO_2	TiO_2	Al_2O_3	FeO_t	MnO	MgO	CaO	Na_2O	K_2O	Total
10020	40.8	10.35	10.31	18.79	0.27	7	11.99	0.38	0.07	99.96
12040	43.68	2.48	7.35	20.91	0.26	16.69	7.81	0.16	0.05	99.39
15016	43.78	2.28	8.17	22.5	0.33	11.58	9.06	0.24	0.04	97.98
15647	44.4	2.44	9	22.35	0.28	10.04	9.65	0.22	0.044	98.42
74235	38.62	12.17	8.61	19.32	0.28	8.35	10.7	0.4	0.07	98.52

Data sources: 10020, Rhodes and Blanchard (1980); 12040, Kushiro and Haramura (1971); 15016, Kushiro (1972); 15647, Ryder and Schuraytz (2001) and 74235, Rhodes et al. (1976).

5.3.2 Sample preparation methods

Each of the above basalt samples was gently crushed in a stainless steel crusher, and olivine grains were manually picked from the crushed samples with an optical microscope. Among the above five samples, a small number of MIs identified in 10020 and 74235 are partially glassy. In addition, interstitial glasses with measurable sizes (>10μm) were found in the

matrix of 74235. These samples were directly polished to expose the target melt inclusion or interstitial glass, and prepared into an indium mount for electron microprobe (EMP) and secondary ion mass spectrometry (SIMS) analyses.

Essentially all melt inclusions found in 12040, 15016 and 15647 are highly crystalized, which requires homogenization experiments to become a homogeneous glass phase for precise EMP and SIMS analyses. Therefore, homogenization experiments were conducted on crystalline MIs from 12040, 15016 and 15647 (plus two from 74235) in a gas-mixing furnace. Each host olivine grain was placed in a graphite crucible, and gradually inserted into the hot spot of a vertical furnace with a constant 99.9999% N_2 flow. By inserting the crucible slowly, heating rate for the sample was controlled at <200 ºC/min to prevent olivine cracking. A wide range of temperatures (1140 to 1300 ºC) and durations (2 to 10 min) were used for melt inclusions from different samples to dissolve the crystals in the inclusions with minimized possibility of H_2O loss. After homogenization, the crucible was quickly taken out of the furnace and quenched in water to room temperature with a cooling rate of ~40 ºC/s. The olivine grain was recovered from the graphite crucible, and polished to expose the melt inclusion inside, then pressed into an indium mount for EMP and SIMS analyses.

5.3.3 Analytical methods

Major element compositions of the MIs and olivines were analyzed using a CAMECA SX-100 electron microprobe at the University of Michigan, with a 10 nA focused beam at the accelerating voltage of 15kV.

Analyses of volatile and trace element compositions for the MIs were done with a CAMECA IMS 7-f GEO SIMS at Caltech during three visits. A total of 33 elements were analyzed for the MIs in three separate sessions: volatiles (H reported as H_2O, F, P, S and Cl), trace elements (Li, Na, K, Sr, Y, Zr, Nb, Ba, La, Ce, Pr, Nd, Sm, Eu, Gd, Tb, Dy, Ho, Er, Tm, Yb and Lu) and transition metals (V, Cr, Mn, Co, Ni and Cu). Analyses were done following similar

procedures as in Chen et al. (2015) and in Chapter IV of this thesis, which are briefly described below.

Volatile elements were measured by sequentially analyzing ^{12}C, $^{16}O^{1}H$, ^{18}O, ^{19}F, ^{30}Si, ^{31}P, ^{32}S and ^{35}Cl generated by a 3-5 nA Cs^{+} primary ion beam. A set of seven MPI-DING glass standards (GOR128-G, GOR132-G, KL2-G, ML3B-G, StHs6/80-G, T1-G, ATHO-G) (Jochum et al., 2006) and a mid-ocean ridge basalt glass (MORB) were used for calibration of H_2O, F, Cl and S. Concentrations of H_2O in the reference glasses are from Chen et al. (2015) and Chapter IV of this thesis. For F, Cl and S, reference values for MPI-DING reference glasses from Jochum et al. (2006) were used. A synthetic basaltic glass, Et1 (Ni and Zhang, 2016) with 12.8 ± 0.6 ppm H_2O was used to assess $^{16}O^{1}H^{-}/^{18}O^{-}$ ratios for low H_2O samples across different indium blocks and during different analytical sessions. The sample blocks were placed in the high vacuum chamber for one or two days prior to volatile measurements, and background $^{16}O^{1}H^{-}/^{18}O^{-}$ ratios of 1×10^{-3} to 3×10^{-3} were achieved. To make sure the beam is on the melt inclusion instead of its host olivine, position of the beam was carefully adjusted based on $^{27}Al^{16}O^{-}$ secondary ion images before acquisition of each data point. Each position was pre-sputtered for 60 to 120 s to remove possible surface contamination before the data acquisition starts. Twenty cycles of data were collected at each point and in each cycle, every ion species was counted for 1 s. Two analyses on the same MI (74235 NMI1b) yielded results that are within 10% difference (Table D1), supporting the reproducibility of our analysis.

Twenty-two trace elements (Li, Na, K, Sr, Y, Zr, Nb, Ba, La, Ce, Pr, Nd, Sm, Eu, Gd, Tb, Dy, Ho, Er, Tm, Yb and Lu) were analyzed with a 10-14 nA O^{-} and 15 μm diameter primary ion beam using the energy-filtering technique (e.g. Zinner and Crozaz, 1986). The position of trace element analysis for each MI was carefully located on or near the previous spot of volatile measurements with the help of $^{27}Al^{+}$ ion images. Besides ion species for the target trace elements, ^{28}Si was also monitored as the internal standard. Two glass standards NIST 610 and NIST 612 (Pearce et al., 1997) from the National Institute of Standards and Technology were used as the

standards for our trace element analyses. During one of the three visits, one additional NIST standard (NIST 614, Gao et al., 2002) and two MPI-DING glass standards (GOR128-G and KL2-G, Jochum et al., 2006) were used as secondary standards to verify our analysis and the results are within 2σ analytical errors compared to the reference values (Fig. C1).

Six transition metal elements (V, Cr, Mn, Co, Ni and Cu) were analyzed in separate sessions with a 12 or 17 nA O^- primary ion beam that is 15 μm in diameter. A mass resolution power (MRP) of 6000 V was used in the analysis to separate target ion species from possible interferences (e.g. $^{47}Ti^{16}O^-$ on $^{63}Cu^-$ and $^{49}Ti^{16}O^-$ on $^{65}Cu^-$). If possible, two isotopes of the same element are measured to cross check the results. $^{28}Si^-$ or $^{30}Si^-$ was used as the internal standard, and two isotopes for Ni (^{60}Ni and ^{62}Ni) and Cu (^{63}Cu and ^{65}Cu) were monitored to check for possible mass interference. Three MPI-DING glasses (GOR128-G, GOR132-G and T1-G), which are more similar to our MIs in major element composition, were used as the standards for transition metal measurements, as strong matrix effects were observed for analyzing Co, Ni and Cu (Figure D1).

5.4 Results

Homogenized melt inclusions from 15016, 12040, 15647 and 74235 are usually one single glassy phase (Fig. 5.1a, b), but can contain a bubble or a Fe metal, and occasionally a spinel crystal. Natural MIs found in 10020 are often highly crystalized with a spinel and a plagioclase. Only one natural MI from 10020 was identified to contain a glassy part that is large enough (e.g. >10 μm) for SIMS analysis (Fig. 5.1c). Natural partially glassy MIs found in 74235 are oval or elongated in shape, and usually contain ilmenite crystals and tiny sulfide globules. Major elements, volatiles, trace element and transition metal concentrations measured for the homogenized and natural MIs are reported in Table D1.

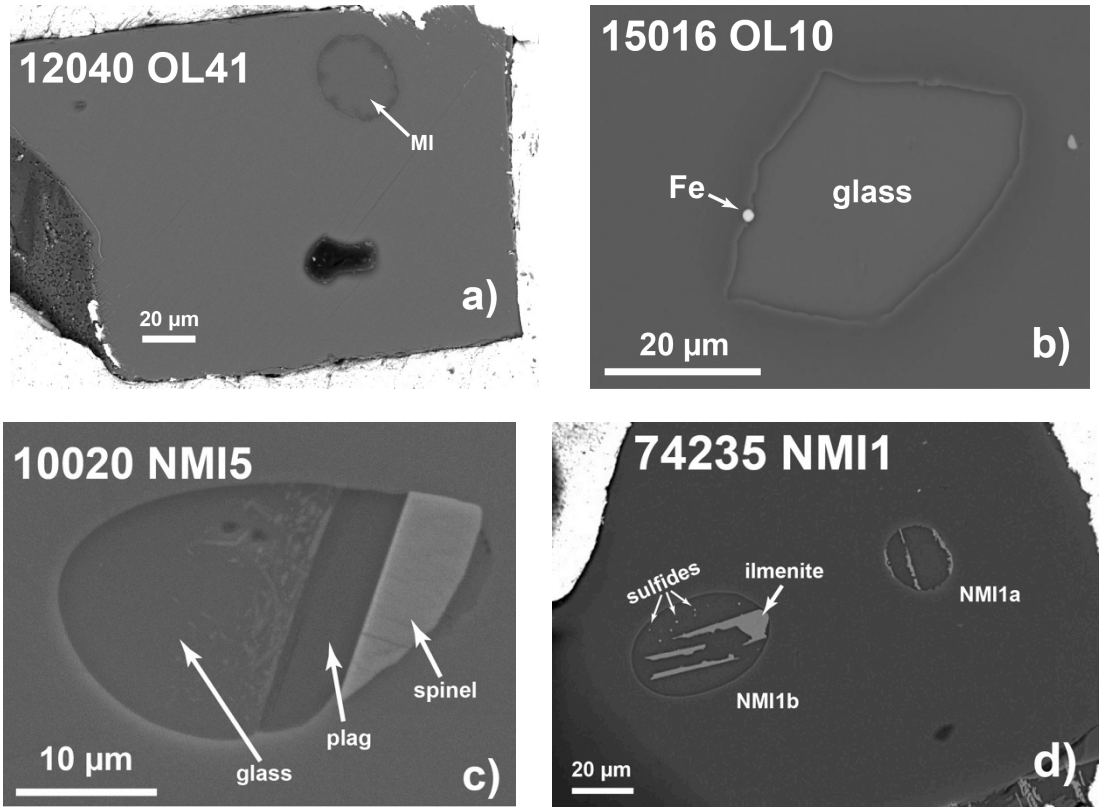

Figure 5.1. Back-scattered electron images for two homogenized (a, b) and two natural (c, d) MIs studied in this work. a) The homogenized MI 12040 OL41 is essentially one single glassy phase; b) Homogenized MI 15016 OL10 contains a tiny Fe metal; c) Natural partially glassy MI 10020 NMI5 contains a spinel and a plagioclase crystal; d) Natural partially glassy MIs discovered in 74235 usually contain ilmenite crystals and tiny sulfide globules.

5.4.1 Major element compositions

In general, major element compositions of the homogenized MIs are relatively close to their whole rock compositions, except for those from 12040, whose whole rock composition is affected by olivine accumulation, (e.g. Walter et al., 1971; Walker et al., 1976; Bombardieri et al., 2005). Concentrations of SiO_2 in the homogenized MIs range from 39.1 wt% to 48.3 wt%, while MgO concentrations vary from 4.3 to 8.6 wt%. On the other hand, major element compositions for partially glassy MIs identified in 10020 and 74235 are significantly more evolved than their parental rocks. For example, 10020 OL15 contains 54.6 wt% SiO_2 and 1.7 wt% MgO, compared to 40.8 wt% SiO_2 and 7.0 wt% MgO in the whole rock of 10020 (Rhodes and Blanchard, 1980), which indicates a high degree of post-entrapment crystallization. Natural partially glassy MIs in

74235 contain 43.2 to 52.4 wt% SiO_2 and 2.1 to 3.2 wt% MgO compared to 38.6 wt% SiO_2 and 8.4 wt% MgO in the whole rock (Rhodes et al., 1976). Post-entrapment crystallization of ilmenite has a great impact on TiO_2 concentrations for MIs from 74235, resulting in as low as 3.1 wt% TiO_2 in the natural partially glassy MIs, compared to the whole rock with 12.2 wt% TiO_2. Interstitial glasses found in the matrix of 74235 are even more evolved in chemical composition, with 56.6 wt% SiO_2, 1.8 wt% MgO and 2.3 wt% TiO_2.

For the homogenized MIs, one way to evaluate whether equilibrium is reached between the MI and its host olivine is to calculate the apparent K_D values (K_D=[Fe/Mg]$_{OL}$/[Fe/Mg]$_{MI}$). According to Xirouchakis et al. (2001), K_D between olivine and melt at equilibrium is ~0.33 for low-Ti basalt, and ~0.28 for high-Ti basalt. Apparent K_D values for the homogenized MIs can depart from the equilibrium values for at least the following reasons: a) inadequate homogenization temperature/duration could result in residue crystal phases in the MI and cause the apparent K_D to be higher or lower than the equilibrium value, depending on whether the residue phase is more enriched in Mg or Fe; b) overheating can cause olivine dissolution into the MI, resulting in elevated K_D values; c) post entrapment loss of Fe through the host olivine can also result in elevated apparent K_D between MI and olivine (Danyushevsky et al., 2000; Bombardieri et al., 2005). To avoid possible complications related to disequilibrium between MI and olivine, only homogenized MIs within a small range of K_D values close to equilibrium (0.25 to 0.44) were measured with SIMS and reported in this study (Fig. 5.2). Compositions for the natural unheated MIs from 10020 and 74235, on the other hand, show lower apparent K_D values due to post entrapment crystallization of olivine. Interestingly, interstitial glasses identified in the matrix of 74235 show even more evolved compositions compared to natural partially glassy MIs in the same sample.

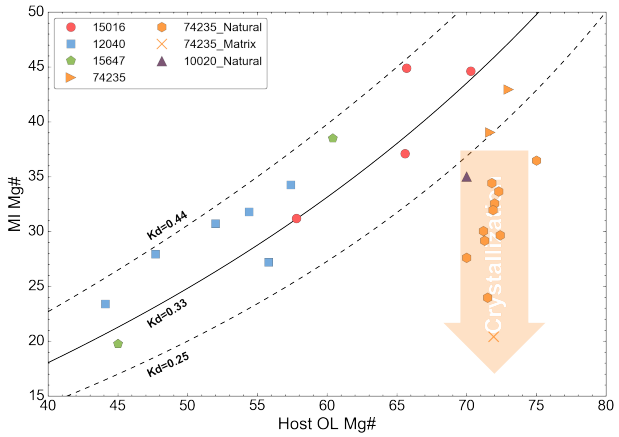

Figure 5.2. Magnesium number (Mg# = Mg/(Mg+Fe), atomic) of the homogenized and natural glassy MIs compared to Mg# of their host olivine. Constant K_D values of 0.25, 0.33 and 0.44 are also plotted on the figure as a comparison. Interstitial glass from 74235, as plotted in the figure, shows more evolved composition compared to the natural MIs. Host olivine Mg# for the matrix glass was assigned to be average Mg# of olivines measured in 74235 (70.0 to 75.0 with an average of 71.9).

5.4.2 Trace element compositions

Spidergrams for all measured melt inclusions in this study are plotted in Fig. 5.3. In general, trace element patterns for MIs from 10020, 15016, 15647 and 74235 are consistent with those in their whole rock data. Trace element concentrations in 12040, however, are significantly elevated compared to the whole rock composition of 12040 (Fig. 5.3b), which can be explained by olivine accumulation in 12040 (e.g. Walter et al., 1971; Walker et al., 1976; Bombardieri et al., 2005). Most samples studied in this work show depletion in K, Sr, P, F and Eu, which are typical for lunar samples. The depletion of K and F is consistent with the expected volatile-depletion nature of the Moon. One exception is sample 12040, whose MIs do not show an obvious depletion in F. Phosphorus depletion and the depletion of other siderophile elements in the Moon was explained by segregation of a small Fe-rich core (Newsom, 1986). Depletion of Eu and Sr, on the other hand, was often explained by plagioclase removal in the mantle source of mare basalts. The wide spread of Eu anomaly in essentially all lunar basalts has been interpreted as a strong support for the lunar magma ocean model (Taylor et al., 2006). For the two high-Ti basalt samples (10020 and 74235), positive anomaly of Ti and Nb is observed, which is caused by

ilmenite addition during formation of high-Ti basalts (Chen et al., 2015). Natural partially glassy MIs in 10020 and 74235, however, often show lower degrees of enrichment in Nb and Ti (sometimes even depletion for Ti), indicating precipitation of ilmenite during post-entrapment crystallization of the natural MIs. As a comparison, the two homogenized MIs from 74235 show essentially the same degrees of enrichment of Nb and Ti compared to the whole rock (Fig. 5.3d).

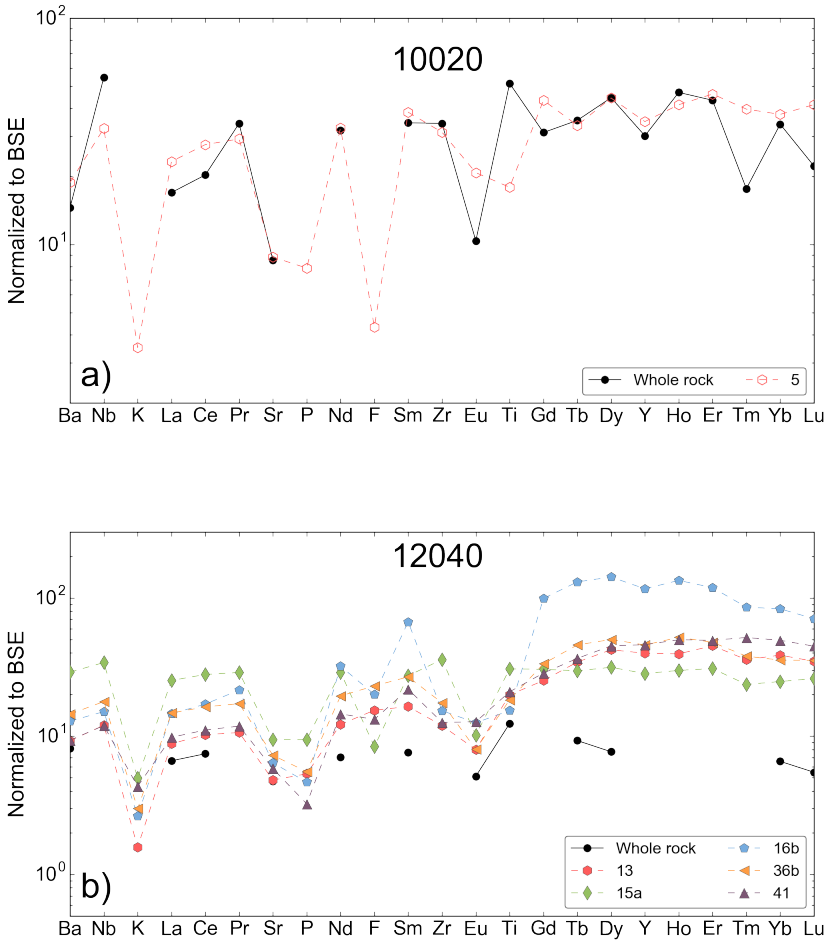

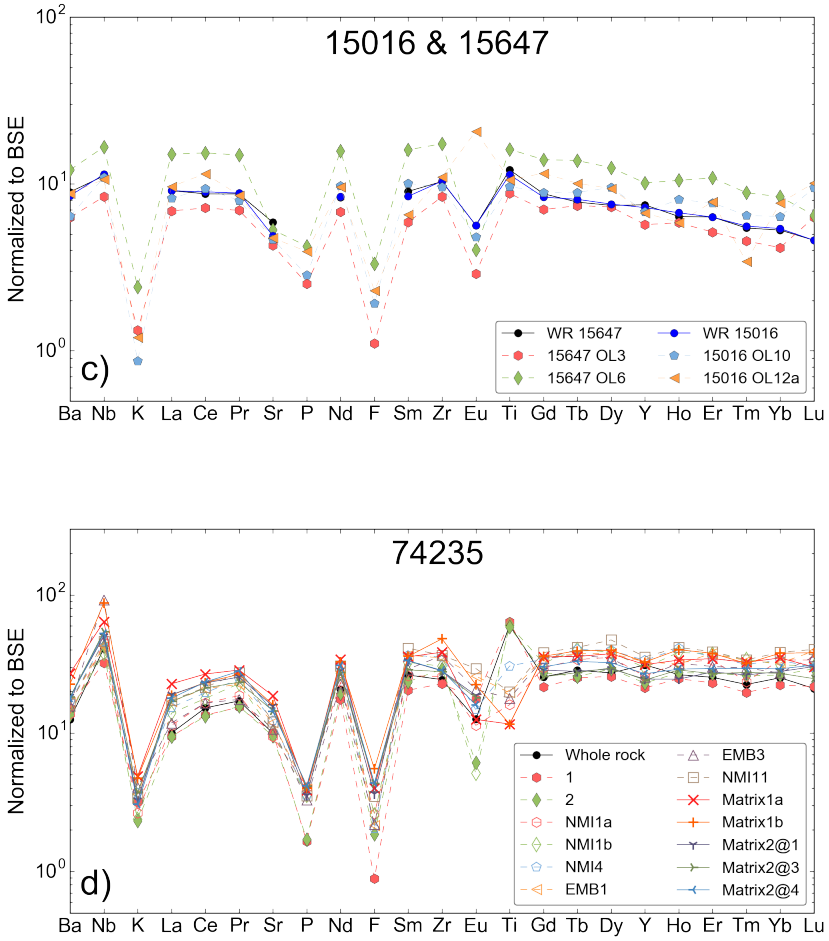

Figure 5.3. Spidergrams of all measured melt inclusions in this study. Whole rock data from the Lunar Sample Compendium are plotted in black or blue solid circles. All other filled symbols are for homogenized MIs, while the open symbols are for natural unheated MIs. Data for interstitial glasses from 74235 are plotted in crosses in d). BSE composition is from McDonough and Sun (1995).

5.4.3 Volatile concentrations

Concentrations of H_2O, F, Cl and S for all the MIs and glasses measured in this study are plotted in Fig. 5.4. The highest H_2O concentration in this study of 434 ppm is found in the natural partially glassy MI from 10020. For the other group of partially glassy MIs from 74235, 51 to 88 ppm H_2O is detected in the MIs. Interestingly, the more evolved interstitial glasses in the matrix of 74235 contain 91 to 138 ppm of H_2O, slightly higher than in 74235 partially glassy MIs, indicating good retention of H_2O in the final stage of magma evolution. Essentially all the

homogenized MIs are relatively dry, with less than ~30 ppm H_2O, similar to the low H_2O concentrations measured in homogenized MIs by Chen et al. (2015).

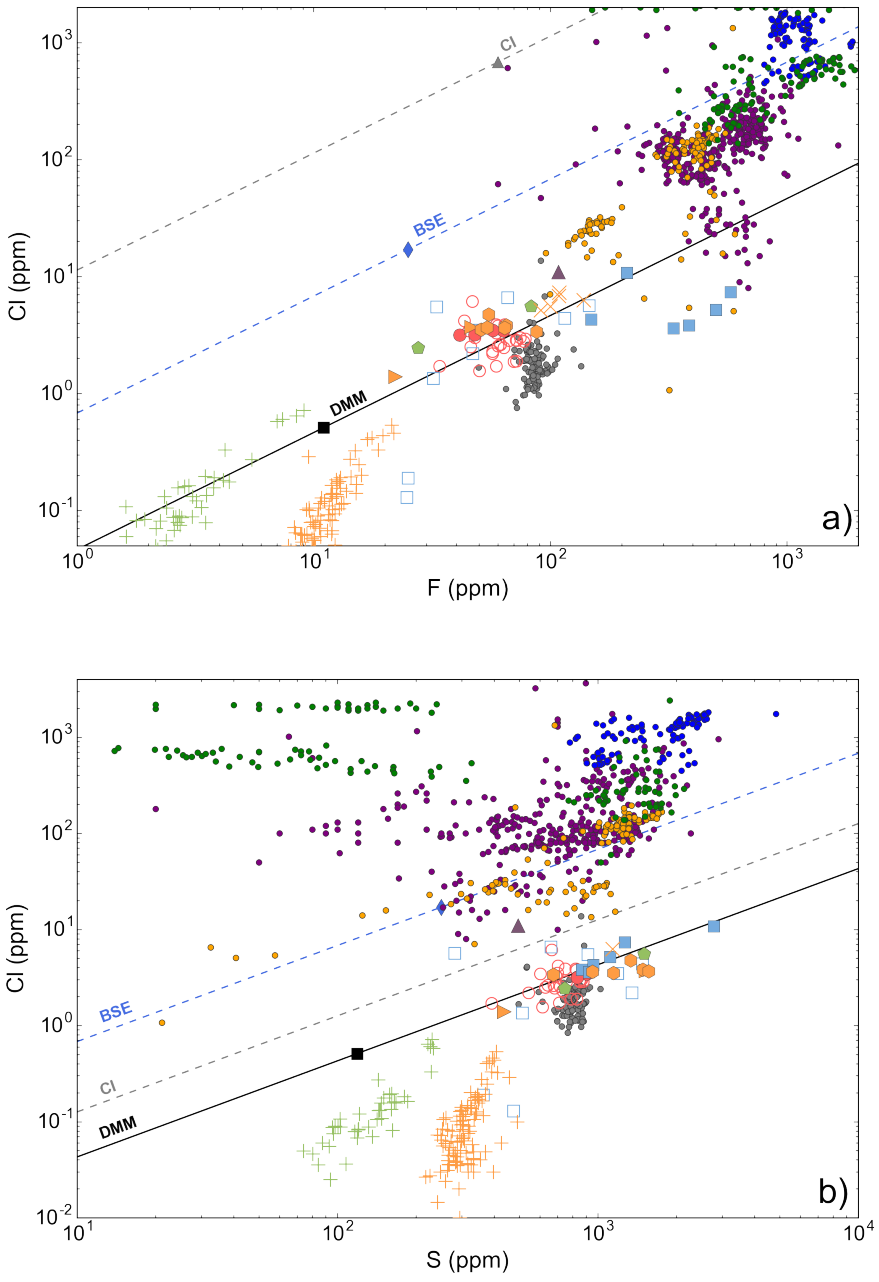

Figure 5.4. Comparing H_2O, F, Cl and S concentrations in lunar MIs from this study to those in lunar MIs and glass beads from the literature, and to those in terrestrial MIs. Their concentrations in the depleted mantle (DMM, Salters and Stracke, 2004), CI condrites and bulk silicate earth (CI and BSE, McDonough and Sun, 1995) are also plotted as a comparison. Volatile concentrations in one homogenized MI from 74235 are systematically lower than other MIs from the same sample possibly due to diffusive loss through micro-cracks in host olivine during homogenization, and this MI is excluded for later discussion.

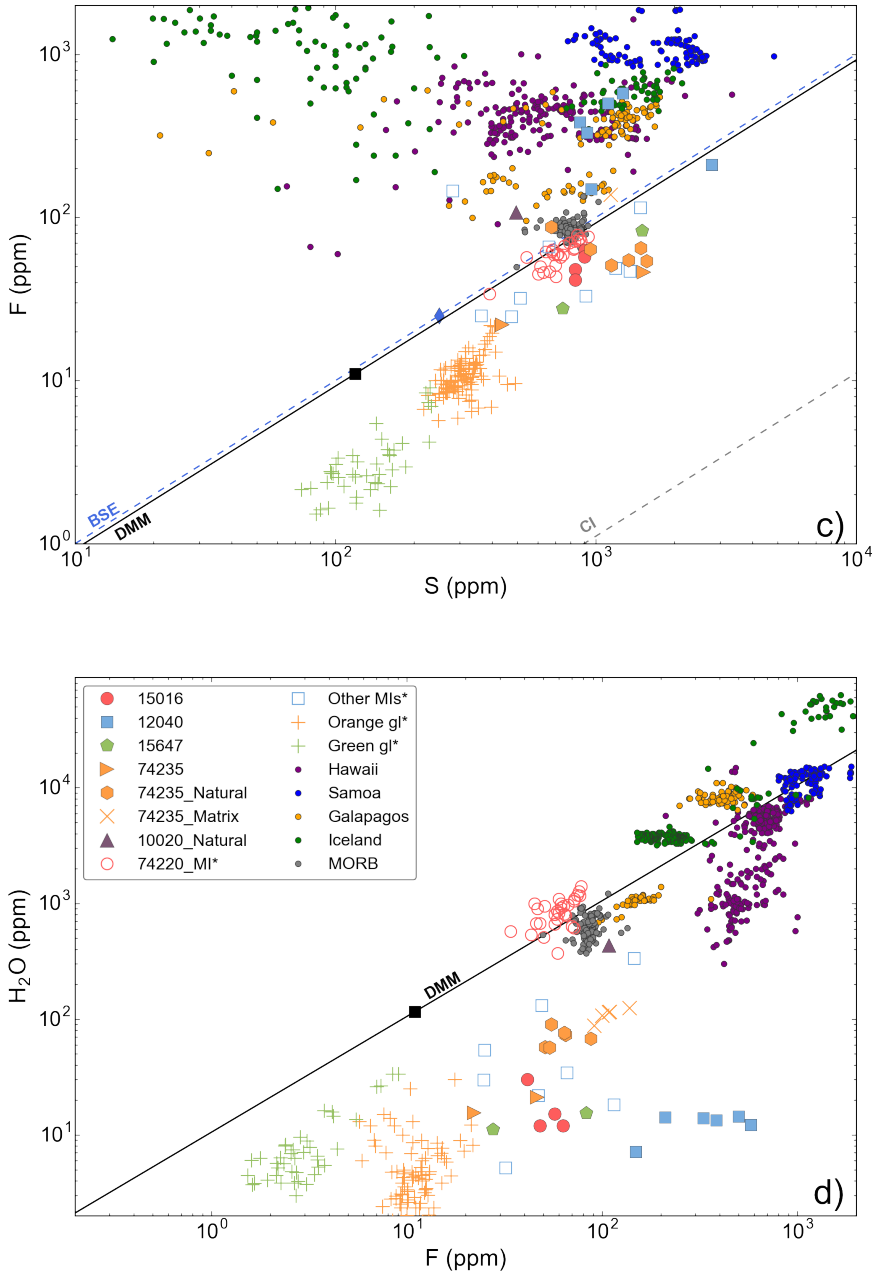

Figure 5.4. Continued.

*74220 MI data are from Hauri et al. (2011), Chen et al. (2015) and Ni et al. (2017). Data for "Other MIs" in the literature are from Chen et al. (2015). Data for lunar glass beads are from Hauri et al. (2015). Volatile data for the terrestrial MIs are from GeoRoc (http://georoc.mpch-mainz.gwdg.de/), except for the MORB MIs, which are from Saal et al. (2002).

In terms of other volatiles in the melt inclusions, Cl and S concentrations are roughly in the same range (mostly ~3 to 11 ppm Cl and ~440 to 1500 ppm S) with published lunar MI data for 74220 and other lunar samples, and their ratios are close to Cl/S ratio in the depleted mantle (Fig. 5.4b). Fluorine concentrations in MIs from 10020, 15016, 15647 and 74235 fall into the range of ~30 ppm to ~140 ppm, similar to previously published lunar MI data. However, F concentrations in MIs from 12040 are 150 to 580 ppm, significantly higher than those in other lunar MIs from this study or in the literature. MIs from 12040 yield elevated F/S ratios and lowered Cl/F ratios, as can be seen in Fig. 5.4b and 5.4c. Compared to terrestrial MIs, F concentrations for MIs from 12040 are higher than in mid-ocean ridge basalt (MORB) MIs, similar to ocean island basalt MIs, suggesting enrichment of F in the parental liquid of 12040. One homogenized MI from 74235 (74235 OL1, Fig. 5.4 and Table D1) is low in all volatile concentrations compared to other MIs in the same sample, attributed to possible diffusive loss of volatiles through micro-cracks during homogenization. Hence, this sample is excluded in later discussions to avoid complications.

5.4.4 Transition metals

First-row transition metal concentrations (V, Cr, Mn, Co, Ni and Cu) for the lunar MIs are plotted in Fig. 5.5 to be compared with their whole rock compositions and the MORB compositions. As can be seen in the figure, transition metal concentration patterns for the MIs are often consistent with the whole rock. For 12040, Ni concentrations in the MIs are lower than in the whole rock by almost two orders of magnitude (Fig. 5.5a). Such a difference cannot be explained by post-entrapment crystallization of olivine, which can lower Ni concentration in the MI by less than one order of magnitude (e.g. Fig. 5.5d). The elevated Ni concentration in the whole rock of 12040 might be caused by olivine accumulation in forming 12040, as Ni concentrations are significantly higher in olivine. Concentrations of V, Cr and Mn in lunar whole rocks are close to 1 when normalized by BSE. The similarity of V, Cr and Mn concentrations in the silicate proportion of

Earth and Moon was interpreted as evidence for the Moon forming out of Earth's mantle (e.g. Dreibus and Wanke, 1979; Ringwood, 1986; Drake et al., 1989; Gessmann and Rubie, 2000), but this interpretation has been challenged by others (Ruzicka et al., 1998 and 2001; Taylor et al., 2006). As can be seen in Fig. 5.5, Cr concentration is depleted in MORB samples compared to in lunar samples, which can be explained by the existence of chrome-spinel in the source region of MORB as a buffer on Cr concentration in the melt (e.g. Sun et al., 1979). In addition, Ni concentrations in the high-Ti basalt 74235 (Fig. 5.5d) are significantly lower than in the low-Ti basalts, indicating genetic differences between these two types of mare basalts (i.e. sourced from different zones of cumulate minerals in lunar mantle).

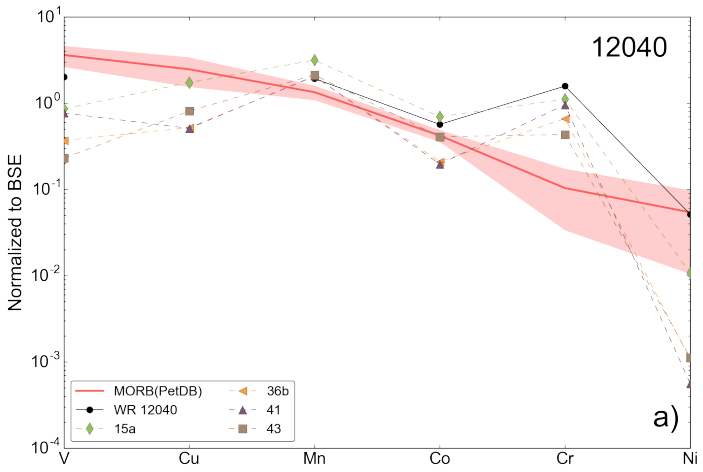

Figure 5.5. Transition metal concentrations in lunar MIs measured in this study compared to their concentrations in the whole rock of each sample and in MORB. Whole rock data for the lunar samples are from Lunar Sample Compendium. MORB data is from PetDB (http://www.earthchem.org/petdb). BSE concentrations are from McDonough and Sun (1995).

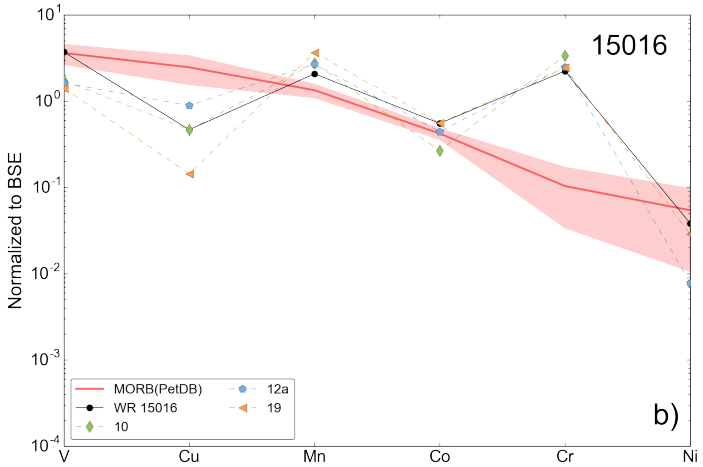

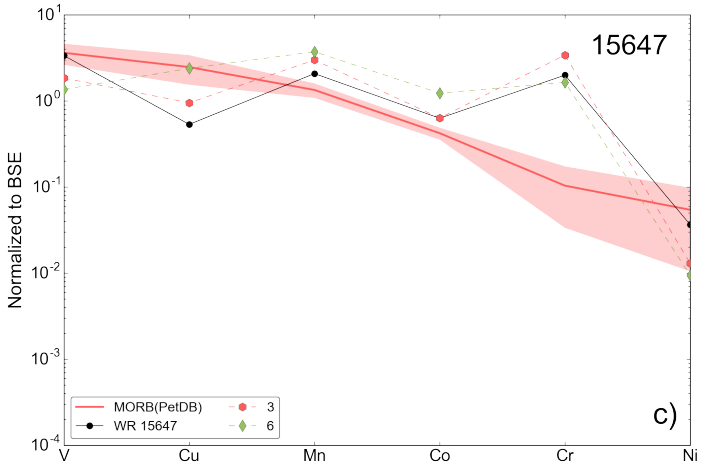

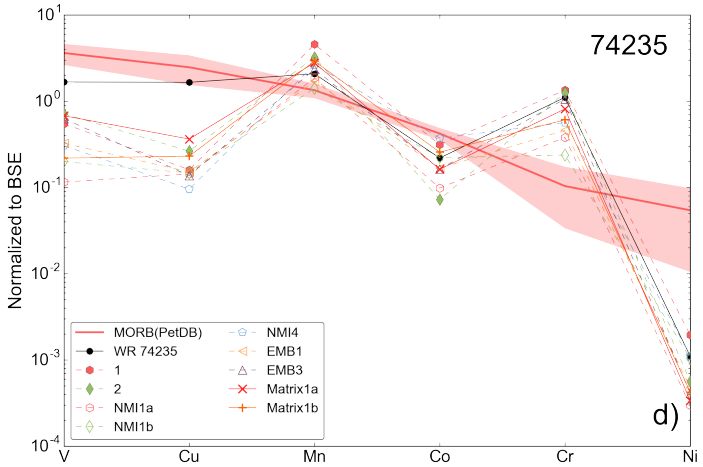

Figure 5.5. Continued.

5.5. Discussion

5.5.1 Comparison of volatile elements with non-volatile trace elements

Volatile concentrations are often compared with non-volatile trace elements that show similar geochemical behaviors during partial melting or crystal fractionation to evaluate degassing and contamination of volatiles during magma evolution or eruption, and to assess volatile contents in the magma sources (e.g. Michael, 1988; Saal et al., 2002; Plank et al., 2009; Koleszar et al., 2009; Chen et al., 2015). For the volatile elements measured in this study (H_2O, F, Cl and S), elemental ratios of H_2O/Ce, F/Nd and S/Dy are used following Chen et al. (2015) to assess volatile abundances in lunar mantle. For Cl, Chen et al. (2015) used Cl/Ba ratios instead of the more common Cl/K because of the lack of precise K data, and because K can also be volatile at high temperatures. In this study, since high precision SIMS data were obtained for K, effort was made to estimate Cl abundance in lunar mantle based on Cl/K ratios. By using the above volatile-refractory element pairs with similar degrees of incompatibility, effects of mantle partial melting and crystal fractionation are partially removed (e.g. H_2O/Ce, F/Nd, Cl/K and S/Dy) during magma processes, which provides a chance to estimate volatile abundances in lunar mantle based on these ratios.

Although ratios of H_2O/Ce, F/Nd, Cl/ K and S/Dy are assumed to be roughly constant during magma processes such as partial melting or crystal fractionation, they can still be affected by volatile degassing during magma transportation, eruption and homogenization in lab. One uncertainty in Chen et al. (2015) was whether or not the low H_2O/Ce ratios in homogenized MIs were affected by diffusive H loss during homogenization. According to experiments conducted by Ni et al. (2016), H_2O can be significantly lost from the MIs in time scales as short as <10 min, while the loss of F, Cl and S is negligible under the same homogenization conditions. In order to assess H_2O/Ce ratios in lunar mantle, it is crucial to clarify the role of diffusive H loss in lab on H_2O/Ce in homogenized MIs. As suggested by model estimations (e.g. Qin et al., 1992; Cottrell et al., 2002; Chen et al., 2013), and supported by experiments on lunar MIs (Ni et al. 2016),

inclusions with large diameters have better chances in preserving their original H_2O content. Considering the limited availabilities of MIs > 50µm in diameter, we assume homogenized MIs with diameters >45 µm are less likely affected by diffusive H loss (<20% under most homogenization conditions), and excluded all homogenized MIs that are < 45 µm in diameter for the H_2O-Ce plot (Fig. 5.6a). One additional MI from 74235 with a diameter of 51 µm was too close to the olivine boundary and was also excluded. In this way, variations in H_2O/Ce ratios across different lunar MIs are only due to natural processes on Moon, while diffusive H loss in lab during homogenization is less likely a concern.

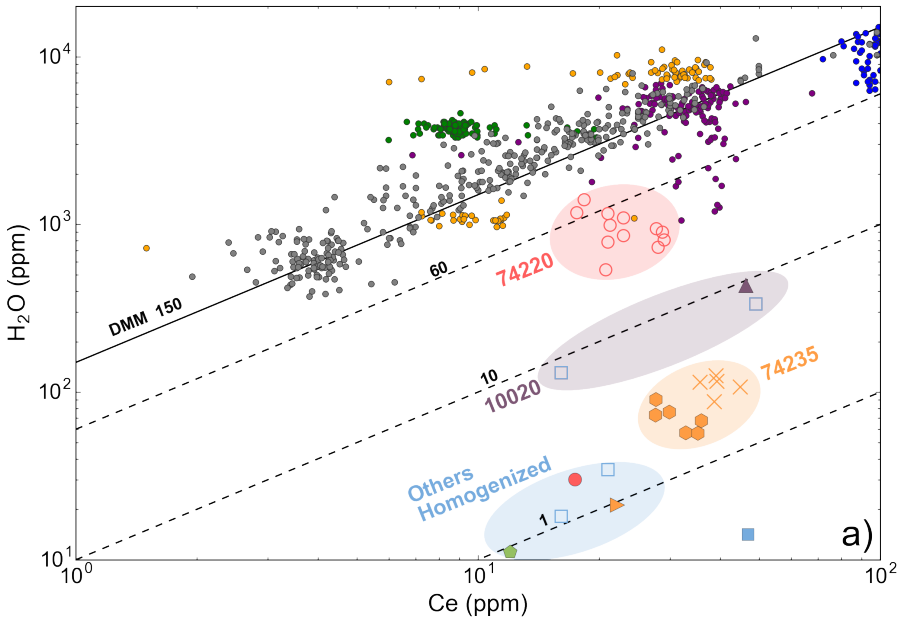

Figure 5.6. Concentrations of volatiles versus refractory elements in terrestrial and lunar olivine-hosted melt inclusions. For homogenized MIs data in a), those for MIs <45µm in diameter from this study and Chen et al. (2015) are excluded to reduce the concern of diffusive H loss during homogenization. Terrestrial MI data are mostly from GeoRoc, except for the MORB data, which are from Michael (1988); Michael (1995); Danyushevsky et al. (2000); Dixon and Clague (2001); Saal et al. (2002); Dixon et al. (2002). Lunar MI and glass data from the literature are marked with stars. Detailed sources for the data can be found in Fig. 5.4.

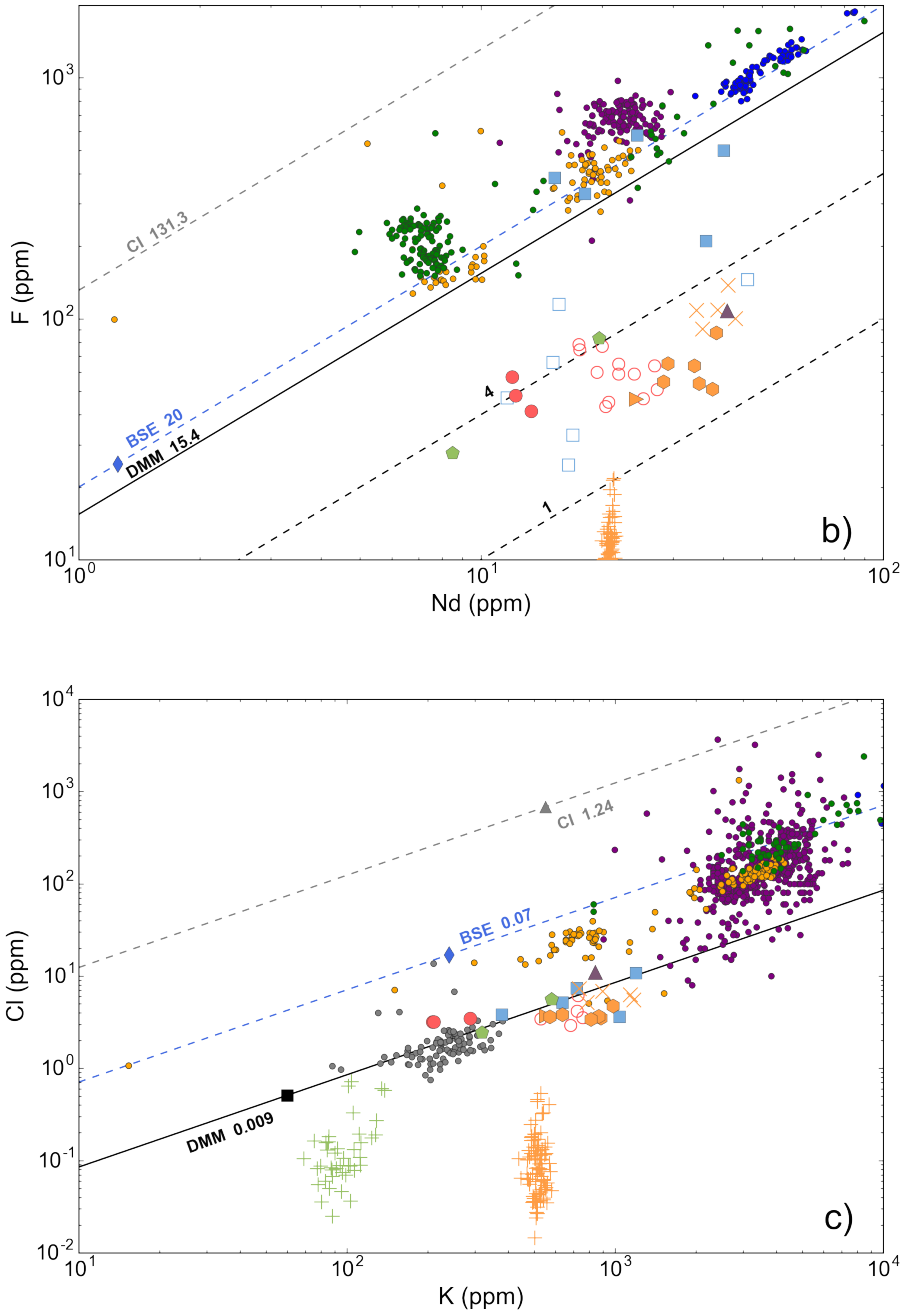

Figure 5.6. Continued.

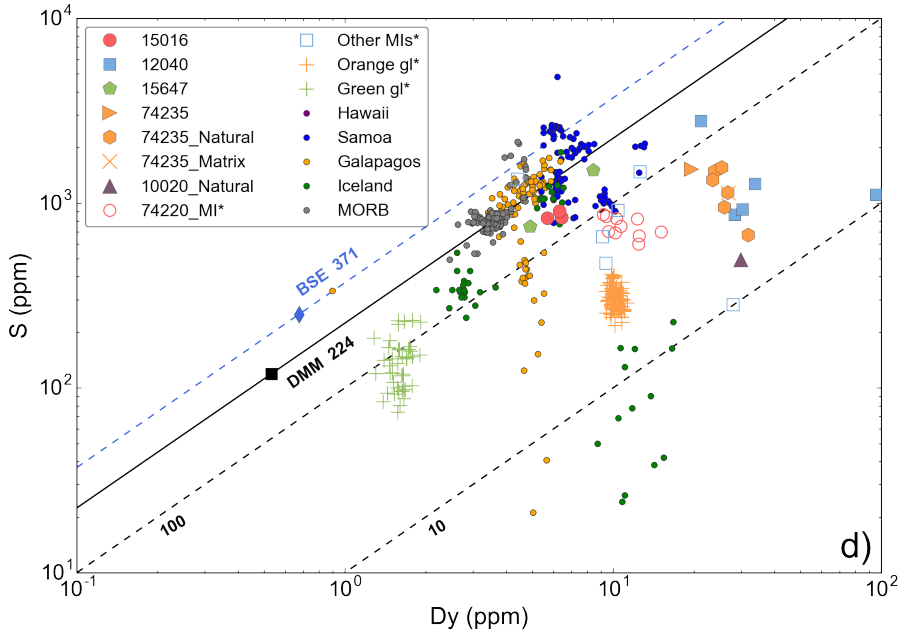

Figure 5.6 Continued.

5.5.1.1 H_2O/Ce ratios in the lunar MIs

As marked in Fig. 5.6a, after excluding data from homogenized MIs <45 μm in diameter, H_2O versus Ce concentrations for lunar MIs can be roughly categorized into four groups. MIs from 74220 show the highest H_2O/Ce ratios among all lunar MIs studied till now. H_2O/Ce ratios for natural MIs in 74220 (Hauri et al., 2015; Chen et al., 2015; Ni et al., 2016) fall between 26 and 77, with the maximum of H_2O/Ce=77 from Hauri et al. (2015). As Ni et al. (2016) pointed out, H_2O concentrations in natural MIs from 74220 show positive correlation with MI diameter, indicating post-eruptive H_2O loss from the MIs. Therefore, the highest H_2O/Ce ratio recorded by 74220 natural MIs is more representative of the pre-eruptive H_2O/Ce in their parental magma.

For high-Ti basalt 10020, three MIs have been measured in terms of H_2O and Ce concentrations. Among these three MIs, one natural MI was measured in this study, another natural MI and one additional homogenized MI were measured by Chen et al. (2015). As can be seen in Fig. 5.6a, the two natural MIs (on the high end of 10020 group) are very similar in composition, with ~50 ppm Ce, and ~400 ppm H_2O. The elevated Ce concentrations in these two

MIs from 10020 are consistent with the highly evolved nature of the melt inclusions with ~55 wt% SiO_2. The homogenized MI from 10020 contains a factor of three lower amounts of H_2O and Ce (131 ppm H_2O, 16.1 ppm Ce) with a similar H_2O/Ce ratio (Fig. 5.6a). The high consistency in H_2O/Ce ratios for these three MIs from 10020 indicate that: a) H_2O was not lost from this homogenized MI during heating; and b) an H_2O/Ce ratio of ~9 is likely representative of the whole rock composition of 10020.

For high-Ti basalt 74235, both natural partially glassy MIs and interstitial glasses are measured by SIMS for H_2O and Ce concentrations. As mentioned earlier, the interstitial glasses in the matrix of 74235 contain higher H_2O concentrations (88 to 125 ppm) than the natural partially glassy MIs (57 to 91 ppm). By comparing them in the H_2O-Ce plot, however, it can be seen that H_2O/Ce ratios for the natural MIs and interstitial glasses are very similar, and the relative high H_2O concentrations in interstitial glasses are due to their more evolved compositions compared to the natural partially glassy MIs. This conclusion is also supported by the major element composition, as the interstitial glasses contain higher SiO_2 (~57 wt%) compared to the glassy parts of natural MIs (43 to 52 wt%), and are lower in Mg# (Fig. 5.2). The fact that interstitial glasses from 74235 preserved similar H_2O/Ce ratios as the olivine-hosted MIs is a bit surprising, and might suggest that 74235 evolved as a close system for H_2O at the last stage when these MIs and interstitial glasses formed. Compared to terrestrial MIs that often contain weight percent level of H_2O, the low concentrations of ~100 ppm H_2O in 74235 is easier to be preserved in a lava flow. Even one meter of basalt lava on Moon would provide sufficient pressure to keep 100 ppm H_2O under-saturated in the magma. H_2O/Ce ratios for the natural MIs and interstitial glasses range from 1.6 to 3.3, about a factor of 20 lower than MIs from 74220, and a factor of 3 lower than MIs from 10020.

Essentially all the other homogenized MIs show low H_2O/Ce ratios in the range between 0.9 and 1.7 (except 0.3 for one MI from 10240). Since only large homogenized MIs >45 μm in diameter were kept in Fig. 5.3a, diffusive loss of H_2O in lab is a less likely explanation to low

H_2O/Ce ratios in the homogenized MIs. Therefore, the variation of H_2O/Ce ratios among different samples (77 for 74220, 9 for 10020, 3 for 74235 and ~1 for other samples with crystallized MIs) are most likely due to a) degassing loss of H_2O during magma transportation or eruption, and b) lunar mantle heterogeneity in H_2O/Ce ratios. For these four groups of samples as marked in Fig. 5.6a, H_2O/Ce ratios seem to be correlated with the occurrence of glassy or partially glassy MIs: most MIs found in 74220 are glassy; partially glassy MIs can occasionally be found in 10020 and 74235; no MIs with a measurable glassy part were found in other samples. Therefore, we argue that H_2O/Ce ratio variations among lunar samples are at least partially due to degassing loss of H_2O during different time scales of cooling on lunar surface.

5.5.1.2 F/Nd, Cl/K and S/Dy ratios in the lunar MIs

In the plot of F versus Nd (Fig. 5.6b), ratios of F/Nd for most MIs analyzed in this study fall into the range of 1 to 4, consistent with the results from Chen et al. (2015). MIs from 12040, however, show much higher F/Nd ratios (6 to 25, ~20 for most MIs) compared to all other lunar samples studied previously or in this work. Note that F/Nd ratios for most terrestrial OIB MIs are between 15 to 40 with an average of ~22 (Chen et al., 2015), a F/Nd ratio of ~20 for 12040 MIs is essentially the same as BSE values. The elevated F/Nd ratios in 12040 might reflect lunar mantle heterogeneity in F abundances or secondary enrichment of F during formation of 12040.

In Fig. 5.6c, Cl is compared to K. Although Cl/K is more commonly used in the literature, somehow Cl/K ratio in DMM (0.009; Salters and Stracke, 2004) is lower than in BSE (0.07; McDonough and Sun, 1995) by a factor of ~8, meaning that this ratio is fractionated significantly during magma processes. On the other hand, MI data from terrestrial MIs are mostly in accordance with Cl/K ratios in DMM and BSE. Cl/K ratios in MORB MIs are very close to the DMM value of 0.009. While the OIB MIs from Samoa, Iceland and Hawaii show Cl/K ratios near an average of ~0.045, slightly lower than the BSE ratio of 0.07. Cl/K ratios are roughly consistent among MIs from all lunar samples studied so far, all in the range between 0.0035 and 0.015, with

an average of ~0.008. This Cl/K ratio of ~0.008 for the lunar MIs is very close to the DMM value of Cl/K=0.009, a factor of 9 lower than the BSE ratio of 0.07, and a factor of 6 lower than the average ratio of ~0.045 in OIB MIs (Fig. 5.6c). The similar Cl/K ratio between lunar MIs and DMM, however, does not mean that Cl abundance is the same between lunar mantle and DMM, as K is volatile and less abundant on Moon compared to BSE, which will be discussed later.

Concentrations of S are plotted versus Dy in Fig. 5.6d. Unlike H_2O/Ce, F/Nd and Cl/K in lunar samples, S/Dy ratios can be affected by not only degassing loss of S, but also sulfide segregation in the melt. For green and orange glass beads, the degassing effect is more dominant in generating variations in their S/Dy ratios (Fig. 5.6d). For the natural partially glassy MIs and interstitial glasses, however, sulfide saturation is playing a more important role in fractionating S/Dy ratios. For example, the homogenized MI from 74235 has a S/Dy ratio of 77.8, but S/Dy ratios in natural MIs from the same sample can be fractionated to < 40. Low S/Dy ratio for the natural MI from 10020 (~17) is also likely due to the formation of sulfides, as it is highly evolved in composition (Fig. 5.2). Since S/Dy ratios could be lowered due to the above two factors, highest S/Dy ratio for each sample is assumed to be more representative of its parental melt. For low-Ti basalts (12008, 12040, 15016 and 15647), highest S/Dy ratio in each sample is 118 to 179 (after excluding one outlier in 12008 from Chen et al., 2015). For the high-Ti basalts (10020, 74220 and 74235), highest S/Dy ratio in each sample is 78 to 95 (Fig. 5.7). This different between low-Ti and high-Ti mare basalts in terms of S/Dy is about 20% to 50%, which needs to be confirmed using more lunar MI data. If this difference is true, however, it might provide valuable constraints on the formation of low-Ti and high-Ti mare basalts (e.g. the mineral mode of sulfides in their source mantle).

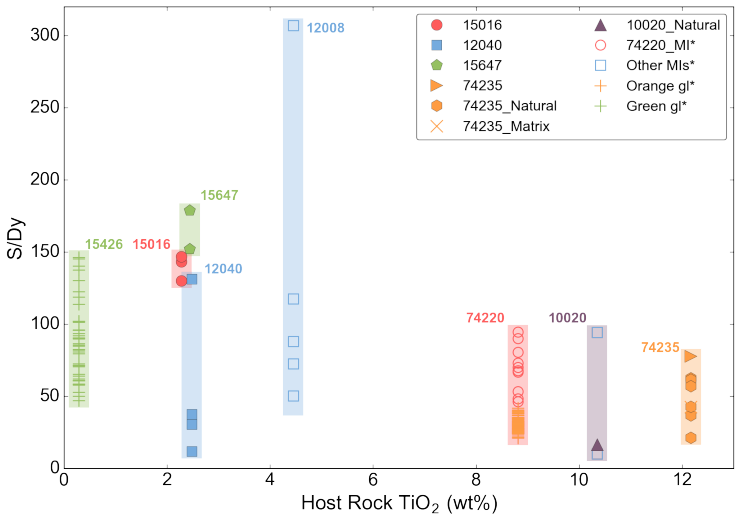

Figure 5.7. S/Dy ratios in olivine-hosted melt inclusions plotted versus the TiO_2 concentrations in their host rock. Host rock TiO_2 concentrations are used because their concentrations in the melt inclusions could have been fractionated due to post-entrapment crystallization. Data sources for the melt inclusions and glass beads are the same as in Fig. 5.6. Host rock concentrations are from Table. 5.1.

5.5.2. Moderately volatile elements (Li and K) versus refractory elements

In this study, concentrations of moderately volatile elements K ($T_{1/2}$=1001 K, Lodders, 2003) and Li ($T_{1/2}$=1135 K, Lodders, 2003) are also measured, and compared to refractory elements to estimate their abundances from an MI perspective. For K, K/U ratios are more commonly used for estimation of K abundance in the source rock (e.g. McDonough and Sun, 1995; Salters and Stracke, 2004). Uranium concentrations in the MIs, however, are difficult to be precisely determined by SIMS, as tested by Chen et al. (2015). Therefore, K/La ratio, which also often appear in the literature (e.g. O'Neill, 1991; Michael, 1995), are used instead of K/U in this study to determine K abundance in lunar mantle. For Li, the ratio of Li/Dy is adopted in this study, as the comparison between DMM and BSE compositions shows that Li and Dy have similar incompatibilities. Plots of K versus La and Li versus Dy are shown in Fig. 5.8. We would like to point out that, Li concentrations in the homogenized MIs from this study could be affected by contamination from the crucibles during homogenization, as high concentration of Li was

detected in the surface melt of 74235 OL2 after experiment. Therefore, only Li concentrations from natural MIs are plotted in Fig. 5.8b.

As shown in Fig. 5.8a, K/La ratio for DMM is similar to that of the BSE, meaning this ratio not fractionated much during magma processes. MORB and OIB MI data fall into a narrow range near the DMM K/La ratio of 256 (Salters and Stracke, 2004), supporting the similar degrees of incompatibility for K and La. Ratios of K/La in green glass beads and orange glass beads (Hauri et al., 2015) are roughly constant and very similar to each other, with an average of K/La=76 (Fig. 5.8a). The absence of fractionation of K/La in lunar volcanic glass beads indicate that, K is probably not behaving as a volatile element during volcanic eruptions on Moon. The non-volatile behavior of K is also supported by the similar K/La ratios in lunar MIs, as shown in Fig. 5.8a. If K/La ratios are compared among MIs from different lunar samples, all samples studied in this work show similar K/La ratios within a factor of 2. Therefore, we adopt a ratio of K/La=76 for lunar MIs and volcanic glass beads, which is similar to K/La=71 estimated by O'Neill, (1991).

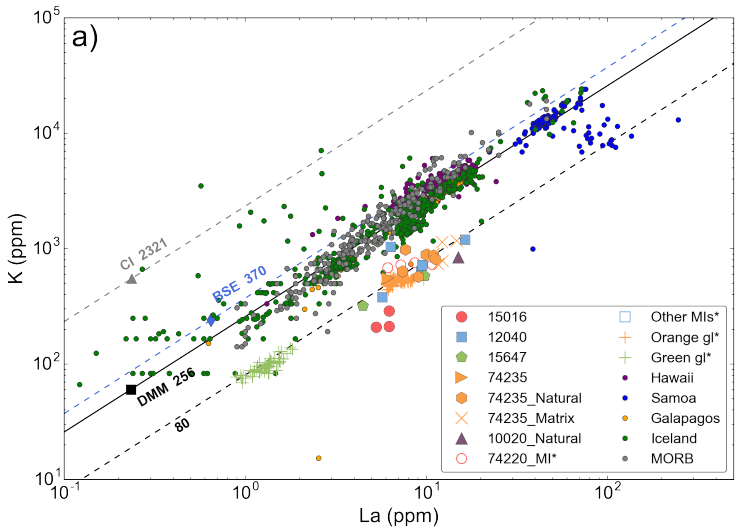

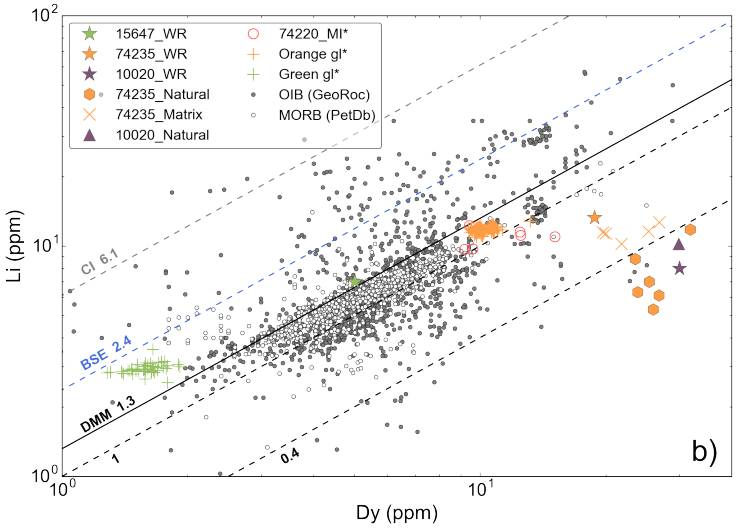

Figure 5.8. Plots of moderately volatile elements versus refractory elements. a) Plot of K versus La. Data sources are the same as in Fig. 5.4 and Fig. 5.6. Potassium concentrations for lunar samples use in this plot are all measured by SIMS. b) Plot of Li versus Dy. Due to the limit availability of Li data in terrestrial MIs, concentrations of Li in MORB and OIB basalts are used. MORB data are from PetDB (http://www.earthchem.org/petdb). OIB data are from GeoRoc (http://georoc.mpch-mainz.gwdg.de/). Whole rock Li and Dy data for lunar samples 10020, 15016, 15647 and 74235 are from Morrison et al. (1970); Cuttitta et al. (1973); Rose et al. (1975); Shih et al. (1975) and Neal (2001).

MORB data on Li and Dy are fairly consistent, falling into a small region between Li/Dy=1 and Li/Dy=1.3. On the other hand, Li data from OIB basalts are more scattered, resulting in high degrees of variation in Li/Dy ratios (Fig. 5.8b). Nonetheless, Li/Dy ratios for the OIB basalts mostly cluster with those for the MORB basalts near Li/Dy = 1.2, indicating that Li and Dy show similar degrees of incompatibility during partial melting and crystallization processes. Besides Li data from lunar melt inclusions and lunar glass beads, whole rock data for lunar samples studied in this work are also plotted in Fig. 5.8b as a comparison. For each individual sample, lunar MI Li/Dy ratios measured in this study agree with those of the whole rock data reported in the literature, indicating that Li is not lost during magma eruption processes. Variations occur, however, among Li/Dy ratios of different lunar samples. Highest Li/Dy ratios of 1.4 to 2.2 are found for green glass beads from 15426 (Hauri et al., 2015). Those for the orange glass beads and melt inclusions from 74220 are slightly lower (1.0 to 1.3). Even lower Li/Dy ratios are found for low-Ti basalt 15016 (0.3) and high-Ti basalt 74235 (0.2 to 0.6). The variations of Li/Dy in lunar

basalts are not correlated with Ti content. In addition, Li/Dy ratio varies by a factor of 3 in natural MIs and interstitial glasses from 74235, indicating that fractionation of Li/Dy ratios in lunar samples could be due to magma formation and crystal fractionation processes. Overall variation in currently available Li/Dy ratios across different lunar samples is from 0.2 to 2.1. Because of the large variations, and the fact that Li/Dy ratios can be fractionated by crystal fractionation, estimation based on Li/Dy ratios might have high uncertainties.

5.5.3 Estimation of volatile abundances (H_2O, F, Cl, S) in lunar mantle

As discussed above, H_2O/Ce ratios vary from 77 for 74220 to 9 for 10020, 3 for 74235 and ~1 for other samples with crystallized MIs. Since the occurrence of glassy MIs is likely related to the cooling history of the sample, the correlation between H_2O/Ce ratio and occurrence of glassy/partially glassy MIs indicate at least a partial role of post-eruptive H_2O loss on variations in H_2O/Ce ratios. If the variation in H_2O/Ce ratios is assumed to be entirely due to H_2O loss on the Moon, the highest H_2O/Ce ratio of 77 for 74220 will be more representative of lunar mantle. With a most recently estimated Ce concentration of 1.728 ppm by Hauri et al. (2015), the lunar mantle would contain ~130 ppm H_2O, similar to the conclusion of ~110 ppm in Chen et al. (2015). The small difference is because an average of all H_2O/Ce ratios in MIs from 74220 was adopted in Chen et al. (2015), while in this study the highest H_2O/Ce ratio is used because post-eruptive loss of H_2O was reported for 74220 natural MIs. On the other hand, if we assume no H_2O was lost on lunar surface during the formation of mare basalts, the variation in H_2O/Ce ratios across different samples would indicate heterogeneities in lunar mantle in terms of its H_2O content. With such assumption, lunar mantle sources for 10020, 74235 and other samples with crystallized MIs would contain 16 ppm, 5 ppm and <2 ppm H_2O, respectively. Since the above two assumptions are resulting in significantly different estimation of H_2O in lunar mantle, without further studies to verify the significance of above two factors (H_2O loss on lunar surface and lunar mantle heterogeneity) in causing the variations in H_2O/Ce ratios across different lunar samples, an

accurate estimation of H_2O content in lunar mantle based on lunar melt inclusions would be difficult.

F/Nd, Cl/K and S/Dy ratios, on the other hand, show much smaller degrees of variation. F/Nd ratios for lunar MIs from most samples range between 1 and 4. Considering that F could be lost during eruption on lunar surface, we adopt a F/Nd=4 on the higher end of data for these samples (12008 from Chen et al., 2015; 10020, 15016, 15647, 74220 and 74235 from this study). Using Nd concentration of 1.327 ppm in lunar mantle estimated by Hauri et al. (2015), F abundance in the source for these basalts can be estimated to be ~5 ppm. For sample 12040, however, F/Nd ratio is ~20 (the same as in BSE), corresponding to ~26 ppm F in the source mantle of 12040 if the source mantle has a BSE Nd concentration of 1.25 ppm. Compared to F abundance of 11 ppm in DMM (Salters and Stracke, 2004) and 25 ppm in BSE (McDonough and Sun, 1995), 26 ppm F in the mantle source of 12040 is the same as BSE, with no F depletion. 12040 is currently the only mare basalt sample with high F abundance similar to BSE. Since 12040 is thought to be formed by olivine accumulation and might be genetically related to other Apollo 12 basalts (e.g. 12018, 12004, 12021 and 12051; Walter et al., 1971), it is recommended that future studies examine F/Nd ratios for these samples either by melt inclusion study or by whole rock measurement to confirm the high F/Nd ratios measured for 12040 in this study, and to better understand the formation of Apollo 12 basalts.

Based on lunar MI data from this study and Chen et al. (2015) and lunar volcanic glass data from Hauri et al. (2015), we found that representative S/Dy ratios for the low-Ti basalts (12008, 12040, 15016 and 15647) and green glass beads (15426) are in the range between 118 to 179, while those for the high-Ti basalts (10020, 74220 and 74235) are between 78 and 95. Since S/Dy ratios can be lowered by either degassing loss of S or the segregation of sulfides, higher S/Dy in each group is adopted for estimation of S abundance in their source lunar mantle. Assuming the variations in S/Dy in their source mantles are due to variation in S abundances but share the same Dy abundance with BSE (0.67 ppm), S abundance in the sources of high-Ti basalt and low-Ti

basalt can be estimated to be 64 ppm and 120 ppm, respectively. The estimated S abundance of 64 ppm for source mantle of high-Ti basalt is about a factor of 2 lower than DMM (119 ppm, Salters and Stracke, 2004), but that for the low-Ti basalt is very similar to DMM (120 ppm compared to 119 ppm).

As shown in Fig. 5.6c, Cl/K ratios in lunar MIs are fairly consistent with an average of ~0.008. Potassium, however, is a moderately volatile element, which also needs to be determined in lunar mantle by compared with refractory elements, resulting in higher errors for estimation of Cl abundance based on Cl/K ratios. If we directly use the estimated K abundance from Hauri et al. (2015), which is 56.8 ppm, we get Cl abundance of 0.45 ppm in lunar mantle. On the other hand, K abundance in lunar mantle can be estimated to be 51 ppm based on K/La ratios in MIs from this study (~76, Fig. 5.8a) and a La abundance of 0.675 ppm (Hauri et al. 2015). Then Cl abundance in the primitive lunar mantle can be calculated accordingly to be 0.41 ppm, which is essentially the same as the previous approach (Chen et al. 2015). Our estimated Cl abundance is about twice the abundance of 0.142 to 0.205 ppm reported in Hauri et al. (2015), because the estimation done in Hauri et al. (2015) was based on Cl/Ba and Cl/Nd ratios for only two MIs from 74220, resulting in relatively large uncertainties. Our data do suggest total variations by a factor of 2 for Cl/Ba and Cl/Nd in MIs from 74220 (Table D1).

5.6 Conclusions

In this chapter we report volatile, major and trace element, and transition metal data in olivine-hosted melt inclusions from 5 mare basalt samples (10020, 12040, 15016, 15647 and 74235). Among these samples, partially glassy MIs were identified in 10020 and 74235, while MIs found in other samples are all highly crystallized with no glassy parts that are large enough for SIMS analyses. After excluding the effect of diffusive H_2O loss in lab for homogenized MIs, H_2O/Ce ratio is found to vary from 9 for 10020 to 3 for 74235, and ~1 for others. The significantly lower H_2O/Ce ratios compared to those of glassy MIs from 74220 (as high as 77)

can be explained by two possibilities: a) loss of H_2O on lunar surface during magma eruption and cooling, and b) lunar mantle heterogeneity in terms of H_2O abundance. Since lunar samples with glassy MIs likely experienced shorter time scale of cooling compared to samples with only crystalline MIs, H_2O loss from lunar MIs on the surface of Moon likely contributed at least partly to the variation in H_2O/Ce ratios in MIs from different samples. In extreme cases, if the variation is assumed to be entirely due to H_2O loss on lunar surface, H_2O concentration in lunar mantle would be ~130 ppm, similar to previous estimation. On the other hand, if lunar mantle heterogeneity is assumed to be the only cause of H_2O/Ce variation, H_2O/Ce ratios would indicate 16 ppm, 5 ppm and < 2ppm H_2O for the mantle sources of 10020, 74235 and other samples with crystallized MIs, respectively.

Based on F/Nd, Cl/K and S/Dy ratios, concentrations of F, Cl and S in lunar mantle for most samples studied are estimated to be 5 ppm, 0.4 ppm and 65-120 ppm, respectively. Abundances of F, Cl and S estimated for lunar sample are comparable to those of the depleted mantle, which contains 11 ppm F, 0.51 ppm Cl and 119 ppm S. In addition, evidences are found in melt inclusions that might suggest lunar mantle heterogeneities in terms of its volatile abundances. In low-Ti basalt 12040, F/Nd ratio is found to be ~20, which corresponds to 26 ppm F in its mantle source and essentially the same as the BSE abundance. Ratios of S/Dy are also found to be different between low-Ti and high-Ti mare basalts studied so far, with representative S/Dy ratios in the range between 118 and 179 for low-Ti basalts, and between 78 and 95 for high-Ti basalts, suggesting 67 ppm and 126 ppm S in their mantle sources, respectively.

To conclude, our new MI data after removing the effect of H_2O loss in the lab still shows large variations in H_2O/Ce ratios across different lunar samples, which need to be explained by either H_2O loss on lunar surface during magma processes, or lunar mantle heterogeneity. Other volatiles show less variation in similar ratios (F/Nd, S/Dy and Cl/K). Based on relative contributions from the above two factors, estimation of H_2O in lunar mantle could shift quite significantly from ~130 ppm to a more complicated case of heterogeneous H_2O abundance

ranging from >100 ppm to ~10 ppm and even lower. Therefore, the priority of future studies is to hopefully constrain the role of H_2O loss on lunar surface in affecting H_2O/Ce variations across MIs from different lunar samples. High F/Nd ratios found in 12040 and S/Dy ratios in low-Ti mare basalts indicate that part of lunar mantle might contain F and S concentrations even higher than previous estimation. With more data available in the future, we might be able to correlate such variations with variations other geochemical signatures (e.g. moderately volatile element isotopes) to better understand their formation in lunar mantle.

5.7 Acknowledgments

We thank NASA CAPTEM for providing the lunar samples, and K. P. Jochum for providing the MPI-DING glass standards. This research is supported by NASA grant NNX15AH37G.

5.8 References

Albarede F., Albalat E. and Lee C.-T. A. (2015) An intrinsic volatility scale relevant to the Earth and Moon and the status of water in the Moon. *Meteorit. Planet. Sci.* **50**, 568–577.

Bombardieri D. J., Norman M. D., Kamenetsky V. S. and Danyushevsky L. V. (2005) Major element and primary sulfur concentrations in Apollo 12 mare basalts: The view from melt inclusions. *Meteorit. Planet. Sci.* **40**, 679–693.

Chen Y., Provost A., Schiano P. and Cluzel N. (2013) Magma ascent rate and initial water concentration inferred from diffusive water loss from olivine-hosted melt inclusions. *Contrib. Mineral. Petrol.* **165**, 525–541.

Chen Y., Zhang Y., Liu Y., Guan Y., Eiler J. and Stolper E. M. (2015) Water, fluorine, and sulfur concentrations in the lunar mantle. *Earth Planet. Sci. Lett.* **427**, 37–46.

Cottrell E., Spiegelman M. and Langmuir C. H. (2002) Consequences of diffusive reequilibration for the interpretation of melt inclusions. *Geochem. Geophys. Geosystems* **3**, 1–26.

Cuttitta F., Rose H. J. Jr., Annell C. S., Carron M. K., Christian R. P., Ligon D. T. Jr., Dwornik E. J., Wright T. L. and Greenland L. P. (1973) Chemistry of twenty-one igneous rocks and soils returned by the Apollo 15 mission. In Lunar and Planetary Science Conference Proceedings. p. 1081. Available at: http://adsabs.harvard.edu/abs/1973LPSC....4.1081C [Accessed April 2, 2017].

Danyushevsky L. V., Della-Pasqua F. N. and Sokolov S. (2000) Re-equilibration of melt inclusions trapped by magnesian olivine phenocrysts from subduction-related magmas: petrological implications. *Contrib. Mineral. Petrol.* **138**, 68–83.

Dixon J. E. and Clague D. A. (2001) Volatiles in Basaltic Glasses from Loihi Seamount, Hawaii: Evidence for a Relatively Dry Plume Component. *J. Petrol.* **42**, 627–654.

Dixon J. E., Leist L., Langmuir C. and Schilling J.-G. (2002) Recycled dehydrated lithosphere observed in plume-influenced mid-ocean-ridge basalt. *Nature* **420**, 385–389.

Drake M. J., Newsom H. E. and Capobianco C. J. (1989) V, Cr, and Mn in the Earth, Moon, EPB, and SPB and the origin of the Moon: Experimental studies. *Geochim. Cosmochim. Acta* **53**, 2101–2111.

Dreibus G. and Wanke H. (1979) On the Chemical Composition of the Moon and the Eucrite Parent Body and a Comparison with the Composition of the Earth; the Case of mn, cr, and V. In Lunar and Planetary Science Conference. pp. 315–317. Available at: http://adsabs.harvard.edu/abs/1979LPI....10..315D [Accessed March 28, 2017].

Gao S., Liu X., Yuan H., Hattendorf B., Gunther D., Chen L. and Hu S. (2002) Determination of Forty Two Major and Trace Elements in USGS and NIST SRM Glasses by Laser Ablation-Inductively Coupled Plasma-Mass Spectrometry. *Geostand. Newsl.* **26**, 181–196.

Gessmann C. K. and Rubie D. C. (2000) The origin of the depletions of V, Cr and Mn in the mantles of the Earth and Moon. *Earth Planet. Sci. Lett.* **184**, 95–107.

Hauri E. H., Saal A. E., Rutherford M. J. and Van Orman J. A. (2015) Water in the Moon's interior: Truth and consequences. *Earth Planet. Sci. Lett.* **409**, 252–264.

Hauri E. H., Weinreich T., Saal A. E., Rutherford M. C. and Orman J. A. V. (2011) High Pre-Eruptive Water Contents Preserved in Lunar Melt Inclusions. *Science* **333**, 213–215.

Hui H., Peslier A. H., Zhang Y. and Neal C. R. (2013) Water in lunar anorthosites and evidence for a wet early Moon. *Nat. Geosci.* **6**, 177–180.

Jochum K. P., Stoll B., Herwig K., Willbold M., Hofmann A. W., Amini M., Aarburg S., Abouchami W., Hellebrand E., Mocek B., Raczek I., Stracke A., Alard O., Bouman C., Becker S., Dücking M., Brätz H., Klemd R., de Bruin D., Canil D., Cornell D., de Hoog C.-J., Dalpé C., Danyushevsky L., Eisenhauer A., Gao Y., Snow J. E., Groschopf N., Günther D., Latkoczy C., Guillong M., Hauri E. H., Höfer H. E., Lahaye Y., Horz K., Jacob D. E., Kasemann S. A., Kent A. J. R., Ludwig T., Zack T., Mason P. R. D., Meixner A., Rosner M., Misawa K., Nash B. P., Pfänder J., Premo W. R., Sun W. D., Tiepolo M., Vannucci R., Vennemann T., Wayne D. and Woodhead J. D. (2006) MPI-DING reference glasses for in situ microanalysis: New reference values for element concentrations and isotope ratios. *Geochem. Geophys. Geosystems* **7**, Q02008.

Koleszar A. M., Saal A. E., Hauri E. H., Nagle A. N., Liang Y. and Kurz M. D. (2009) The volatile contents of the Galapagos plume; evidence for H2O and F open system behavior in melt inclusions. Earth Planet. Sci. Lett. 287, 442–452.

Kushiro, I. (1972) Petrology of some Apollo 15 mare basalts. In *The Apollo 15 Lunar Samples*, 128-130.

Kushiro, I. and Haramura, H. (1971) Major element variation and possible source materials of Apollo 12 crystalline rocks. Science 171, 1235-1237.

Lodders K. (2003) Solar System Abundances and Condensation Temperatures of the Elements. *Astrophys. J.* **591**, 1220.

McDonough W. F. and Sun S. -s. (1995) The composition of the Earth. *Chem. Geol.* **120**, 223–253.

Michael P. (1995) Regionally distinctive sources of depleted MORB: Evidence from trace elements and H2O. *Earth Planet. Sci. Lett.* **131**, 301–320.

Michael P. J. (1988) The concentration, behavior and storage of H2O in the suboceanic upper mantle: Implications for mantle metasomatism. *Geochim. Cosmochim. Acta* **52**, 555–566.

Mills R. D., Simon J. I., Alexander C., Wang J. and Hauri E. H. (2017) Water in alkali feldspar: The effect of rhyolite generation on the lunar hydrogen budget. Available at: http://www.geochemicalperspectivesletters.org/documents/GPL1712_SI.pdf [Accessed February 17, 2017].

Morrison G. H., Gerard J. T., Kashuba A. T., Gangadharam E. V., Rothenberg A. M., Potter N. M. and Miller G. B. (1970) Elemental abundances of lunar soil and rocks. *Geochim. Cosmochim. Acta Suppl.* **1**, 1383.

Neal C. R. (2001) Interior of the Moon: The presence of garnet in the primitive deep lunar mantle. *J. Geophys. Res. Planets* **106**, 27865–27885.

Newsom H. E. (1986) Constraints on the origin of the Moon from the abundance of molybdenum and other siderophile elements. In Origin of the Moon. p. 203. Available at: http://adsabs.harvard.edu/abs/1986ormo.conf..203N [Accessed February 8, 2017].

Ni P. and Zhang Y. (2016) Cu diffusion in a basaltic melt. *Am. Mineral.* **101**, 1474–1482.

Ni P., Zhang Y. and Guan Y. (2016) Melt Inclusion Study on Water and Other Volatiles in the Lunar Mantle. In American Geophysical Union Fall Meeting. San Francisco, Calif. Available at: https://agu.confex.com/agu/fm16/meetingapp.cgi/Paper/191809.

O'Neill H. S. C. (1991) The origin of the moon and the early history of the earth—A chemical model. Part 1: The moon. *Geochim. Cosmochim. Acta* **55**, 1135–1157.

Pearce N. J. G., Perkins W. T., Westgate J. A., Gorton M. P., Jackson S. E., Neal C. R. and Chenery S. P. (1997) A Compilation of New and Published Major and Trace Element Data for NIST SRM 610 and NIST SRM 612 Glass Reference Materials. *Geostand. Newsl.* **21**, 115–144.

Plank T., Cooper L. B. and Manning C. E. (2009) Emerging geothermometers for estimating slab surface temperatures. *Nat. Geosci.* **2**, 611–615.

Qin Z., Lu F. and Anderson A. T. (1992) Diffuse reequilibration of melt and fluid inclusions. *Am. Mineral.* **77**, 565–576.

Rhodes J. M. and Blanchard D. P. (1980) Chemistry of Apollo 11 low-K mare basalts. In Lunar and Planetary Science Conference Proceedings. pp. 49–66. Available at: http://adsabs.harvard.edu/abs/1980LPSC...11...49R [Accessed March 24, 2017].

Rhodes J. M., Wiesmann H., Rodgers K. V., Brannon J. C., Bansal B. M. and Hubbard N. J. (1976) Chemistry, classification, and petrogenesis of Apollo 17 mare basalts. In Lunar and Planetary Science Conference Proceedings. pp. 1467–1489. Available at: http://adsabs.harvard.edu/abs/1976LPSC....7.1467R [Accessed March 24, 2017].

Ringwood A. E. (1986) Terrestrial origin of the Moon. *Nature* **322**, 323–328.

Rose H. J. Jr., Baedecker P. A., Berman S., Christian R. P., Dwornik E. J., Finkelman R. B. and Schnepfe M. M. (1975) Chemical composition of rocks and soils returned by the Apollo 15, 16, and 17 missions. In Lunar and Planetary Science Conference Proceedings. pp. 1363–1373. Available at: http://adsabs.harvard.edu/abs/1975LPSC....6.1363R [Accessed April 1, 2017].

Ruzicka A., Snyder G. A. and Taylor L. A. (2001) Comparative geochemistry of basalts from the moon, earth, HED asteroid, and Mars: implications for the origin of the moon. *Geochim. Cosmochim. Acta* **65**, 979–997.

Ruzicka A., Snyder G. A. and Taylor L. A. (1998) Giant Impact and Fission Hypotheses for the Origin of the Moon: A Critical Review of Some Geochemical Evidence. *Int. Geol. Rev.* **40**, 851–864.

Ryder, G. and Schuraytz, B. C. (2001) Chemical variation of the large Apollo 15 olivine-normative mare basalt rock samples. *Journal of Geophysical Research: Planets* **106**, 1435-1451.

Saal A. E., Hauri E. H., Cascio M. L., Van Orman J. A., Rutherford M. C. and Cooper R. F. (2008) Volatile content of lunar volcanic glasses and the presence of water in the Moon's interior. *Nature* **454**, 192–195.

Saal A. E., Hauri E. H., Langmuir C. H. and Perfit M. R. (2002) Vapour undersaturation in primitive mid-ocean-ridge basalt and the volatile content of Earth's upper mantle. *Nature* **419**, 451–455.

Saal A. E., Hauri E. H., Orman J. A. V. and Rutherford M. J. (2013) Hydrogen Isotopes in Lunar Volcanic Glasses and Melt Inclusions Reveal a Carbonaceous Chondrite Heritage. *Science* **340**, 1317–1320.

Salters V. J. M. and Stracke A. (2004) Composition of the depleted mantle. *Geochem. Geophys. Geosystems* **5**, Q05B07.

Shih C.-Y., Wiesmann H., Bansal B. M., Brannon J. C. and Haskin L. A. (1975) On the origin of high-Ti mare basalts. In Lunar and Planetary Science Conference Proceedings. pp. 1255–1285. Available at: http://adsabs.harvard.edu/abs/1975LPSC....6.1255S [Accessed April 1, 2017].

Sun S.-S., Nesbitt R. W. and Sharaskin A. Y. (1979) Geochemical characteristics of mid-ocean ridge basalts. *Earth Planet. Sci. Lett.* **44**, 119–138.

Taylor S. R., Pieters C. M. and MacPherson G. J. (2006) Earth-Moon System, Planetary Science, and Lessons Learned. *Rev. Mineral. Geochem.* **60**, 657–704.

Walker D., Hays J. F., Longhi J. and Kirkpatrick R. J. (1976) Differentiation of an Apollo 12 picrite magma. In Lunar and Planetary Science Conference Proceedings. pp. 1365–1389. Available at: http://adsabs.harvard.edu/abs/1976LPSC....7.1365W [Accessed March 24, 2017].

Walter L. S., French B. M., Heinrich K. J. F., Lowman P. D. Jr., Doan A. S. and Adler I. (1971) Mineralogical studies of Apollo 12 samples. In Lunar and Planetary Science Conference Proceedings. p. 343. Available at: http://adsabs.harvard.edu/abs/1971LPSC....2..343W [Accessed March 24, 2017].

Xirouchakis D., Hirschmann M. M. and Simpson J. A. (2001) The effect of titanium on the silica content and on mineral-liquid partitioning of mantle-equilibrated melts. *Geochim. Cosmochim. Acta* **65**, 2201–2217.

Zinner E. and Crozaz G. (1986) A method for the quantitative measurement of rare earth elements in the ion microprobe. *Int. J. Mass Spectrom. Ion Process.* **69**, 17–38.

CHAPTER VI

Conclusions

6.1 Summary of results

In Chapters II and III, Cu diffusivities in natural silicate melts are experimentally studied. In Chapter II, Cu diffusivities in anhydrous basaltic melt are determined by diffusion couple experiments at temperatures between 1298 and 1581 ºC, and pressures of 0.5 GPa, 1 GPa and 1.5 GPa. All Cu diffusion data in anhydrous basaltic melt considering the pressure effect can be described as:

$$D_{\mathrm{Cu}}^{\mathrm{basalt}} = \exp\left[-(13.59 \pm 0.81) - \frac{(12153 \pm 1229) + (620 \pm 241)P}{T}\right],$$

where $D_{\mathrm{Cu}}^{\mathrm{basalt}}$ is the diffusivity in m^2/s, T is the temperature in K, P is the pressure in GPa and errors are given at 1σ level. In Chapter III, Cu diffusivities in anhydrous and hydrous rhyolitic melts are determined by chalcocite (Cu_2S) "dissolution" experiments. Experiments were done in the temperature range between 750 to 1391 ºC at pressures of 0.5 and 1.0 GPa. Starting rhyolitic glasses with 0.10 to 5.95 wt% H_2O were used to assess the effect of H_2O on Cu diffusivity. All Cu diffusion data from Chapter III in rhyolitic melts can be described as:

$$D_{\mathrm{Cu}}^{\mathrm{Rhy}} = \exp\left[-(14.75 \pm 0.35) - (0.23 \pm 0.10)w - \frac{(11647 \pm 491) - (698 \pm 117)w}{T}\right],$$

where w is H_2O concentration in the rhyolitic melt in wt%. Combining Cu diffusion data from Chapters II and III, a general equation for Cu diffusion in natural silicate melts:

$$D_{\mathrm{Cu}} = \exp\left[-(17.3 \pm 0.9) + (3.8 \pm 1.5)(\mathrm{Si+Al\text{-}H}) - \frac{(4403 \pm 1094) + (9700 \pm 1921)(\mathrm{Si+Al\text{-}H})}{T}\right],$$

where Si+Al-H is the cation mole fraction of Si plus Al minus H in the silicate melt on a wet basis.

In general, our results show that Cu diffusivity is high, similar to that of Na in silicate melts, with a low activation energy of ~100 kJ/mol. In hydrous rhyolitic melts with 6wt% H2O, Cu diffusivity is found to be even faster than H_2O. The high diffusivity and low activation energy is in accordance with the expectation that Cu is diffusing as Cu^+ in silicate melts. Due to the high diffusivity of Cu, there is no kinetic barrier for Cu to be enriched in sulfides during magmatic sulfide deposition, or in magmatic fluids during porphyry-type ore formation. Hence, it is easier for Cu to be enriched into ore deposits compared to other metals. Moreover, the high diffusivity of Cu ensures equilibrium between silicate phase and the sulfide/fluid phase, which means Cu concentration in the sulfide/fluid phase during formation of magmatic sulfide deposits or porphyry-type Cu deposits can be simply estimated assuming equilibrium partitioning. In addition, applying our data in isotope fractionation of Cu in tektites supports previous work in explaining that, the more fractionated Cu isotopes in tektites compared to Zn isotopes is due to the high diffusivity of Cu.

In Chapter IV, loss of H_2O, F, Cl and S from lunar melt inclusions during homogenization is experimentally studied. Our results suggest that H_2O could be lost in <10 min during homogenization experiments. Whereas F, Cl and S are not significantly affected even in small inclusions with a radius of ~5μm. The trend in H_2O loss from homogenized melt inclusions is fit by a diffusive equilibrium model and compared to previous experimental results using terrestrial samples. Surprisingly, no significant effect of low oxygen fugacity on Moon is observed in affecting loss of H_2O from lunar melt inclusions during homogenization, indicating that diffusive H loss through olivine might be insensitive to low oxygen fugacity on Moon. Our results are used to estimate degrees of H_2O loss under a wide range of homogenization conditions as a reference for future homogenization experiments. In addition, a similar trend for degassing loss of H_2O is observed in natural melt inclusions from 74220. By comparing the trend in natural

inclusions and our homogenized melt inclusions, cooling rate for 74220 is estimated to be ~1ºC/s or slower.

In Chapter V, major elements, volatiles, trace element and transition metal data in olivine-hosted melt inclusions and interstitial glasses from 5 lunar mare samples (10020, 12040, 15647 and 74235) are reported. Ratios of H_2O/Ce are found to vary among different mare samples (9 for 10020; 3 for 74235 and ~1 for others) but all lower than H_2O/Ce=77 for 74220. Since the variation in H_2O/Ce ratios are correlated with the occurrence of glassy or partially glassy MIs in different lunar samples, at least part of the variation is due to degassing loss of H_2O from the inclusions on lunar surface. Heterogeneous distribution of H_2O in lunar mantle is also a possibility causing H_2O/Ce variations in lunar samples. Concentrations of F, Cl and S are estimated based on F/Nd, Cl/K and S/Dy ratios in the melt inclusions to be 5 ppm, 0.4 ppm and 67-126 ppm, respectively. The estimated abundances for F, Cl and S are similar to or slightly lower than those in terrestrial depleted mantle, and comparable to previous studies. In addition, evidences are found that might suggest lunar mantle heterogeneity in volatile abundances. In low-Ti basalt 12040, F/Nd ratios are found to be ~20, a factor of 5 higher than for other lunar samples. In addition, S/Dy ratios in low-Ti basalts (118 to 179) are found to be higher than in high-Ti basalts (78 to 95) by almost a factor of 2. The relatively high S/Dy ratios in low-Ti basalts correspond to 126 ppm S in their source mantle, which is similar to in the depleted mantle. These newly discovered heterogeneities in F and S abundance bring previous estimations of volatile abundances in Moon even closer to the terrestrial values, indicating that part of the lunar mantle might contain similar volatile abundances as the depleted mantle.

6.2 Perspectives and future research

6.2.1 High diffusivity of Cu and its isotope fractionation

Isotope fractionation during chemical diffusion is one type of kinetic isotope fractionation, as the lighter isotopes of an element diffuses faster than its heavier isotopes.

Lithium is likely the element that shows highest degrees of isotope fractionation caused by diffusion in silicate melts, due to its high diffusivity and large relative mass difference between ^{6}Li and ^{7}Li (14.3%). Experiments by Richter et al. (2003) showed high degrees of Li isotope fractionation by about 40‰ during Li diffusion into rhyolite melts. Although the mass difference between the two stable isotopes of Cu is small (3.1%) compared to Li, the high diffusivity of Cu^{+} suggests that Cu might be diffusing in silicate melts by itself or in the form of a small complex, making it possible for significant Cu isotope fractionation during diffusion.

During formation of magmatic sulfide deposits and porphyry-type deposits, if the enrichment of Cu in sulfides or fluids is kinetically controlled, there could be Cu isotope fractionation in the resulting sulfide ore or porphyry ore deposit. However, Cu isotope measurements show that, Cu isotopes for primary mineralization in porphyry-type deposits fall between a tight range between -1 to 1‰ (Mathur et al. 2009), roughly consistent with the average Cu isotope composition of the BSE (δ^{65}Cu=0.07±0.10‰, Moynier et al. 2017). The limited variation in Cu isotopes from porphyry-type deposits indicate that, the enrichment of Cu during formation of porphyry-type deposits is unlikely controlled by kinetic processes. This conclusion agrees with our previous conclusions based on Cu diffusivities.

6.2.2 Application of Cu diffusion data in lunar studies

As a moderately volatile element, Cu could be degassed at high temperatures, resulting in both compositional depletion and isotope fractionation. For example, Cu isotopes are highly fractionated in tektites and correlated with Cu loss, as discussed in Chapters II and III. On the surface of planetary bodies without an atmosphere (e.g. Moon), impact processes are more common, and our Cu diffusion data can be used to better understand the behavior of Cu and its isotopes during such processes. According to our preliminary data, Cu is volatile on lunar surface even at magmatic temperatures. Hence, Cu degassing profiles could occur in lunar volcanic glass beads and olivine-hosted embayments. Future studies could be done to analyze these Cu

degassing profiles, and our Cu diffusion data would be useful in modeling the profiles to interpret the eruption nature for these glass beads and olivine-hosted embayments, and in understanding isotope fractionation for Cu during degassing.

6.2.3 Volatile abundances in Moon

The most important contribution to lunar melt inclusion studies in this thesis is to settle down the issue of diffusive H_2O loss. Previously, it was unclear whether the low H_2O/Ce ratios for homogenized lunar melt inclusions are due to H_2O in lab during homogenization. Work in Chapter IV of this thesis clarified this concern and confirmed that the low H_2O/Ce ratios for homogenized lunar melt inclusions are real, not because of loss during homogenization. Prior to this thesis work, naturally glassy or partially glassy melt inclusions were only identified in 74220 (with one from 10020, Chen et al. 2015). Another important contribution of this thesis is that more partially glassy melt inclusions from lunar samples 10020 and 74235 are identified and analyzed. Concentrations of H_2O in naturally glassy and partially glassy lunar melt inclusions are systematically higher than those in the crystalline ones, indicating that crystalline melt inclusions might have suffered H_2O loss during slow cooling on the lunar surface. Future studies are recommended to focus on natural partially glassy melt inclusions, as these inclusions are likely formed during more rapid cooling, and have higher chances to preserve pre-degassing H_2O concentrations.

The discovery of variations in H_2O/Ce, F/Nd and S/Dy ratios in different lunar samples brings uncertainties to the formation of lunar mantle, and questions the occurrence of a "primitive" lunar mantle. Both the terrestrial mantle and the lunar mantle are known to be heterogeneous. For example, composition of the terrestrial depleted mantle (DMM, Salters and Stracke 2004) is significantly different from the bulk silicate earth (BSE, McDonough and Sun 1995) due to billions of years' partial melting and melt extraction from the upper mantle. Ratios of H_2O/Ce, F/Nd and S/Dy, however, are roughly consistent among different terrestrial reservoirs,

because they are not significantly affected by magma processes. Therefore, the variations in theses ratios among different lunar samples indicate that, either they are affected by secondary processes, or they are intrinsic heterogeneities in the lunar mantle since Moon formation. Further studies are necessary to confirm such variations in H_2O/Ce, F/Nd and S/Dy ratios. One intuitive way, as mentioned in Chapter V, is to examine more Apollo 12 samples that might be genetically related to sample 12040, and confirm the high F/Nd ratios we measured in this sample.

Since about a decade ago when tens of ppm H_2O was reported in lunar glass beads, effort has been made to reconcile the presence of highly volatile elements in the lunar mantle with the giant impact model. Several possible explanations have been proposed based on the assumption that the giant impact model is correct (e.g. Saal et al. 2008, 2013; Hauri et al. 2011, 2015; Robinson and Taylor 2014): (a) a high-temperature convective atmosphere envelope was present at the time when Moon solidified, and aided the exchange of highly volatile elements between Earth and Moon; (b) part of the lunar interior survived the aftermath of the giant impact and preserved its initial volatile abundances; (c) H_2O and other volatiles were added to Moon after the giant impact by a flux of carbonaceous condrites. Our discovery of heterogeneities in F/Nd ratios is in favor of explanations (b) and (c). Nevertheless, evidences are still too limited to conclude which one of the above explanations is correct. Future studies need to first pin down the role of degassing on decreasing H_2O/Ce ratios in lunar melt inclusions. From there, variations in H_2O/Ce, F/Nd and S/Dy ratios among different lunar samples need to be correlated with each other, and with variations in isotope signatures (e.g. Sr and Nd isotopes, isotopes of moderately volatile elements) to gain insights on how these heterogeneities were generated during formation of Moon.

6.3 References

Chen, Y., Zhang, Y., Liu, Y., Guan, Y., Eiler, J., and Stolper, E.M. (2015) Water, fluorine, and sulfur concentrations in the lunar mantle. Earth and Planetary Science Letters, 427, 37–46.

Hauri, E.H., Weinreich, T., Saal, A.E., Rutherford, M.C., and Orman, J.A.V. (2011) High Pre-Eruptive Water Contents Preserved in Lunar Melt Inclusions. Science, 333, 213–215.

Hauri, E.H., Saal, A.E., Rutherford, M.J., and Van Orman, J.A. (2015) Water in the Moon's interior: Truth and consequences. Earth and Planetary Science Letters, 409, 252–264.

Mathur, R., Titley, S., Barra, F., Brantley, S., Wilson, M., Phillips, A., Munizaga, F., Maksaev, V., Vervoort, J., and Hart, G. (2009) Exploration potential of Cu isotope fractionation in porphyry copper deposits. Journal of Geochemical Exploration, 102, 1–6.

McDonough, W.F., and Sun, S. -s. (1995) The composition of the Earth. Chemical Geology, 120, 223–253.

Moynier, F., Vance, D., Fujii, T., and Savage, P. (2017) The Isotope Geochemistry of Zinc and Copper. Reviews in Mineralogy and Geochemistry, 82, 543–600.

Richter, F.M., Davis, A.M., DePaolo, D.J., and Watson, E.B. (2003) Isotope fractionation by chemical diffusion between molten basalt and rhyolite. Geochimica et Cosmochimica Acta, 67, 3905–3923.

Robinson, K.L., and Taylor, G.J. (2014) Heterogeneous distribution of water in the Moon. Nature Geoscience, 7, 401–408.

Saal, A.E., Hauri, E.H., Cascio, M.L., Van Orman, J.A., Rutherford, M.C., and Cooper, R.F. (2008) Volatile content of lunar volcanic glasses and the presence of water in the Moon's interior. Nature, 454, 192–195.

Saal, A.E., Hauri, E.H., Orman, J.A.V., and Rutherford, M.J. (2013) Hydrogen Isotopes in Lunar Volcanic Glasses and Melt Inclusions Reveal a Carbonaceous Chondrite Heritage. Science, 340, 1317–1320.

Salters, V.J.M., and Stracke, A. (2004) Composition of the depleted mantle. Geochemistry, Geophysics, Geosystems, 5, Q05B07.

Appendix A

Copper diffusion profiles for Chapter II

Cudiffcp 1.1

x (μm)	Cu (wt%)	*x* (μm)	Cu (wt%)	*x* (μm)	Cu (wt%)	*x* (μm)	Cu (wt%)
32	0.0594	-148	0.0728	1006	0.0192	812	0.0203
62	0.0632	-208	0.0723	1116	0.0176	937	0.0149
92	0.0568	-268	0.082	1216	0.0125	1062	0.0151
122	0.06	-328	0.0802	1316	0.0148	1162	0.0175
152	0.0582	-388	0.0849	1416	0.0179	1262	0.0201
212	0.055	-494.7	0.0909	-23	0.0632	1362	0.0159
272	0.0505	-601.3	0.0917	-143	0.0739	1462	0.014
332	0.0424	-708	0.0953	-263	0.0819	-43	0.0695
392	0.0398	-814.7	0.1093	-383	0.0916	-73	0.0646
498.7	0.0322	-921.3	0.1085	-503	0.0962	-180.8	0.0705
605.3	0.0245	-1028	0.1124	-623	0.0952	-288.6	0.0831
712	0.0241	-1128	0.1106	-743	0.1053	-396.3	0.0816
818.7	0.0251	-1253	0.1041	-863	0.1079	-504.1	0.0918
925.3	0.0179	-1378	0.1036	-983	0.1073	-611.9	0.0951
1032	0.0175	16	0.0632	-1103	0.1113	-719.7	0.1001
1122	0.0198	126	0.0561	-1223	0.1167	-827.5	0.0969
1222	0.0132	236	0.0509	-1343	0.1106	-935.2	0.104
1322	0.0199	346	0.0348	62	0.0589	-1043	0.1056
1422	0.015	456	0.0359	187	0.055	-1143	0.1062
-28	0.0646	566	0.0346	312	0.0452	-1243	0.1053
-58	0.0671	676	0.0234	437	0.0428	-1343	0.1079
-88	0.0714	786	0.0254	562	0.0311		
-118	0.0665	896	0.0195	687	0.0255		

Cudiffcp 1.2

x (µm)	Cu (wt%)	*x* (µm)	Cu (wt%)	*x* (µm)	Cu (wt%)	*x* (µm)	Cu (wt%)
18.56	0.0649	1478.42	0.0173	-1286.32	0.1349	-605.27	0.1206
28.56	0.0674	-1.44	0.065	-1411.31	0.1309	-805.25	0.1285
38.55	0.0677	-11.44	0.0686	14.67	0.0751	-1005.24	0.126
48.55	0.0643	-21.44	0.0713	64.67	0.0605	-1165.22	0.1378
58.55	0.0695	-31.44	0.0738	114.66	0.0569	-1290.21	0.1288
78.55	0.0617	-41.44	0.0736	164.66	0.0512	-1415.20	0.1304
98.55	0.057	-61.44	0.077	314.64	0.0366	20.60	0.07
118.55	0.0566	-81.43	0.0771	464.63	0.031	170.59	0.0536
138.55	0.0582	-101.43	0.0877	614.62	0.0247	320.58	0.0352
188.54	0.0451	-121.43	0.0853	814.60	0.0158	670.55	0.019
238.54	0.041	-171.43	0.089	1014.58	0.0195	1020.51	0.02
288.53	0.0354	-221.42	0.0946	1214.56	0.0188	1217.50	0.021
338.53	0.0354	-271.42	0.1023	1364.55	0.0202	1517.47	0.0235
438.52	0.0306	-321.41	0.1039	1514.54	0.0239	-0.61	0.0629
538.51	0.0214	-421.40	0.1165	-5.33	0.0672	-149.38	0.0858
698.50	0.0165	-521.39	0.1122	-55.32	0.0765	-299.37	0.1042
858.48	0.0175	-681.38	0.1284	-105.32	0.0829	-649.34	0.1274
1018.47	0.0158	-841.37	0.1291	-155.31	0.0893	-999.30	0.133
1178.45	0.0137	-1001.35	0.1337	-305.30	0.1062	-1199.29	0.1308
1328.44	0.0138	-1161.34	0.1337	-455.29	0.1136	-1449.26	0.1325

Cudiffcp 2.1

x (μm)	Cu (wt%)	*x* (μm)	Cu (wt%)	*x* (μm)	Cu (wt%)	*x* (μm)	Cu (wt%)
22	0.0742	1472	0.0118	-1402	0.1299	27	0.0699
37	0.069	-52	0.0775	17	0.0777	127	0.0635
52	0.0673	-67	0.0757	167	0.0623	227	0.0552
67	0.0653	-82	0.0839	317	0.0466	427	0.0401
102	0.067	-97	0.0831	667	0.0295	627	0.0329
137	0.0605	-132	0.0878	1017	0.0161	1027	0.0157
172	0.0556	-167	0.0869	1217	0.0167	1427	0.0196
247	0.0504	-202	0.0948	1467	0.0184	-56	0.0828
322	0.0411	-277	0.1018	-46	0.0855	-156	0.0947
397	0.0358	-352	0.1069	-146	0.0907	-256	0.0999
553.3	0.0311	-427	0.1141	-246	0.0979	-456	0.1139
709.5	0.0239	-583.3	0.1225	-496	0.1166	-656	0.1209
865.8	0.0197	-739.5	0.1274	-746	0.1324	-1031	0.1337
1022	0.0165	-895.8	0.1292	-1086	0.1282	-1406	0.1298
1172	0.0177	-1052	0.1282	-1426	0.1336		
1322	0.0116	-1202	0.1313	27	0.0699		

Cudiffcp 3.1 – analysis 1

x (µm)	Cu (wt%)	*x* (µm)	Cu (wt%)	*x* (µm)	Cu (wt%)	*x* (µm)	Cu (wt%)
1.7	0.0612	1001.5	0.0223	-456.5	0.0969	373.6	0.0425
26.7	0.066	1101.5	0.0188	-569.9	0.1052	693.6	0.0251
51.7	0.0629	1234.8	0.0202	-683.1	0.1049	1013.5	0.0171
76.7	0.0603	1368.2	0.0234	-796.4	0.1011	1333.4	0.0152
101.7	0.0608	1501.4	0.0192	-909.8	0.1089	1533.4	0.0168
156.7	0.062	-23.3	0.0727	-1023.1	0.1115	-11.3	0.067
211.7	0.0522	-48.3	0.072	-1123.1	0.1155	-71.3	0.0659
266.7	0.0523	-73.3	0.0706	-1256.3	0.1151	-131.3	0.0821
321.7	0.0463	-98.2	0.077	-1389.7	0.1153	-251.3	0.0863
435.0	0.0377	-123.2	0.0764	-1523.0	0.1127	-371.2	0.0955
548.3	0.0377	-178.2	0.0822	13.7	0.0624	-717.9	0.1082
661.6	0.0282	-233.2	0.0878	73.7	0.0628	-1064.4	0.1103
774.9	0.0247	-288.2	0.0898	133.7	0.0563	-1411.0	0.1138
888.3	0.0186	-343.2	0.0953	253.6	0.0512		

Cudiffcp 3.1 – analysis 2

x (µm)	Cu (wt%)	*x* (µm)	Cu (wt%)	*x* (µm)	Cu (wt%)	*x* (µm)	Cu (wt%)
4.8	0.0839	-215.2	0.0988	856.0	0.0456	202.0	0.0689
44.8	0.0778	-295.2	0.1045	1180.9	0.0403	297.0	0.0709
84.8	0.0766	-375.2	0.1073	1505.9	0.0414	392.0	0.0611
124.8	0.0714	-538.1	0.1168	-14.0	0.0897	592.0	0.0517
204.8	0.0667	-700.9	0.1192	-64.0	0.0928	792.0	0.0458
284.7	0.0588	-863.8	0.1266	-114.0	0.0999	1152.0	0.0393
364.7	0.0586	-1026.6	0.1303	-164.0	0.1017	1511.9	0.0373
444.7	0.0517	-1189.5	0.1283	-264.0	0.1053	-88.0	0.0946
621.4	0.0469	-1352.3	0.1306	-364.0	0.1108	-133.0	0.0965
798.0	0.0436	-1515.2	0.1341	-464.0	0.1147	-178.0	0.0985
974.7	0.0415	6.0	0.087	-664.0	0.1245	-223.0	0.1035
1151.4	0.0372	56.0	0.0883	-864.0	0.1259	-318.0	0.109
1328.0	0.0423	106.0	0.082	-1189.0	0.1291	-413.0	0.1125
1504.7	0.0416	156.0	0.0767	-1513.9	0.1287	-508.0	0.1162
-15.2	0.0819	256.0	0.0735	28.0	0.0901	-708.0	0.1257
-55.2	0.0882	356.0	0.0659	17.0	0.0858	-908.0	0.127
-95.2	0.0908	456.0	0.0642	62.0	0.0773	-1222.9	0.1304
-135.2	0.0933	656.0	0.055	107.0	0.0776	-1537.9	0.1317

Cudiffcp 4.2

x (μm)	Cu (wt%)	*x* (μm)	Cu (wt%)	*x* (μm)	Cu (wt%)	*x* (μm)	Cu (wt%)
10	0.0797	-90	0.0922	615	0.0341	200	0.0619
30	0.0816	-130	0.0975	755	0.0261	265	0.0563
50	0.081	-170	0.0895	1012.5	0.0136	395	0.0443
70	0.0791	-210	0.0939	1270	0.0155	525	0.0388
90	0.0773	-250	0.1001	-20	0.0912	776.7	0.0177
130	0.0748	-330	0.1065	-55	0.0946	1028.3	0.0183
170	0.0711	-410	0.1083	-90	0.0925	1280	0.018
210	0.0681	-490	0.1011	-125	0.0994	-70	0.0816
250	0.0585	-570	0.104	-195	0.1042	-100	0.0841
330	0.0569	-742.5	0.1038	-265	0.1066	-130	0.0901
410	0.0479	-915	0.1042	-335	0.0998	-160	0.0935
490	0.0395	-1087.5	0.105	-475	0.1116	-225	0.0896
570	0.0319	-1260	0.1127	-615	0.1061	-290	0.0911
742.5	0.0209	20	0.088	-755	0.1131	-355	0.0967
915	0.0136	55	0.0801	-1012.5	0.1085	-485	0.1025
1087.5	0.0118	90	0.0779	-1270	0.1176	-615	0.0996
1260	0.0142	125	0.0782	-20	0.0846	-826.7	0.1079
-10	0.0835	195	0.0702	10	0.0771	-1038.3	0.1032
-30	0.082	265	0.0681	40	0.0791	-1250	0.1074
-50	0.0947	335	0.063	70	0.0739		
-70	0.0883	475	0.0423	135	0.0678		

Cudiffcp 4.3

x (μm)	Cu (wt%)	*x* (μm)	Cu (wt%)	*x* (μm)	Cu (wt%)	*x* (μm)	Cu (wt%)
9.9	0.0899	-45.1	0.0917	171.2	0.077	-668.8	0.0931
44.9	0.083	-80.1	0.0947	291.2	0.0772	-788.8	0.0996
79.9	0.0881	-115.1	0.0914	411.2	0.0646	-1018.8	0.0979
114.9	0.0795	-150.1	0.0909	531.2	0.0524	-1248.8	0.0995
149.9	0.0821	-210.1	0.0924	651.2	0.0493	18.6	0.0803
209.9	0.0811	-270.1	0.0978	771.2	0.0392	268.6	0.0664
269.9	0.0755	-330.1	0.0963	891.2	0.0292	518.6	0.0377
329.9	0.0686	-390.1	0.0964	1071.2	0.0181	693.6	0.0272
389.9	0.065	-510.1	0.0984	1251.2	0.01	1243.6	0.0143
509.9	0.0532	-630.1	0.0957	-71.2	0.0901	-21.4	0.0847
629.9	0.0451	-750.1	0.0965	-1.2	0.091	-271.4	0.0938
749.9	0.0319	-870.1	0.0943	-68.8	0.0917	-521.4	0.097
869.9	0.0275	-1050.1	0.1019	-188.8	0.0913	-696.4	0.0935
1049.9	0.0119	-1230.1	0.1039	-308.8	0.0918	-1246.4	0.0989
1229.9	0.017	31.2	0.0887	-428.8	0.0934		
-10.1	0.091	101.2	0.0849	-548.8	0.0943		

Cudiffcp 4.4

x (μm)	Cu (wt%)	*x* (μm)	Cu (wt%)	*x* (μm)	Cu (wt%)	*x* (μm)	Cu (wt%)
42.8	0.0938	-318.5	0.104	1226.1	0.0163	505.0	0.0156
70.2	0.071	-377.9	0.1126	-14.9	0.0715	604.2	0.0118
101.5	0.0582	-498.6	0.1072	-54.7	0.0752	753.8	0.0086
131.5	0.0489	-617.4	0.1172	-94.4	0.0777	903.3	0.0072
190.9	0.0596	-737.4	0.1121	-134.2	0.0834	1053.6	0.0071
252.2	0.0415	-857.5	0.1154	-174.9	0.0744	1205.0	0.0082
311.0	0.0277	-978.2	0.124	-243.8	0.1	-49.1	0.0707
370.7	0.0187	-1097.0	0.1221	-315.4	0.097	-98.2	0.0811
493.0	0.0134	-1217.0	0.1239	-385.6	0.1107	-147.4	0.0834
611.1	0.015	24.9	0.0637	-455.5	0.1147	-198.3	0.0899
731.2	0.0168	65.8	0.0598	-606.9	0.1293	-247.0	0.0927
851.2	0.0129	105.4	0.0489	-759.2	0.1254	-348.2	0.1053
971.3	0.0139	145.0	0.0477	-911.5	0.116	-448.8	0.1168
1090.7	0.0161	186.5	0.038	-1062.5	0.1247	-548.1	0.1224
1213.0	0.0059	256.7	0.0322	-1215.1	0.1231	-647.7	0.1214
-18.1	0.0691	326.3	0.0241	2.4	0.067	-796.8	0.1161
-48.4	0.0728	396.6	0.0257	53.6	0.0617	-946.9	0.1227
-77.5	0.0778	465.5	0.0243	104.1	0.0545	-1097.3	0.1294
-107.8	0.0748	618.8	0.0123	155.2	0.0384	-1247.7	0.1246
-137.8	0.0835	770.1	0.0125	204.3	0.0374		
-198.3	0.0914	922.1	0.0101	303.6	0.0219		
-257.2	0.0929	1074.7	0.0104	405.2	0.0231		

Cudiffcp 5.1

x (μm)	Cu (wt%)	*x* (μm)	Cu (wt%)	*x* (μm)	Cu (wt%)	*x* (μm)	Cu (wt%)
41.3	0.0502	-227.9	0.0676	1427.9	0.0127	371.6	0.0324
71.3	0.0448	-287.9	0.0716	-43.6	0.0449	471.6	0.0312
101.3	0.0448	-407.9	0.077	-83.6	0.0479	671.5	0.0199
161.3	0.0431	-527.9	0.0858	-123.6	0.0559	871.5	0.0116
221.3	0.0369	-647.8	0.0838	-163.6	0.0639	1051.4	0.0143
281.2	0.0303	-1177.7	0.1029	-243.6	0.0621	1231.4	0.0128
401.2	0.0299	-1357.7	0.0957	-323.6	0.0671	1411.3	0.0045
521.1	0.0222	28.1	0.0455	-403.6	0.0687	-45.4	0.0507
641.1	0.0197	68.1	0.0437	-563.6	0.076	-95.4	0.0562
761.0	0.0177	108.1	0.0455	-723.6	0.0838	-145.4	0.0644
881.0	0.0123	148.1	0.0377	-883.6	0.0807	-195.4	0.0656
1001.0	0.0083	228.1	0.032	-1043.5	0.0951	-295.4	0.0715
1205.9	0.009	308.1	0.0283	-1203.5	0.0973	-395.4	0.077
1410.8	0.0118	388.1	0.0293	-1363.5	0.094	-495.4	0.0817
-18.0	0.0524	548.0	0.0183	21.8	0.048	-695.4	0.0881
-48.0	0.0566	708.0	0.0181	71.7	0.0487	-895.4	0.0974
-78.0	0.0582	868.0	0.0106	121.7	0.0465	-1095.4	0.0967
-108.0	0.058	1027.9	0.0135	171.7	0.041	-1295.4	0.1018
-167.9	0.0605	1187.9	0.0096	271.7	0.0385		

Cudiffcp 6.1

x (μm)	Cu (wt%)	*x* (μm)	Cu (wt%)	*x* (μm)	Cu (wt%)	*x* (μm)	Cu (wt%)
34.0	0.0627	-726.7	0.1095	-236.0	0.0893	1014.4	0.0134
137.0	0.051	-829.9	0.1129	-360.2	0.0944	1112.7	0.0075
240.0	0.0378	-933.1	0.1152	-484.2	0.1022	1211.0	0.0155
342.9	0.0291	-1036.3	0.1121	-608.4	0.1092	1309.2	0.0145
445.9	0.0225	-1139.5	0.1132	-732.5	0.1073	-91.2	0.0764
548.9	0.025	-1242.8	0.1145	-856.7	0.1099	-188.6	0.0852
651.9	0.0202	-1346.0	0.1127	-980.7	0.1127	-285.9	0.0914
754.8	0.0164	58.6	0.0556	-1104.9	0.1085	-383.2	0.1016
857.9	0.0132	178.2	0.0467	-1229.0	0.1163	-480.5	0.1106
960.9	0.0086	297.9	0.0368	-1353.1	0.1114	-577.9	0.112
1063.9	0.0161	417.5	0.0236	31.8	0.0576	-675.1	0.107
1166.8	0.0134	537.1	0.0168	130.1	0.051	-772.4	0.1083
1269.8	0.0104	656.8	0.0186	228.3	0.0431	-869.8	0.1136
1372.8	0.011	776.5	0.0094	326.6	0.0357	-967.1	0.1138
-107.3	0.0767	896.2	0.0107	424.8	0.0237	-1064.4	0.1219
-210.5	0.088	1015.8	0.0129	523.1	0.0283	-1161.7	0.1146
-313.8	0.0987	1135.5	0.0096	621.3	0.0206	-1259.1	0.1087
-417.0	0.1013	1255.1	0.0118	719.6	0.0152	-1356.4	0.1154
-520.2	0.109	1374.7	0.0131	817.9	0.0113		
-623.4	0.1129	-111.9	0.0771	916.1	0.013		

Cudiffcp 6.1

x (μm)	Cu (wt%)	*x* (μm)	Cu (wt%)	*x* (μm)	Cu (wt%)	*x* (μm)	Cu (wt%)
42.4	0.0569	-363.5	0.0867	1058.8	0.0222	574.4	0.0359
62.4	0.0562	-425.5	0.0932	1133.8	0.0185	654.4	0.0242
82.4	0.0517	-487.5	0.0927	1208.8	0.0164	734.4	0.0299
102.4	0.052	-549.5	0.1037	1288.8	0.0187	814.4	0.0238
142.4	0.0508	-611.5	0.1034	1368.8	0.0222	894.4	0.026
182.4	0.0487	-673.5	0.1044	-17.1	0.0667	974.4	0.0251
222.4	0.0453	-735.5	0.1061	-92.1	0.0662	1054.4	0.0261
262.4	0.0406	-797.5	0.1112	-167.1	0.0755	1134.4	0.0204
322.4	0.0388	-859.5	0.1168	-242.1	0.0743	1214.4	0.0181
382.4	0.0354	-921.5	0.1174	-317.1	0.0839	1294.4	0.0205
442.4	0.037	-983.5	0.1222	-392.1	0.088	1394.4	0.0195
502.4	0.0292	-1045.5	0.1112	-467.1	0.0954	-14.4	0.0632
562.4	0.0284	-1107.5	0.1166	-542.1	0.1031	-92.4	0.0725
622.4	0.0274	-1169.5	0.1253	-617.1	0.1028	-170.4	0.0732
682.4	0.0256	-1231.5	0.1211	-692.1	0.1074	-248.4	0.08
742.4	0.0268	-1293.5	0.1211	-767.1	0.1119	-326.4	0.0895
802.4	0.0207	-1355.5	0.1161	-842.1	0.113	-404.4	0.0911
862.4	0.0248	-1417.5	0.115	-917.1	0.1158	-482.4	0.0984
922.4	0.0202	8.8	0.0597	-992.1	0.1165	-560.4	0.1004
982.4	0.0209	83.8	0.0498	-1067.1	0.1209	-638.4	0.1089
1042.4	0.0185	158.8	0.051	-1142.1	0.1198	-716.4	0.1087
1102.4	0.0233	233.8	0.0501	-1217.1	0.125	-794.4	0.1127
1182.4	0.0189	308.8	0.0466	-1292.1	0.1275	-872.4	0.1115
1262.4	0.0209	383.8	0.0357	-1352.1	0.1215	-950.4	0.1168
1342.4	0.013	458.8	0.0344	-1426.1	0.1176	-1028.4	0.122
-17.5	0.062	533.8	0.0319	14.4	0.0621	-1106.4	0.1226
-57.5	0.0628	608.8	0.0327	94.4	0.0576	-1184.4	0.1201
-97.5	0.0706	683.8	0.0258	174.4	0.0536	-1262.4	0.1209
-137.5	0.0699	758.8	0.0269	254.4	0.049	-1340.4	0.1199
-177.5	0.0726	833.8	0.0275	334.4	0.0362	-1418.4	0.1201
-239.5	0.0786	908.8	0.0275	414.4	0.0412		
-301.5	0.0846	983.8	0.0206	494.4	0.0357		

Appendix B1

Copper diffusion profiles for Chapter III

Chal-Rhy-1-2, EMPA profile

x (µm)	Cu (wt%)	*x* (µm)	Cu (wt%)	*x* (µm)	Cu (wt%)	*x* (µm)	Cu (wt%)
12.5	0.0525	860.0	0.0149	408.7	0.0272	128.4	0.057
22.3	0.0676	986.5	0.0095	439.4	0.0273	159.8	0.0481
30.2	0.0722	1113.4	0.0088	473.1	0.0257	191.1	0.0468
38.9	0.0757	12.1	0.0433	505.8	0.0267	222.1	0.0467
47.2	0.0736	21.4	0.0614	537.5	0.0269	252.8	0.0445
55.3	0.0775	29.6	0.0696	569.3	0.0212	283.9	0.0359
70.5	0.0684	37.5	0.074	634.8	0.0211	315.1	0.0375
86.1	0.0636	45.1	0.0783	696.8	0.0175	345.8	0.0316
102.9	0.0628	53.8	0.0708	761.7	0.0143	376.5	0.0317
117.5	0.0617	68.9	0.0676	889.1	0.0181	408.2	0.0299
134.4	0.0586	85.5	0.0661	1015.5	0.0116	438.8	0.0248
165.6	0.0516	101.5	0.0625	1142.0	0.0166	472.2	0.0173
197.7	0.0504	117.1	0.0604	7.3	0.0345	503.9	0.0244
229.0	0.0398	133.7	0.0586	17.4	0.0636	535.7	0.0239
261.5	0.0416	160.1	0.0504	25.1	0.0729	567.4	0.0244
293.1	0.0394	190.4	0.0468	33.4	0.0761	630.9	0.0185
356.8	0.0321	222.1	0.0473	41.4	0.0735	694.3	0.0121
418.5	0.0281	252.8	0.0387	49.4	0.0744	757.8	0.0152
481.5	0.0209	284.9	0.0362	65.7	0.0682	886.2	0.0107
545.0	0.0253	314.8	0.0327	81.1	0.0614	1023.2	0.0145
609.3	0.019	346.1	0.032	96.7	0.0584	1142.0	0.0087
734.7	0.0146	377.8	0.0334	113.5	0.0625		

Chal-Rhy-1-2, LAICPMS profile

x (µm)	Cu (wt%)	*x* (µm)	Cu (wt%)	*x* (µm)	Cu (wt%)	*x* (µm)	Cu (wt%)
29.3	0.0487	218.6	0.0289	452.9	0.0123	866.9	0.0016
66.8	0.0497	259.6	0.0253	528.6	0.0089	960.9	0.0012
102.5	0.0439	296.6	0.0226	604.7	0.0061	1055.0	0.0010
144.1	0.0377	338.2	0.0194	681.4	0.0041	1160.8	0.0010
182.5	0.0326	381.3	0.0164	766.6	0.0027	866.9	0.0016

Chal-Rhy-3-1, EMPA profile

x (µm)	Cu (wt%)	*x* (µm)	Cu (wt%)	*x* (µm)	Cu (wt%)	*x* (µm)	Cu (wt%)
15.5	0.0736	753.6	0.0166	276.3	0.0449	276.0	0.0458
34.5	0.0636	853.1	0.0165	377.4	0.0373	326.5	0.0407
54.4	0.0751	955.9	0.0137	475.6	0.0296	375.5	0.0403
74.1	0.0738	1055.6	0.0058	575.7	0.0216	436.1	0.0344
94.6	0.0584	11.0	0.0587	676.1	0.0171	475.8	0.0304
134.5	0.0583	26.0	0.0849	775.6	0.0213	576.0	0.0232
184.6	0.0459	45.9	0.0678	875.4	0.0172	676.4	0.0218
234.4	0.0449	66.4	0.0756	975.1	0.0103	737.0	0.022
334.7	0.0409	86.5	0.0617	1074.7	0.0104	837.9	0.0161
434.0	0.0295	116.6	0.0541	16.1	0.0654	937.9	0.0148
533.8	0.0263	156.7	0.0503	116.8	0.0603	1036.4	0.0133
635.3	0.0188	206.3	0.0526	276.3	0.0449	276.0	0.0458

Chal-Rhy-3-1, LAICPMS profile

x (µm)	Cu (wt%)	*x* (µm)	Cu (wt%)	*x* (µm)	Cu (wt%)	*x* (µm)	Cu (wt%)
51	0.0611	298	0.0362	615	0.0193	936	0.0110
97	0.0572	351	0.0325	676	0.0172	1007	0.0098
145	0.0510	410	0.0293	735	0.0154	1066	0.0090
195	0.0456	474	0.0257	797	0.0138		
246	0.0405	544	0.0223	866	0.0122		

Chal-Rhy-3-2, LAICPMS profile

x (μm)	Cu (wt%)	*x* (μm)	Cu (wt%)	*x* (μm)	Cu (wt%)	*x* (μm)	Cu (wt%)
20	0.0468	167	0.0160	476	0.0004	1045	0.0003
38	0.0471	189	0.0131	543	0.0003	1121	0.0002
54	0.0423	206	0.0108	613	0.0003	1196	0.0003
75	0.0350	230	0.0084	688	0.0002	1264	0.0003
91	0.0336	274	0.0050	759	0.0002	1335	0.0006
113	0.0264	318	0.0028	832	0.0002	1404	0.0005
131	0.0232	364	0.0015	905	0.0002		
149	0.0191	411	0.0009	975	0.0002		

Chal-Rhy-4-2, EMPA profile

x (μm)	Cu (wt%)	*x* (μm)	Cu (wt%)	*x* (μm)	Cu (wt%)	*x* (μm)	Cu (wt%)
10.5	0.0253	559.4	0.0109	197.7	0.0137	85.2	0.0194
20.4	0.0215	608.9	0.011	232.7	0.0148	115.9	0.0209
31.4	0.0203	710.0	0.0064	266.8	0.0134	148.8	0.0174
41.0	0.0189	808.5	0.009	302.5	0.0103	147.6	0.0143
62.2	0.0123	901.1	0.0073	337.1	0.0139	178.0	0.0146
72.1	0.0135	1002.8	0.0078	371.9	0.0109	209.5	0.0126
92.5	0.0205	1103.1	0.0053	406.9	0.008	237.4	0.0143
112.8	0.0139	7.1	0.0169	472.2	0.0083	274.7	0.0152
132.8	0.0166	16.5	0.0203	534.5	0.0121	309.5	0.0169
152.0	0.014	24.7	0.022	596.1	0.0079	372.9	0.009
200.7	0.018	32.9	0.021	705.0	0.0081	445.2	0.0107
251.5	0.013	41.3	0.019	815.3	0.0069	510.3	0.0083
301.9	0.0106	49.3	0.0214	923.7	0.0065	575.1	0.0099
351.8	0.0136	64.7	0.0177	1070.6	0.0069	641.3	0.0062
400.7	0.0067	80.2	0.0201	1216.1	0.0047	771.5	0.0108
356.9	0.0092	97.1	0.0171	8.1	0.0162	897.6	0.0087
406.0	0.0111	112.9	0.0184	24.7	0.0224		
457.7	0.0108	129.5	0.0161	54.9	0.0194		
507.5	0.0113	162.0	0.0144	71.5	0.0197		

Chal-Rhy-4-2, LAICPMS profile

x (μm)	Cu (wt%)	*x* (μm)	Cu (wt%)	*x* (μm)	Cu (wt%)	*x* (μm)	Cu (wt%)
40.1	0.0141	209.8	0.0086	389.9	0.0049	713.5	0.0013
75.2	0.0115	242.9	0.0078	447.8	0.0041	799.6	0.0010
107.4	0.0107	281.9	0.0070	508.4	0.0032	890.8	0.0007
138.6	0.0100	310.4	0.0063	570.3	0.0022	989.7	0.0007
174.2	0.0092	351.1	0.0055	637.9	0.0018	713.5	0.0013

Chal-Rhy-4-3, EMPA profile

x (μm)	Cu (wt%)	*x* (μm)	Cu (wt%)	*x* (μm)	Cu (wt%)	*x* (μm)	Cu (wt%)
5.4	0.0136	470.4	0.0106	172.6	0.0217	222.1	0.0171
21.8	0.022	501.1	0.0114	222.8	0.0179	260.9	0.0204
35.7	0.0233	530.9	0.0127	273.2	0.0169	300.7	0.0147
51.7	0.0259	560.7	0.0093	322.1	0.0133	340.8	0.0161
80.4	0.0191	590.5	0.0101	429.9	0.013	416.3	0.0146
111.2	0.0243	651.7	0.0075	537.7	0.0092	491.3	0.014
141.5	0.017	710.9	0.0111	644.1	0.0113	566.3	0.0072
171.4	0.0162	771.4	0.0058	753.7	0.01	641.7	0.0107
200.4	0.0161	830.6	0.0088	860.5	0.012	718.4	0.0031
230.0	0.0174	889.5	0.0074	965.8	0.0113	793.4	0.0088
260.2	0.0143	949.9	0.0079	1071.1	0.0099	865.7	0.0075
291.2	0.014	1009.8	0.0096	10.3	0.0275	939.2	0.0074
320.7	0.019	1069.2	0.0106	21.2	0.0285	1013.9	0.007
350.9	0.0152	7.6	0.0236	61.9	0.0225	1090.5	0.0099
380.3	0.0148	22.8	0.0221	100.8	0.0234		
410.5	0.0087	72.9	0.0231	141.8	0.0219		
440.5	0.0113	123.2	0.0201	180.4	0.0217		

Chal-Rhy-4-3, LAICPMS profile

x (μm)	Cu (wt%)	*x* (μm)	Cu (wt%)	*x* (μm)	Cu (wt%)	*x* (μm)	Cu (wt%)
15.2	0.0165	249.3	0.0106	526.5	0.0047	931.2	0.0021
59.2	0.0167	291.6	0.0094	607.9	0.0035	1030.3	0.0024
109.1	0.0144	329.9	0.0084	695.1	0.0028		
156.7	0.0131	369.8	0.0077	785.7	0.0023		
209.1	0.0125	444.8	0.0061	862.1	0.0021		

Chal-Rhy-5-1, EMPA profile

x (µm)	Cu (wt%)	*x* (µm)	Cu (wt%)	*x* (µm)	Cu (wt%)	*x* (µm)	Cu (wt%)
4.8	0.0168	699.0	0.0072	439.4	0.0127	206.5	0.0194
14.4	0.0239	786.3	0.0118	508.9	0.0083	270.9	0.0167
24.8	0.0251	857.9	0.009	597.6	0.0105	315.8	0.0154
64.4	0.0232	5.0	0.018	678.0	0.0128	395.8	0.014
104.0	0.0194	14.3	0.0215	756.7	0.0091	475.2	0.011
143.5	0.016	24.7	0.0211	836.9	0.0132	554.7	0.0105
223.1	0.0085	44.4	0.0218	7.6	0.0215	634.1	0.0113
302.7	0.0144	103.9	0.0226	18.3	0.0265	712.8	0.013
383.0	0.0128	189.0	0.02	27.8	0.0219	793.0	0.0118
461.1	0.0076	229.6	0.0155	38.3	0.0205	861.7	0.0115
539.9	0.0099	289.9	0.0137	67.8	0.0195		
619.1	0.0063	360.1	0.0149	146.2	0.0196		

Chal-Rhy-5-1, LAICPMS profile

x (µm)	Cu (wt%)	*x* (µm)	Cu (wt%)	*x* (µm)	Cu (wt%)	*x* (µm)	Cu (wt%)
38.8	0.0201	226.3	0.0092	436.1	0.0040	675.8	0.0017
77.2	0.0167	264.2	0.0080	482.1	0.0030	723.4	0.0016
114.5	0.0152	310.0	0.0070	531.7	0.0024	768.1	0.0016
151.9	0.0131	350.5	0.0058	577.0	0.0021	821.5	0.0017
188.9	0.0106	392.1	0.0047	625.3	0.0017		

Chal-Rhy-7-1, EMPA profile

x (µm)	Cu (wt%)	*x* (µm)	Cu (wt%)	*x* (µm)	Cu (wt%)	*x* (µm)	Cu (wt%)
20.7	0.0548	460.6	0.0227	135.8	0.0447	53.4	0.0542
40.4	0.0544	540.6	0.02	165.9	0.0454	78.5	0.0533
60.3	0.0495	620.2	0.0138	215.6	0.0419	104.6	0.0491
80.4	0.0591	700.8	0.0186	265.9	0.0336	153.2	0.0448
100.6	0.0515	779.9	0.0118	315.6	0.0253	213.4	0.037
140.2	0.0539	860.0	0.0117	415.8	0.0283	273.4	0.0353
180.9	0.0493	921.3	0.0115	516.5	0.017	393.3	0.0242
220.7	0.0349	973.0	0.0107	597.3	0.0185	515.0	0.0194
261.0	0.0343	15.9	0.0485	695.7	0.0179	633.3	0.0172
301.3	0.0348	46.3	0.0611	797.2	0.0109	744.4	0.0102
340.6	0.0278	76.2	0.057	896.4	0.0113	963.4	0.0174
381.4	0.0315	106.4	0.05	18.5	0.0548		

Chal-Rhy-7-1, LAICPMS profile

x (µm)	Cu (wt%)	*x* (µm)	Cu (wt%)	*x* (µm)	Cu (wt%)	*x* (µm)	Cu (wt%)
31.8	0.0388	264.0	0.0194	522.7	0.0066	812.1	0.0016
68.4	0.0367	304.4	0.0167	569.3	0.0053	860.2	0.0013
105.4	0.0340	340.9	0.0143	615.9	0.0042	904.5	0.0010
146.2	0.0300	383.7	0.0124	666.4	0.0033	953.3	0.0009
183.3	0.0264	428.9	0.0101	718.4	0.0025		
223.2	0.0228	473.2	0.0082	764.5	0.0020		

Chal-Rhy-8-1, EMPA profile

x (μm)	Cu (wt%)	*x* (μm)	Cu (wt%)	*x* (μm)	Cu (wt%)	*x* (μm)	Cu (wt%)
10.7	0.0174	99.2	0.011	13.6	0.0168	434.1	0.0036
21.3	0.0186	119.1	0.0098	43.8	0.015	484.1	0.0072
31.6	0.0186	139.5	0.0096	64.2	0.0135	13.5	0.0141
41.5	0.0152	168.8	0.0075	84.2	0.0126	43.4	0.013
51.6	0.016	189.4	0.0087	104.0	0.0091	74.0	0.0135
71.0	0.0152	209.3	0.0038	123.8	0.0077	103.9	0.0107
90.8	0.014	223.9	0.0071	144.3	0.0088	134.3	0.0111
131.3	0.0106	246.0	0.0104	164.5	0.0124	163.8	0.0093
160.9	0.0104	266.3	0.0057	184.4	0.007	198.9	0.0059
211.7	0.0063	291.3	0.0049	204.1	0.0087	229.4	0.0061
261.8	0.0074	311.4	0.0046	228.8	0.0069	259.1	0.0073
361.8	0.0076	331.1	0.0023	253.7	0.008	289.0	0.0072
401.6	0.0062	350.8	0.0067	273.6	0.0029	318.8	0.0018
14.8	0.0209	370.7	0.0063	298.8	0.004	349.0	0.0062
29.1	0.0165	397.0	0.006	323.7	0.0042	394.1	0.0067
44.0	0.0165	427.0	0.0041	348.7	0.0048	423.9	0.0055
60.0	0.0147	466.8	0.0059	373.4	0.006	454.8	0.0044
79.6	0.0122	506.7	0.0048	403.6	0.0047		

Chal-Rhy-8-1, LAICPMS profile

x (μm)	Cu (wt%)	*x* (μm)	Cu (wt%)	*x* (μm)	Cu (wt%)	*x* (μm)	Cu (wt%)
37.4	0.0106	161.8	0.0052	300.9	0.0017	461.0	0.0003
60.6	0.0095	190.5	0.0042	336.0	0.0012	511.8	0.0002
82.9	0.0086	218.0	0.0034	357.7	0.0010	565.3	0.0002
111.0	0.0071	242.5	0.0028	391.3	0.0007	610.3	0.0001
133.4	0.0061	276.4	0.0021	418.1	0.0005	461.0	0.0003

Chal-Rhy-9-1, EMPA profile

x (µm)	Cu (wt%)	*x* (µm)	Cu (wt%)	*x* (µm)	Cu (wt%)	*x* (µm)	Cu (wt%)
28.6	0.0605	952.2	0.0038	376.5	0.016	177.1	0.0403
48.3	0.066	1032.6	0.0022	426.2	0.0144	206.9	0.0338
67.7	0.0635	1111.0	0.0043	486.0	0.0131	242.3	0.033
87.7	0.0621	18.6	0.0465	536.7	0.0073	276.9	0.0234
104.2	0.0494	33.8	0.0631	585.5	0.0073	312.0	0.0192
134.4	0.0475	48.9	0.0694	635.9	0.0069	347.1	0.0189
154.0	0.0431	63.5	0.0626	685.6	0.0016	382.2	0.0147
193.8	0.0368	78.8	0.0646	765.5	0.0053	417.1	0.0127
223.9	0.0334	88.6	0.0619	862.8	0.0064	461.8	0.0088
262.7	0.023	87.1	0.0558	942.4	0.0094	497.2	0.008
382.7	0.021	116.9	0.0461	14.9	0.0369	531.6	0.0099
303.8	0.0177	146.7	0.0426	30.1	0.0565	566.9	0.0088
462.4	0.0095	177.0	0.0421	44.6	0.0622	602.3	0.0088
542.0	0.0064	206.6	0.0328	59.7	0.0588	636.7	0.0033
630.9	0.0078	237.1	0.0347	74.9	0.0587	696.3	0.0032
714.1	0.0044	267.0	0.0258	87.1	0.0559	757.2	0.0046
792.4	0.0047	296.6	0.0171	117.5	0.0491	811.4	0.0022
871.7	0.0089	326.5	0.0165	147.4	0.0451	911.5	0.0119

Chal-Rhy-9-1, LAICPMS profile

x (µm)	Cu (wt%)	*x* (µm)	Cu (wt%)	*x* (µm)	Cu (wt%)	*x* (µm)	Cu (wt%)
25.8	0.0561	206.9	0.0315	511.2	0.0048	1017.0	0.0007
47.3	0.0602	231.3	0.0278	576.1	0.0029	1119.3	0.0008
64.6	0.0577	265.1	0.0232	637.7	0.0019	1221.1	0.0009
96.4	0.0494	286.6	0.0208	699.0	0.0013	1327.8	0.0012
125.2	0.0444	328.7	0.0163	765.9	0.0010	1524.2	0.0020
154.7	0.0389	378.6	0.0115	831.5	0.0008		
175.9	0.0361	443.1	0.0080	912.3	0.0007		

Chal-Rhy-10-1, EMPA profile

x (μm)	Cu (wt%)	*x* (μm)	Cu (wt%)	*x* (μm)	Cu (wt%)	*x* (μm)	Cu (wt%)
6.4	0.025	766.3	0.0103	147.5	0.0758	33.9	0.0911
26.6	0.0745	805.7	0.009	197.4	0.0613	64.7	0.0926
46.8	0.0949	845.8	0.0047	247.3	0.0549	107.0	0.083
66.8	0.0932	884.3	0.0075	297.2	0.0467	144.9	0.0778
96.6	0.0795	925.8	0.006	347.7	0.0431	204.6	0.063
126.8	0.0803	964.4	0.0074	408.1	0.0357	265.1	0.0547
166.8	0.0749	1004.8	0.0053	467.8	0.0265	325.6	0.0427
207.2	0.0641	1045.9	0.0054	527.7	0.0233	405.8	0.0315
247.5	0.0609	1083.8	0.0024	587.7	0.0156	487.2	0.0283
287.3	0.0495	1126.1	0.0105	648.4	0.0103	647.9	0.0105
327.8	0.0494	1165.8	0.006	707.7	0.0116	748.3	0.0003
367.3	0.0447	1205.7	0.0042	787.5	0.0115	849.4	0.0096
407.8	0.0329	1245.5	0.0029	868.2	0.0122	948.1	0.0052
447.3	0.0317	1285.1	0.0034	946.6	0.0112	1048.7	0.0035
487.4	0.028	1345.5	0.0093	1026.1	0.007	1149.2	0.0076
526.6	0.0206	1403.4	0.0094	1106.9	0.0066	1300.2	0.0074
565.3	0.0182	1462.3	0.0074	1186.6	0.0097	1451.1	0.0106
606.7	0.0159	6.3	0.021	1266.6	0.0031		
646.1	0.0156	36.8	0.0908	1346.7	0.0079		
686.1	0.0165	67.3	0.0913	1426.0	0.0121		
725.5	0.0106	107.5	0.0786	3.4	0.0166		

Chal-Rhy-10-1, LAICPMS profile

x (μm)	Cu (wt%)	*x* (μm)	Cu (wt%)	*x* (μm)	Cu (wt%)	*x* (μm)	Cu (wt%)
29.7	0.0840	604.3	0.0107	302.5	0.0430	55.4	0.0985
73.4	0.0965	684.9	0.0067	380.1	0.0311	137.8	0.0754
113.8	0.0826	759.6	0.0044	467.2	0.0210	225.9	0.0567
148.8	0.0732	847.6	0.0028	564.0	0.0129	327.4	0.0397
191.0	0.0650	958.7	0.0017	653.0	0.0076	445.2	0.0238
229.7	0.0545	1069.1	0.0015	762.2	0.0044	569.8	0.0128
277.9	0.0474	1187.0	0.0016	860.9	0.0029	679.9	0.0072
324.6	0.0404	1319.8	0.0020	959.6	0.0021	801.6	0.0041
373.7	0.0326	1473.1	0.0031	1060.1	0.0017	920.3	0.0028
420.2	0.0257	59.2	0.0997	1155.9	0.0020	1074.6	0.0024
470.4	0.0209	137.7	0.0749	1246.0	0.0022	1201.9	0.0027
525.9	0.0160	220.1	0.0589	1337.9	0.0027	1321.7	0.0033

Chal-Rhy-11-1, EMPA profile

x (μm)	Cu (wt%)	*x* (μm)	Cu (wt%)	*x* (μm)	Cu (wt%)	*x* (μm)	Cu (wt%)
20.5	0.0358	780.8	0.0057	391.5	0.0138	155.7	0.0262
60.7	0.0356	840.9	0.0043	441.6	0.0104	227.2	0.0195
100.4	0.0347	900.7	0.0053	491.9	0.0071	297.2	0.0174
141.2	0.0296	962.0	0.0073	542.8	0.0078	357.5	0.012
181.3	0.0267	1022.3	0.0064	598.1	0.0041	428.4	0.0112
220.9	0.0173	1092.3	0.0101	648.1	0.0064	496.8	0.0093
260.6	0.017	1152.6	0.0111	698.1	0.0081	566.5	0.0097
300.7	0.016	1212.0	0.0128	748.1	0.005	636.7	0.0064
340.9	0.0148	1272.3	0.0069	797.2	0.0094	707.4	0.0075
381.5	0.011	1323.1	0.0113	847.2	0.0092	776.6	0.0086
421.2	0.0122	11.0	0.0316	898.8	0.0086	847.3	0.0086
460.9	0.01	31.1	0.0386	948.6	0.0056	917.0	0.0108
501.0	0.0107	71.7	0.0347	998.4	0.0064	986.9	0.0085
540.4	0.0098	111.2	0.0314	1069.3	0.0061	1056.8	0.005
581.3	0.0063	151.0	0.024	1138.3	0.0096	1126.8	0.0074
621.2	0.0083	191.5	0.0238	1209.1	0.0123	1197.6	0.0076
661.1	0.0059	241.6	0.0146	1279.1	0.0095	1267.6	0.012
701.0	0.0073	291.5	0.0126	15.5	0.0345		
740.9	0.0041	341.8	0.0146	85.9	0.0317		

Chal-Rhy-11-1, LAICPMS profile

x (μm)	Cu (wt%)	*x* (μm)	Cu (wt%)	*x* (μm)	Cu (wt%)	*x* (μm)	Cu (wt%)
35.5	0.0264	181.2	0.0148	350.9	0.0060	742.3	0.0003
60.0	0.0246	208.6	0.0130	392.3	0.0046	872.2	0.0002
84.4	0.0223	226.4	0.0117	437.0	0.0034	986.2	0.0001
111.5	0.0200	252.8	0.0102	507.6	0.0021	1086.7	0.0001
133.6	0.0180	273.1	0.0092	579.8	0.0012	1190.5	0.0002
157.8	0.0165	309.6	0.0075	662.9	0.0006	1294.6	0.0002

Chal-Rhy-12-1, EMPA profile

x (µm)	Cu (wt%)	*x* (µm)	Cu (wt%)	*x* (µm)	Cu (wt%)	*x* (µm)	Cu (wt%)
10.3	0.0505	747.7	0.0068	444.0	0.0099	233.8	0.0233
30.0	0.0628	807.8	0.0062	493.9	0.0069	293.4	0.0195
49.8	0.0533	867.4	0.0036	544.4	0.0036	354.0	0.0129
90.0	0.0485	928.0	0.0001	593.4	0.0055	414.1	0.0095
129.6	0.0398	987.5	0.0065	643.9	0.0072	473.9	0.0082
169.7	0.0243	1087.8	0.0062	693.4	0.0048	533.5	0.0031
209.5	0.0276	1187.4	0.0038	773.2	0.0022	594.1	0.0037
249.3	0.0205	1287.7	0.0057	873.7	0.0044	653.7	0.0055
289.1	0.022	34.0	0.0558	974.1	0.0013	713.8	0.0019
329.2	0.0148	64.0	0.059	1074.4	0.0007	773.4	0.0058
369.2	0.0116	94.0	0.0417	1174.5	0.0071	833.0	0.0046
408.8	0.0081	143.9	0.0339	1275.2	0.006	933.6	0.0126
448.7	0.012	194.2	0.0213	13.3	0.0489	1033.5	0.0032
508.3	0.0066	243.9	0.0227	53.6	0.0545	1134.4	0.0056
568.9	0.0052	294.1	0.0189	93.2	0.0444	1234.4	0.0071
628.5	0.005	344.1	0.0102	133.4	0.034		
687.6	0.0043	394.2	0.0076	173.7	0.0334		

Chal-Rhy-12-1, LAICPMS profile

x (µm)	Cu (wt%)	*x* (µm)	Cu (wt%)	*x* (µm)	Cu (wt%)	*x* (µm)	Cu (wt%)
49.5	0.0400	207.8	0.0185	418.1	0.0053	902.0	0.0005
76.1	0.0359	234.3	0.0159	485.5	0.0034	1017.2	0.0005
100.1	0.0314	260.5	0.0138	554.4	0.0021	1119.1	0.0005
129.8	0.0269	294.2	0.0115	615.7	0.0014	1220.0	0.0005
157.7	0.0236	324.0	0.0096	709.5	0.0008	1323.4	0.0005
180.2	0.0208	365.3	0.0074	801.2	0.0006		

Chal-Rhy-13-1, EMPA profile

x (µm)	Cu (wt%)	*x* (µm)	Cu (wt%)	*x* (µm)	Cu (wt%)	*x* (µm)	Cu (wt%)
11.1	0.021	520.6	0.0104	253.1	0.0149	130.7	0.0185
26.6	0.0275	561.0	0.0119	292.9	0.0112	191.5	0.0135
41.2	0.0233	600.4	0.0108	333.1	0.0106	250.8	0.0123
61.3	0.0216	641.3	0.014	372.8	0.0127	310.9	0.0118
81.4	0.0191	680.7	0.0099	412.6	0.0094	371.1	0.0138
121.2	0.0192	740.8	0.0097	473.2	0.0101	431.1	0.0117
161.7	0.0174	800.9	0.0113	533.4	0.0104	490.8	0.0106
201.4	0.0153	860.5	0.0087	593.0	0.0107	550.3	0.0107
241.3	0.0138	895.6	0.0076	653.0	0.0101	610.6	0.0103
281.4	0.0128	12.4	0.0259	713.4	0.0086	670.4	0.0112
321.2	0.0109	52.8	0.0218	773.4	0.0085	730.2	0.0087
361.5	0.0102	93.0	0.0197	833.4	0.0092	810.7	0.0104
401.3	0.0117	132.7	0.0145	893.9	0.0101	890.8	0.0105
441.3	0.0111	173.2	0.0163	10.7	0.0222		
481.2	0.006	212.7	0.0157	70.4	0.0189		

Chal-Rhy-13-1, LAICPMS profile

x (µm)	Cu (wt%)	*x* (µm)	Cu (wt%)	*x* (µm)	Cu (wt%)	*x* (µm)	Cu (wt%)
30.0	0.0131	338.1	0.0014	672.4	0.0002	104.5	0.0079
67.0	0.0106	377.1	0.0010	713.1	0.0002	142.7	0.0061
106.4	0.0082	415.5	0.0007	756.9	0.0002	185.9	0.0045
145.4	0.0063	458.3	0.0005	798.2	0.0001	226.3	0.0033
184.3	0.0048	502.1	0.0004	836.9	0.0001	269.5	0.0024
221.3	0.0037	543.9	0.0003	884.5	0.0001		
259.8	0.0027	587.7	0.0003	32.3	0.0121		
298.7	0.0020	629.0	0.0002	68.0	0.0099		

Chal-Rhy-14-1, EMPA profile

x (µm)	Cu (wt%)	*x* (µm)	Cu (wt%)	*x* (µm)	Cu (wt%)	*x* (µm)	Cu (wt%)
41.5	0.1421	796.3	0.0108	615.8	0.0126	739.3	0.0131
80.6	0.1174	857.4	0.0113	676.1	0.0082	819.5	0.0106
120.6	0.0993	916.6	0.0102	745.3	0.0107	899.3	0.0054
157.3	0.0936	976.0	0.0133	825.6	0.0077	979.6	0.012
198.0	0.0722	1036.3	0.0083	905.3	0.0112	1060.4	0.0091
237.7	0.0561	1096.7	0.0098	986.5	0.004	1140.9	0.0122
277.6	0.0442	1157.0	0.0098	1065.9	0.0084	1201.2	0.0134
317.6	0.0416	1211.6	0.0115	1146.3	0.0139	63.0	0.1318
357.4	0.0297	16.7	0.1549	1196.1	0.0091	103.0	0.105
397.7	0.0288	76.3	0.1243	20.7	0.1498	143.5	0.0791
437.2	0.02	136.6	0.0912	99.8	0.1095	183.1	0.0693
477.0	0.0176	196.6	0.0763	178.6	0.0956	223.1	0.0604
517.0	0.0169	255.9	0.0539	258.3	0.0513	263.1	0.0559
556.9	0.0134	315.9	0.0427	338.2	0.032	303.2	0.048
596.3	0.0116	376.2	0.0293	418.6	0.0215	343.2	0.0333
636.7	0.0115	435.7	0.0207	498.7	0.0149	382.7	0.0318
676.1	0.0099	495.3	0.0159	578.7	0.0059	423.2	0.0248
736.2	0.0074	555.5	0.0119	659.1	0.0136	461.3	0.0225

Chal-Rhy-14-1, LAICPMS profile

x (µm)	Cu (wt%)	*x* (µm)	Cu (wt%)	*x* (µm)	Cu (wt%)	*x* (µm)	Cu (wt%)
26.6	0.1138	171.7	0.0576	382.5	0.0162	834.6	0.0003
51.7	0.1081	198.3	0.0509	431.9	0.0113	946.7	0.0001
75.6	0.0955	223.7	0.0441	496.7	0.0068	1057.5	0.0001
96.4	0.0871	250.6	0.0380	560.1	0.0040	1179.5	0.0001
122.4	0.0741	292.6	0.0295	639.1	0.0019		
145.1	0.0667	339.0	0.0218	736.2	0.0007		

Appendix B2

Iron diffusion profiles for Chapter III

Chal-Rhy-3-1, major element profile

x (μm)	SiO_2	TiO_2	Al_2O_3	FeO	MgO	CaO	Na_2O	K_2O	Total
5.6	76.12	0.25	13.67	0.44	0.28	1.18	3.22	3.78	98.94
11.7	74.95	0.36	13.41	0.73	0.28	1.11	3.20	3.84	97.87
16.8	75.00	0.20	13.58	0.94	0.29	1.23	3.10	3.80	98.15
21.8	75.19	0.30	13.61	1.14	0.32	1.32	3.15	3.77	98.78
26.2	75.14	0.24	13.64	1.21	0.28	1.27	2.99	3.76	98.53
32.2	75.07	0.30	13.59	1.38	0.29	1.32	3.10	3.86	98.91
36.9	74.75	0.30	13.55	1.49	0.28	1.30	2.93	3.81	98.39
42.2	74.61	0.21	13.52	1.60	0.26	1.29	3.03	3.73	98.24
46.7	74.19	0.32	13.41	1.58	0.26	1.28	3.05	3.80	97.89
52.3	74.43	0.30	13.43	1.58	0.22	1.21	2.94	3.83	97.93
56.9	74.55	0.29	13.64	1.62	0.32	1.30	3.19	3.73	98.63
62.2	74.68	0.29	13.44	1.64	0.29	1.27	3.00	3.79	98.39
67.2	74.56	0.28	13.61	1.70	0.29	1.23	3.11	3.79	98.57
71.8	74.27	0.28	13.64	1.74	0.29	1.24	2.96	3.76	98.18
76.6	74.10	0.28	13.54	1.65	0.27	1.19	2.85	3.79	97.67
81.9	74.42	0.28	13.52	1.68	0.24	1.18	2.91	3.80	98.03
86.7	74.24	0.27	13.51	1.70	0.27	1.27	2.99	3.77	98.03
91.8	74.40	0.33	13.77	1.70	0.28	1.24	2.81	3.78	98.30
96.7	74.16	0.29	13.49	1.68	0.25	1.23	3.07	3.76	97.94
101.8	74.46	0.28	13.58	1.74	0.26	1.21	2.93	3.72	98.18
106.3	74.24	0.28	13.30	1.65	0.26	1.21	3.06	3.76	97.77
6.1	74.49	0.27	13.48	0.41	0.28	1.18	3.86	4.40	98.38
12.2	74.66	0.31	13.72	0.72	0.26	1.25	3.75	4.48	99.15
17.0	74.42	0.25	13.48	1.02	0.25	1.30	3.88	4.34	98.95
22.6	73.80	0.24	13.47	1.15	0.32	1.27	3.97	4.35	98.58
27.7	73.63	0.25	13.47	1.39	0.27	1.27	4.00	4.35	98.62
31.7	73.53	0.25	13.66	1.37	0.28	1.37	3.57	4.30	98.34
37.7	74.30	0.24	13.45	1.51	0.33	1.33	3.79	4.33	99.29
42.9	73.59	0.33	13.41	1.58	0.25	1.28	3.68	4.34	98.46
47.7	73.74	0.26	13.35	1.63	0.24	1.24	3.58	4.38	98.43
52.0	73.40	0.26	13.65	1.65	0.29	1.30	3.71	4.40	98.66
57.7	73.40	0.30	13.29	1.67	0.31	1.23	3.80	4.26	98.26

62.7	73.56	0.22	13.61	1.64	0.28	1.30	3.85	4.29	98.75
67.8	73.34	0.30	13.41	1.66	0.23	1.25	3.68	4.37	98.24
77.3	73.75	0.26	13.34	1.67	0.28	1.21	3.70	4.40	98.61
87.9	73.67	0.24	13.56	1.74	0.26	1.27	3.63	4.35	98.72
96.5	73.58	0.24	13.35	1.73	0.31	1.16	3.75	4.37	98.49
106.8	73.47	0.34	13.70	1.65	0.25	1.19	3.55	4.33	98.48
117.7	73.25	0.35	13.50	1.71	0.22	1.14	3.59	4.34	98.11
127.4	73.62	0.28	13.61	1.74	0.25	1.25	3.50	4.31	98.57
137.1	73.78	0.30	13.67	1.75	0.27	1.24	3.72	4.41	99.12
148.0	74.08	0.20	13.76	1.77	0.31	1.24	3.68	4.32	99.36
5.6	75.56	0.17	13.59	0.40	0.27	1.20	3.78	4.30	99.28
11.6	74.90	0.24	13.53	0.73	0.23	1.23	3.78	4.36	99.00
15.3	74.44	0.30	13.64	0.86	0.28	1.27	3.68	4.33	98.81
19.2	74.58	0.24	13.62	1.04	0.29	1.26	3.55	4.25	98.83
23.0	74.47	0.20	13.69	1.16	0.24	1.30	3.59	4.25	98.91
28.6	74.08	0.29	13.57	1.34	0.32	1.29	3.74	4.22	98.85
32.3	74.09	0.26	13.61	1.38	0.27	1.34	3.69	4.24	98.88
38.1	74.17	0.29	13.58	1.50	0.29	1.36	3.58	4.28	99.06
43.6	74.32	0.23	13.45	1.56	0.27	1.34	3.62	4.34	99.13
48.6	73.92	0.31	13.65	1.61	0.25	1.28	3.66	4.25	98.94
52.9	73.97	0.23	13.53	1.65	0.30	1.32	3.62	4.22	98.83
58.0	74.31	0.29	13.60	1.71	0.27	1.29	3.55	4.19	99.22
63.7	74.18	0.32	13.52	1.71	0.27	1.29	3.63	4.22	99.13
71.2	74.05	0.28	13.47	1.74	0.27	1.23	3.44	4.29	98.77
79.0	73.69	0.24	13.61	1.71	0.27	1.28	3.43	4.29	98.53
87.5	74.31	0.28	13.74	1.76	0.27	1.19	3.51	4.29	99.34
95.5	73.65	0.25	13.64	1.74	0.29	1.25	3.59	4.27	98.68
102.5	74.02	0.29	13.59	1.72	0.26	1.27	3.56	4.31	99.04
111.2	74.07	0.35	13.61	1.77	0.30	1.24	3.66	4.26	99.27
119.4	74.22	0.21	13.56	1.74	0.29	1.21	3.58	4.28	99.10
127.0	73.83	0.23	13.48	1.67	0.27	1.16	3.35	4.25	98.23
3.7	78.15	0.26	13.37	0.30	0.25	1.11	4.08	4.07	101.58
9.1	75.86	0.23	13.58	0.65	0.22	1.23	3.89	4.35	100.01
14.9	74.87	0.30	13.59	0.93	0.29	1.28	3.75	4.29	99.30
19.7	74.70	0.29	13.61	1.09	0.29	1.25	3.52	4.26	99.02
24.8	74.58	0.27	13.56	1.24	0.29	1.33	3.41	4.19	98.86
29.6	74.36	0.30	13.40	1.39	0.29	1.37	3.47	4.26	98.83
34.9	74.17	0.29	13.61	1.43	0.28	1.35	3.58	4.28	98.99
39.2	74.07	0.33	13.63	1.55	0.28	1.38	3.48	4.25	98.97

45.1	74.73	0.24	13.56	1.63	0.29	1.27	3.58	4.29	99.60
49.6	74.17	0.26	13.67	1.63	0.27	1.33	3.49	4.26	99.09
54.6	74.09	0.32	13.65	1.62	0.27	1.28	3.55	4.21	98.99
58.9	74.48	0.30	13.62	1.68	0.27	1.30	3.49	4.22	99.36
64.9	73.94	0.37	13.66	1.69	0.24	1.27	3.34	4.24	98.75
75.0	72.56	0.24	13.85	1.63	0.29	1.25	3.39	4.23	97.44
84.3	73.93	0.27	13.38	1.74	0.24	1.25	3.25	4.20	98.25
95.2	74.11	0.25	13.48	1.71	0.27	1.24	3.30	4.25	98.63
104.6	73.94	0.23	13.58	1.75	0.23	1.18	3.34	4.26	98.52
113.8	73.70	0.27	13.54	1.70	0.27	1.24	3.28	4.13	98.13
124.7	74.42	0.23	13.43	1.79	0.27	1.23	3.27	4.24	98.88
134.4	74.04	0.22	13.52	1.73	0.26	1.20	3.65	4.33	98.95
144.9	74.11	0.25	13.51	1.74	0.25	1.20	3.53	4.24	98.84
4.9	76.02	0.20	13.69	0.42	0.25	1.18	3.96	4.33	100.04
10.2	75.13	0.26	13.67	0.67	0.29	1.22	3.68	4.33	99.25
15.5	74.39	0.26	13.57	0.89	0.26	1.28	3.61	4.30	98.55
20.5	74.47	0.36	13.41	1.06	0.24	1.35	3.76	4.28	98.93
25.1	74.68	0.25	13.48	1.27	0.31	1.30	3.56	4.15	99.01
30.5	73.90	0.26	13.50	1.41	0.29	1.31	3.61	4.18	98.48
35.4	74.18	0.27	13.40	1.49	0.27	1.34	3.62	4.24	98.80
40.3	73.93	0.23	13.48	1.54	0.26	1.28	3.66	4.30	98.68
45.5	74.23	0.26	13.58	1.55	0.29	1.30	3.56	4.30	99.07
50.7	74.00	0.30	13.42	1.62	0.28	1.33	3.46	4.24	98.65
55.4	73.87	0.34	13.59	1.63	0.26	1.35	3.57	4.18	98.80
60.1	74.15	0.15	13.68	1.63	0.28	1.27	3.65	4.30	99.12
65.3	74.03	0.29	13.52	1.76	0.28	1.29	3.63	4.25	99.05

Chal-Rhy-7-1, major element profile

x (μm)	SiO_2	TiO_2	Al_2O_3	FeO	MgO	CaO	Na_2O	K_2O	Total
6.7	72.30	0.23	13.32	1.06	0.26	1.17	2.52	2.76	93.62
13.2	72.81	0.25	12.90	1.13	0.26	1.12	2.06	2.81	93.33
17.5	71.96	0.31	12.94	1.24	0.26	1.18	1.82	2.78	92.48
22.4	71.55	0.23	12.55	1.23	0.28	1.14	1.97	2.77	91.72
28.0	71.76	0.24	12.89	1.32	0.27	1.17	2.06	2.80	92.51
33.2	72.15	0.30	12.87	1.40	0.30	1.15	2.25	2.76	93.20
37.7	71.12	0.21	12.75	1.37	0.22	1.18	1.86	2.76	91.48
42.8	71.40	0.24	12.89	1.49	0.28	1.13	1.92	2.75	92.10
47.9	71.79	0.21	12.98	1.43	0.26	1.13	2.18	2.77	92.75
52.7	71.31	0.28	12.92	1.49	0.25	1.14	2.18	2.76	92.33
57.7	71.70	0.31	12.98	1.57	0.25	1.13	2.14	2.80	92.88
63.0	71.86	0.31	13.05	1.52	0.23	1.16	2.19	2.80	93.11
68.0	71.47	0.23	12.72	1.53	0.25	1.15	2.08	2.78	92.21
72.7	71.72	0.21	13.02	1.55	0.24	1.12	1.88	2.78	92.53
77.7	71.45	0.23	12.96	1.51	0.25	1.12	2.10	2.72	92.35
83.0	71.69	0.31	12.95	1.50	0.27	1.16	2.07	2.76	92.71
87.8	71.57	0.23	12.83	1.56	0.24	1.12	2.06	2.66	92.27
92.9	71.50	0.22	13.02	1.60	0.24	1.11	2.05	2.77	92.51
97.8	71.36	0.27	13.02	1.55	0.27	1.12	2.09	2.74	92.41
102.3	71.78	0.28	12.85	1.58	0.24	1.10	1.79	2.77	92.39
107.7	71.46	0.23	13.06	1.55	0.21	1.15	2.00	2.75	92.40
118.1	71.45	0.25	13.07	1.57	0.24	1.05	2.33	2.77	92.74
127.6	71.31	0.26	12.75	1.59	0.26	1.11	2.33	2.68	92.29
137.9	71.91	0.20	13.06	1.60	0.24	1.12	2.25	2.75	93.11
147.9	71.53	0.23	12.82	1.57	0.26	1.08	2.28	2.74	92.52
157.6	71.93	0.28	13.09	1.64	0.22	1.15	2.23	2.75	93.29
168.1	71.08	0.22	13.02	1.63	0.25	1.10	2.34	2.73	92.37
176.7	71.43	0.21	12.92	1.60	0.22	1.12	2.42	2.85	92.77
187.7	71.79	0.27	13.01	1.56	0.28	1.07	2.37	2.74	93.09
196.8	71.70	0.30	13.00	1.64	0.24	1.14	2.34	2.71	93.06
206.9	71.42	0.22	12.96	1.61	0.21	1.05	2.29	2.75	92.50
5.3	71.45	0.27	13.02	0.97	0.23	1.16	2.31	2.81	92.24
13.0	72.17	0.23	12.90	1.14	0.27	1.23	2.19	2.87	93.01
18.7	71.86	0.24	12.87	1.22	0.22	1.16	2.16	2.78	92.53
24.3	71.91	0.25	12.84	1.26	0.25	1.19	2.14	2.82	92.65
31.2	71.17	0.23	12.95	1.34	0.24	1.21	2.22	2.81	92.18
37.2	71.10	0.21	12.90	1.45	0.23	1.18	1.96	2.81	91.84

42.9	72.43	0.33	12.97	1.36	0.27	1.16	2.13	2.79	93.43
48.6	72.03	0.26	12.86	1.39	0.21	1.13	2.26	2.73	92.87
55.2	72.06	0.21	12.92	1.54	0.25	1.15	2.18	2.80	93.11
61.0	72.68	0.24	12.92	1.52	0.25	1.16	2.12	2.81	93.69
67.0	71.72	0.22	12.78	1.49	0.22	1.15	2.18	2.78	92.54
73.0	71.67	0.31	12.91	1.53	0.24	1.14	2.21	2.75	92.75
78.6	71.47	0.23	12.86	1.52	0.24	1.16	2.12	2.79	92.41
85.0	71.74	0.31	13.03	1.54	0.23	1.11	2.00	2.78	92.73
90.5	71.75	0.23	12.65	1.57	0.27	1.17	2.23	2.77	92.64
97.0	71.57	0.28	12.95	1.52	0.24	1.14	2.17	2.77	92.64
102.6	71.54	0.26	12.95	1.58	0.28	1.13	2.18	2.78	92.70
113.0	71.63	0.21	13.09	1.59	0.24	1.08	2.42	2.74	92.99
123.4	69.94	0.25	12.94	1.52	0.26	1.11	2.24	2.67	90.93
132.6	71.26	0.28	12.91	1.57	0.23	1.07	2.23	2.64	92.19
143.2	72.13	0.23	12.88	1.54	0.20	1.13	2.12	2.75	92.98
153.5	71.26	0.23	12.87	1.54	0.24	1.08	2.39	2.68	92.29
163.1	71.94	0.24	13.00	1.59	0.27	1.09	2.21	2.71	93.06
173.1	71.05	0.28	13.06	1.55	0.22	1.15	2.25	2.68	92.25
182.7	71.64	0.28	12.94	1.55	0.23	1.11	2.27	2.69	92.72
193.2	71.71	0.24	13.06	1.65	0.28	1.03	2.18	2.71	92.85
202.8	72.05	0.24	13.06	1.60	0.26	1.10	2.32	2.68	93.31
4.0	72.76	0.27	12.97	1.06	0.26	1.21	2.61	2.77	93.91
11.0	72.25	0.22	12.95	1.24	0.29	1.18	2.33	2.85	93.31
17.2	72.44	0.23	13.03	1.29	0.26	1.19	2.29	2.71	93.44
23.4	72.39	0.26	12.99	1.39	0.26	1.22	2.43	2.75	93.68
29.4	72.26	0.31	13.01	1.44	0.25	1.17	2.10	2.79	93.33
35.7	72.08	0.22	12.82	1.46	0.27	1.14	2.36	2.75	93.10
41.7	72.09	0.29	12.86	1.48	0.25	1.20	2.29	2.73	93.19
47.5	72.17	0.24	13.12	1.61	0.27	1.19	2.27	2.76	93.62
53.5	72.05	0.21	12.80	1.56	0.29	1.14	2.18	2.69	92.92
59.9	72.11	0.24	13.04	1.50	0.26	1.16	2.36	2.70	93.37
65.3	72.50	0.28	12.89	1.56	0.22	1.15	2.14	2.70	93.44
71.3	72.00	0.23	13.01	1.51	0.28	1.09	1.88	2.59	92.59
77.9	71.85	0.32	12.93	1.54	0.26	1.09	2.16	2.74	92.89
83.8	72.12	0.29	13.00	1.60	0.25	1.12	2.22	2.73	93.34
89.3	71.96	0.22	12.84	1.54	0.25	1.16	2.15	2.69	92.80
95.4	72.16	0.26	13.01	1.55	0.23	1.15	2.23	2.69	93.27
106.1	72.08	0.21	13.04	1.62	0.28	1.15	2.50	2.68	93.56
115.3	71.99	0.27	12.92	1.59	0.28	1.09	2.35	2.72	93.21

125.5	71.97	0.25	13.00	1.56	0.22	1.13	2.46	2.71	93.29
135.8	71.45	0.31	13.01	1.61	0.25	1.12	2.39	2.70	92.86
145.5	71.67	0.24	12.86	1.62	0.22	1.12	2.48	2.76	92.96
155.8	72.37	0.23	12.99	1.53	0.26	1.15	2.29	2.70	93.51
166.0	70.63	0.20	12.87	1.54	0.26	1.11	2.23	2.76	91.60
175.5	71.95	0.30	13.07	1.53	0.25	1.14	2.47	2.65	93.37
185.2	71.94	0.23	13.06	1.53	0.26	1.12	2.36	2.68	93.17
195.3	71.52	0.26	12.88	1.59	0.23	1.04	2.55	2.72	92.78
206.0	71.62	0.18	12.82	1.59	0.25	1.11	2.24	2.68	92.49
6.6	72.55	0.25	12.94	1.01	0.23	1.17	2.44	2.80	93.38
14.0	72.22	0.23	13.04	1.09	0.26	1.23	2.44	2.86	93.37
21.1	71.59	0.25	12.74	1.17	0.26	1.18	2.32	2.85	92.35
28.1	71.86	0.28	12.99	1.27	0.29	1.19	2.36	2.84	93.09
35.3	71.62	0.28	13.06	1.34	0.24	1.18	2.42	2.75	92.91
42.2	71.63	0.24	12.76	1.38	0.27	1.13	2.19	2.78	92.39
49.3	71.57	0.18	12.71	1.47	0.27	1.18	2.30	2.75	92.43
56.1	71.75	0.26	12.97	1.44	0.27	1.20	2.31	2.73	92.93
63.3	71.53	0.18	12.90	1.50	0.23	1.19	2.31	2.73	92.58
70.6	71.60	0.30	12.97	1.59	0.25	1.14	2.29	2.74	92.88
77.2	71.82	0.24	12.99	1.50	0.27	1.20	2.30	2.77	93.09
84.1	72.12	0.21	12.99	1.57	0.24	1.18	2.25	2.72	93.28
91.7	71.20	0.32	12.98	1.50	0.24	1.11	2.23	2.73	92.30
98.5	72.38	0.27	12.80	1.57	0.25	1.16	2.57	2.82	93.83
105.2	71.19	0.19	12.77	1.57	0.25	1.13	2.31	2.68	92.10
112.4	71.51	0.21	12.87	1.59	0.27	1.15	2.17	2.74	92.51

Chal-Rhy-9-1, major element profile

x (μm)	SiO_2	TiO_2	Al_2O_3	FeO	MgO	CaO	Na_2O	K_2O	Total
6.6	77.42	0.22	14.41	1.13	0.23	0.91	4.33	3.52	102.18
27.4	76.60	0.22	14.07	1.90	0.16	0.79	3.86	3.44	101.03
47.6	75.92	0.20	14.11	1.96	0.16	0.80	3.88	3.45	100.48
67.1	75.93	0.25	14.13	2.01	0.15	0.88	3.68	3.45	100.49
4.6	77.08	0.30	13.98	0.85	0.18	0.82	4.25	3.29	100.74
10.5	75.64	0.17	13.93	1.50	0.20	0.97	3.83	3.31	99.56
15.2	75.41	0.23	13.86	1.67	0.17	0.92	3.96	3.29	99.51
20.6	75.35	0.23	13.87	1.83	0.17	0.93	3.88	3.39	99.66
25.6	75.36	0.16	14.00	1.89	0.12	0.88	3.72	3.40	99.53
30.1	74.95	0.21	13.91	1.86	0.14	0.84	3.96	3.37	99.24
35.0	74.92	0.17	13.92	1.83	0.15	0.84	3.87	3.32	99.01
40.5	75.30	0.21	13.68	1.74	0.11	0.77	3.94	3.30	99.05
45.7	75.29	0.21	13.95	1.85	0.15	0.78	3.92	3.38	99.53
51.3	74.76	0.29	13.98	1.90	0.13	0.77	3.75	3.36	98.94
55.5	74.60	0.20	14.23	1.93	0.16	0.82	4.38	3.51	99.83
60.8	75.07	0.25	14.23	2.00	0.15	0.78	3.76	3.39	99.63
65.5	74.78	0.25	13.85	1.94	0.13	0.82	3.96	3.39	99.12
70.8	74.86	0.23	13.93	1.96	0.18	0.85	3.91	3.35	99.27
76.1	74.50	0.17	13.80	1.96	0.21	0.81	3.65	3.34	98.45
80.3	74.16	0.22	14.19	2.11	0.20	0.87	3.80	3.38	98.93
85.5	74.28	0.22	14.22	2.06	0.18	0.85	3.78	3.36	98.96
90.4	74.33	0.15	14.08	1.93	0.15	0.83	3.74	3.33	98.52
9.5	75.43	0.21	13.91	1.42	0.28	1.03	4.05	3.28	99.62
15.1	75.13	0.23	14.12	1.80	0.25	1.02	3.98	3.35	99.88
20.3	75.14	0.22	14.30	1.90	0.17	0.97	4.03	3.38	100.11
25.4	75.02	0.19	14.03	1.93	0.17	0.89	4.05	3.34	99.61
29.6	74.83	0.22	13.91	1.99	0.15	0.87	4.13	3.51	99.60
34.6	75.13	0.21	13.83	1.93	0.15	0.79	3.89	3.40	99.33
40.6	74.84	0.21	14.05	1.94	0.16	0.81	3.97	3.38	99.36
45.2	74.87	0.20	13.97	2.02	0.14	0.82	3.69	3.46	99.16
49.4	74.90	0.22	13.97	1.92	0.16	0.78	3.87	3.35	99.18
54.4	74.67	0.24	13.98	1.95	0.18	0.76	3.81	3.40	98.98
59.2	74.39	0.21	14.07	1.91	0.14	0.78	3.74	3.58	98.82
62.6	74.26	0.19	14.35	1.84	0.13	0.72	3.87	3.60	98.94
6.6	76.03	0.24	13.98	1.25	0.30	0.92	3.84	3.31	99.85
12.0	75.38	0.24	13.94	1.68	0.20	0.94	3.95	3.43	99.77
16.3	75.05	0.13	14.11	1.81	0.21	0.94	4.18	3.33	99.77

19.9	75.37	0.24	14.14	1.89	0.18	0.97	4.05	3.39	100.23
24.6	75.19	0.18	13.95	1.87	0.18	0.85	3.89	3.42	99.52
29.2	74.99	0.22	13.96	1.86	0.15	0.87	3.84	3.45	99.35
32.8	75.57	0.20	13.90	1.86	0.17	0.81	3.88	3.39	99.78
36.9	75.40	0.23	13.76	1.85	0.16	0.75	3.83	3.36	99.35
41.8	75.08	0.23	14.18	1.94	0.15	0.79	3.87	3.44	99.69
45.4	75.34	0.22	14.14	1.96	0.12	0.79	3.89	3.38	99.83
49.4	75.50	0.23	14.07	1.95	0.15	0.78	3.99	3.51	100.19
53.1	74.56	0.18	14.47	1.89	0.14	0.79	3.61	3.53	99.17
5.3	76.80	0.26	14.26	1.00	0.24	0.96	5.09	4.03	102.64
9.8	75.78	0.24	14.36	1.54	0.24	0.98	5.09	4.01	102.23
13.5	75.94	0.23	14.11	1.79	0.21	0.98	4.98	4.00	102.25
17.6	75.46	0.19	14.17	1.83	0.19	0.97	5.07	4.07	101.94
21.4	75.90	0.27	14.19	1.97	0.16	0.90	5.06	4.06	102.52
25.5	76.00	0.22	14.31	2.01	0.17	0.91	4.82	4.02	102.46
30.2	75.60	0.19	14.05	1.92	0.17	0.86	4.96	4.12	101.86
33.4	76.01	0.21	14.31	1.89	0.11	0.81	4.65	4.05	102.04
37.4	75.61	0.19	14.26	1.90	0.14	0.82	5.06	4.13	102.12
41.3	75.63	0.19	14.36	1.96	0.12	0.78	4.94	4.20	102.16
45.5	75.60	0.19	14.25	2.08	0.17	0.81	4.87	4.13	102.10
5.5	75.98	0.24	14.05	0.91	0.28	0.94	5.00	4.17	101.57
10.4	76.13	0.24	14.29	1.42	0.21	0.97	5.24	4.11	102.61
14.0	75.90	0.27	14.22	1.68	0.20	0.98	4.97	4.12	102.33
17.9	75.47	0.19	14.15	1.75	0.17	0.93	4.96	4.11	101.74
21.5	75.58	0.24	14.08	1.85	0.18	0.93	4.97	4.09	101.92
25.8	75.50	0.23	14.32	1.99	0.15	0.88	4.82	4.16	102.04
29.2	75.34	0.12	14.19	1.83	0.15	0.87	5.12	4.19	101.82
33.1	75.42	0.20	14.23	1.89	0.15	0.87	4.67	4.21	101.64
37.4	75.75	0.21	14.31	1.91	0.17	0.86	5.08	4.14	102.42
41.3	75.18	0.22	14.25	1.88	0.15	0.81	4.64	4.09	101.21
45.1	75.30	0.23	14.29	2.05	0.14	0.78	4.83	4.14	101.75

Chal-Rhy-10-1, major element profile

x (μm)	SiO_2	TiO_2	Al_2O_3	FeO	MgO	CaO	Na_2O	K_2O	Total
5.2	78.03	0.19	14.32	0.46	0.21	0.76	4.41	3.63	102.00
25.1	76.41	0.21	14.25	1.60	0.17	0.89	4.10	3.51	101.15
45.0	76.04	0.27	14.18	1.85	0.16	0.87	3.90	3.41	100.68
64.8	76.08	0.24	14.31	2.01	0.13	0.81	4.04	3.58	101.20
5.6	75.97	0.18	14.12	0.47	0.14	0.86	4.14	3.34	99.23
12.3	75.69	0.20	14.03	0.93	0.14	0.87	3.85	3.37	99.09
17.3	75.36	0.20	13.88	1.21	0.18	0.84	4.10	3.35	99.13
22.5	74.75	0.21	13.73	1.45	0.16	0.88	3.85	3.40	98.43
27.1	74.48	0.14	13.77	1.60	0.15	0.91	3.98	3.30	98.33
32.3	74.80	0.30	13.94	1.68	0.15	0.87	3.71	3.34	98.80
37.7	75.13	0.19	14.04	1.79	0.14	0.87	4.00	3.35	99.51
42.7	74.19	0.21	13.98	1.86	0.15	0.89	3.86	3.33	98.46
46.8	74.36	0.22	13.85	1.80	0.16	0.86	3.83	3.44	98.52
53.7	74.62	0.17	13.90	1.81	0.16	0.80	3.85	3.36	98.67
63.9	74.34	0.30	13.79	1.93	0.14	0.77	3.81	3.40	98.48
71.4	74.26	0.21	13.88	1.90	0.18	0.79	3.85	3.42	98.49
79.3	74.47	0.25	14.02	1.94	0.15	0.79	3.80	3.45	98.86
87.3	74.59	0.19	13.95	1.99	0.15	0.75	3.65	3.39	98.65
95.0	74.01	0.23	13.95	1.85	0.16	0.78	3.86	3.41	98.26
103.1	73.94	0.29	13.95	1.95	0.14	0.79	3.61	3.41	98.08
110.7	73.93	0.20	13.77	1.97	0.13	0.77	3.56	3.37	97.71
123.6	74.01	0.25	13.70	1.99	0.13	0.83	3.72	3.42	98.05
135.0	73.72	0.24	14.03	1.98	0.14	0.86	3.72	3.45	98.14
146.7	73.09	0.21	14.08	2.07	0.18	0.90	3.60	3.47	97.60
159.0	71.90	0.19	15.06	2.16	0.18	1.00	4.15	3.57	98.20
171.7	73.24	0.23	13.84	1.89	0.17	0.89	3.77	3.50	97.52
184.0	73.54	0.22	13.84	1.99	0.14	0.84	3.88	3.47	97.92
195.5	73.66	0.26	13.84	1.96	0.18	0.85	3.68	3.46	97.88
207.8	73.26	0.22	13.79	2.07	0.18	0.84	3.65	3.49	97.50
5.9	75.32	0.23	13.96	0.49	0.14	0.84	3.99	3.42	98.38
12.0	74.84	0.20	13.99	0.92	0.15	0.82	4.04	3.40	98.36
17.3	74.62	0.18	14.02	1.25	0.13	0.84	4.06	3.43	98.53
21.9	74.28	0.19	13.90	1.43	0.18	0.91	3.89	3.39	98.18
27.3	74.40	0.24	13.87	1.62	0.17	0.92	3.77	3.41	98.40
32.4	74.07	0.16	13.76	1.67	0.17	0.84	3.74	3.39	97.80
37.9	73.81	0.21	13.94	1.70	0.16	0.88	3.78	3.33	97.83
42.3	73.73	0.16	13.99	1.75	0.16	0.91	3.82	3.42	97.94

46.7	73.98	0.26	13.85	1.87	0.17	0.88	3.81	3.38	98.21
55.7	73.85	0.28	13.92	1.96	0.11	0.85	3.73	3.45	98.15
63.2	73.69	0.25	14.14	1.86	0.13	0.87	3.95	3.34	98.23
69.8	73.80	0.20	14.03	1.90	0.15	0.79	3.87	3.40	98.13
77.8	73.83	0.21	13.78	1.87	0.16	0.79	3.97	3.44	98.06
85.2	73.64	0.17	13.83	1.89	0.17	0.77	3.81	3.43	97.71
93.6	73.36	0.25	13.91	1.97	0.16	0.80	3.70	3.44	97.61
102.4	73.23	0.21	13.84	1.99	0.17	0.79	3.77	3.44	97.44
111.9	73.66	0.22	14.03	2.06	0.14	0.79	3.83	3.52	98.24
123.3	73.31	0.26	13.95	1.98	0.17	0.80	3.67	3.36	97.50
133.6	73.48	0.27	13.90	2.00	0.14	0.83	3.67	3.42	97.71
145.3	73.33	0.21	13.63	2.08	0.16	0.78	3.83	3.47	97.51
159.4	73.21	0.22	13.81	2.03	0.17	0.86	3.77	3.41	97.46
169.2	73.21	0.25	13.87	2.06	0.20	0.87	3.85	3.40	97.70
183.1	73.03	0.20	13.82	2.11	0.15	0.84	3.71	3.47	97.33
195.6	72.97	0.25	13.80	2.16	0.15	0.85	3.68	3.47	97.32
206.6	73.20	0.23	13.69	2.14	0.15	0.79	3.90	3.45	97.54
5.6	75.45	0.18	14.11	0.53	0.15	0.79	3.96	3.44	98.61
10.8	75.36	0.29	13.99	0.84	0.15	0.81	3.96	3.38	98.78
14.9	75.18	0.28	14.02	1.06	0.15	0.87	4.27	3.41	99.24
18.7	75.04	0.24	13.95	1.22	0.21	0.90	4.03	3.32	98.90
23.9	74.76	0.26	14.22	1.46	0.19	0.94	4.07	3.31	99.21
29.5	74.79	0.18	14.15	1.68	0.17	0.90	4.00	3.48	99.35
34.4	74.40	0.20	13.83	1.77	0.18	0.90	3.01	3.43	97.73
38.6	74.51	0.18	13.85	1.77	0.14	0.89	3.88	3.39	98.60
44.1	74.64	0.17	13.89	1.75	0.15	0.84	3.96	3.41	98.82
49.6	74.40	0.23	13.72	1.80	0.15	0.82	3.88	3.42	98.42
59.5	74.19	0.20	13.77	1.81	0.14	0.78	3.77	3.38	98.04
69.2	74.51	0.27	13.94	1.97	0.10	0.77	3.82	3.44	98.83
79.6	74.24	0.21	13.86	1.95	0.15	0.72	3.68	3.54	98.35
88.1	73.92	0.23	13.99	2.04	0.11	0.76	3.94	3.36	98.36
97.9	74.00	0.17	14.00	2.05	0.17	0.77	3.76	3.44	98.37
108.4	73.91	0.24	14.01	2.04	0.17	0.79	3.71	3.52	98.38
118.4	73.66	0.26	13.91	2.01	0.13	0.80	3.65	3.51	97.94
128.5	73.71	0.27	13.87	1.96	0.13	0.84	3.76	3.48	98.02
138.2	73.62	0.25	13.79	2.02	0.15	0.81	3.75	3.48	97.88
149.4	73.86	0.20	13.88	1.99	0.13	0.82	3.72	3.48	98.08
159.3	73.76	0.20	13.84	2.02	0.14	0.79	3.73	3.37	97.86
4.9	75.67	0.26	14.26	0.50	0.17	0.85	4.16	3.38	99.25

10.5	75.46	0.24	14.35	0.88	0.15	0.87	3.94	3.37	99.25
14.4	74.76	0.17	14.05	1.05	0.16	0.92	3.98	3.38	98.47
17.6	74.24	0.25	13.97	1.31	0.17	0.92	3.87	3.32	98.05
21.4	74.91	0.18	13.98	1.40	0.17	0.91	3.74	3.41	98.69
27.3	74.52	0.23	13.96	1.65	0.16	0.87	3.98	3.44	98.80
32.0	74.42	0.27	13.83	1.70	0.15	0.92	4.53	3.44	99.26
36.6	74.42	0.28	13.91	1.78	0.16	0.90	3.90	3.38	98.74
41.8	74.39	0.25	13.96	1.79	0.15	0.82	3.78	3.35	98.49
47.3	74.06	0.23	13.79	1.86	0.11	0.88	3.94	3.39	98.27
56.5	73.98	0.27	13.98	1.96	0.13	0.81	3.80	3.42	98.34
67.4	74.14	0.15	13.94	1.96	0.15	0.82	3.89	3.38	98.41
77.5	73.90	0.26	13.90	1.98	0.16	0.77	3.91	3.41	98.29
86.8	73.96	0.20	13.91	1.94	0.19	0.81	3.74	3.43	98.17
97.0	73.78	0.20	13.87	1.97	0.15	0.76	3.88	3.44	98.06
106.5	74.03	0.20	13.83	1.93	0.14	0.80	3.55	3.47	97.97
117.5	73.74	0.22	13.88	1.95	0.13	0.81	3.65	3.42	97.79
126.6	73.74	0.21	13.74	1.97	0.11	0.82	3.82	3.50	97.91
136.8	73.84	0.20	13.98	2.08	0.12	0.86	3.76	3.37	98.21
147.1	73.38	0.27	13.89	2.16	0.17	0.87	3.55	3.55	97.84
157.4	73.23	0.17	13.86	2.14	0.16	0.88	3.69	3.44	97.58

Chal-Rhy-12-1, major element profile

x (μm)	SiO_2	TiO_2	Al_2O_3	FeO	MgO	CaO	Na_2O	K_2O	Total
5.6	73.56	0.24	13.19	0.65	0.22	1.13	2.90	3.32	95.21
9.6	73.56	0.24	12.83	0.88	0.27	1.16	2.81	3.21	94.95
14.0	73.02	0.27	13.06	1.11	0.27	1.20	2.75	3.21	94.90
18.3	72.83	0.20	13.14	1.24	0.27	1.21	2.63	3.17	94.70
23.1	73.67	0.26	12.94	1.37	0.26	1.18	2.61	3.15	95.44
28.5	73.15	0.30	13.22	1.53	0.26	1.23	2.66	3.14	95.49
33.9	73.84	0.23	13.21	1.55	0.26	1.21	2.74	3.07	96.12
38.6	73.14	0.31	13.05	1.59	0.26	1.14	2.60	3.13	95.24
43.3	73.38	0.33	13.11	1.58	0.22	1.14	2.57	3.10	95.43
53.3	73.23	0.26	13.18	1.58	0.28	1.12	2.78	3.22	95.66
62.5	73.14	0.30	13.22	1.63	0.26	1.16	2.68	3.07	95.47
72.4	73.12	0.28	13.13	1.65	0.25	1.13	2.61	3.06	95.23
81.4	73.82	0.22	13.16	1.63	0.26	1.09	2.82	3.32	96.32
92.6	73.59	0.22	13.20	1.60	0.25	1.16	2.68	3.06	95.75
100.8	73.45	0.25	13.25	1.56	0.25	1.07	2.59	3.07	95.50
111.5	74.25	0.26	13.54	1.62	0.27	1.14	2.58	3.17	96.82
121.1	72.90	0.24	13.36	1.60	0.24	1.13	2.63	3.03	95.14
4.1	74.97	0.23	13.03	0.59	0.26	1.10	3.05	3.29	96.52
8.5	73.63	0.34	13.10	0.83	0.26	1.20	2.79	3.24	95.39
12.7	73.47	0.33	13.32	1.04	0.24	1.16	2.83	3.16	95.55
17.9	73.48	0.18	12.99	1.24	0.29	1.23	2.71	3.12	95.23
22.4	73.56	0.22	12.93	1.39	0.26	1.20	2.83	3.09	95.48
27.4	73.21	0.24	12.99	1.37	0.28	1.22	2.62	3.07	95.00
32.4	73.82	0.19	13.35	1.52	0.22	1.13	2.72	3.18	96.12
37.8	73.71	0.27	13.05	1.55	0.25	1.18	2.57	3.15	95.72
42.5	73.24	0.21	13.04	1.60	0.25	1.11	2.75	3.08	95.27
52.4	73.03	0.23	13.11	1.62	0.27	1.13	2.70	3.12	95.20
61.6	73.42	0.32	13.04	1.58	0.25	1.12	2.55	3.08	95.37
71.6	73.54	0.25	13.11	1.51	0.26	1.10	2.51	3.07	95.34
81.2	73.55	0.29	13.17	1.58	0.27	1.08	2.65	3.06	95.66
91.4	73.86	0.28	13.24	1.57	0.22	1.10	2.62	3.07	95.96
100.0	73.20	0.26	13.02	1.61	0.27	1.12	2.80	3.06	95.34
109.8	73.49	0.36	13.03	1.60	0.26	1.14	2.60	2.96	95.44
120.0	73.58	0.26	13.26	1.68	0.25	1.12	2.71	3.12	95.98
3.5	73.23	0.26	13.00	0.47	0.25	1.12	2.87	3.32	94.52
7.7	74.05	0.23	13.04	0.76	0.22	1.14	2.76	3.27	95.48
12.1	73.59	0.29	13.04	0.95	0.28	1.22	2.80	3.19	95.36

17.3	73.55	0.25	13.04	1.16	0.25	1.19	2.74	3.12	95.29
22.1	73.59	0.29	13.08	1.30	0.23	1.15	2.72	3.13	95.50
26.6	73.42	0.29	12.95	1.49	0.23	1.20	2.79	3.11	95.46
32.0	73.65	0.28	12.84	1.53	0.25	1.15	2.65	3.12	95.48
37.1	73.21	0.26	13.19	1.52	0.24	1.17	2.56	3.03	95.20
42.1	73.41	0.25	13.14	1.54	0.24	1.14	2.64	3.10	95.46
51.6	73.19	0.26	13.03	1.55	0.26	1.17	2.74	3.09	95.29
60.8	73.37	0.24	12.90	1.65	0.26	1.12	2.62	3.11	95.28
71.0	73.24	0.27	13.15	1.64	0.23	1.11	2.53	3.06	95.24
80.7	73.33	0.23	13.05	1.61	0.25	1.10	2.60	3.06	95.24
90.9	73.48	0.23	13.10	1.58	0.25	1.10	2.74	3.07	95.55
99.8	73.48	0.27	13.24	1.59	0.22	1.05	2.46	3.04	95.35
109.8	73.43	0.24	13.17	1.59	0.26	1.07	2.55	3.10	95.41
120.0	73.83	0.24	13.14	1.56	0.25	1.12	2.63	3.01	95.77
5.1	74.14	0.25	12.94	0.63	0.18	1.09	2.87	3.28	95.39
9.2	73.91	0.29	13.01	0.82	0.26	1.17	2.72	3.24	95.42
13.5	73.39	0.21	13.01	1.00	0.26	1.21	2.74	3.18	95.01
18.9	73.18	0.26	12.97	1.24	0.26	1.19	2.64	3.11	94.85
23.8	73.49	0.28	12.93	1.40	0.25	1.19	2.74	3.13	95.41
28.3	73.25	0.29	12.83	1.51	0.27	1.19	2.83	3.08	95.24
33.4	73.65	0.30	13.00	1.46	0.25	1.17	2.66	3.07	95.56
38.7	73.54	0.31	13.01	1.56	0.24	1.20	2.65	3.15	95.65
43.6	73.49	0.29	13.10	1.59	0.24	1.16	2.77	3.10	95.73
53.3	73.50	0.24	13.11	1.60	0.25	1.09	2.78	3.12	95.68
62.6	73.72	0.26	12.99	1.62	0.24	1.10	2.54	3.10	95.58
72.4	73.46	0.25	13.09	1.65	0.25	1.10	2.69	3.02	95.53
82.6	73.45	0.22	13.04	1.55	0.21	1.13	2.68	3.05	95.32
92.5	73.66	0.21	13.22	1.61	0.27	1.11	2.75	3.04	95.88
101.4	73.61	0.29	13.11	1.60	0.27	1.14	2.58	3.11	95.70
111.2	73.81	0.28	13.14	1.59	0.29	1.11	2.52	3.05	95.79
121.5	73.86	0.27	13.18	1.59	0.24	1.09	2.64	3.03	95.89

Chal-Rhy-13-1, major element profile

x (μm)	SiO_2	TiO_2	Al_2O_3	FeO	MgO	CaO	Na_2O	K_2O	Total
5.4	73.32	0.21	12.83	1.19	0.23	1.16	2.58	3.19	94.71
9.0	72.45	0.32	12.73	1.33	0.23	1.06	2.39	3.05	93.56
13.0	72.66	0.23	12.71	1.46	0.19	1.14	2.71	3.07	94.17
18.3	72.27	0.21	12.76	1.61	0.29	1.14	2.59	3.10	93.97
23.9	72.27	0.21	12.93	1.53	0.23	1.12	2.67	3.06	94.03
28.4	72.93	0.25	12.93	1.56	0.20	1.15	2.71	3.07	94.81
33.3	72.74	0.23	13.06	1.55	0.23	1.10	2.49	3.07	94.45
43.7	72.93	0.18	13.18	1.56	0.23	1.20	2.50	3.05	94.84
52.4	73.24	0.22	12.99	1.59	0.23	1.17	2.67	3.05	95.16
62.4	72.29	0.28	12.99	1.59	0.27	1.12	2.64	3.00	94.19
72.1	72.50	0.26	13.05	1.52	0.27	1.15	2.57	3.03	94.35
82.4	73.19	0.29	13.40	1.66	0.33	1.15	2.65	3.12	95.79
90.9	71.01	0.27	12.74	1.52	0.26	1.12	2.49	3.07	92.48
101.5	72.67	0.26	12.92	1.50	0.24	1.14	2.53	3.03	94.29
3.4	72.36	0.32	12.59	1.06	0.24	1.16	2.62	3.16	93.50
6.7	73.04	0.31	12.79	1.21	0.22	1.11	2.66	3.13	94.48
11.0	72.65	0.29	12.93	1.34	0.24	1.18	2.62	3.15	94.40
16.1	72.80	0.23	13.03	1.52	0.23	1.20	2.64	3.09	94.75
21.4	73.13	0.27	12.88	1.57	0.23	1.13	2.76	3.08	95.05
26.3	72.79	0.29	13.03	1.60	0.25	1.13	2.55	3.00	94.64
31.1	72.92	0.23	13.04	1.53	0.23	1.12	2.49	3.09	94.65
41.2	73.01	0.24	13.09	1.72	0.33	1.10	2.57	3.09	95.15
50.1	72.88	0.33	13.03	1.62	0.23	1.13	2.56	3.09	94.88
59.9	73.12	0.25	13.05	1.60	0.23	1.11	2.56	3.04	94.95
69.6	73.02	0.27	13.13	1.59	0.24	1.13	2.50	3.07	94.96
80.1	73.49	0.21	13.02	1.56	0.24	1.15	2.48	3.08	95.24
88.6	73.14	0.29	13.29	1.59	0.23	1.13	2.58	3.06	95.32
98.9	72.80	0.30	12.91	1.75	0.25	1.12	2.61	3.07	94.80
6.3	73.59	0.22	12.95	1.05	0.22	1.18	2.56	3.23	94.99
10.0	73.04	0.25	12.87	1.26	0.22	1.16	2.59	3.03	94.42
13.7	73.08	0.24	12.75	1.37	0.24	1.12	2.46	3.03	94.29
19.2	73.57	0.34	12.90	1.56	0.26	1.14	2.51	3.10	95.38
24.3	73.59	0.26	12.90	1.60	0.26	1.16	2.57	3.07	95.39
29.6	73.41	0.21	12.96	1.54	0.24	1.17	2.46	3.15	95.14
34.0	72.90	0.26	13.12	1.55	0.23	1.08	2.56	3.09	94.80
44.2	73.54	0.28	13.25	1.62	0.21	1.20	2.61	3.05	95.75
53.2	73.94	0.20	13.12	1.60	0.22	1.10	2.66	3.15	95.99

63.0	73.55	0.25	13.10	1.62	0.25	1.13	2.65	3.07	95.61
72.9	72.82	0.25	13.04	1.49	0.23	1.09	2.66	3.06	94.65
82.8	73.25	0.25	13.09	1.67	0.25	1.12	2.53	3.07	95.23
91.8	72.46	0.32	13.06	1.63	0.36	1.10	2.42	3.11	94.45
102.0	73.74	0.31	13.12	1.85	0.26	1.10	2.61	3.10	96.09
2.1	73.25	0.24	12.77	0.77	0.26	1.07	2.89	3.11	94.37
7.8	73.41	0.30	12.88	1.18	0.27	1.13	2.87	3.24	95.29
11.0	73.43	0.24	12.91	1.29	0.23	1.16	2.60	3.14	95.00
15.3	73.59	0.24	13.06	1.40	0.23	1.23	2.65	3.02	95.43
20.4	73.67	0.14	13.37	1.55	0.24	1.23	2.61	3.13	95.94
25.9	73.28	0.27	13.03	1.56	0.22	1.19	2.68	3.03	95.27
30.7	73.23	0.19	13.08	1.55	0.25	1.11	2.61	3.11	95.12
35.3	73.24	0.21	12.86	1.56	0.23	1.11	2.53	3.05	94.80
45.9	73.02	0.29	12.89	1.53	0.24	1.09	2.46	3.16	94.69
54.7	73.61	0.25	13.04	1.62	0.24	1.10	2.55	3.00	95.41
64.3	73.20	0.29	13.33	1.61	0.24	1.10	2.68	3.09	95.54
74.3	73.27	0.28	13.11	1.63	0.21	1.12	2.69	3.01	95.31
84.4	73.20	0.16	12.95	1.58	0.26	1.11	2.60	3.14	95.01
93.0	73.31	0.26	13.16	1.55	0.26	1.09	2.54	3.01	95.18
103.3	73.62	0.29	13.19	1.49	0.29	1.15	2.57	3.04	95.63
1.6	73.25	0.24	13.06	1.39	0.22	1.13	2.59	3.12	95.00
7.0	72.47	0.25	13.35	1.55	0.24	1.15	2.47	3.12	94.60
11.9	73.03	0.24	13.27	1.59	0.27	1.16	2.54	3.01	95.10
17.1	73.17	0.26	13.24	1.49	0.24	1.18	2.50	3.05	95.12
21.5	73.03	0.23	13.07	1.56	0.27	1.14	2.30	3.06	94.66
27.2	72.88	0.27	13.12	1.51	0.18	1.16	2.45	3.09	94.64
34.5	73.14	0.27	13.19	1.57	0.26	1.14	2.52	3.17	95.26
40.9	72.84	0.24	13.09	1.54	0.24	1.17	2.42	3.14	94.68
47.9	72.36	0.27	13.19	1.63	0.25	1.14	2.57	3.13	94.54
55.5	72.89	0.29	13.22	1.66	0.26	1.15	2.59	3.00	95.06
61.8	72.79	0.26	13.02	1.62	0.23	1.16	2.48	3.01	94.57
68.9	73.12	0.31	13.34	1.62	0.22	1.15	2.49	3.12	95.36
76.3	73.03	0.31	13.26	1.61	0.25	1.15	2.55	3.10	95.25
82.7	69.94	0.24	14.67	1.60	0.24	1.19	2.39	3.03	93.30
89.9	72.84	0.17	13.13	1.58	0.27	1.12	2.47	3.05	94.62
97.2	73.57	0.22	13.27	1.58	0.24	1.13	2.55	3.10	95.66

Chal-Rhy-14-1, major element profile

x (μm)	SiO_2	TiO_2	Al_2O_3	FeO	MgO	CaO	Na_2O	K_2O	Total
19.2	73.41	0.25	13.42	1.18	0.30	1.30	3.89	4.26	98.02
26.4	73.40	0.23	13.45	1.39	0.29	1.28	3.61	4.23	97.87
31.4	73.08	0.29	13.36	1.47	0.29	1.25	3.70	4.22	97.66
36.9	73.35	0.29	13.59	1.53	0.29	1.30	3.80	4.28	98.43
41.8	73.33	0.23	13.36	1.60	0.27	1.31	3.68	4.22	98.01
46.7	73.36	0.25	13.63	1.53	0.28	1.32	3.63	4.19	98.18
51.7	73.36	0.22	13.55	1.60	0.25	1.26	3.76	4.23	98.23
61.4	73.02	0.27	13.67	1.64	0.28	1.25	3.44	4.18	97.75
71.5	73.24	0.25	13.42	1.67	0.27	1.20	3.58	4.24	97.88
80.9	73.25	0.19	13.63	1.61	0.27	1.21	3.57	4.19	97.92
91.5	73.40	0.25	13.62	1.66	0.27	1.21	3.51	4.16	98.08
101.1	72.97	0.25	13.50	1.61	0.29	1.18	3.57	4.16	97.52
110.8	72.97	0.23	13.45	1.61	0.24	1.22	3.67	4.18	97.56
127.0	73.38	0.21	13.62	1.66	0.26	1.21	3.50	4.17	98.03
9.9	73.86	0.28	13.03	0.84	0.26	1.14	2.80	3.26	95.46
14.6	73.54	0.29	12.92	1.02	0.28	1.16	2.79	3.19	95.19
20.2	74.08	0.16	13.06	1.18	0.26	1.23	2.69	3.22	95.87
25.2	73.53	0.22	13.08	1.33	0.26	1.18	2.61	3.28	95.50
30.0	73.42	0.17	13.04	1.40	0.24	1.19	2.68	3.16	95.30
34.7	73.52	0.19	13.18	1.54	0.26	1.18	2.65	3.20	95.71
40.0	73.78	0.22	13.10	1.50	0.26	1.17	2.68	3.17	95.88
45.2	73.85	0.27	13.07	1.56	0.24	1.14	2.74	3.16	96.03
50.1	73.27	0.29	13.08	1.55	0.28	1.15	2.50	3.14	95.27
54.9	73.91	0.31	13.20	1.54	0.26	1.13	2.65	3.09	96.09
59.8	73.73	0.19	13.12	1.58	0.24	1.12	2.70	3.15	95.83
64.6	73.18	0.24	12.98	1.57	0.25	1.12	2.75	3.12	95.21
69.5	73.65	0.27	13.05	1.62	0.22	1.12	2.56	3.12	95.62
74.8	73.90	0.14	13.24	1.64	0.23	1.14	2.74	3.17	96.20
79.6	73.57	0.31	13.18	1.55	0.29	1.14	2.56	3.09	95.70
84.3	73.73	0.23	12.96	1.63	0.25	1.09	2.49	3.15	95.52
89.0	73.47	0.18	13.14	1.65	0.24	1.10	2.74	3.20	95.71
94.3	73.70	0.26	13.08	1.51	0.25	1.09	2.65	3.20	95.75
100.2	73.42	0.27	13.14	1.63	0.26	1.09	2.63	3.12	95.57
104.5	73.45	0.23	13.51	1.65	0.25	1.09	2.59	3.08	95.86
109.4	73.24	0.25	12.97	1.57	0.27	1.16	2.68	3.13	95.27
114.5	73.60	0.24	13.11	1.57	0.26	1.06	2.68	3.10	95.61
7.9	74.06	0.31	12.78	0.75	0.27	1.14	2.89	3.23	95.43

13.1	74.02	0.23	13.00	0.98	0.27	1.18	2.81	3.16	95.66
17.7	73.51	0.24	12.98	1.11	0.27	1.19	2.71	3.16	95.17
23.0	73.44	0.26	13.11	1.23	0.33	1.13	2.81	3.14	95.45
28.1	73.35	0.28	13.17	1.38	0.27	1.19	2.56	3.09	95.29
33.5	73.08	0.27	13.11	1.50	0.28	1.19	2.61	3.16	95.20
37.8	73.65	0.26	13.03	1.46	0.30	1.15	2.58	3.16	95.59
42.4	73.75	0.27	13.02	1.57	0.28	1.17	2.69	3.11	95.85
47.8	73.52	0.28	13.21	1.57	0.24	1.17	2.63	3.13	95.75
53.0	73.87	0.28	13.19	1.59	0.27	1.13	2.66	3.12	96.11
57.8	74.22	0.25	13.12	1.63	0.25	1.19	2.78	3.18	96.62
62.9	73.43	0.25	13.12	1.56	0.25	1.14	2.73	3.17	95.65
67.9	73.08	0.18	12.98	1.59	0.22	1.13	2.57	3.14	94.89
72.7	73.42	0.29	13.03	1.61	0.25	1.13	2.63	3.15	95.51
77.3	73.10	0.20	13.00	1.60	0.27	1.11	2.68	3.08	95.03
83.0	73.62	0.26	13.11	1.58	0.26	1.06	2.52	3.16	95.58
88.0	73.35	0.31	13.06	1.59	0.25	1.12	2.48	3.13	95.29
92.6	72.67	0.22	13.28	1.65	0.25	1.12	2.53	3.09	94.81
97.3	73.33	0.22	13.22	1.60	0.21	1.11	2.52	3.08	95.30
102.5	73.55	0.26	13.13	1.55	0.27	1.14	2.60	3.15	95.65
108.0	73.79	0.22	13.23	1.61	0.26	1.11	2.63	3.09	95.94
112.5	73.56	0.21	13.29	1.58	0.26	1.11	2.62	3.17	95.79
117.4	73.45	0.25	13.12	1.53	0.24	1.07	2.50	3.15	95.31
9.5	73.87	0.25	13.05	0.84	0.28	1.21	2.95	3.22	95.69
13.7	73.17	0.28	12.91	1.01	0.25	1.17	2.85	3.18	94.81
19.1	72.46	0.24	13.04	1.13	0.28	1.25	2.73	3.20	94.32
24.0	72.55	0.25	13.21	1.22	0.25	1.19	2.89	3.19	94.76
29.4	72.58	0.36	13.12	1.39	0.28	1.22	2.63	3.16	94.74
38.5	72.62	0.26	13.13	1.50	0.25	1.20	2.85	3.15	94.97
48.2	72.42	0.20	12.97	1.57	0.26	1.11	2.52	3.14	94.18
57.2	73.56	0.29	13.35	1.52	0.24	1.13	2.83	3.12	96.04
67.1	72.62	0.31	13.26	1.52	0.24	1.14	2.87	3.10	95.07
75.8	72.16	0.32	13.08	1.58	0.27	1.12	2.59	3.12	94.24
86.5	72.65	0.27	13.19	1.60	0.26	1.11	2.65	3.15	94.88
94.7	72.35	0.30	12.97	1.60	0.27	1.12	2.49	3.08	94.18
105.5	72.28	0.32	13.16	1.52	0.25	1.10	2.69	3.12	94.44
113.8	72.53	0.26	12.98	1.53	0.26	1.12	2.64	3.10	94.42
123.8	72.39	0.26	13.11	1.54	0.26	1.08	2.58	3.05	94.27
5.3	75.66	0.23	12.44	0.68	0.23	1.18	3.52	3.05	96.99
11.0	71.48	0.22	12.94	0.81	0.27	1.21	2.81	3.18	92.93

16.2	72.36	0.25	13.08	1.12	0.28	1.23	2.76	3.24	94.33
20.9	72.28	0.28	13.07	1.23	0.26	1.16	2.57	3.18	94.02
26.7	72.48	0.24	13.01	1.30	0.24	1.20	2.67	3.17	94.33
31.1	72.93	0.28	13.21	1.41	0.27	1.14	2.54	3.20	94.99
36.6	72.64	0.24	13.03	1.45	0.24	1.19	2.63	3.13	94.56
41.1	73.05	0.22	13.18	1.58	0.26	1.18	2.73	3.21	95.40
46.5	72.82	0.26	13.22	1.55	0.26	1.17	2.89	3.19	95.35
50.9	72.55	0.22	13.06	1.60	0.26	1.13	2.56	3.18	94.56
56.6	72.51	0.19	13.12	1.57	0.27	1.14	2.73	3.15	94.68
66.7	72.89	0.29	13.21	1.58	0.27	1.10	2.65	3.07	95.05
76.4	72.82	0.28	13.32	1.59	0.43	1.24	2.59	3.10	95.37
86.7	72.99	0.26	12.84	1.57	0.37	1.21	2.59	3.04	94.88

APPENDIX C

Supplemental data and figure for Chapter IV

Figure C1. Comparing measured trace element concentrations in the secondary standards (NIST 612, NIST 614, GOR128-G and KL2-G) and the reference values. Error bars in the figure are at 1σ level.

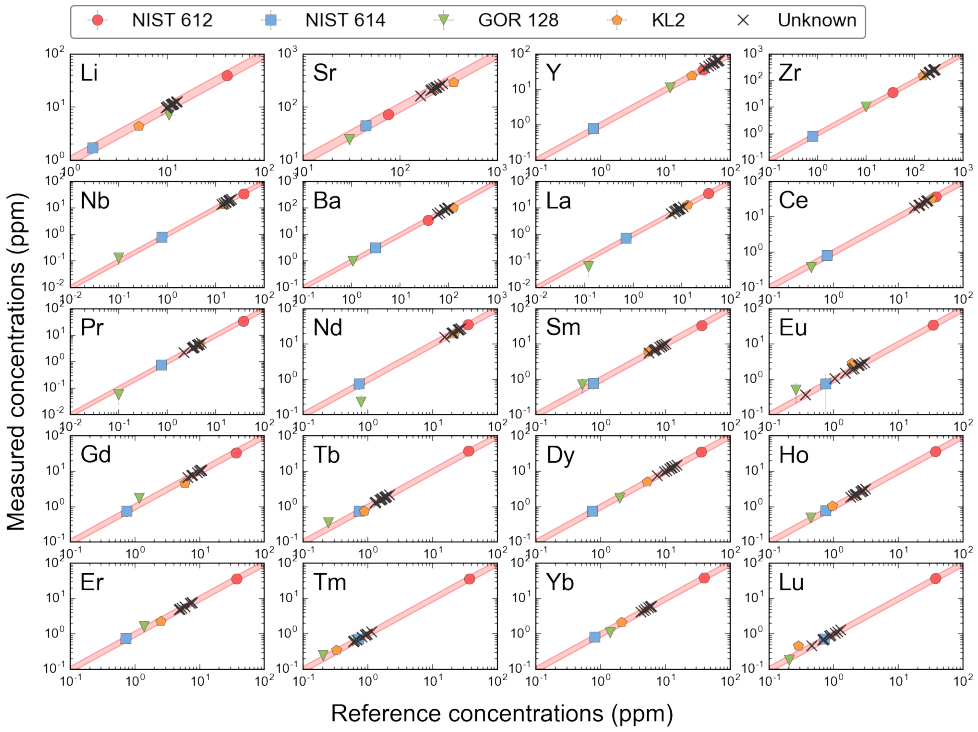

Table C1. Summarize of melt inclusion data for Chapter IV.

Lunar sample #	74220					
MI type	Homogenized					
MI#	1a	OldOL1	9	10Ba	12a	12b
Host olivine Fo#	81	81	81	80	79	79
Olivine radius (μm)	114	97	99	157	166	166
MI radius (μm)	22	9	10	10	19	9
SiO_2 (wt%)	39.42	41.33	40.43	40.02	39.71	41.27
TiO_2	11.79	12.2	11.82	11.28	11.55	12.38
Al_2O_3	7.82	8.77	7.9	7.61	7.84	8.74
FeO	21.74	15.5	18.87	21.75	20.4	18.17
MnO	0.31	0.34	0.32	0.3	0.33	0.32
MgO	6.23	4.95	5.645	4.85	6.53	4.93
CaO	10.1	13.97	11.54	10.69	10.64	12.1
Na_2O	0.45	0.4	0.454	0.45	0.44	0.53
K_2O	0.09	0.07	0.09	0.09	0.08	0.09
H_2O (ppm)	716	308	364	127	639	235
F	52.5	55.8	54.3	17.4	48.5	51.4
P	192	144	127	91	171	107
S	716	689	676	305	673	621
Cl	3.16	2.49	2.31	1.26	2.08	4.12
Li		11.7	12.7	10.3	12.4	
Na		4702	4045	3196	3519	
K		932	787	534	611	
Sr		239	254	162	237	
Y		57.0	63.6	40.7	66.4	
Zr		242	251	170	252	
Nb		19.4	19.5	13.2	18.7	
Ba		96	96	59	83	
La		9.1	8.3	6.1	9.4	
Ce		24.5	28.4	17.7	27.3	
Pr		3.56	4.24	2.23	4.56	
Nd		21	26	15.4	25	
Sm		8	9	5.6	10	
Eu		2	3	0.4	2	
Gd		11	10	7.8	11	
Tb		1.6	2.0	1.3	2.2	
Dy		11.7	12.8	7.5	13.8	
Ho		2.2	3.1	1.8	2.9	
Er		5.9	7.7	4.8	7.2	
Tm		0.9	1.1	0.6	0.9	
Yb		4.6	5.8	4.2	5.9	
Lu		0.7	0.9	0.7	1.2	

Table C1. Continued.

Lunar sample #	74220				
MI type	Homogeniz	Unheated			
MI#	15	8a	10A	11	OldOl2
Host olivine Fo#	81	81	81	81	80
Olivine radius (μm)	47	147	132	125	197
MI radius (μm)	5	19	9	31	14
SiO_2 (wt%)	40.69	39.57	42.06	38.3	40.29
TiO_2	13.33	10.92	12.56	10.29	11.07
Al_2O_3	8.68	7.5	8.62	8.09	8.21
FeO	15.56	22.19	19.23	22.75	21.67
MnO	0.35	0.34	0.28	0.31	0.31
MgO	6.22	5.145	4.03	6.68	4.65
CaO	11.9	10.92	11.45	9.97	11.06
Na_2O	0.5	0.43	0.62	0.38	0.4
K_2O	0.1	0.08	0.13	0.072	0.09
H_2O (ppm)	97	948	538	994	902
F	48.3	50.9	43.4	45.1	46.7
P	202	161.2	203	122.8	277
S	800	699	702	602	664
Cl	3.84	3.53	4.19	3.44	6.13
Li	9.9	11.0	9.7	11.5	11.1
Na	3354	4192	3744	3051	3644
K	648	757	722	529	726
Sr	205	274	211	221	230
Y	50.5	67.6	46.3	54.4	63.4
Zr	204	265	200	209	261
Nb	16.0	20.9	16.3	14.7	18.3
Ba	84	95	83	66	98
La	7.7	8.7	7.2	7.1	10.8
Ce	21.6	27.7	20.8	21.3	28.7
Pr	3.40	4.15	3.58	3.28	5.07
Nd	20	27	20	21	25
Sm	7	10	7	6.6	8.7
Eu	1	3	3	2.1	1.5
Gd	8	10	6.6	9.2	11
Tb	1.8	1.9	1.7	1.3	1.5
Dy	10.5	15.1	9.6	12.5	12.5
Ho	2.3	2.8	2.2	2.0	2.6
Er	5.9	7.6	5.0	5.4	7.7
Tm	0.7	1.0	0.6	0.8	1.0
Yb	6.0	5.9	4.9	5.5	6.1
Lu	0.5	1.3	1.1	0.7	0.9

Table C2. Measured trace element concentrations for secondary standards compared to reference values. Their concentrations are also plotted in Fig. C1. Numbers in the bracket are 1σ errors for the last two digits. For some references, only one digit error is shown due to availability in literature

Sample	NIST 612	NIST 612 (ref)	NIST 614	NIST 614 (ref)	GOR128	GOR128 (ref)	KL2	KL2 (ref)
Li (ppm)	39.25(51)	41.5(29)	1.45(16)	1.7(02)	7.07(33)	10.4(17)	4.35(23)	5.10(50)
Na	95899(66)	103861	104492	93469	4271(21)	4258(193)	17381(38)	17434
K	70.3(23)	66.26(37)	38.7(27)		277.4(69)	299(42)	3834(23)	3985(83)
Sr	71.9(12)	76.2(23)	42.6(15)	44.3(6)	24.3(11)	30(1)	291.0(33)	356(8)
Y	35.25(40)	38.3(21)	0.89(10)	0.77(3)	11.04(34	11.8(5)	24.80(46)	25.4(11)
Zr	35.89(65)	36.0(13)	0.76(16)	0.80(4)	10.36(54)	10.0(5)	152.4(18)	152(5)
Nb	33.83(58)	38.06(86)	0.66(13)	0.78(3)	0.13(06)	0.099(7)	13.28(50)	15.0(5)
Ba	34.45(70)	37.7(13)	3.32(35)	3.1(2)	0.99(18)	1.06(3)	98.7(16)	123(5)
La	34.89(57)	35.8(22)	0.64(12)	0.72(3)	0.061(35)	0.121(4)	12.90(47)	13.1(2)
Ce	36.36(62)	38.4(16)	1.13(17)	0.79(3)	0.367(96)	0.450(16)	31.89(79)	32.4(7)
Pr	33.39(53)	37.16(93)	0.78(13)	0.75(3)	0.055(31)	0.100(4)	4.56(27)	4.6(1)
Nd	34.96(89)	35.2(24)	0.80(22)	0.74(3)	0.23(12)	0.784(47)	19.53(90)	21.6(4)
Sm	33.6(13)	36.7(26)	0.51(27)	0.77(8)	0.71(30)	0.525(20)	6.11(77)	5.54(9)
Eu	33.9(24)	34.4(16)	1.25(62)	0.75(5)	0.50(27)	0.264(8)	2.89(80)	1.92(4)
Gd	32.6(11)	37.0(11)	0.60(23)	0.75(6)	1.74(32)	1.17(4)	4.57(66)	5.9(2)
Tb	36.73(60)	35.9(27)	0.96(15)	0.74(3)	0.354(86)	0.248(12)	0.74(14)	0.890(31)
Dy	34.83(71)	35.97(82)	0.83(18)	0.74(6)	1.74(32)	1.98(7)	5.02(39)	5.22(12)
Ho	36.14(60)	37.9(11)	1.13(17)	0.76(4)	0.48(10)	0.443(19)	1.04(15)	0.961(22)
Er	36.11(84)	37.4(15)	0.59(18)	0.73(5)	1.64(26)	1.40(6)	2.29(30)	2.54(7)
Tm	35.69(61)	37.6(13)	0.75(14)	0.72(6)	0.249(74)	0.204(9)	0.352(88)	0.331(9)
Yb	38.17(72)	40.0(29)	0.78(16)	0.81(9)	1.09(20)	1.41(6)	2.15(25)	2.10(5)
Lu	36.87(71)	37.7(20)	0.52(14)	0.72(5)	0.18(08)	0.206(9)	0.47(12)	0.285(9)

APPENDIX D

Supplemental figure and data for Chapter V

Figure D1. Matrix effect in SIMS analyses for alkali elements and transition metals. Red solid lines and blue dashed lines in the figure are calibration curves based on MPI-DING standards and NIST standards, respectively. Matrix effect is significant for Co, Ni and Cu.

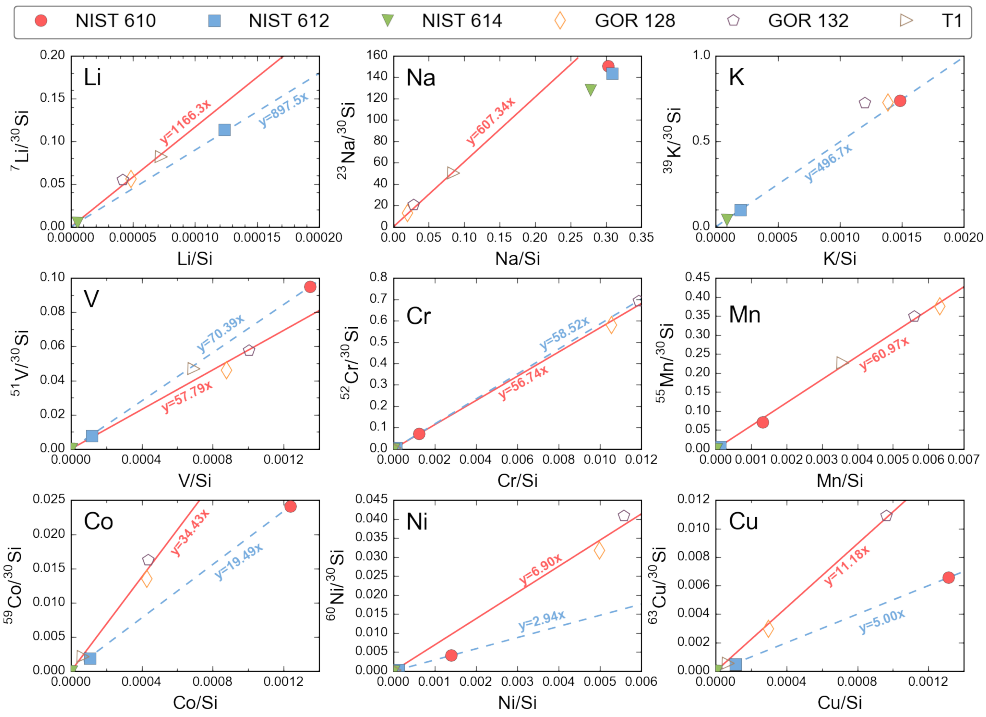

Table D1. Summarize of melt inclusion data for Chapter V.

Lunar sample #	15016				12040	
MI type	Homogenized				Homogenized	
Homogenization T (ºC)	1270	1300	1287	1300	1210	1200
Homogenization t (min)	2	10	2	10	10	8
MI#	OL8	OL10	OL12a	OL19	OL13	OL15a
Host olivine Fo#	65.0	69.5	57.1	64.8	51.4	53.9
Host olivine	0.26	0.76	0.24	0.25	0.38	0.73
MI diameter (μm)	25	29	31	49	34	70
SiO_2 (wt%)	48.01	48.3	45.12	44.26	44.88	41.57
TiO_2	2.13	1.94	2.13	2.04	4	6.17
Al_2O_3	9.77	9.12	9.2	8.15	7.93	7.9
FeO	17.22	19.04	23.64	24.5	25.71	26.04
MnO	0.21	0.24	0.25	0.34	0.25	0.27
MgO	7.87	8.6	6.01	8.1	6.4	6.81
CaO	11.31	10.41	10.04	9.05	8.95	8.74
Na_2O	0.26	0.24	0.27	0.35	0.26	0.32
K_2O	0.04	0.03	0.05	0.04	0.06	0.18
H_2O (ppm)	12.0	12.0	15.1	30.1	13.4	14.2
F	63.2	48.0	57.3	41.4	385	210
P	277	255	354	251	481	849
S†	907	834	905	833	867	2788
Cl	3.44	3.19	3.5	3.17	3.83	10.75
Li‡		*2.7*	*4.2*	*27.5*	*8.6*	*4.7*
Na		2092	2031	2773	2301	2676
K		209	288	211	377	1194
Sr		93	94	92	96	188
Y		29.3	28.8	32.0	171.1	122.0
Zr		101	116	106	125	376
Nb		7.2	7.0	6.4	7.9	22.4
Ba		42	58	50	61	192
La		5.3	6.2	6.3	5.7	16.4
Ce		15.7	19.3	17.4	17.2	46.8
Pr		2.0	2.2	2.8	2.7	7.3
Nd		12.2	12.0	13.3	15.2	36.3
Sm		4.1	2.7	3.7	6.7	11.1
Eu		0.7	3.2	0.7	1.2	1.6
Gd		4.8	6.3	6.9	13.7	16.6
Tb		0.9	1.0	0.8	3.4	2.9
Dy		6.4	6.3	5.7	28.4	21.2
Ho		1.2	0.9	1.5	5.9	4.5
Er		3.4	3.4	2.9	19.8	13.5
Tm		0.4	0.23	0.5	2.4	1.6

Yb		2.8	3.4	2.3	17.0	11.0
Lu		0.6	0.7	0.2	2.3	1.8
V		141.6	133.5	115.8		70.4
Cr		8835	6525	6439		2918
Mn		2860	2823	3833		3301
Co		28	46.5	58.4		73
Ni			15.2	56		21
Cu		14.0	26.6	4.3		52

† S concentrations for natural MIs in 74235 could be affected by sulfide globules in the MIs. Italicized S concentrations are corrected by excluding the cycles affected by sulfides and are less reliable.
‡ Italicized Li concentrations are for homogenized MIs, which have the concern of contamination during heating. Lithium concentrations for two MIs from 74235 are clearly affected by contamination and hence marked in red.

Table D1. Continued.

Lunar sample #	12040				15647	
MI type	Homogenized				Homogenized	
Homogenization T (ºC)	1180	1140	1160	1160	1280	1280
Homogenization t (min)	10	10	10	10	10	2
MI#	OL16b	OL36b	OL41	OL43	OL3	OL6
Host olivine Fo#	55.2	43.6	56.8	47.2	59.8	44.4
Host olivine	0.68	0.38	0.19	0.70	0.50	0.56
MI diameter (μm)	22	28	31	35	45	40
SiO_2 (wt%)	48.03	46.28	46.49	45.43	46.83	42.12
TiO_2	2.79	3.08	3.68	4.21	1.76	3.24
Al_2O_3	9.26	8.42	10.6	9.4	7.74	6.71
FeO	22.47	25.34	20.33	24.28	24.26	32.82
MnO	0.27	0.27	0.23	0.25	0.26	0.35
MgO	4.71	4.34	5.94	5.28	8.52	4.53
CaO	10.91	9.42	11.1	9.3	8.96	8.16
Na_2O	0.33	0.36	0.46	0.39	0.23	0.24
K_2O	0.05	0.09	0.1	0.14	0.05	0.08
H_2O (ppm)	7.1	14.4	12.2	14.0	11	15.4
F	149	501	578	331	27.7	82.9
P	310	419	498	291	227	382
S†	960	1113	1269	926	745	1507
Cl	4.29	5.18	7.38	3.61	2.44	5.57
Li‡		*5.1*	*4.8*	*4.5*	*4.0*	*6.2*
Na		3065	3484	3079	1763	1996
K		635	718	1037	319	580
Sr		128	145	116	85	105
Y		501.0	196.5	197.4	24.5	43.6
Zr		161	183	132	88	183
Nb		9.9	11.7	7.8	5.5	10.9
Ba		85	95	62	42	80
La		9.4	9.5	6.4	4.5	9.8
Ce		28.6	27.3	18.6	12.0	25.7
Pr		5.5	4.4	3.0	1.8	3.8
Nd		40.1	24.4	18.1	8.5	19.7
Sm		27.3	10.9	8.9	2.4	6.5
Eu		1.9	1.2	2.0	0.4	0.6
Gd		53.9	18.2	15.6	3.8	7.6
Tb		12.9	4.5	3.6	0.7	1.4
Dy		95.6	33.8	30.3	4.9	8.4
Ho		20.0	7.7	7.4	0.87	1.6
Er		52.0	20.9	21.6	2.3	4.8
Tm		5.8	2.6	3.5	0.31	0.60

Yb		36.8	15.7	21.8	1.8	3.7
Lu		4.8	2.4	3.0	0.43	0.44
V		30	63	18.9	150.7	111
Cr		1735	2516	1136	8941	4308
Mn		2129	2161	2222	3123	3891
Co		22	21	43	67	129
Ni		2.1	1.1	2.2	25.4	18
Cu		16	15	24	28.5	72

† S concentrations for natural MIs in 74235 could be affected by sulfide globules in the MIs. Italicized S concentrations are corrected by excluding the cycles affected by sulfides and are less reliable.
‡ Italicized Li concentrations are for homogenized MIs, which have the concern of contamination during heating. Lithium concentrations for two MIs from 74235 are clearly affected by contamination and hence marked in red.

Table D1. Continued.

Lunar sample #	10020	74235				
MI type	Natural	Homogenized		Natural		
Homogenization T (ºC)	N/A	1280	1285	N/A		
Homogenization t (min)	N/A	10	2	N/A		
MI#	OL5	OL1*	OL2	NMI1a	NMI1b	NMI1b (repeated)
Host olivine Fo#	69.3	73.0	71.7	72.4	71.5	71.5
Host olivine	0.37	0.18	0.38	0.22	0.22	0.22
MI diameter (µm)	23	12	51	21	36	36
SiO_2 (wt%)	54.57	41.74	39.12	50.36	43.21	
TiO_2	3.6	12.84	11.77	3.23	12.13	
Al_2O_3	13.46	8.71	8.45	13.46	11.17	
FeO	5.55	13.66	20.16	10.1	15.5	
MnO	0.09	0.45	0.27		0.216	
MgO	1.68	5.77	7.24	2.39	2.74	
CaO	19.23	14.03	10.21	17.4	13.4	
Na_2O	0.564	0.34	0.46	0.56	0.51	
K_2O	0.09	0.13	0.07	0.05	0.1	
H_2O (ppm)	434	15.5	21.2	72.9	76.1	75.8
F	108.0	22.1	46.4	65.1	64.0	68.1
P	709	148	153	365	319	347
S†	495	437	1526	1490	952	*754*
Cl	10.98	1.39	3.70	3.8	3.64	3.81
Li‡	10.2	*275.5*	*62.6*	6.3	5.3	
Na	4472	2301	4154	3714	3488	
K	843	760	554	636	570	
Sr	175	200	189	188	201	
Y	150.2	91.3	99.2	111	128	
Zr	329	239	306	270	321	
Nb	21.4	21.2	28.0	29.5	24.9	
Ba	124	101	89	91	95	
La	15.1	6.1	6.1	7.4	9.0	
Ce	46.3	22.6	22.2	27.6	29.8	
Pr	7.4	3.9	4.0	4.8	5.8	
Nd	40.9	21.9	24.3	29	34	
Sm	15.6	8.3	9.6	11	13	
Eu	3.2	2.7	0.9	2	0.8	
Gd	23.6	11.7	14.9	16	17	
Tb	3.3	2.5	2.5	3.4	4.0	
Dy	29.9	17.3	19.6	23.8	26.0	
Ho	6.2	3.7	4.1	4.9	5.7	
Er	20.2	10.1	11.9	14.8	16.3	
Tm	2.7	1.3	1.8	1.6	2.3	

Yb	16.6	9.9	11.6	14.9	13.8	
Lu	2.8	1.5	2.0	2.3	2.1	
V		45.0	58.5	9.5	16.3	
Cr		3523	3298	997	622	
Mn		4768	3373	1936	1475	
Co		33	7.6	10	23	
Ni		3.8	1.1	0.6	2	
Cu		4.8	7.9	4.3	4	

* 74235 OL1 contains lower concentrations for all volatiles, which might be caused by diffusive volatile loss through micro-cracks during homogenization.
† S concentrations for natural MIs in 74235 could be affected by sulfide globules in the MIs. Italicized S concentrations are corrected by excluding the cycles affected by sulfides and are less reliable.
‡ Italicized Li concentrations are for homogenized MIs, which have the concern of contamination during heating. Lithium concentrations for two MIs from 74235 are clearly affected by contamination and hence marked in red.

Table D1. Continued.

Lunar sample #	74235					
MI type	Natural					
Homogenization T (ºC)	N/A					
Homogenization t (min)	N/A					
MI#	NMI3b	NMI4	EMB1	EMB3	NMI5	NMI6
Host olivine Fo#	72.0	75.0	72.3	71.9	70.6	71.3
Host olivine	0.50	0.62	0.22	0.20	0.22	0.18
MI diameter (µm)	14	58	45	37	13.9	11.9
SiO_2 (wt%)	53.15	50.33	49.46	51.69	51.17	52.39
TiO_2	3.07	6.15	3.94	3.6	5.77	3.2
Al_2O_3	14.15	12.89	12.58	12.94	13.55	13.95
FeO	8.38	9.57	11.14	10.33	9	8.12
MnO	0.14	0.14		0.17	0.15	0.14
MgO	2.27	3.08	3.17	2.72	2.08	2.39
CaO	17.22	17.12	17.21	16.72	17.37	17.98
Na_2O	0.65	0.63	0.55	0.56	0.6	0.58
K_2O	0.11	0.1	0.11	0.09	0.09	0.1
H_2O (ppm)	57.9	57.2	57	91	58.6	63.9
F	54.8	51.0	53.9	54.8	62.0	57.9
P	299	317	354	298	329	299
S†	*763*	*1145*	1566	1338	1037	810
Cl	3.23	3.52	3.66	4.8	4.15	3.69
Li‡		6.1	7.0	8.8		
Na		5363	5083	5012		
K		885	869	981		
Sr		245	237	214		
Y		144.6	141	110		
Zr		374	368	382		
Nb		30.4	28.0	61		
Ba		111	110	104		
La		10.0	11.0	7.7		
Ce		32.8	35.2	28		
Pr		6.3	5.7	4.5		
Nd		37.6	35	28		
Sm		14.8	15	12		
Eu		2.3	4	3		
Gd		18.7	19	19		
Tb		4.0	3.7	3.6		
Dy		26.8	25.4	24		
Ho		6.1	4.7	4.8		
Er		15.6	16.6	13.3		
Tm		2.1	2.3	2.0		

Yb		14.9	14.2	12.0		
Lu		2.0	2.6	2.4		
V		25.0	26.6	52		
Cr		1479	1206	2778		
Mn		2746	1772	2451		
Co		39	18	17		
Ni		2	0.9	0.8		
Cu		2.9	5	4		

† S concentrations for natural MIs in 74235 could be affected by sulfide globules in the MIs. Italicized S concentrations are corrected by excluding the cycles affected by sulfides and are less reliable.
‡ Italicized Li concentrations are for homogenized MIs, which have the concern of contamination during heating. Lithium concentrations for two MIs from 74235 are clearly affected by contamination and hence marked in red.

Table D1. Continued.

Lunar sample #	74235						
MI type	Natural		Interstitial glass				
Homogenization T (ºC)	N/A		N/A				
Homogenization t (min)	N/A		N/A				
MI#	NMI7	NMI11	Matrix1a	Matrix1b	Matrix2@1	Matrix2@3	Matrix2@4
Host olivine Fo#	69.3	70.5					
Host olivine	0.14	0.21					
MI diameter (μm)	35.4	23.7					
SiO_2 (wt%)	50.97	52.18	56.56	56.56			
TiO_2	4.34	3.998	2.34	2.34			
Al_2O_3	12.59	13.51	16.15	16.15			
FeO	10.71	9.59	12.37	12.37			
MnO	0.19	0.19	0.18	0.18			
MgO	2.29	2.31	1.78	1.78			
CaO	17.03	16.73	9.8	9.8			
Na_2O	0.57	0.63	1.13	1.13			
K_2O	0.09	0.11	0.186	0.186			
H_2O (ppm)	88.4	68	108	125	88	115	116
F	75.7	88	100.1	138.1	91	108	109.1
P	356	317	347	361	320	373	375
S†	1187	675		*1138*			
Cl	4.06	3.38	5.5	6.3	5.2	6.8	7.28
Li‡		11.8	11.6	12.7	11.5	11.3	10.2
Na		5255	8008	7873	5156	5547	4760
K		812	1173	1137	785	897	735
Sr		241	371	320	312	288	285
Y		153	134.7	140.6	105.9	104.2	115.8
Zr		384	405	506	296	293	299
Nb		30.3	42.1	57.7	33.0	35.7	34.7
Ba		108	179	149	121	121	118
La		11.2	14.7	12.2	12.3	11.0	11.6
Ce		35.9	44.9	39.0	38.7	35.6	39.3
Pr		6.9	7.3	6.8	6.5	5.9	7.1
Nd		38	42.9	41.1	35.5	34.3	39
Sm		17	14.5	14.6	13.5	11.7	13.6
Eu		5	1.9	3.5	2.9	2.8	2.5
Gd		21	19.4	19.6	15.5	13.9	16.4
Tb		4.1	3.6	3.9	2.8	2.7	3.3
Dy		31.9	25.3	26.8	19.7	20.0	21.8
Ho		6.2	5.0	6.0	3.7	4.3	4.3
Er		17.0	15.2	16.6	12.1	11.8	12.9
Tm		2.3	2.2	2.17	1.8	1.9	2.0

Yb		17.0	15.4	16.7	12.3	11.9	12.9
Lu		2.7	2.0	2.6	2.0	1.7	2.1
V			56	17.9			
Cr			2133	1596			
Mn			2912	3036			
Co			17	27			
Ni			0.7	0.8			
Cu			11	7			

† S concentrations for natural MIs in 74235 could be affected by sulfide globules in the MIs. Italicized S concentrations are corrected by excluding the cycles affected by sulfides and are less reliable.
‡ Italicized Li concentrations are for homogenized MIs, which have the concern of contamination during heating. Lithium concentrations for two MIs from 74235 are clearly affected by contamination and hence marked in red.